Cranfield University

Abilio Neves Garcia

Multiple Site Damage of Aeronautical Riveted Joints

School of Industrial and Manufacturing Science

PhD Thesis

Cranfield University

School of Industrial and Manufacturing Science

Advanced Materials Department

PhD Thesis

2005

Abilio Neves Garcia

Multiple Site Damage of Aeronautical Riveted Joints

Supervisor: Prof. P. E. Irving

September 2005

This thesis is submitted to fulfil the requirements for the degree of Doctor of Philosophy

ABSTRACT

Among all aeronautical structures prone to develop MSD, riveted lap joints in the fuselage have been identified as being the most susceptible. Recent recommendations by regulators to avoid MSD threat stipulate an Inspection Starting Point (ISP) and a Structural Modification Point (SMP) in the life of aircraft. These points can be defined in terms of MSD analysis and the capability to accurately calculate service life to MSD onset becomes of considerable importance. To investigate this failure mode, a probabilistic model for MSD assessment considering both fatigue crack initiation and crack propagation as random variables was proposed. The fatigue crack initiation stage of the model differed from other published models for incorporating continuing damage assumption instead of a damage accumulation technique for re-initiation of fatigue cracks at crack-free fatigue critical locations. The crack propagation stage of the model was firstly performed deterministically by means of a dual boundary element computer code; and, secondly, probabilistic crack growth treatment was incorporated in a simple way. The results from the MSD assessment model provided good agreement with published experimental work on fatigue of lap-splice joints and with other model for the same geometrical configuration. In order to fulfil a lack from the literature, the probabilistic MSD model was employed to investigate variables influencing MSD. The variables were related to possible changes in the standard deviation for fatigue crack initiation, uniform and non-uniform hole pin-loadings, nominal stress level and high rivet squeeze force. The parametric study showed that the ISP and the SMP can be considerably affected. Further results include the identification of a conflict between two different structural safety criteria and the proposition of a new one; the use of uniform pin-loading distribution with peak loads from a non-uniform pin-loading distribution was suggested to avoid non-conservatism specially at low cumulative probabilities of failure; a clear tendency to decrease the mean time for the lead crack propagation as the number of MSD-like scenarios increased was verified, but not always a bigger number of nucleated cracks per damage scenario gave the smallest time for crack propagation and the crack nucleation sequence was more important than the number of nucleated cracks per damage scenario. To investigate the effects of high rivet squeeze on MSD, an experimental work was carried out to obtain input S-N fatigue data. Recent findings from the literature established the benefits that high squeeze force can provide for the mean time to fatigue crack initiation, but no probabilistic analysis was undertaken comparing different squeeze force values. The results of such analysis reviewed that the whole MSD failure process was retarded and the number of MSD-like scenarios considerably reduced, demonstrating that high rivet squeeze force is extremely beneficial for MSD prevention. Finally, the probabilistic model was employed for comparison to in-service MSD data from pressurized fuselage panels. During the preliminary modelling stage, it was found clear evidences that S-N input data obtained from good quality riveted test specimens could not be used for MSD assessment of real pressurized fuselage panels, and it was assumed open hole quality input S-N fatigue data. The results demonstrated to be rationally conservative compared to in-service findings. In-service data indicated that both the ISP and the SMP were well established from the simulations, and failure due to MSD occurrence would not threaten structural safety during the monitoring period.

ACKNOWLEDMENTS

I would like to express my sincere appreciation and my best regards to Professor Phil Irving for his support, supervision and guidance during the whole period of this research.

I would like to express my appreciation to Dr. Nelson Krahenbuhl Salgado for his help on the dual boundary element technique and for his permission to use the DTD code in this work.

My acknowledgements to the Brazilian Air Force, in regards to Brigadier General Sabino Freire and Eng. Flavio Araripe d'Oliveira, and to the Civil Aviation Authority (CAA) from the U.K., in regards to Prof. John Bristow and Mr. Richard Minter, for trusting myself and sponsoring this work.

Finally, I would like to express my gratitude to my wife Celina and my children Marjorie and Victor for their love and for supporting me in moments of difficulty; and to my parents Sergio and Neusa for their guidance in my life.

LIST OF CONTENTS

LIST OF FIGURES

LIST OF TABLES

NOMENCLATURE AND ABBREVIATIONS

a	Crack half-length for a crack free to extend at both ends, or crack length for a crack free to extend at one end only
A	Cross sectional area (W.t)
a_c	Critical crack size
a_{cd}	Crack size for continuing damage assumption (0.127 mm)
$a_{crit\ LD}$	Critical crack size for local damage
$a_{crit\ WFD}$	Critical crack size for WFD
a_{det}	Detectable crack size
a_f	Final crack size
a_{lead}	Lead crack size
a_{msd}	MSD crack size
a_0	Initial crack size
A_1, A_2	Empirical constants for different fastener material
α	Gaussian random distribution
BE	Boundary element
BEM	Boundary element method
β	Geometric correction factor
β_{lead}	Lead crack geometric correction factor
β_{msd}	MSD crack geometric correction factor
CAA	Civil Aviation Authority
d	Rivet formed head due to riveting process
DBE	Dual boundary element
DBEM	Dual boundary element method
DSG	Design service goal
DTD	Damage tolerance design
da/dn	Fatigue crack growth rate
d/d_0	Rivet formed head ratio
d_0	Original hole diameter

Δ	Non-recoverable work associated with the permanent deformation at the crack tip
Δa	Crack increment size
e	Edge distance
E	Young modulus
EIFS	Equivalent initial flaw size
FE	Finite element
FEM	Finite element method
FCL	Fatigue critical location
F_{sq}	Rivet squeeze force
F_{WFD}	Repeat inspection intervals factor
$f_{ij}(\theta)$	Trigonometric functions
ϕ	Fastener diameter
G	Strain energy release rate per unit area of crack growth
h_1, h_2	Sheet thicknesses
IP	Inspection Period
ISP	Inspection Starting Point
I_{WFD}	Repeat inspection intervals
J	J-integral
J^I	J-integral for mode I loading
J^{II}	J-integral for mode II loading
K	Stress intensity factor
K_t	Elastic stress concentration factor
ΔK	Stress intensity factor range ($K_{max} - K_{min}$)
ΔK_{eff}	Effective stress intensity factor range
K_c	Critical value of stress intensity factor or plane stress fracture toughness
K_0	$\sigma\sqrt{\pi a}$; where σ as the same definition of S
K_I	Stress intensity factor (mode I)
K_{Ic}	Plane strain fracture toughness in Mode I
K_{II}	Stress intensity factor (mode II)

L	Ligament yield length
LD	Local damage
LEFM	Linear elastic fracture mechanics
LPSF	Limit to proper structural functioning
LTR	Load transfer ratio
L_{LD}	Period for detectable local damage
L_{WFD}	Period for detectable WFD
MSD	Multiple site damage
N	Number of cycles in general
NU	Non-uniform pin-loading
N_f	Number of cycles to failure (TTCI + TCP)
$\overline{N_f}$	$\overline{TTCI} + \overline{TCP}$
N_0	Number of cycles to develop a crack size a_0
μ	Mean value
OEM	Original equipment manufactures
p	Pitch distance
P_{bp}	Bypass load
P_i	Tensile load
P_{max}	Maximum tensile load
P_{min}	Minimum tensile load
P_{pin}	Pin-load
P_{gross}	Gross load
R	Stress amplitude ratio (S_{min} / S_{max})
RFL	Random fatigue life
(r,θ)	Polar coordinates with origin at the crack tip
s	Estimated standard deviation
S	Nominal gross section stress in crack-free part of component
S	Local stress
S_i	Tensile stress
SIF	Stress intensity factor
SMP	Structural Modification Point

S_c	Critical stress at failure
SIF	Stress intensity factor
S-N	Stress-life curve
S_0	Remote tensile stress
ΔS_{eff}	Effective stress range
S_{max}	Maximum stress value
S_{min}	Minimum stress value
S_{op}	Crack opening stress value
σ	Standard deviation
σ_{bp}	Bypass stress
σ_{br}	Bearing stress
σ_c	Critical stress corresponding to a_c
σ_{gross}	Gross stress or far field nominal stress
σ_{ij}	Stress field component
σ_{LU}	Link-up stress
σ_{YS}	Yield strength of the material
t	Thickness
TCP	Time for crack propagation
$\overline{TCP}$	Mean time for the lead crack propagation
TTCI	Time to crack initiation
$\overline{TTCI}$	Mean time for the lead crack initiation
θ_t	Angular coordinate centred at the crack tip
Γ	Work required to form a unit area of new crack surface
U	Uniform pin-loading
UK	United Kingdom
USAF	United States Air Force
v	Coefficient of variation
v'	Estimated coefficient of variation
W	Width

WFD	Widespread fatigue damage
$\bar{x}$	Estimated mean value

Chapter 1

1. INTRODUCTION

1.1. Multiple Site Damage and its Importance as a Research Case

On 28th of April of 1988, the civil aviation world experienced the accident of the Aloha Airlines Boeing 737. The airplane had a sudden fatigue failure of longitudinal riveted lap splice joints which caused part of its fuselage to be lost during flight (Figure 1.1.1). Many small collinear cracks occurred and linked up forming a large crack as a result of internal pressurization of the fuselage [1]; and this type of failure, once completely neglected, has its own name: Multiple Site Damage (MSD).

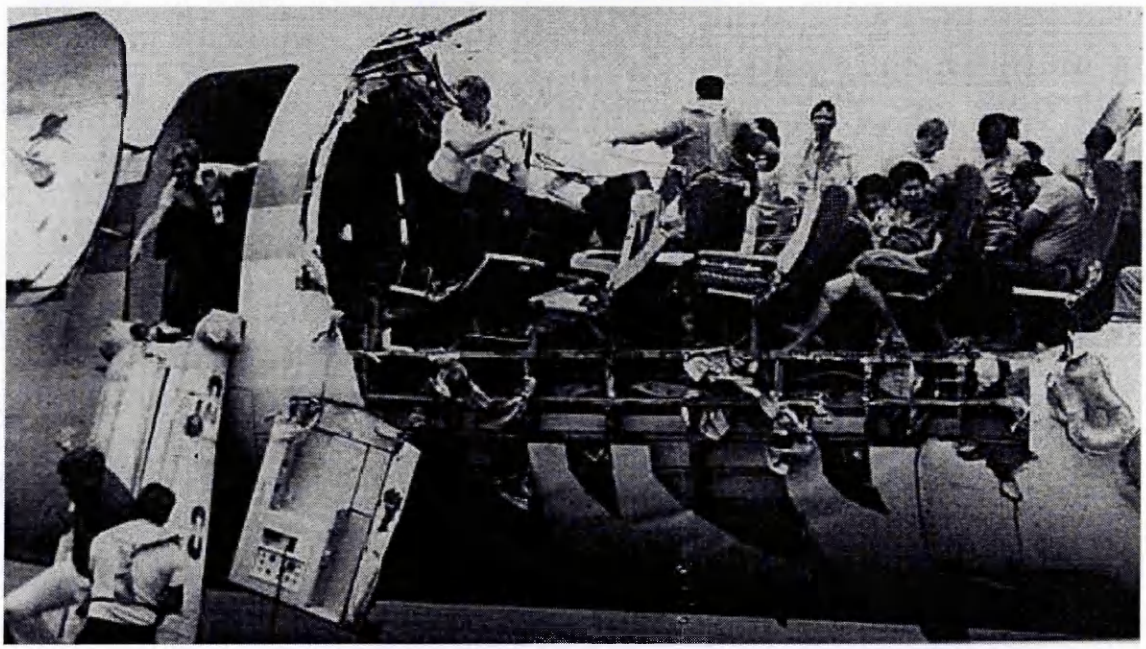

Figure 1.1.1: Aloha Airlines Flight 243 after landing [1].

MSD is basically a problem connected to ageing aircraft, and it is characterized by the development of simultaneous small fatigue cracks at multiple sites in the same structural element (Figure 1.1.2). Figure 1.1.3 illustrates the difference between a local damage and MSD damage at the same structural element; where 'LD' means local damage, 'WFD' means widespread fatigue damage, '$a_{crit\ LD}$' means critical crack size

for local damage, '$a_{crit\ WFD}$' means critical crack size for WFD, 'a_{det}' means detectable crack size, 'L_{LD}' means period for detectable local damage and 'L_{WFD}' means period for detectable WFD.

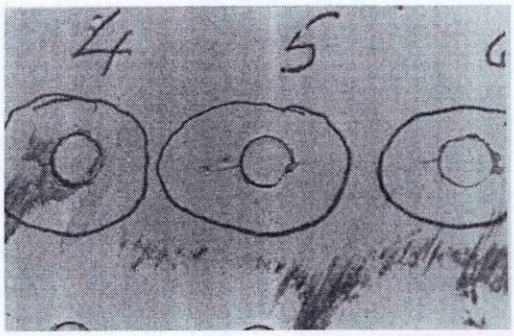

Figure 1.1.2: MSD in a row of riveted holes at a pressurized fuselage panel. [2]

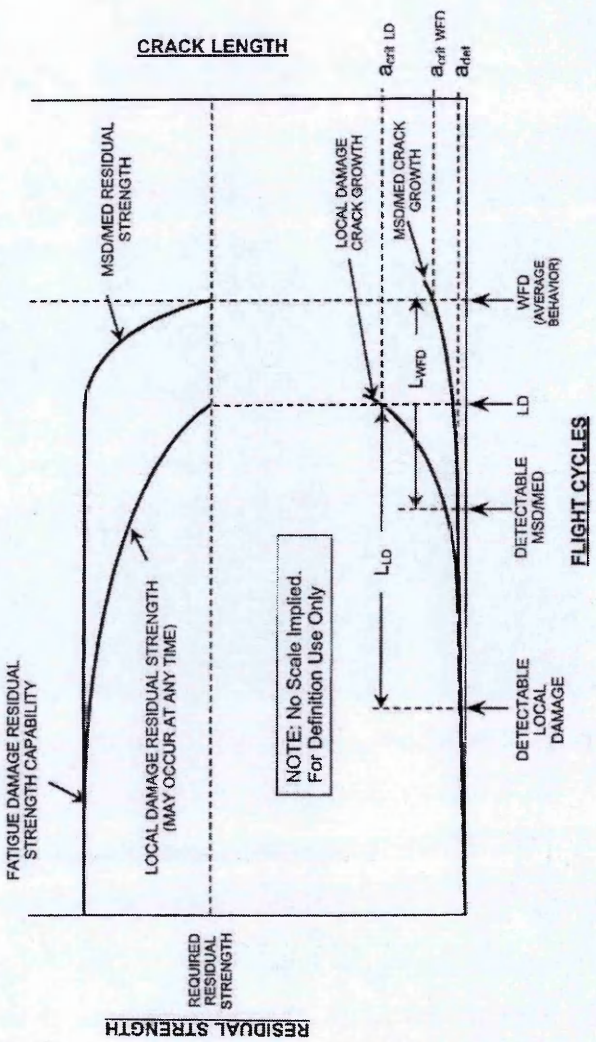

Figure 1.1.3: Difference between local damage and MSD behaviours [3].

From Figure 1.1.3, it can be seen that in MSD situations there is a rapid decrease in residual strength and crack growth is accelerated compared to the local damage case; showing that crack growth and residual strength degradation occurs in a faster way in the presence of MSD. It is also expected that MSD occurs later in the life of a structural component than for the case of a local damage development, and the inspection period for the case of MSD occurrence is diminished compared to the local damage one.

Large passenger aircraft when kept in service for an extended period of time suffer from the development of a range of damage processes associated with ageing aircraft. These can take the form of corrosion, together with various forms of fatigue failure. MSD is one of the major threats to airworthiness of such ageing aircraft. Statistics show that after the year 2000, more than 60 % of the worldwide fleet of aircraft manufactured in the US would already be more than 20 years old [4]; and that by the year 2005 more than 30 Airbus A300 will be operating beyond their design service goal [5]. The reason for this crescent number of aging aircraft relies on economical reasons. While an average cost of a new commercial aircraft is about US$ 55 million, a major overhaul for an aging aircraft Boeing 727 can reach up to US$ 2 million depending on how much work needs to be done [4]; and these costs explain the increase in the aging aircraft fleet as well as fatigue life extension programs being undertaken by aircraft manufactures [5]. One of the main targets of such aging aircraft life extension programs is to prevent MSD occurrence by its prediction based on fatigue tests, service experience and analysis performed by MSD assessment models.

Among all aeronautical structures prone to develop MSD, riveted lap-splice joints in the fuselage have been identified as being the most susceptible [3]. Recent recommendations by regulators to avoid this MSD threat [3] stipulate an Inspection Starting Point (ISP) and a Structural Modification Point (SMP) in the service life of aircraft. These points can be defined in terms of MSD analysis results, test results or by service experience. The intention is that the aircraft shall not be operated while there is a significant probability that MSD is present. Capability to accurately calculate service

life to MSD onset becomes of considerable importance, and MSD modelling plays a fundamental role for helping MSD prevention.

One of the most important achievements in MSD understanding, during the past decade, is that there is general agreement throughout the literature that MSD largely depends on probabilistic effects; and approaches intending for MSD assessment might consider these effects [5].

Although several MSD models have been proposed, and they have varied in their built-in assumptions and calculation techniques, MSD assessment models which can incorporate simplifying assumptions are still welcome; and the use of such models for investigation of variables influencing MSD assessment is an open field. The work described in this thesis is concerned in giving its contribution to some fields which are in need of further investigation on MSD modelling and on variables that might influence its behaviour.

1.2. Objectives of This Work

The research presented in this thesis has the following objectives:

1. Develop a methodology for MSD assessment incorporating a simplifying assumption.
2. Compare the methodology to laboratory MSD fatigue tests of lap joints and/or in-service data for validation of the results.
3. Use the methodology to perform a parametric study to investigate variables that might influence MSD assessment.
4. Conduct fatigue tests on riveted lap joints to investigate the effect of rivet squeeze force on MSD behaviour.

1.3. Thesis Structure

The current research is reported in this thesis in the following sequence:

Chapter 2: Presents a review on the literature regarding terminologies, definitions and concepts for multiple cracking; a theoretical background; methodologies for multiple site damage assessment and rivet squeeze force experimental work from the literature.

Chapter 3: Presents the fundaments of the dual boundary element computer code used for crack propagation in this work; a dual boundary elements cracked strap lap joint model and a wide lap joint model subjected to MSD. Both lap joint models idealized are compared to corresponding finite element models.

Chapter 4: Presents the methodology proposed in this work for MSD assessment of riveted joints.

Chapter 5: Presents the experimental work procedures.

Chapter 6: Presents the results of this work regarding the experimental work; the MSD assessment model comparison to experimental data from the literature; a parametric study performed with the proposed MSD assessment model; and a comparison of the MSD assessment model output to in-service data from the literature.

Chapter 7: Presents the discussions on the results from chapter 6.

Chapter 8: Presents the conclusions from the discussions given in chapter 7.

Chapter 9: Presents suggestions for future work.

Chapter 2

2. LITERATURE REVIEW

2.1. Terminologies and Definitions for Multiple Cracking Occurrence

The Airworthiness Assurance Working Group (AAWG) [3] developed a terminology regarding the subject of multiple cracking scenarios. This terminology, which is used throughout this work, is presented as follows:

Damage Tolerance - is the attribute of the structure that permits it to retain its required residual strength without detrimental structural deformation for a period of use after the structure has sustained specific levels of fatigue, corrosion, accidental or discrete source damage.

Widespread Fatigue Damage (WFD) - is the presence of simultaneous cracks at multiple structural details that are of sufficient size and density whereby the structure will no longer meet its damage tolerance requirement (i.e. to maintain its required residual strength after partial structural failure).

Multiple Site Damage (MSD) - is a source of widespread fatigue damage characterized by the simultaneous presence of fatigue cracks in the same structural element (i.e. fatigue cracks that may coalesce with or without other damage leading to a loss of required residual strength).

Fatigue Crack Initiation – is a point in time when a finite fatigue crack is first expected.

Monitoring Period – is the period of time when special inspections of the fleet are initiated due to an increased risk of MSD, and ending when the point of WFD is established.

Point of WFD – is a point reduced from the average expected behaviour, i.e. lower bound, so that operation up to that point provides equivalent protection to that of a two-lifetime fatigue test.

Inspection Starting Point (ISP) – point in time where the **monitoring period** is started.

Structural Modification Point (SMP) – this point is also called the **point of WFD.** When the **point of WFD** (or **SMP**) is reached, no airplane may be operated without further structural evaluation, structural modification or part replacement.

Figure 2.1.1 presents an illustration on how the monitoring period is established [3]; where 'I_{WFD}' means repeat inspections interval and 'WFD' means widespread fatigue damage. The establishment of the monitoring period is the main reason for the existence of MSD models. From Figure 2.1.1, the monitoring period starts at the point of MSD fatigue crack initiation, which is usually called by ISP, and ends at the point of WFD (SMP point). The monitoring period might be established in a region of detectable MSD cracks, and the probability for MSD occurrence should be small. If no MSD cracking is detected by the time the point of WFD is reached, then the predicted point of WFD could be re-evaluated. During the monitoring period, it is defined the I_{WFD} which is the repeat inspections interval. The I_{WFD} is established in a form that several opportunities for MSD crack detection should exist. The establishment of the monitoring period is derived from the mean failure behaviour of the WFD distribution (or the MSD failure distribution). The points of ISP and SMP are established by dividing the mean cycles for MSD failure by typical factors of, respectively, 3 and 2; in such a sense that the point of SMP provides equivalent protection to that of a two-lifetime fatigue test.

Figure 2.1.2 presents a graphical illustration with a hypothetical example for the establishment of the ISP and the SMP points. As is can be seen, the mean MSD failure behaviour was 'calculated' as 90,000 flight cycles, and by dividing this value by 3 and 2 the values of, respectively, the ISP and the SMP are 30,000 and 45,000 flight cycles.

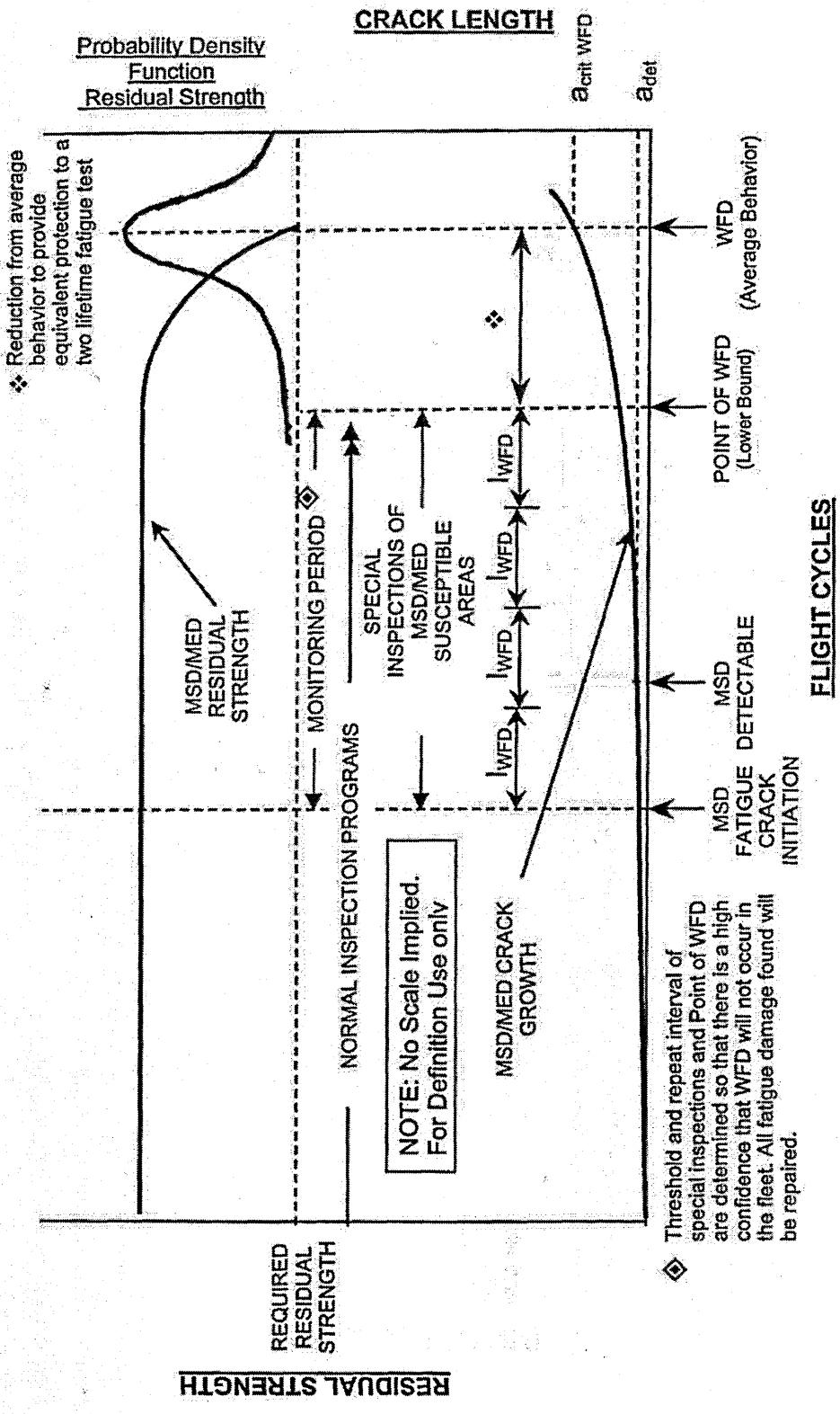

Figure 2.1.1: Determination of the monitoring period [3].

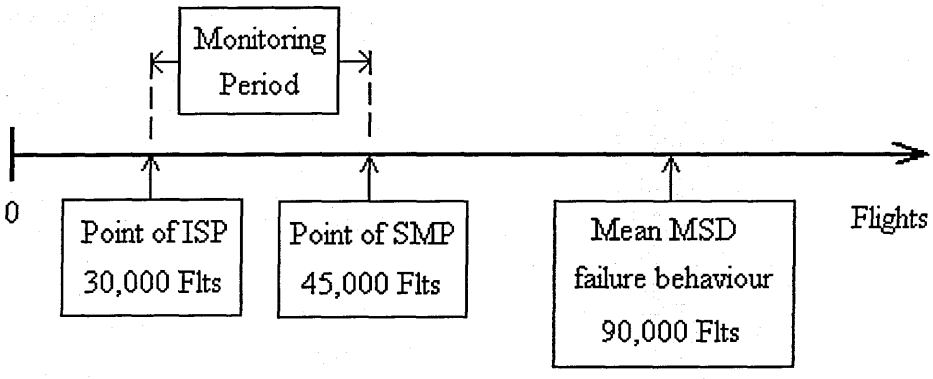

Figure 2.1.2: Graphical example for the establishment of the ISP and the SMP.

2.2. Background Theory

Metal Fatigue failure is defined as cracking resulting from repeated applications of stress bellow the material ultimate static strength. Structures are not designed to fail at a single application of the load and fatigue failure happens after the application of thousands of load cycles [6]. The whole fatigue failure process is normally approached by separating it into three stages: fatigue crack initiation (nucleation), fatigue crack propagation and final fracture (failure). The time in life when fatigue crack initiation ends and fatigue crack propagation starts is a complete arbitrary definition, since fatigue can be considered as a smooth process [7].

In this work, the end of fatigue crack initiation stage is identified by the occurrence of a detectable through-the-thickness macro crack obtained from S-N fatigue test data of simple coupon specimens (stress-life approach). From the point of the end of fatigue crack initiation, the crack propagation stage is started and it is calculated based on Linear Elastic Fracture Mechanics (LEFM) theory until the residual strength of the structure is lost.

There are many published theories to describe the previous stages and they can be found in several textbooks. It is out of the scope of this thesis to provide a complete lesson on metal fatigue and fracture mechanics theories. The aim of this section is to describe the fundamental concepts of fatigue and fracture mechanics that are relevant to this research

investigation. Unless otherwise stated, all theory presented has been derived from Suresh [8], Niu [9], Broek [10], Aliabadi [11], Irving [12] and Zhang [6].

2.2.1. The Origin of Fatigue Problem in Riveted Joints

Airframes are mostly constructed by assembling many pieces of metal sheets together by means of countless rows of rivets, and riveted lap joint fuselage panels are a typical example of it. The basic problem with such structures is that holes are a well known source for stress concentration which is the primary factor affecting fatigue life. The elastic stress concentration factor K_t is defined by the following expression,

$$K_t = \frac{S}{\sigma_{gross}} \qquad 2.2.1.1$$

Where S is the local stress and σ_{gross} is the far field nominal stress applied.

Figure 2.2.1.1 presents the case of a localized stress concentration at the 3 and 9 o'clock positions of an open hole border in an infinite plate under uniaxial tension with value σ_{gross}. As it can be seen, in such a case the local stresses are raised to a value of $3\sigma_{gross}$. In the case of a row of pin-loaded holes, the stress concentration at the 3 and 9 o'clock positions of each single hole border is even worse, and the nominal local elastic stress (theoretical stress) can easily reach 4 or 5 times the value of the nominal tension applied. In real life, the local stress values are limited due to plasticity and elastic stress values higher than the ultimate failure stress of the material are never achieved. Figure 2.2.1.2 illustrates an example of the variation of the elastic stress concentration factor for a hole with fastener, in a row of fastened holes, as a function of the number of fastener rows.

In riveted lap joints the fastener load distribution may vary depending on the number of riveted rows. Considering the example of a strap lap joint, if a single or a double row of fastened holes is employed then the load each rivet carries is equal and, in the case of 2

rows, is equally divided by them. For the case of 3 or more rows of fastened holes then the external rows are overloaded compared to the inner ones. Figure 2.2.1.3 shows an example of a strap lap joint containing 3 rows of fastened holes. As it can be seen, the fastener load carried by the external rows is equal but higher than the load carried by the inner row. The observed differences on the fastener loads are related to different types of fasteners flexibility, and the more flexible the fastener the more evenly fastener load distribution will be.

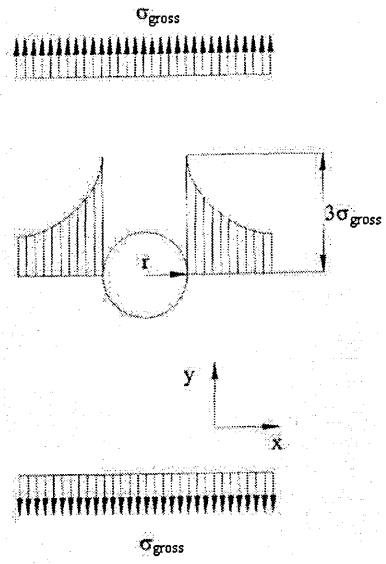

Figure 2.2.1.1: Localized stress concentration in a hole under uniaxial tension in an infinite plate.

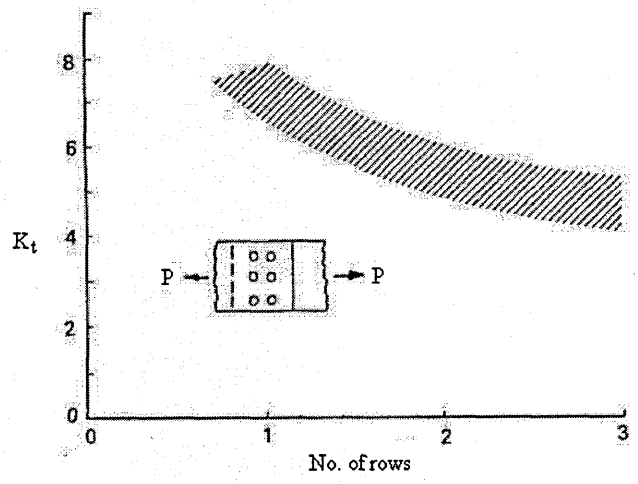

Figure 2.2.1.2: Variation of stress concentration factor as a function of the number of rows of fasteners [9].

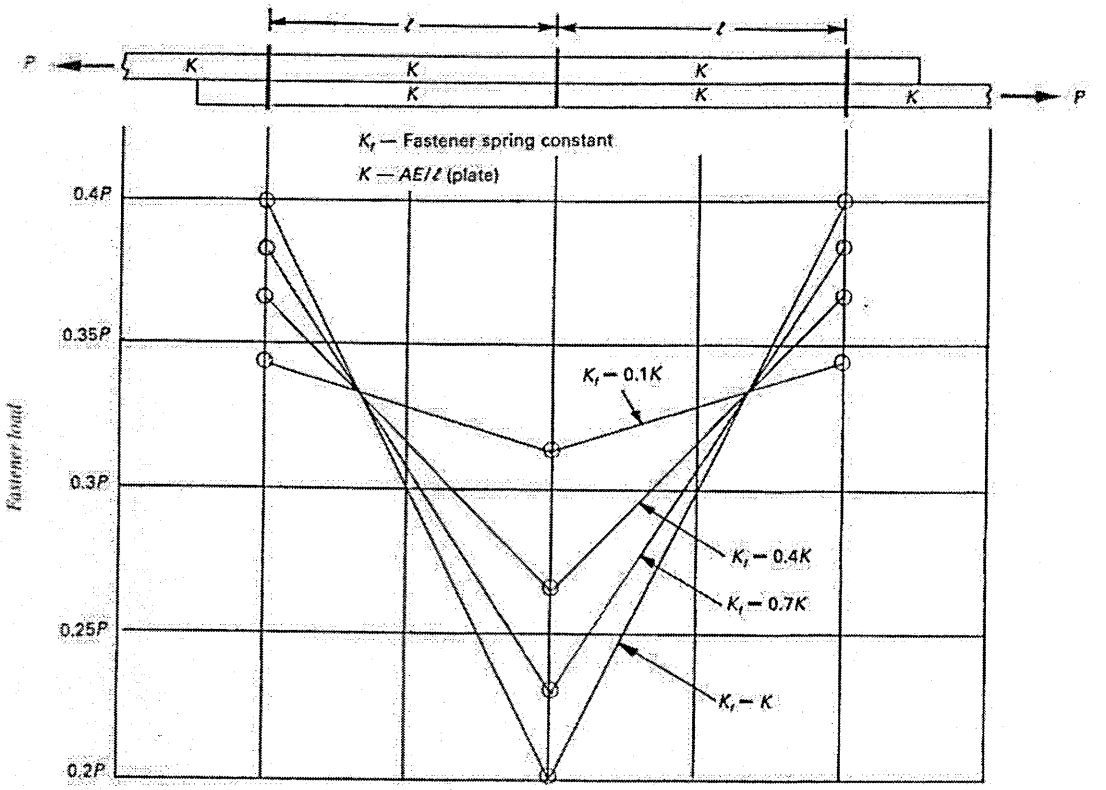

Figure 2.2.1.3: Fastener load distribution of three rows of fasteners [9].

The MSD threat is, therefore, closely connected to the proximity of many structural details (such as pin-loaded holes) which are prone to develop fatigue cracks, due to its stress raising characteristics, in a relatively close period of time [3]. This multiple cracking pattern can, in a sudden, link-up to form a huge crack that degrades the capability of the entire structure to sustain normal operational loads. One possible way to assess the period of time to multiple cracking existences is described in the following section.

2.2.2. MSD Life Prediction in Riveted Joints by Means of S-N Fatigue Data

The stress-life approach to characterize the fatigue life in terms of nominal stress amplitudes as a function of number of load cycles originated from the work of Wöhler in mid 1800s. The Wöhler curve or S-N curve can be obtained experimentally for a particular structural component by conducting a number of fatigue tests performed with a constant mean stress and constant stress amplitude (constant amplitude fatigue tests).

By selecting different stress levels, the resulting S-N curve is represented by a best-fit plot that crosses the corresponding mean value for the experimental points obtained. The S-N curve is, therefore, a best-fit curve which is also called the 50% probability curve; and it is quite commonly presented in the literature without any information of the scatter inherent to the fatigue process.

When it comes to analyse the fatigue life of fuselage riveted lap joints, MSD is the main concern since many structural details, such as pin-loaded holes, are placed side-by-side in a single row. A typical aeronautical configuration for the fuselage consists of a lap joint containing 3 rows of fastened holes. From the point of view of the analyst only one row of fastened holes is generally assessed for MSD occurrence. As illustrated in Figure 2.2.1.3, the external rows are the ones that carry the biggest fastener loads and fatigue cracks are prone to develop firstly in such places. The tendency for fatigue crack occurrence at the upper or lower rows (critical rows) of lap joints is supported by fatigue tests [13, 14] and in-service findings [2, 15].

Once the critical row of fastened holes is defined (highly stressed one), the fatigue analysis for MSD assessment starts by determining the fatigue properties of a single structural detail. For the case of fuselage lap joints, the simplest way to obtain such fatigue properties is by performing constant amplitude fatigue tests of simple coupon specimens manufactured with the same material, construction techniques and subjected to the same loads as for the lap joint intended for analysis. The test specimen geometry is the same as for the lap joint but with width equal to one pitch distance (distance from centre-to-centre of two adjacent fastened holes in the same row). This procedure is widely accepted and it is presented in many publications, such as in references [3, 16, 17, 18].

It is well known that the fatigue life of structural components present considerable scatter when loaded under the same stress cycles. The sources for such scatter are numerous and they are described in many publications, such as Schijve [19]. Figure 2.2.2.1 presents a sketch of a typical S-N curve together with 3 different statistical distributions to represent the scatter bands. This work is concerned with the log-normal

distribution for fatigue crack initiation and the probability density function of this distribution is represented as the top one from Figure 2.2.2.1 for the alternate stress level S_{a1}. The log-normal distribution has been reported to consistently provide a best fit to fatigue data obtained from numerous sources of constant amplitude fatigue tests for aluminium 2024 [20].

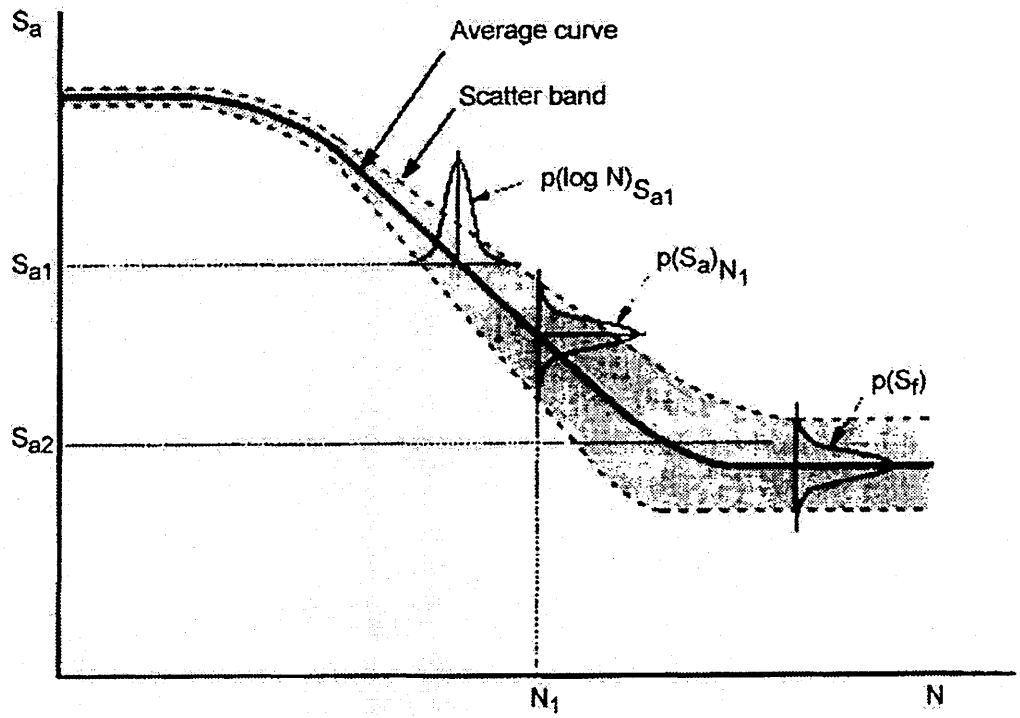

Figure 2.2.2.1: Typical S-N curve and scatter bands plotted with three different probability density functions [19].

The most well known distribution function is called the normal or Gaussian distribution, and it is defined by the probability density function [20],

$$p(x)dx = \frac{1}{\sqrt{2\pi\sigma^2}} \exp -\frac{1}{2}\left(\frac{\mu - x}{\sigma}\right)^2 dx \qquad 2.2.2.1$$

Where $p(x)d(x)$ is the probability of occurrence of an event between x and $x+dx$, and μ and σ are the population mean and standard deviation respectively. When a

normal distribution of the logarithm of the number of cycles to failure is used, the above expression must be replaced by [20],

$$p(\log N)d(\log N) = \frac{1}{\sqrt{2\pi\sigma^2}}\exp -\frac{1}{2}\left(\frac{\mu - \log N}{\sigma}\right)^2 d(\log N) \qquad 2.2.2.2$$

Where μ and σ are now the mean and standard deviation of log (life) and N is the number of cycles to failure of a randomly selected specimen. For equation 2.2.2.2, the best estimates of μ and σ that can be obtained from a sample of 'n' test specimens are given by [20],

$$\bar{x} = \overline{\log(N)} = \frac{\sum_{i=1}^{n} \log N_i}{n} \qquad 2.2.2.3$$

$$s = \left\{\frac{\sum_{i=1}^{n} (\log N_i)^2 - n(\overline{\log N})^2}{n-1}\right\}^{\frac{1}{2}} \qquad 2.2.2.4$$

What can be clearly seen from Figure 2.2.2.1 (log-normal distribution) is that the fatigue life for crack initiation is not deterministic for the same stress amplitude, and this fact is the basis for initiation of MSD cracks in a row of holes. Supposing that each hole is subjected to the same loading conditions and that there are 2 fatigue critical locations per hole (3 and 9 o'clock positions of the hole border), then if 'n' holes are considered '2n' different fatigue crack initiation lives can be assigned, within the same row of holes, by the log-normal distribution from Figure 2.2.2.1. If the mean time to crack initiation and the corresponding standard deviation (scatter) values for a single rivet pitch are known, it is possible to use a random process to derive as many damage scenarios as necessary for the initiation of fatigue cracks in a row of fastened holes (critical row). As far as the fatigue life follows a log-normal distribution, the

randomization process from Press [21] can be used [18]. This process is detailed in another chapter where the MSD assessment methodology from this work is proposed.

2.2.3. Fracture Mechanics Fundaments

The fracture phenomenon was firstly investigated by Griffith [22] by carrying out experimental studies on glass. To explain the differences on residual strengths in glass rods, Griffith postulated that the existence of crack-like flaws could increase in size by the application of external load and that crack growth was controlled by the balance between the available strain energy and the energy required to form new crack surfaces. He postulated that if the strain energy released by the strain field when the crack advanced a small distance was greater than the energy required to form the new surfaces then unstable crack growth would take place if,

$$G \geq 2\Gamma \qquad 2.2.3.1$$

Where G is the strain energy release rate per unit area of crack growth and Γ is the work required to form a unit area of new crack surface (2 surfaces). Griffith showed that the strain energy release rate was given by,

$$G = \frac{\pi\sigma^2 a}{E} \qquad 2.2.3.2$$

Where σ is the remotely applied tensile stress from the crack, a is the semi-length of a crack and E is the Young's modulus of the material. From equations 2.2.3.1 and 2.2.3.2, at the onset of instability the failure stress σ_c is related to the critical crack length a_c by,

$$\sigma_c \sqrt{a_c} = \text{constant} \qquad 2.2.3.3$$

Griffith experiments were conducted on glass which is a brittle material where fracture happens with little or no permanent deformation. Some years later, Irwin [23] and

Orowan [24] extended the work of Griffith to ductile materials, which is the case of metals. They suggested that unstable crack growth would occur if,

$$G \geq 2\Gamma + \Delta \qquad 2.2.3.4$$

Where Δ is the non-recoverable work associated with the permanent deformation at the crack tip.

By using linear elasticity theory, Irwin [25] showed that the two dimensional stress field in the vicinity of the crack tip (Figure 2.2.3.1) was given by,

$$\sigma_{ij}(r,\theta) = \frac{K}{\sqrt{2\pi r}} f_{ij}(\theta) + \text{other terms} \qquad 2.2.3.5$$

Where 'i' and 'j' mean 'x' and/or 'y' coordinates, σ_{ij} is the stress field component at the point (r,θ) near the crack tip, (r,θ) are polar coordinates with origin at the crack tip and $f_{ij}(\theta)$ contains trigonometric functions. As the value of r tends to zero, the first term in equation 2.2.3.5 dominates and the other terms are constant or tend to zero. The constant K in the first term is known as the stress intensity factor and, therefore, it follows that the stress field in the vicinity of the crack tip is characterized by K.

Irwin [25] also derived a relationship between the strain energy release rate and the stress intensity factor near the crack tip,

$$G \propto K^2 \qquad 2.2.3.6$$

The proportionality in equation 2.2.3.6 is a function of elastic constants of the material. Equation 2.2.3.6 provides a relationship between the crack tip stress field and the energy balance criterion that can be interpreted in terms of critical values of K required for crack growth (stable or unstable). Therefore, the crack growth is characterized by the parameter K. This implies that two different cracks having the same value of K will

behave in the same manner. K is a function of the crack size and shape, the type of loading and the geometrical configuration of the structure. It has to be highlighted that K is not the true stress at the crack tip but it is a measure of the intensity of stress. The stress intensity factor is often written in the following form,

$$K = \beta\sigma\sqrt{\pi a} \qquad 2.2.3.7$$

Where β is a non-dimensional function of geometry, σ is the remote applied stress and a is a measure of crack length.

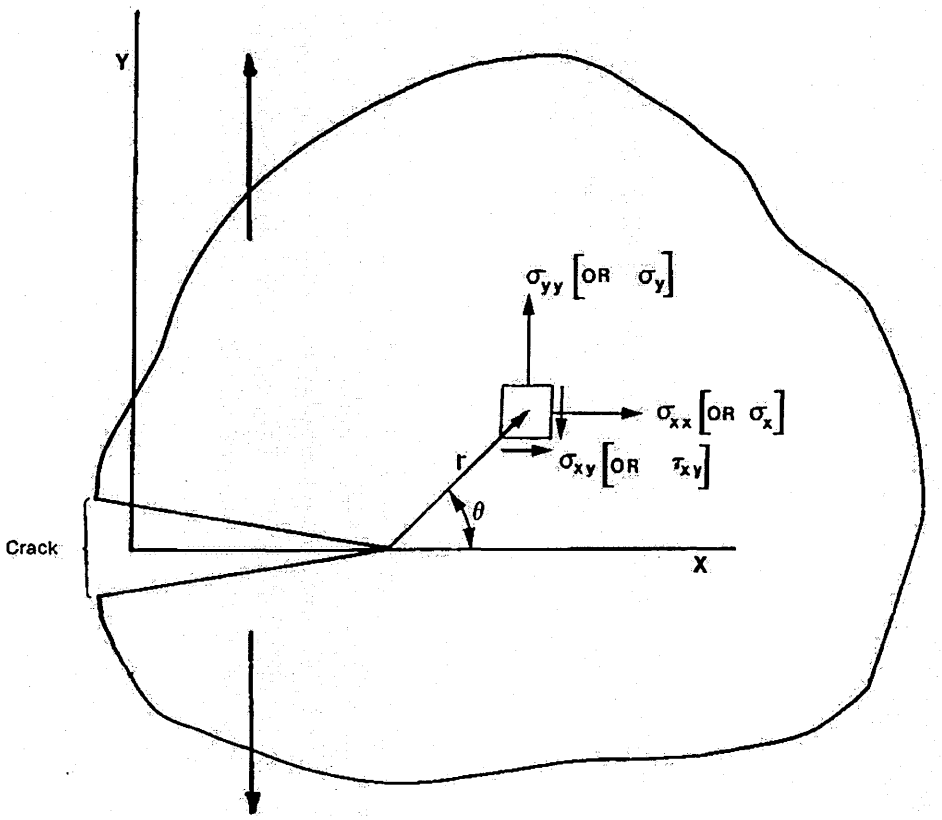

Figure 2.2.3.1: Two dimensional stress field in the vicinity of the crack tip [10].

It has to be noted that the basic assumption of Linear Elastic Fracture Mechanics (LEFM) is that the growth of a crack is controlled by the stress field at the crack tip. From equation 2.2.3.5, it can be seen that at the crack tip r=0 and, therefore, the linear elastic theory predicts stress values which tend to infinity. In real materials, infinite

stresses cannot exist and plastic deformation occurs at the vicinity of the crack tip. Provided that these deformations are small compared to the region dominated by the K term in the stress field, then the LEFM concepts can still be used.

Regarding the stress intensity factor expression from equation 2.2.3.7, it has already been said that K is a function of the type of loading. Figure 2.2.3.2 presents the 3 different types of loading. The mode I is the tension or the opening mode, mode II is the in-plane shear mode and mode III is the out-of-plane shear mode or the tearing mode. As the three different loading modes, there are stress intensity factors corresponding to each one of these modes; and this work is concerned about mode I loading type.

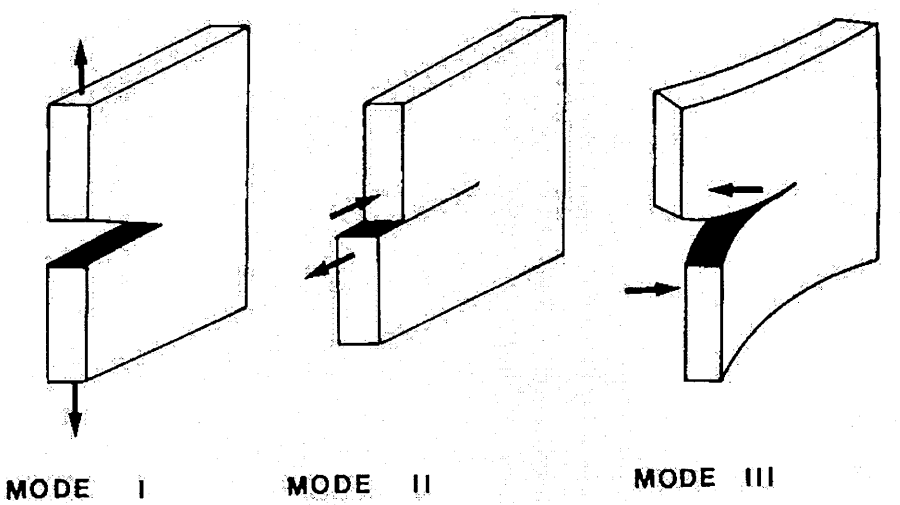

Figure 2.2.3.2: Modes of loading. Mode I opening mode. Mode II shear mode. Mode III tearing mode [10].

2.2.4. Residual Strength and the Fracture Toughness

The criterion for failure due to unstable crack growth of a crack can be expressed in the following manner,

$$K \geq K_{IC} \quad \text{(plane strain condition)} \qquad 2.2.4.1$$

$$K \geq K_c \quad \text{(plane stress condition)} \qquad 2.2.4.2$$

Failure will occur (or residual strength is lost) if equations 2.2.4.1 and 2.2.4.2 are satisfied, where K_{IC} and K_c are called by the fracture toughness of the material. The definitions of plane strain and plane stress conditions are not presented here but can be found in Broek [10].

K_{IC} and K_c values are material constants and they depend upon the material thickness as illustrated in Figure 2.2.4.1. The value of K_{IC} is applicable to thick materials while K_c is applicable for thin ones.

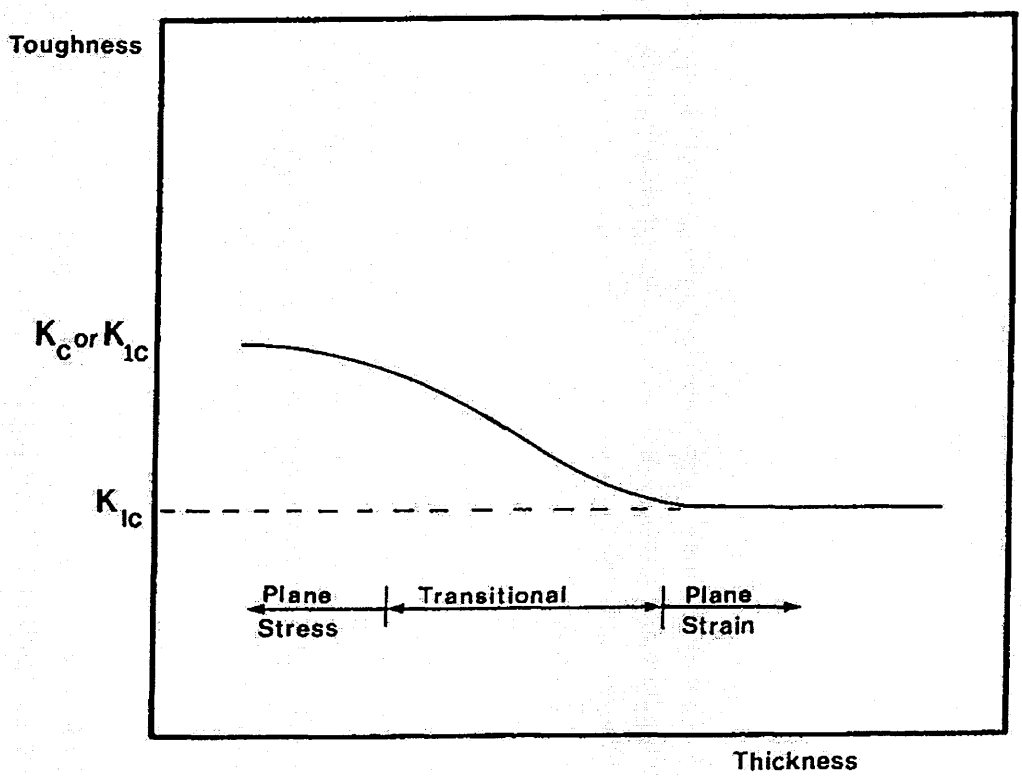

Figure 2.2.4.1: Effect of thickness on toughness [10].

Considering equations 2.2.3.7 and 2.2.4.2, then the fracture toughness failure criterion for the plane stress condition can be expressed by,

$$\beta\sigma_c\sqrt{\pi a_c} = K_c \qquad 2.2.4.3$$

Where σ_c and a_c are, respectively, the critical stress and the critical crack length at failure. It has to be noted that the left hand side of equation 2.2.4.3 is related to the geometry of a cracked body and the stress amplitude, while the right hand side of equation 2.2.4.3 is related to material property.

From equation 2.2.4.3, and for a known value of K_c, it can be seen that given the critical stress value it can be determined the critical crack length or given the critical crack length it can be determined the critical stress level at failure.

2.2.5. Fatigue Crack Growth

After the introduction of the concept of the stress intensity factor, Paris [26] suggested that the growth of cracks due to the variation in stress (fatigue loads) could be described as a function of the stress intensity factor. Paris postulated that the rate of growth per cycle of stress da/dn was a function of the stress intensity range ΔK given by,

$$\frac{da}{dn} = C\Delta K^n \qquad 2.2.5.1$$

Where C and n are material constants. ΔK is the stress intensity factor range given by $\Delta K = K_{max} - K_{min} = \beta(S_{max} - S_{min})\sqrt{\pi a}$ due to a cyclic variation in the applied stress.

In practice equation 2.2.5.1 can only represent part of experimental data. The plot of da/dn versus ΔK has a sigmoid shape, as illustrated in Figure 2.2.5.1, and fatigue crack growth life may be divided in three regions.

The first region is for slow crack growth rates ($< 10^{-8}$ m/cycle), the second region is for macro crack growth rates (10^{-8} to 10^{-6} m/cycle) and the third region is for fast crack growth rates ($> 10^{-6}$ m/cycles) for unstable crack growth and failure.

In a log-log plot of da/dn versus ΔK, the Paris equation (2.2.5.1) falls on a straight line and it covers macro-crack growth rates (region 2 from Figure 2.2.5.1) which is typically representative of most practical engineering cases for structural components containing macro-cracks [27].

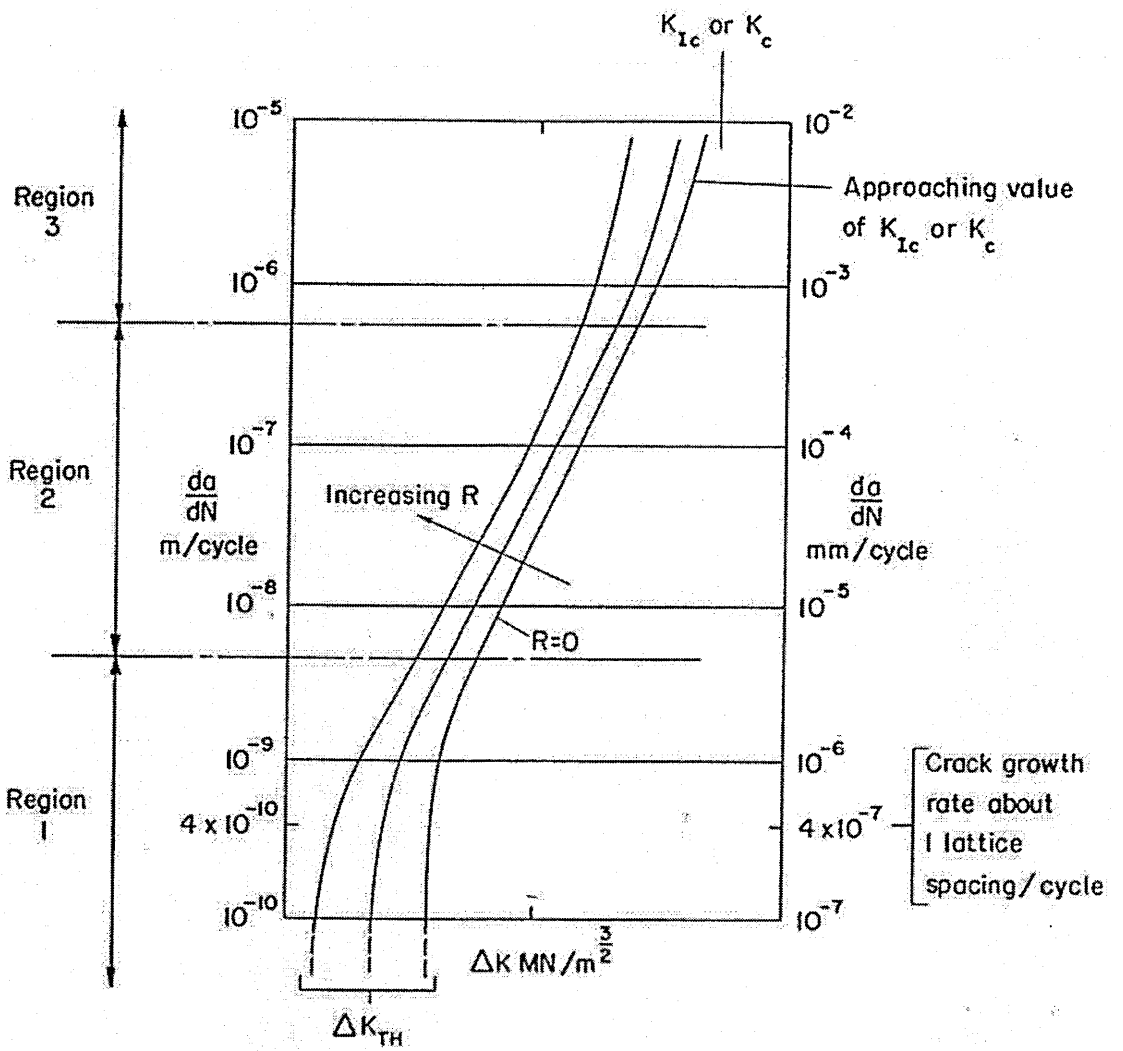

Figure 2.2.5.1: Relation between stress intensity factor range and crack growth rate [6].

Regarding fatigue crack growth on a sheet specimen of Aluminium 2024-T3, Elber [28] observed what he described as the crack closure effect: a crack can be closed at a positive tensile stress. By means of experimental work, Elber discovered that under a certain stress level, which he called S_{op} (crack opening stress), the crack would remain partially opened or fully closed. Therefore, Elber argued that fatigue crack propagation

would only occur under an effective stress range $\Delta S_{eff} = S_{max} - S_{op}$. Bearing this in mind, Elber defined the effective stress intensity factor ΔK_{eff} as

$$\Delta K_{eff} = \beta \Delta S_{eff} \sqrt{\pi a} \qquad 2.2.5.2$$

And he also modified the Paris equation 2.2.5.1 by introducing his definition of ΔK_{eff} as follows,

$$\frac{da}{dn} = C(\Delta K_{eff})^n \qquad 2.2.5.3$$

Both forms of Paris equation given by 2.2.5.1 and 2.2.5.3 are still widely employed nowadays due to its simplicity and effectiveness for engineering applications.

2.3. MSD Assessment Methodologies Review

A review of the methodologies to assess MSD indicates that previous workers have approached this problem by considering the probabilistic nature of MSD occurrence. Monte Carlo techniques have been widely employed to simulate the stochastic nature of fatigue crack initiation at fastener holes and /or subsequent crack propagation to calculate the distribution of lives to MSD onset and ultimate failure.

The general approach for the crack initiation stage consists of randomly placing initial fatigue cracks at the 3 and 9 o'clock positions in a row of holes. This row of holes is the one that represent the critical ones (highest stressed rows) [29] of, for example, a riveted joint. The 3 and 9 o'clock positions at each hole is called Fatigue Critical Location (FCL). One initial damage scenario is generated in a row of holes when cracks of a_0 size are placed at each FCL according to a randomized fatigue life distribution established via Monte Carlo simulation (probabilistic models). This process is then repeated to create the necessary number of different initial damage scenarios for the posterior crack propagation stage.

The crack initiation stage is commonly addressed by applying Monte Carlo simulation to lognormal [16-18, 30-41] or Weibull [15, 35, 42, 43] distributions of lives to achieve a specified crack size a_0. Some authors [44-46] do not use Monte Carlo simulation, but predict fatigue crack initiation using a strain-life approach incorporating Miner rule for cumulative damage calculation. Liao [47] also employs a strain-life approach for crack initiation prediction, but he derived analytical expressions for local stress as a function of squeeze force and coefficient of friction as random variables generated by Monte Carlo simulation. From the previous models, it can be realized that they treat crack initiation probabilistically. Noticeably, the lognormal distribution coupled with Monte Carlo simulation is widely employed from most models derived, as also reported by Tong [48].

After damage scenarios are generated from the previous crack initiation stage, multiple crack propagation for each scenario generated is started. The crack propagation stage is simulated either deterministically or probabilistically in current MSD assessment models. The deterministic crack propagation is performed based on traditional linear elastic fracture mechanics principles. When cracks reach sufficient length, interaction effects with other cracks, holes, stiffeners, etc. become an important issue because the geometric correction factor term β (equation 2.2.3.7) changes considerably for each single crack at each different cracked scenario. Therefore, the technique used for stress intensity calculation must be accurate and economical of computer time, if it is to be used in a repeated simulation such as the Monte Carlo, in order to effectively represent multiple crack growth. In previous MSD methodologies compounding method [5, 18, 30, 33-35, 44-46, 49], finite element [16, 31, 37, 50], boundary elements [11] and dual boundary elements [39] have been used to calculate stress intensities of MSD cracks in a deterministic crack growth approach.

Although many workers have calculated multiple crack growth deterministically, it has already been demonstrated by other authors that the nature of crack propagation is probabilistic due to variability in material properties and, therefore, deterministic crack growth models cannot represent it. The first verification that fatigue crack propagation

process presents scatter, and so does the crack growth rate, was done by Virkler experimental work [51]. Proppe [40] also mentions the work of Ghonem [52] as a verification of the probabilistic nature of crack propagation. Since Virkler experimental work, several probabilistic crack growth models have been developed [17, 32, 36, 40, 41, 43, 53-59].

Yang [54] approach to probabilistic crack growth utilizes a lognormal distribution to characterize the crack growth rate dispersion. The parameters that characterize this dispersion are determined from experimental test results by means of the log-log plot of the crack growth rate versus the crack length. The Yang approach is, therefore, an experimental based probabilistic crack growth model and it has been employed by other authors [36, 57]. Wang [55, 56, 59] developed a probabilistic crack growth model for aluminium 2024-T3 based on a comprehensive analysis of scatter in fatigue crack propagation in both small and large crack size regions. Wang utilizes a modified version of the Paris equation (equation 2.2.5.1) incorporating the crack closure effect from Elber [28] and an empirical fitting factor as a function of the maximum stress intensity factor to account for crack growth rate near the threshold range. Other authors [17, 32, 40, 41, 43] have modelled the probabilistic nature of crack growth by assuming the 'n' coefficient as a fixed value and by randomizing the 'C' coefficient of the Paris equation (equation 2.2.5.1) according to a lognormal distribution. This assumption is widely employed due to implementation simplicity reasons; and its effectiveness has been demonstrated by Ostergaard [60] who concluded that the variability of the 'C' coefficient does give very good results compared to the variability of both 'C' and 'n' coefficients.

Regarding the stress intensity factor calculation for the probabilistic crack growth models reported in the previous paragraphs, it has to be highlighted that the probabilistic models based on Yang [54] are fitted equations to match specific test configuration data and do not request the determination of stress intensity factors. On the other hand, Cavallini [17, 58], Lazzeri [32], Proppe [40], Shkarayev [41] and Shoji [43] approaches consider the variability of crack propagation inherent to material properties and they request stress intensity calculation to account for different cracked

scenarios. The main difference among Cavallini, Lazzeri, Proppe, Shkarayev and Shoji is the formulation employed for stress intensity factor determination. While Cavallini and Lazzeri employ the compounding method; Shoji employs a Bayesian procedure to determine a modification coefficient to replace the geometric correction factor β (equation 2.2.3.7); Proppe implemented an algorithm which employs the finite element alternating method which avoids the need for re-meshing inherent to FE models when crack size is varied; and Shkarayev utilized an increment finite element algorithm as a function of crack size and time increments. Unlike the deterministic crack growth approaches, no model has been implemented using boundary element techniques for probabilistic crack growth.

Among the MSD assessment models, the equivalent initial flaw size (EIFS) approach is being used by several authors [32, 58, 61-73]. The idea of EIFS has been introduced by Rudd [68] and has been developed by Manning and Yang [69-73]. The EIFS concept relies on deriving a fictitious distribution of crack sizes (EIFS distribution) for the short crack range by using crack propagation equations valid for the long crack range. In order to obtain the EIFS distribution, the time to crack initiation (TTCI) distribution for a fixed crack length is firstly established from experimental work. Afterwards, a crack propagation law from LEFM is back-extrapolated from the TTCI distribution to an arbitrary reference time (also called zero time). The result of this back-extrapolation to a fixed time will lead to the EIFS distribution. When the EIFS distribution is established for a certain structural component, life assessment analysis can be performed from the zero time up to the long crack range and failure. An example of EIFS application and results can be found in Harris [74]. Harris has reported that EIFS is a quite suitable engineering approach for predicting total fatigue life of fuselage panels; but he also concluded that EIFS has to be determined for each unique combination of structural geometry and service environment. Therefore, the need for a specific experimental database in order to derive an appropriate EIFS distribution is obvious, otherwise wrong fatigue life predictions are obtained.

The next paragraphs present the MSD methodologies derived by some Original Equipment Manufactures (OEM), as well as one aircraft operator. Details about each

one of these approaches can be found in the final report from the Airworthiness Assurance Working Group (AAWG) [3]. The USAF approach is also presented and details of it can be found in Gallagher [75].

The Airbus Industry MSD methodology [3] consists of allocating different fatigue endurance to each fastener hole (two per fastener hole). The fatigue endurance is randomly allocated by means of Monte Carlo simulation applied to a lognormal or to a Weibull distribution of lives to grow a crack to a macro crack size. The distribution of lives are obtained from simple coupon test specimens which are built using the same material and construction technique applied to fuselage panels manufacturing. Crack growth for each initiated fatigue crack is performed using LEFM principles and the Paris equation (2.2.5.1); stress intensity factors are calculated using the compounding method or by means of FE analysis. The crack link-up criterion is according to the touching crack tip plastic zones. Crack growth is stopped at a pre-defined condition such as fixed value for the lead crack size.

The Boeing Commercial Airplanes approach [3] for MSD consists of determination of the time to crack initiation using a two-parameter Weibull probability distribution, which treats MSD initiation the same as MSD detectable, i.e., the initial crack size is the detectable one according to current field inspection techniques. Considering the Weibull distribution, the characteristic fatigue life of a critical detail is statistically estimated from in-service/test data; as well as the shape parameter. The initial lead crack is placed in the most likely or stressed structural detail determined from stress analysis or field experience. Secondary cracks are placed accordingly around the lead crack and in adjacent structural details. Crack growth for each initiated fatigue crack is performed using LEFM principles and the Paris equation (2.2.5.1); stress intensity factors are calculated using the compounding method. Crack growth is limited to a conservative final crack length.

Lockheed-Martin Aeronautical Systems [3] plans for future approach of MSD by means of EIFS application. The implementation of this approach is depending on teardown programs to derive EIFS distributions for structural details. Meanwhile, Lockheed-

Martin uses a single crack growth curve to establish recurring inspection intervals. This crack growth curve is obtained from an upper and a lower bound crack growth curves. The upper and lower crack growth curve bounds are, respectively, a crack growth curve of a single crack from a fastened hole (least conservative assumption – highest time for crack propagation) and a crack growth curve from two adjacent cracked holes containing four equal length collinear cracks (most conservative assumption – smallest time for crack propagation). A single crack growth curve, which will serve as the basis for the recurring inspection scheme, is then calculated to be 90% more conservative than all crack growth curve possibilities that may arise between the upper and the lower crack growth curve bounds.

Delta Airlines approach [3] to MSD assumes fatigue crack initiation based on the number of cycles to grow a crack up to 1.27 mm (0.05 in). The calculation of the number of cycles to reach a 1.27 mm initial flaw size is done by statistical analysis based on coupon testing of similar MSD susceptible details to derive a characteristic life. After the determination of the characteristic life, a scatter for aluminium 2024 is assumed and a crack initiation table is created for posterior use in the crack propagation stage. Instead of placing cracks randomly in a row of holes, a cracking sequence is assumed where the first crack starts to propagate from the highest stressed location. New cracks are introduced in the model according to the crack initiation table sequence generated, and each crack is placed at the following high stressed location available. According to Delta [3] this cracking sequence is a rational approach that matches their in-service findings while repairing cracked fuselage panels. Multiple crack propagation is performed by using an iterative sequence of FEA models. The crack propagation stops when two cracks growing from adjacent holes link-up according to the touching crack tip plastic zones criterion.

The USAF approach [75] to MSD is a risk analysis methodology based on probabilistic and deterministic assumptions. For airframe structure applications, the risk analysis determines the probability that the maximum stress in a flight will produce a stress intensity factor (for current crack size) that exceeds the material fracture toughness based on fracture mechanics principles. The probabilistic input data consists of

equivalent flaw size, repair flaw size, fracture toughness, probability of crack detection and the maximum stress per flight. The deterministic data required is obtained from the crack growth analyses that are conducted for fatigue critical locations and includes the normalized stress intensity factor and the fatigue crack growth curve. The maximum acceptable frequency for structural failure which is considered adequate for long term operation of the airplane must be bellow 1 x 10^{-7} occurrences per flight. To apply the methodology, a computer program called PROF was written and the program can determine the probability of failure due to fatigue cracking, discrete source damage, widespread fatigue damage and corrosion thinning in metallic structures.

As far as MSD crack initiation modelling is concerned, it can be observed that probabilistic approaches based on Monte Carlo simulation represent the great majority of MSD models, with exception to a few authors [44-46] or in the case of approaches based on EIFS and Yang [54]. Considering a row of holes, Monte Carlo simulation is used to initially establish random fatigue lives at each FCL for posterior crack propagation. After crack propagation is started, each crack-free FCL has its initial assigned fatigue life updated by some damage accumulation technique as cracks grow step-by-step by a pre-defined crack increment size. This procedure is, therefore, a step-routine utilized to calculate fatigue crack re-initiation lives from the initially assigned fatigue life given by Monte Carlo simulation for each crack-free FCL. Regarding the MSD models presented in this section, linear damage accumulation is the technique used to calculate fatigue crack re-initiation lives for crack-free FCLs, except in some cases such as in Proppe [40] and Wang [59]. Proppe calculates fatigue crack re-initiation life for each hole by an empirical correlation factor that assigns the crack-free FCL a fatigue life based on the fatigue life of the first initiated crack at either the 3 or the 9 o'clock position. Wang developed a probabilistic damage accumulation solution based on crack closure that takes into account, among other factors, plastic yield at each crack-free FCL. Surprisingly, the continuing damage assumption [76], which constitutes a simplifying alternative to a damage accumulation technique, has not been reported in any of the previous MSD methodologies presented.

Considering the crack propagation stage of the MSD models presented in this section, it can be noticed that probabilistic crack propagation is not so commonly employed. One reason for this fact is that based on in-service teardown data some authors [77] describe that deterministic crack propagation is enough for engineering applications. It may be that for engineering applications deterministic crack propagation is acceptable but certainly probabilistic crack growth represents a refinement is this field. Despite of the approach adopted, the overwhelming majority of the MSD models reported previously employ the Paris equation (equation 2.2.5.1) or some modified version of it (equation 2.2.5.3). In the case of probabilistic models the 'C' coefficient is the randomized parameter used to simulate the probabilistic nature of crack propagation (equations 2.2.5.1 and 2.2.5.3). The stress intensity factor calculation used for crack propagation is performed by either analytical or numerical techniques. Among the numerical techniques employed for MSD crack propagation, only Proppe [40] and Shkarayev [41] developed a probabilistic approach based on FEM. Proppe and Shkarayev derived their own algorithms to act as a step-routine integrated to their FE analysis. The need for a step-routine, or a loop-routine, incorporated to numerical techniques is quite important as invariably the value of the 'C' coefficient of the Paris equation changes due to the randomization process. The absence of a step-routine would cause the numerical crack growth analysis to be frequently stopped for changing the 'C' coefficient value, which would be unlikely to be used when a great number of simulations, such as the ones from Monte Carlo, are performed. A complicating problem when performing probabilistic crack growth with a numerical technique is that commercial FE or BE computer codes normally do not allow the user to access the font code and, therefore, an integrated step-routine is unlikely to be implemented.

One surprising issue from all MSD models reviewed in this section is the absence of any type of parametric study to investigate factors that influence MSD by employing the models derived. The majority of papers presented are limited to description of the MSD model developed and comparison of its results to experimental test data. The exception to this lack of investigation on MSD behaviour belongs to Horst [30, 35] who conducted some parametric studies employing his model. From his work Horst [30] concluded that the mean TTCI, the scatter of the mean TTCI and the detectable crack length are the

main parameters that influence the establishment of fatigue crack inspection intervals and its threshold. In another work Horst [35] studied the influence of different scatter values on the mean MSD failure behaviour (used to determine the inspection starting point and the structural modification point) by means of the log-normal and Weibull distributions. By varying the scatter value for initiation of fatigue cracks, Horst concluded that the mean value of the failure curve is not very closely linked to the question of MSD onset and, therefore, the establishment of the inspection starting point and the structural modification point should be done in a 'very critical mood'. Horst also demonstrated that log-normal and Weibull distributions provided similar MSD failure distributions; but the distribution for fatigue crack initiation can differ (especially when more than 18 fatigue critical locations are considered) due to the unbounded nature of the log-normal distribution when compared to the Weibull one. Horst also mentioned that a more 'MSD-like' situation (greater number of cracks per damage scenario) is obtained when low scatter values for fatigue crack initiation are employed.

In the light of the literature review presented in this section, it can be realized that since the Aloha accident much effort in MSD understanding has been done and improvement in this field has been achieved. For example, the recognition that MSD presents a probabilistic nature is clearly reflected from the many crack initiation and/or crack propagation approaches presented.

2.4. Rivet Squeeze Force Experimental Work Review

From the vast experimental work reported in the literature regarding MSD investigation, the effect of rivet squeeze force on fatigue life for crack initiation has been devoted a special attention in this work and this review is concerned about this theme. The reason for the focus on riveting squeeze force is that although riveted joints have been used for several decades in the aeronautical industry for fuselage panel construction, it is only recently that some authors have reported that great improvement in the mean fatigue life to crack initiation is obtained by increasing the rivet squeeze force. As fatigue crack initiation is definitely an important part in the whole MSD process, it becomes of

interest within this research to assess how rivet squeeze force might influence MSD behaviour.

As reported by Slagter [78], Hartman was possibly one of the first researchers to notice that the improvement in the mean fatigue life of riveted joints was related to the increase of solid rivet driven head diameter formed after the riveting process. Muller [79] extended the work of Hartman by unequivocally showing that the main governing factor for fatigue life improvement was not the size of the driven head formed, but the value of the squeeze force employed. To reach this conclusion, Muller investigated and compared a wide range of lap joint geometries of aluminium 2024-T3 and Glare 3. For the same material type, Muller showed that by varying the geometries and rivet type, the same driven head size could be formed but different fatigue lives were obtained; and that similar fatigue lives were connected by similar rivet squeeze forces and not by similar driven head sizes.

Muller and Hart-Smith [80] investigated three-row riveted joints of aluminium 2024-T3 subjected to four different nominal stresses and manufactured with three different levels of squeeze force. The main conclusion that can be drawn from their work is that a combination of high squeeze force together with an optimum geometrical configuration can lead fuselage panels design to be simplified and still keep a very long crack-free fatigue life.

Chiarelli [53] also conducted a wide investigation on the effect of riveting for different aluminium 2024-T42 lap joint geometries. The rivet type, material and heat treatment were varied in his investigation. From the conclusions drawn by Chiarelli, the most impressive one is the fact that among the many parameters that have influence on fatigue behaviour 'rivet squeeze force is perhaps the most significant one'.

Fawaz [81] calculated stress intensity factor solutions for fatigue crack growth from holes riveted with different rivet squeeze forces. He concluded that for part through cracks, the variation in stress intensity factor range is three times larger when rivets are

installed with low squeeze force values compared to high squeeze force ones, demonstrating that crack propagation was affected in the vicinity of the hole border.

Vlieger [14] conducted a series of fatigues tests and tried to correlate the formed rivet head diameter produced by different rivet squeeze forces to the fatigue crack initiation location. Vlieger concluded that it was not possible to establish this correlation.

Wang [82] investigated four different rivet squeeze forces and he was able to correlate experimentally the hole expansion to rivet squeeze force installation: hole expansion increases for increasing rivet squeeze force.

Harish [83] studied the effect of rivet squeeze force on residual stress distribution around a pin-loaded hole by a FE model; he also conducted two experimental fatigue tests for each combination of four different rivet squeeze forces and five different nominal stress levels. Harish results showed that the observed fatigue life increased with increase in squeeze force; and that as the squeeze force increased, the location of crack nucleation moved further away from the 3 and 9 o'clock positions of the pin-loaded hole border (due to changes in residual stresses around the hole).

Terada [84], among other factors, examined the effect of three different rivet squeeze forces by fatigue testing of flat riveted panels. Terada states that 'the magnitude of the squeezing force plays the most important role on the fatigue life of joint structures'. Also, he found out that the effect of the squeezing force was more pronounced in thinner joints than in thicker ones; and that squeeze force alters the loading mechanism in a riveted joint: for low squeeze force values the load is mainly transmitted by the rivets themselves, while for higher squeeze force values the load is mostly transmitted by surface friction of the mating sheets. This last conclusion is in accordance to what has been observed by Harish [85] in previous work.

Ofsthun [86] investigated fatigue quality enhancers such as cold work, shoot peening and controlled interference fit to fastener holes. Regarding the interference fitting of holes caused by different rivet squeeze forces, Ofsthun observed that the fatigue life

improved with increasing interference fit at holes up to a limit. When the interference fit was excessive, the fatigue life degraded instead of improving.

From what has been presented in the previous paragraphs regarding rivet squeeze force, the most significant findings concerning different rivet squeeze force applications were obtained in the last 10 years; and the number of authors who investigated this theme is relatively small. It is also evident that rivet squeeze force is one of the major factors that control fatigue life for crack initiation. Another fact that can be observed from the previous review is that no information on scatter values is available for comparison purposes when different rivet squeeze forces are employed. As the crack initiation stage describes a probabilistic nature, information on scatter values for different rivet squeeze forces is still missing for the application of probabilistic-based MSD models. Therefore, the effect of rivet squeeze force on MSD behaviour is not fully established yet.

2.5. This Research Work in the Context of Literature Review

Based on the literature review presented in sections 2.3 and 2.4, four topics are presented in this section regarding MSD investigation where a contribution to knowledge can be given. It is, therefore, an identification of some gaps that need further clarification. These topics are: (a) Simplification on MSD modelling; (b) Parametric study on MSD; (c) The effect of high rivet squeeze force on MSD; and (d) MSD assessment comparison to in-service data.

(a) From the review on MSD assessment models, it can be seen that models have differed in their built-in assumptions and in their calculation techniques, but they also have some assumptions in common. One assumption that is employed in all MSD models reported in section 2.3 is the use of a damage accumulation technique to calculate fatigue crack re-initiation lives for crack-free fatigue critical locations. This is a curious observation because continuing damage assumption [76], which is widely employed in traditional damage tolerance analysis, has been completely forgotten when it comes to MSD assessment based on probabilistic models. If the

continuing damage assumption can be successfully implemented for MSD assessment, then a simplification can be established in the field of MSD modelling.

(b) The need for a parametric study for investigation of factors that might influence MSD behaviour, judging by the lack of work in this area, is quite obvious and dismisses further comments.

(c) Regarding the experimental work review on rivet squeeze force, it is clearly established by the literature that high squeeze force values greatly improve the mean time to crack initiation; but what is the probabilistic effect of high rivet squeeze force on MSD behaviour has not been established.

(d) From the MSD assessment models presented in section 2.3, it has not been reported a comparison of models output to teardown data obtained from in-service fuselage panels of aging aircraft; and this issue is of extreme importance when it comes to MSD models application.

Chapter 3

3. RIVETED LAP JOINT MODEL SUBJECTED TO MSD

As described in Chapter 2, multiple site damage can be approached by considering a theoretical separation of multiple crack development into a crack initiation stage and a crack propagation stage up to a failure criterion. In order to perform multiple crack growth (different-sized cracks propagating simultaneously), crack interaction effects must be considered when calculating stress intensities due to, for example, the proximity of a crack to another crack, to a pin-loaded hole, to a free border or to a stiffening member. If different cracked lap joint configurations (different damage scenarios) are to be analysed, the Stress Intensity Factor (SIF) values for each crack in each different damage scenario is changed as invariably these scenarios are changed. One of the possible ways of calculating crack growth for different cracked configurations is by employing numerical techniques based on Finite Element (FE) or Boundary Element (BE) methods. In this work the Damage Tolerance Design (DTD) code [87], based on the Dual Boundary Element Method (DBEM), was selected to perform deterministic multiple crack growth.

Among all aeronautical structures prone to develop MSD, riveted lap-splice joints in the fuselage have been identified as being the most susceptible [3]. One of the central tasks in MSD analysis is the effective evaluation of stress intensity factors for cracks emanating from fastener holes which are employed during the crack propagation stage. Also, when Monte Carlo simulation is employed to generate hundreds of different initial damage scenarios for posterior crack propagation to MSD assessment, computer time saving becomes a fundamental matter.

To introduce the DTD code, in section 3.1 it is firstly presented a basic concept on how BE based computer codes work and some references where BE theory and formulation can be found. Secondly, the well established advantages of the BE technique compared to the FE one are stated. Finally, the DTD code formulation is outlined to point out how stress intensity factor, crack growth analysis and the riveted connections are modelled.

In sections 3.2 and 3.3, the DTD code is employed to idealize two simple and effective DBE lap-splice joint models. The first model (section 3.2) is of a strap lap-splice joint containing one crack; and the second model (section 3.3) is of a large lap-splice joint containing multiple crack situations. The geometrical correction factors and stress intensity values obtained from the two models idealized in this chapter are compared to results from the literature for the same lap joint configurations, but modelled by means of Finite Element Method (FEM).

3.1. The Damage Tolerance Design (DTD) Code Outlines

The Boundary Element Method (BEM) is a firmly established engineering numerical technique that can be used as an alternative to the Finite Element Method (FEM) [11]. The DTD Code [87] is based on the Dual Boundary Element Method (DBEM), which is a variation of the Boundary Element Method (BEM). The main advantage of the DBEM over the BEM is that the former can be used to solve general (mixed mode) crack problems while the latter can be used to solve symmetric crack ones. Details of the DBE technique can be found in Portela, Aliabadi and Rooke [88].

The BEM is a technique for the numerical solution of differential equations with initial boundary conditions [89]. The theory of elasticity, for example, describes the equilibrium of stresses in an elemental volume of a loaded three-dimensional body via differential equations. The BE method allows the transfer of the differential equation set for some continuous region of an arbitrary shape into a corresponding equivalent integral equation. After the equivalent integral equation is obtained, it is converted to a form that involves only a surface integral, i.e., an integral over the boundary. The solution of this surface integral generally involves replacing it by a linear system of equations. To do so, the boundary is divided into elements and the integral over the boundary becomes simply the sum of the integration over each element, resulting in a dense and non-symmetric matrix system of linear equations. The solution of this matrix will give the unknown boundary displacements and boundary tractions at each boundary element. Once the boundary elements have been solved, the surface integral solution is obtained and the way back can be done to compute any interior points of the body. As it

can be seen, the BEM has no need to render the entire volume into discrete finite elements but only the surface (the boundaries). Although the concept of the BEM is simple, the many steps described previously involve a series of laborious calculations which are out of the scope of this work. A detailed description of the BE theory and of the steps for its computational implementation can be found in textbooks such as the ones in references [11] and [89].

The most attractive feature of the BEM, and its variations such as the DBEM, is the reduction of the dimensionality of the numerical model compared to the FEM. For three-dimensional problems only the domain surface needs to be discretized, and for two-dimensional problems only the line boundaries of the domain needs to be discretized. The reduction of the dimensionality leads to a much smaller system of equations to be solved numerically [11]. This fact is especially attractive for fracture mechanics problems because regions with high stress concentration can be modelled more efficiently as the number of necessary grid points is confined to one less dimension [90]. Crack propagation can take advantage of the BEM since algorithms treating this problem need continuous updating of the mesh as crack size is changed; and the re-meshing is less laborious with BE techniques compared to FE ones, which discretizes the entire continuum [91]. Another clear advantage of the BE technique over the FE one is that it provides continuous modelling of the interior since no descretization is required leading to a high resolution of interior stresses and displacements [11]. Also, Cartwright and Rooke [92] showed that a boundary element analysis produced more accurate stress intensity factors than the finite element analysis.

Regarding the DTD code formulation, when the matrix system of linear equations, as described previously, is solved for the unknown boundary displacements and boundary tractions, the stress intensity factor can be calculated via the J-integral. Portela, Aliabadi and Rooke [93] concluded that the J-integral technique is the best suited for SIF calculations in the DBEM. A detailed formulation of the DTD code can be found in Salgado and Aliabadi [90, 94, 95]. Its fundamentals for stress intensity factor calculation, crack growth analysis and riveting connection modelling are resumed in the next paragraphs; with emphasis on crack growth.

Once the J-integral is calculated, the stress intensity factor (under plane stress conditions) is given by the following relationship,

$$J^{I} = K_{I}^{2} / E \quad \text{and} \quad J^{II} = K_{II}^{2} / E \tag{3.1.1}$$

Where J^{I} and J^{II} are the J-integrals for mode I and for mode II, respectively; K_{I} and K_{II} are the mode I and mode II stress intensity factors, respectively; and E is the Young modulus.

In the DTD code, the crack growth analysis is calculated according to the maximum principal stress criterion [96]. This criterion states that crack growth occurs in a direction perpendicular to the maximum principal stress. The local crack extension direction is determined when the shear stress at the crack tip is zero,

$$K_{I} \sin\theta_{t} + K_{II}(3\cos\theta_{t} - 1) = 0 \tag{3.1.2}$$

Where θ_{t} is the angular coordinate measured along the crack axis and centred at the crack tip. The maximum principal stress criterion does not take into account the crack extension increment modelling and thus a prediction correction scheme [93] is adopted in the DTD code.

In multiple crack problems it is necessary to determine not only the direction of the crack extension but also the relative crack size increments due to differences in crack growth rate among the various crack tips. In the DTD code, the crack growth rate (da/dn) is given by the modified Paris equation (equation 2.2.5.3) by using the effective stress intensity factor range ΔK_{eff}

$$\frac{da}{dN} = C(\Delta K_{eff})^{n} \tag{3.1.3}$$

Where C and n are material parameters and ΔK_{eff} is given by Tanaka [97],

$$\Delta K_{eff}^2 = \Delta K_I^2 + 2\Delta K_{II}^2 \qquad 3.1.4$$

For constant amplitude fatigue load with stress amplitude ratio R, $\Delta K_I = K_I(1-R)$ and $\Delta K_{II} = K_{II}(1-R)$.

To determine the crack increment sizes, firstly the effective stress intensity factors are calculated and the crack growth equation 3.1.3 is integrated to determine the necessary number of cycles ΔN_i to grow an arbitrary reference crack size (RS) for each crack tip i,

$$\Delta N_i = \frac{1}{C}\int_{a_i}^{a_1+RS} \frac{1}{(\Delta K_{eff})^n} da \qquad 3.1.5$$

Where the integration is performed assuming that the stress intensity factors remain constant as the crack grows from the initial size a_i to $a_i + RS$. It is then assumed that the fast-growing crack tip, the one with smallest number of cycles $\Delta NC = \min(\Delta N_i)$, will grow the pre-defined size RS. The increment sizes of the other cracks are then calculated by integrating the inverse of the crack growth equation

$$\Delta a_i = C\int_{NC}^{NC+\Delta NC} (\Delta K_{eff})^n \, dn \qquad 3.1.6$$

Using the minimum number of cycles previously determined (ΔNC) to calculate the growth length. Again the stress intensity factors are assumed to remain constant.

The boundary element mesh is then updated to include the new increments, and a structural analysis is performed at the end of which new stress intensity factors are evaluated. The increments size is then re-calculated, now taking into account the variation of the stress intensity factors when integrating equations 3.1.5 and 3.1.6. The

increments are re-meshed and a new structural analysis is performed. This procedure is repeated until convergence for the increments size is achieved. The increments direction and size are calculated simultaneously as summarized:

1. Perform structural analysis.
2. Calculate the effective stress intensity factors range.
3. Calculate the crack increments direction and size assuming that, as the cracks grow, the effective stress intensity factors range remains constant.
4. Update mesh to include the crack increments.
5. Perform new structural analysis.
6. Calculate new effective stress intensity factors range.
7. Correct the crack increments direction and size considering the variation of the stress intensity factors from their former to new values.
8. Verify convergence for the increments direction and size. If no convergence is achieved, then return to step 4.

In the DTD code, a riveted joint is modelled as two 2D flat sheets connected by spring elements which simulate fasteners. The entire load is transmitted from one sheet to the other in shear exclusively by the spring elements and no friction is considered between the mating sheets or at the boundary of pin-loaded holes. According to Swift [98], fastener displacements may comprise more than 75 % of the displacement in joints; and riveted joint model idealizations that consider fasteners as rigid can lead to errors greater than 50 % on the determination of SIF values at the crack tips. In the DTD code formulation, the displacement compatibility between the fasteners (spring elements) and the sheets is taken into account by considering the fastener flexibility via the empirical equation proposed by Swift [98] for the fasteners shear deformation coefficient,

$$\Phi=\left[A_1+A_2\left(\frac{\phi}{h_1}+\frac{\phi}{h_2}\right)\frac{1}{E\phi}\right] \qquad 3.1.7$$

Where A_1 and A_2 are empirical constants which depend on fastener material type, ϕ is the fastener diameter, h_1 and h_2 are the sheets thickness and E is the modulus of elasticity.

In the next sections, the DTD code will be employed to model two different lap-splice joint geometrical configurations, in the presence of cracks, and the results obtained will be compared to ones from the literature.

3.2. Riveted Strap Lap Joint Model

The strap lap joint geometry selected to be modelled is the one presented in Figure 3.2.1 and it has been analysed by Cope [99] by means of FE modelling. The lap joint is subjected to a remote tensile stress of S_0 = 68.95 MPa and is constructed of two W = 25.4 mm wide 2024-T3 aluminium panels (t = 1.6 mm) fastened together with steel rivets (ϕ = 4.76 mm). The pitch distance (p) and edge distance (e) are 25.4 mm and 12.7 mm, respectively.

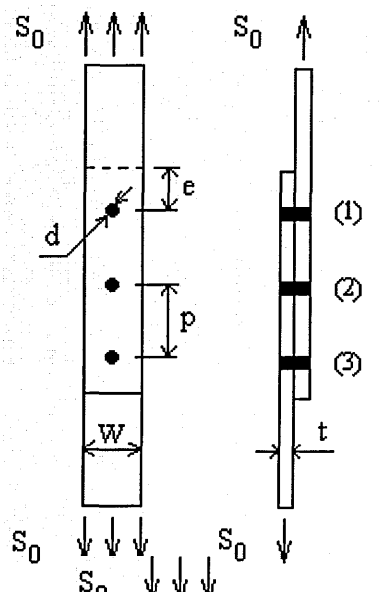

Figure 3.2.1: Riveted strap lap joint sketch.

To determine the load transferred by the rivets, the remote tensile stress of S_0 = 68.95 MPa was applied to the lap joint illustrated in Figure 3.2.1. The global model idealized

with the DTD code consists of two rectangular sheets discretized by 48 boundary elements and 96 nodes each. The sheets are connected by 3 steel fasteners simulated by spring elements. To take fastener flexibility into account, the fastener shear deformation coefficient was calculated by the empirical equation 3.1.7 repeated as follows,

$$\Phi=\left[A_1+A_2\left(\frac{\phi}{h_1}+\frac{\phi}{h_2}\right)\frac{1}{E\phi}\right] \qquad 3.2.1$$

Where A_1 and A_2 are empirical constants which, for steel fasteners, are $A_1=1.67$ and $A_2=0.86$ according to experimental work from Swift [98]. ϕ is the fastener diameter ($\phi=4.76mm$), h_1 and h_2 are the sheet thicknesses ($h_1=h_2=1.6mm$) and E is the modulus of elasticity for the aluminium ($E=73{,}000\,MPa$).

The rivet reaction loads 'P_{pin}' obtained from the DTD code ($P_{pin\text{-}dtd}$) and the ones from Cope [99] ($P_{pin\text{-}ref.}$) are presented in Table 3.2.1, together with the differences in percentage for the values presented. The fastener position 1, 2 and 3 represent the ones illustrated in Figure 3.2.1.

Table 3.2.1: Fasteners reaction loads from Figure 3.2.1.

Position	$P_{pin\text{-}dtd}$ (N)	$P_{pin\text{-}ref.}$ (N)	Difference (%)
1	995.2	1000.9	- 0.6
2	811.7	800.2	+ 1.4
3	995.2	1000.9	- 0.6

The maximum $P_{pin\text{-}dtd}$ value obtained was 995.2 N, and it is located at the external fastener positions (positions 1 and 3 from Figure 3.2.1) of the lap joint outer rows. It has to be noted that the values of rivet reaction loads for the upper and lower rows (outer rows) are the same, and that the inner row carries less load compared with the outer ones. Also, it can be seen from Table 3.2.1 that the differences between the values of $P_{pin\text{-}dtd}$ and $P_{pin\text{-}ref.}$ vary from -0.6% to +1.4%, with a mean difference of +0.4%.

Once the fastener reaction loads have been calculated, a DBE lap joint model is idealized by using the load transfer within one of the aluminium sheets, and only one row of the lap joint from Figure 3.2.1 is modelled. According to the results from Table 3.2.1, it can be seen that the critical positions are the ones from the external rows of Figure 3.2.1 because they carry the highest pin-loads and, therefore, present a reduced fatigue life for crack initiation character [100]. For this reason, only one of the external rows will be modelled in this work as conceptually presented in Figure 3.2.2.

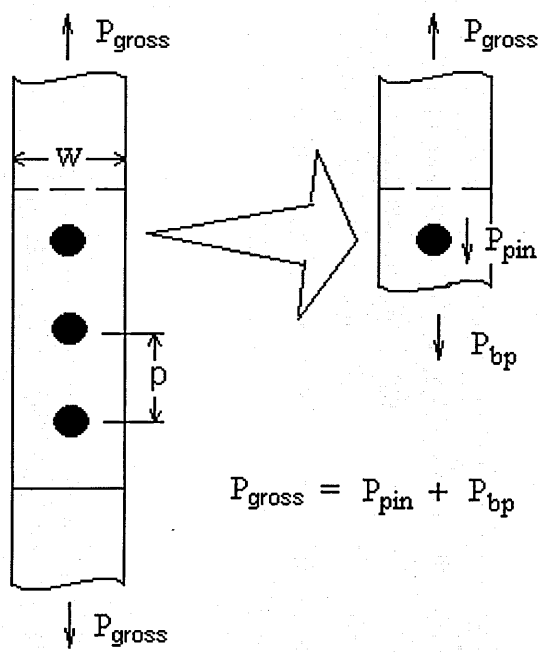

Figure 3.2.2: Load equilibrium in a strap lap joint.

From Figure 3.2.2, it can be seen that the load equilibrium for the upper row in one of the sheets is given by,

$$P_{gross} = P_{pin} + P_{bp} \qquad 3.2.2$$

Where:

$$P_{gross} = \sigma_{gross} .A, \qquad \sigma_{gross} \text{ is the gross stress and } A = W.t; \qquad 3.2.3$$

$P_{pin} = \sigma_{br} . \phi . t$, σ_{br} is the bearing stress; and 3.2.4

$P_{bp} = \sigma_{bp} . A$, σ_{bp} is the bypass stress. 3.2.5

Considering that the lap joint configuration, material and loading conditions sketched in Figure 3.2.2 are the same as in Figure 3.2.1; from the results presented in Table 3.2.1 and equation 3.2.2, it follows that P_{pin} = 995.2 N; P_{gross} = 2,802.1 N and P_{bp} = 1,806.9 N. From the values of P_{gross}, P_{pin}, and P_{bp}, and from equations 3.2.3 to 3.2.5; it follows that σ_{gross} = 68.95 MPa, σ_{br} = 130.67 MPa and σ_{bp} = 44.46 MPa.

Once the values of σ_{gross} , σ_{br} and σ_{bp} have been obtained, the sketch of the idealized local DBE model for the upper row of rivet (position 1 from Figure 3.2.1) is presented in Figure 3.2.3. The mesh of the idealized model is presented in Figure 3.2.4.

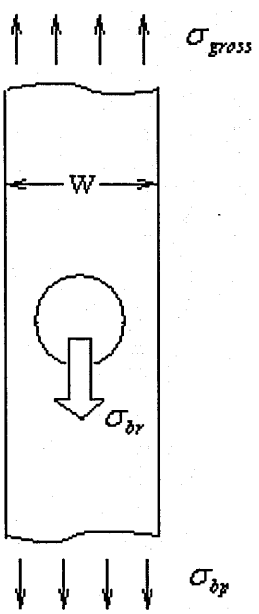

Figure 3.2.3: Sketch of the DBE model for the upper row of Figure 3.2.1.

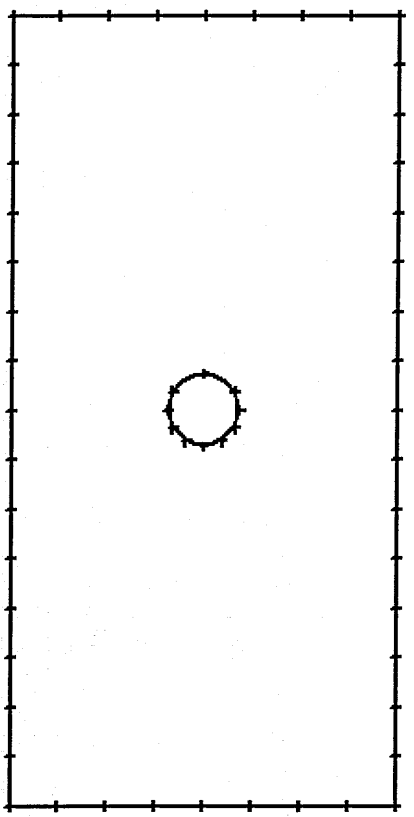

Figure 3.2.4: DBE model mesh for the upper row of Figure 3.2.1.

The model illustrated in Figure 3.2.5, which is the same as in Figure 3.2.4, consists of one rectangular sheet, 52.0 mm high and 25.4 mm wide, discretized by 58 boundary elements and 116 nodes, with a central hole with diameter 4.76 mm (representing a single sheet upper row of the lap joint illustrated in Figure 3.2.1) and sheet thickness 1.6 mm. There are upper and lower displacement constraints (D_x) in the x direction and lateral displacement constraints (D_y) in the y direction due to symmetry. The material (Al 2024-T3) and remote applied stress (68.95 MPa) are as in Figure 3.2.1. The concept of load transfer, as illustrated in Figure 3.2.3, is used and the values of stresses applied to the model illustrated in Figure 3.2.5 are the ones calculated in this section, i.e., σ_{gross} = 68.95 MPa (represented by T_y in the top of Figure 3.2.5) and σ_{bp} = 44.46 MPa (represented by T_y in the bottom of Figure 3.2.5).

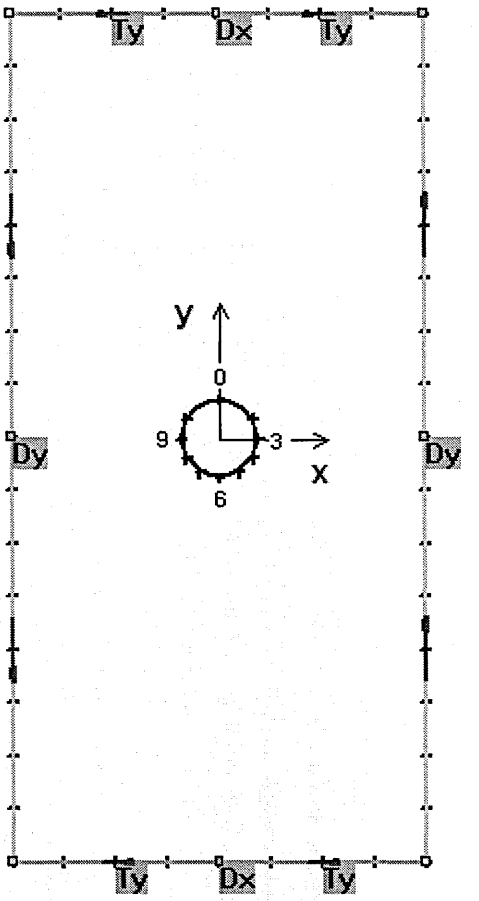

Figure 3.2.5: Boundary tractions and displacements of Figure 3.2.4.

The value of σ_{br} = 130.67 MPa is applied in the central hole of Figure 3.2.5 according to the details shown in Figure 3.2.6. The direction of the applied stresses in the hole border is according to Figure 3.2.3. Figure 3.2.6 shows details of the hole border loading. The hole model is discretized by 10 boundary elements and 20 nodes. The load (T_y) is applied in the y direction, between 3 and 9 o'clock positions, respectively, points 1 and 7 (Figure 3.2.6), with interpolated intermediate values between the segments 1-2, 2-3, 3-4, 4-5, 5-6 and 6-7.

The load values applied in segments 1-2, 2-3 and 3-4 are, respectively, equal to the load values applied in segments 6-7, 5-6 and 4-5. The minimum load values are assigned in positions 1 and 7 (3 and 9 o'clock positions), and they are equal to zero. The maximum load value, as calculated in this section, is assigned in position 4, and is equal to σ_{br} = 130.67 MPa (σ_{br} .sin 90^0). The load in nodes 2 and 6 are given by σ_{br} .sin 30^0, and the

loads in nodes 3 and 5 are given by σ_{br}.sin 60^0. From Figure 3.2.6 it can also be seen the displacement constraints (D_x) in the x direction which are used to simulate the presence of a fastener restricting the hole border not to act as an open hole.

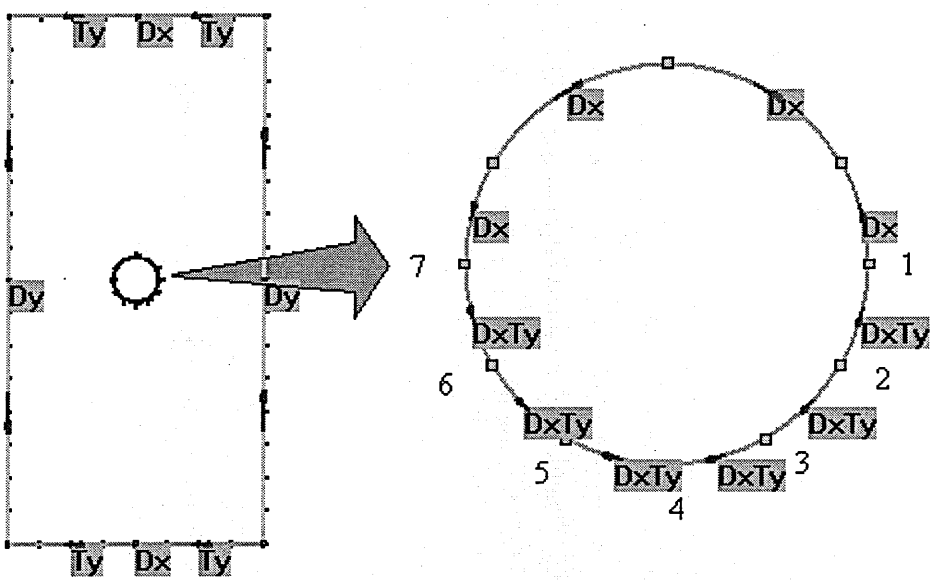

Figure 3.2.6: Hole boundary tractions and displacements of Figure 3.2.4.

With the boundary elements model established (Figure 3.2.4), a through-the-thickness crack with an initial crack size of 1.27 mm will be placed at the hole border 3 o'clock position in order to obtain the geometrical correction factors β (as the initial crack size is grown by crack increments of 1.27 mm) and compare these values to the ones from Cope [99]. The mesh containing the initial crack a_0 = 1.27 mm is shown in Figure 3.2.7, and the number one in the figure is a reference to crack tip 1. The mesh in Figure 3.2.7 is increased by 12 boundary elements compared to the one from Figure 3.2.4 due to the presence of a_0.

The geometrical correction factors β are given as a function of the mode I stress intensity factor K_I divided by $K_0 = \sigma\sqrt{\pi.a}$ given by,

$$\beta = \frac{K_I}{K_0} \qquad 3.2.6$$

Where σ is the nominal gross stress σ_{gross} = 68.95 MPa and a is the crack size. The values of β calculated with the DTD code are defined as β_{dtd} while the ones from Cope [99] are defined as $\beta_{ref.}$. The comparison of both β_{dtd} and $\beta_{ref.}$ is presented in Table 3.2.2. The DBE mesh from Figure 3.2.7, but for a detail of the hole with a crack size a = 6.35 mm, is presented in Figure 3.2.8.

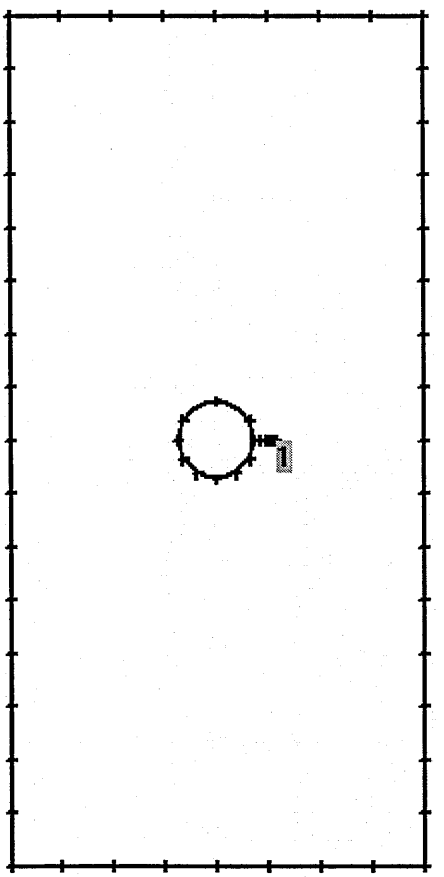

Figure 3.2.7: Cracked DBE model mesh for the upper row of Figure 3.2.1.

Table 3.2.2: Geometric correction factors comparison.

a (mm)	β_{dtd}	$\beta_{ref.}$	Difference (%)
1.27	1.962	1.966	-0.20
2.54	1.444	1.431	+0.98
3.81	1.226	1.215	+0.91
5.08	1.116	1.107	+0.90
6.35	1.068	1.068	0.00

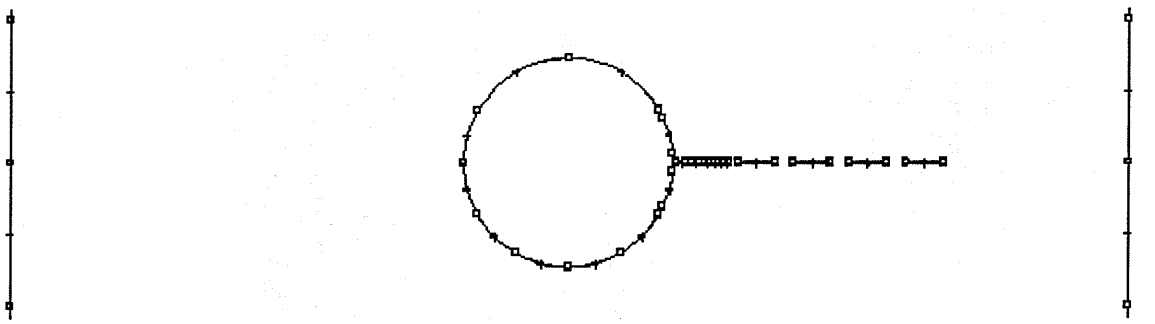

Figure 3.2.8: Detail of the DBE mesh for the pin-loaded hole with a crack of 6.35 mm.

As it can be seen from Table 3.2.2 , the differences between the values of β_{dtd} and $\beta_{ref.}$ vary from - 0.20 % to + 0.98 %, so within ± 1.0 %. The comparison demonstrates the effectiveness of the idealized DBE cracked strap lap joint model from Figure 3.2.7, based on load transfer between two fastener rows (upper row and the middle row) for a single lap joint sheet, when compared to the same lap joint model based on the FE analysis from Cope [99].

3.3. Riveted Lap Joint Model

In order to simulate MSD behaviour in riveted lap joints, a wide DBE lap joint model is idealized in this section and the values obtained for the Stress Intensity Factor (SIF) with the DTD code [87] are compared to the ones obtained from the literature [99].

The lap joint geometry selected to be modelled is the one presented in Figure 3.3.1 and it has been analysed by Cope [99] by means of FE modelling. The lap joint is subjected to a remote tensile stress of S_0 = 68.95 MPa and is constructed of two W = 609.6 mm wide 2024-T3 aluminium panels (t = 1.6 mm) fastened together with steel rivets (ϕ = 4.76 mm). The pitch distance (p), row spacing (s) and edge distance (e) are 25.4 mm. A 203.2 mm slot connected the nine centre fasteners in the upper row, and a lead crack is introduced at each of the outer two fasteners of the slot. MSD cracks are introduced at adjacent fastener holes to the lead crack tips.

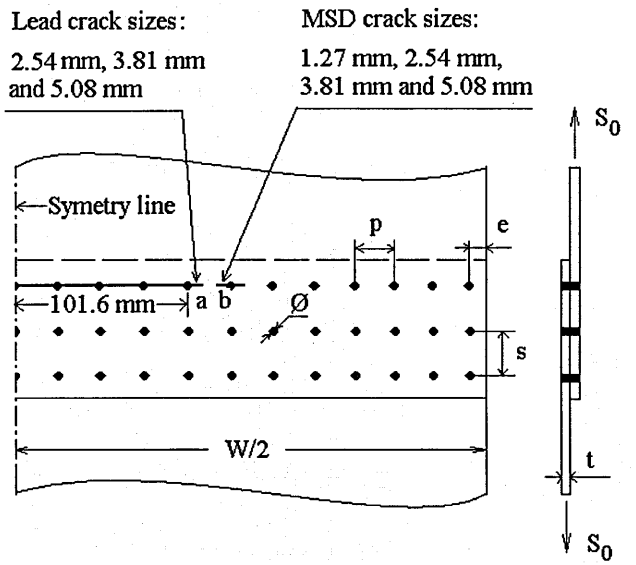

Figure 3.3.1: Riveted lap joint subjected to MSD.

The lap joint idealized with the DTD code is illustrated in Figure 3.3.2 and, as in section 3.2, only the upper row of holes from Figure 3.3.1 is modelled. The model consists of one rectangular sheet of aluminium 2024-T3, 609.6 mm long and 304.8 mm wide, discretized by 94 boundary elements and 188 nodes, with a lead crack and two MSD cracks represented by the numbers 3, 2 and 1, respectively; with a central row of seven pin-loaded holes (representing the upper row of holes of the lap joint illustrated in Figure 3.3.1), left constraint (D_x) in the x direction to simulate symmetry and a lateral constraint (D_y) in the y direction where no displacements are expected. The hole diameter, pitch distance, edge distance and sheet thickness are the same as illustrated in Figure 3.3.1. The concept of load transfer (as in Figure 3.2.3) is used and the values of stresses applied in the model are the remote tensile stress S_0 = 68.95 MPa in the top of Figure 3.3.2 and the bypass stress σ_{bp} = 54.07 MPa in the bottom of Figure 3.3.2; both of them represented by the T_y traction vectors. The value of σ_{bp} is obtained considering that the holes traversed by the lead crack do not react to the remote stress S_0 (Figure 3.3.1) and these loads are redistributed as bypass loads.

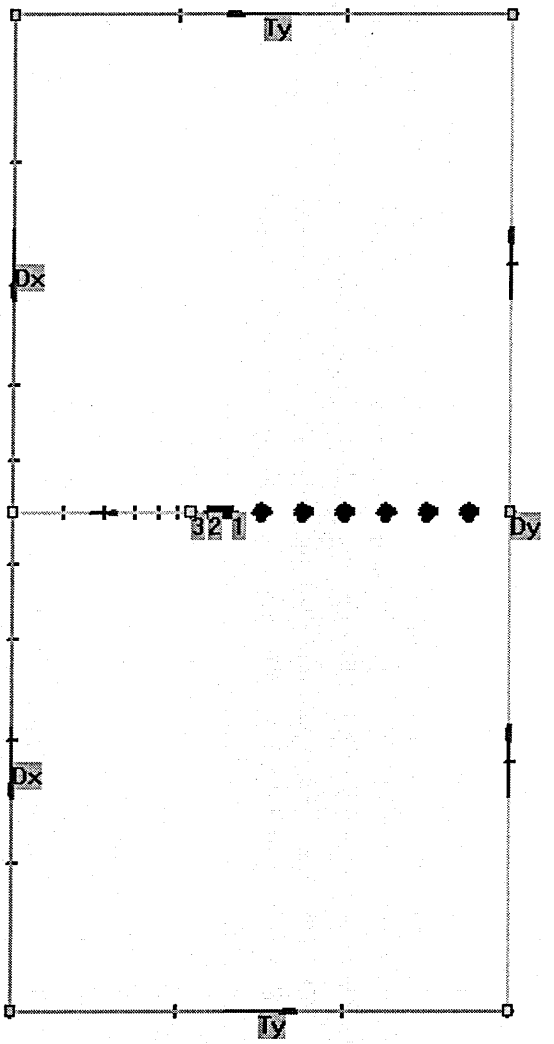

Figure 3.3.2: DBE model for the lap joint from Figure 3.3.1.

The model shown in Figure 3.3.2 is then run by the DTD code, and the results of the SIF values for the lead crack 'a' (Figure 3.3.1) $K_{Ia\text{-}dtd}$ (from this work) and $K_{Ia\text{-}ref.}$ (from Reference [99]) are presented in Table 3.3.1. It can be seen that the differences (E) between both models ranged from – 2.22 % to – 1.19 %, with a mean difference of – 1.84 %. The SIF values for the MSD crack 'b' (Figure 3.3.1) $K_{Ib\text{-}dtd}$ (from this work) and $K_{Ib\text{-}ref.}$ (from Reference [99]) are presented in Table 3.3.2. From Table 3.3.2, the differences (E) between both models ranged from – 3.29 % to +1.08 %, with a mean difference of – 1.34 %.

Table 3.3.1: Comparison of SIF values for the lead crack of Figure 3.3.1.

a_{lead} (m)	a_{msd} (m)	$K_{Ia\text{ - }dtd}$ ($MPa\sqrt{m}$)	$K_{Ia\text{ - }ref.}$ ($MPa\sqrt{m}$)	E (%)
2.54E-03	-	43.54	44.27	-1.64
2.54E-03	1.27E-03	43.64	44.46	-1.85
2.54E-03	2.54E-03	44.08	44.81	-1.62
3.81E-03	-	43.86	44.74	-1.98
3.81E-03	1.27E-03	43.95	44.93	-2.18
3.81E-03	2.54E-03	44.46	45.37	-2.02
3.81E-03	3.81E-03	45.31	45.98	-1.44
5.08E-03	-	44.33	45.12	-1.75
5.08E-03	1.27E-03	44.46	45.34	-1.95
5.08E-03	2.54E-03	45.18	45.85	-1.45
5.08E-03	3.81E-03	45.53	46.54	-2.17
5.08E-03	5.08E-03	46.54	47.49	-2.00

Table 3.3.2: Comparison of SIF for the MSD crack of Figure 3.3.1.

a_{lead} (m)	a_{msd} (m)	$K_{Ia\text{ - }dtd}$ ($MPa\sqrt{m}$)	$K_{Ia\text{ - }ref.}$ ($MPa\sqrt{m}$)	E (%)
2.54E-03	1.27E-03	15.78	15.65	+0.85
2.54E-03	2.54E-03	18.73	19.15	-2.18
3.81E-03	1.27E-03	16.19	16.15	+0.22
3.81E-03	2.54E-03	19.25	19.72	-2.39
3.81E-03	3.81E-03	22.23	22.65	-1.86
5.08E-03	1.27E-03	16.89	16.71	+1.08
5.08E-03	2.54E-03	20.15	20.50	-1.73
5.08E-03	3.81E-03	22.85	23.62	-3.29
5.08E-03	5.08E-03	25.97	26.70	-2.75

The results comparison shown in Tables 3.3.1 and 3.3.2 demonstrate a good level of agreement for the whole range of lead and MSD crack sizes, despite the differences inherent to both models (see Reference [99]). The simple DBE lap joint model subjected to MSD (Figure 3.3.2) shows its effectiveness when it comes to analysing a complex lap joint configuration such as the one illustrated in Figure 3.3.1; and therefore this type of model will be used in the next chapters of this work for calculation of SIF values for a range of crack configurations in lap joints.

3.4. Summary

In section 3.1 of this chapter, an overview of how boundary element based computer codes work and the advantages of using the BEM over the FEM as a numerical technique for crack propagation was presented. The DTD code formulation was outlined and special attention was given to the crack growth calculation procedure.

In sections 3.2 and 3.3, respectively, a riveted cracked strap lap joint and a riveted lap joint subjected to MSD have been modelled and the geometrical correction factors and stress intensity factors compared to equivalent FE models from the literature. The results indicated that the geometrical correction factors difference are within ± 1.0 % for the case of the riveted cracked strap lap joint model; and that the stress intensity factors for the whole range of lead cracks and MSD cracks are within – 3.29 % to + 1.08 % for the case of the riveted lap joint model. The results comparison demonstrate the effectiveness of both BE models derived in this chapter; and therefore these type of models will be used in the next chapters of this work for calculation of geometrical correction factor and stress intensity factor values for a range of crack configurations in lap joints.

Chapter 4

4. A METHODOLOGY FOR ASSESSING MULTIPLE SITE DAMAGE IN MECHANICALLY ATTACHED LAP-SPLICE JOINTS

Details of the MSD assessment model proposed in this chapter are presented in the next sections. The modelling procedures are separated into different stages: fatigue crack initiation, deterministic crack propagation, probabilistic crack propagation and failure.

4.1. Fatigue Crack Initiation

Considering a typical riveted lap-splice joint configuration, such as the one from Figure 4.1.1, cracks are expected to start nucleation at the critical rows (external rows) which present holes with the biggest pin-loadings [2, 14, 15, 50].

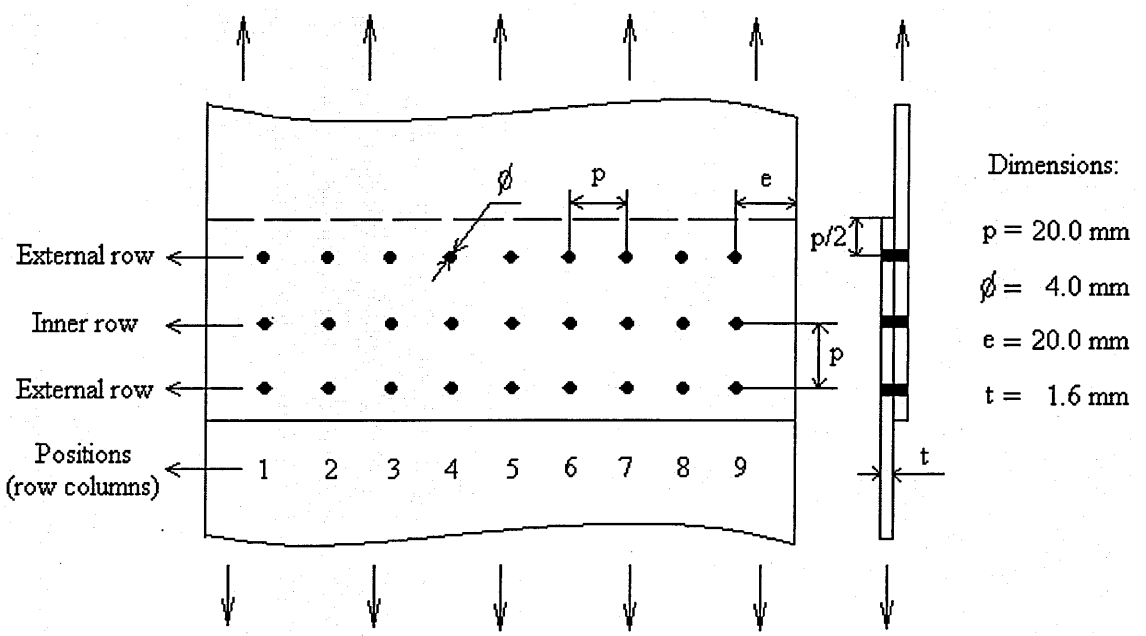

Figure 4.1.1: Riveted lap-splice joint configuration.

In the present model, fatigue crack initiation is defined as the number of cycles 'N_0' necessary to develop a through-the-thickness crack up to an initial macro crack size 'a_0'. To simulate MSD behaviour in lap joints, only a single row of pin-loaded holes

representative of the external row of holes is taken into account (Figure 4.1.1). In the case of the lap joint from Figure 4.1.1, for example, a row of nine pin-loaded holes would serve as basis to the MSD assessment model proposed in this section. For each pin-loaded hole, two fatigue critical locations (FCLs) are defined at the 3 and 9 o'clock positions of the hole border. Considering one row of nine holes, eighteen FCLs are present.

To represent the probabilistic character of the fatigue crack initiation life 'N_0', a lognormal distribution of lives to achieve the initial crack size of 'a_0' is employed. For each FCL, the normal distribution '$\log(N_0)$' is defined by the mean S-N fatigue life 'μ[log]', the standard deviation 'σ[log]' associated with 'μ' and a random value chosen from the standard normal distribution 'α' (zero mean and standard deviation equal to one) given by the following expression [31],

$$\log(N_0) = \mu + \alpha.\sigma \qquad 4.1.1$$

Where: N_0 is the initial fatigue life to grow a crack of a_o size for each FCL;

μ is the mean fatigue life in log-scale;

σ is the standard deviation (log-scale) associated with μ;

α is a Gaussian distribution [$N(0,1)$].

Considering the equality that follows

$$\log_{10}(X) = \frac{\ln(X)}{\ln 10} \qquad 4.1.2$$

From equations 4.1.1 and 4.1.2, the value of N_0 can be calculated as

$$N_0 = \exp[\ln 10(\mu + \alpha.\sigma)] \qquad 4.1.3$$

In the case of Figure 4.1.1, for example, eighteen random values from the standard normal distribution 'α' are selected to attribute each FCL a different fatigue life given by expression 4.1.3. The FCL which develops the first crack is the one with the lowest fatigue life. The second crack to enter the model is given by the second lowest fatigue life given by equation 4.1.3 and so on.

The Monte Carlo simulation technique used to generate Gaussian random numbers, which form a standard normal distribution 'α', is presented in Press [21] as the Box-Muller transformation. The Box-Muller transformation produces a Gaussian distribution with zero mean and standard deviation of one from pairs of numbers taken from an uniform random distribution in the interval [-1, 1]. This transformation has been incorporated in the gauss3.exe FORTRAN code [101] and an output plot from three thousand Gaussian random numbers is compared to the theoretical standard normal distribution in Figure 4.1.2.

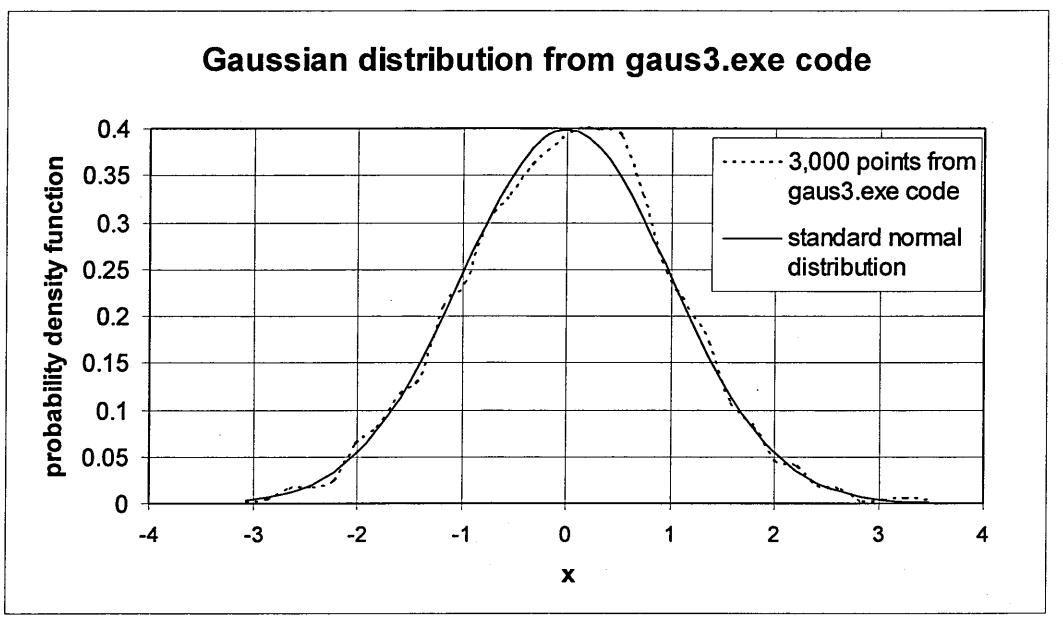

Figure 4.1.2: Gaussian distribution generated by gaus3.exe code.

It has to be noted that making $\alpha=0$ in expression 4.1.1 will let $\log N_0$ be equal to μ, which represents the mean fatigue value given by the 50 % S-N curve. Figure 4.1.3 schematically presents a 50 % S-N curve and one possible Random Fatigue Life (RFL) outcome from Monte Carlo simulation.

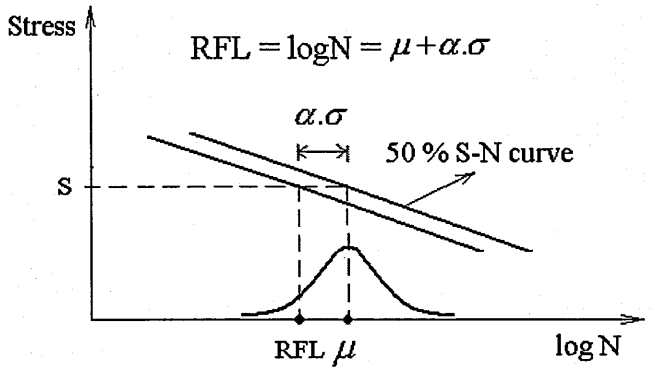

Figure 4.1.3: Schematic of a possible outcome for a random fatigue life.

When the Randomized Fatigue Life (RFL) is established for each FCL in a row of pin-loaded holes, one initial damage scenario is generated and the next stage of the MSD assessment model starts: the crack propagation stage. This process is repeated as many times as necessary to create a variety of different initial damage scenarios.

4.2. Deterministic Fatigue Crack Propagation

After an initial damage scenario is generated by Monte Carlo simulation as described in section 4.1, deterministic crack propagation for through-the-thickness cracks is performed for each scenario generated by employing the DTD code [87]. The formulation of the DTD code, which has been described by Salgado and Aliabadi [90, 94, 95], has been presented in chapter 3 for stress intensity factor calculation and for crack growth procedure.

The present crack propagation analysis is based on the established two-dimensional DBE model for a row of pin-loaded holes containing through-the-thickness cracks, as presented in section 3.3.

The main limits, simplifications and assumptions of this work with respect to crack propagation for riveted lap-joints are the ones from the DTD code [87] formulation, as presented in chapter 3, added to the following,

- Single-row pin-loaded holes two-dimensional model for crack propagation (as proposed in chapter 3 – section 3.3);
- Only through-the-thickness cracks (macro crack size range) are considered as initial crack size at any FCL;
- Constant amplitude loading and $R \geq 0$ (pressurized fuselage structures);
- Crack link-up according to Swift criterion; and
- Continuing damage assumption.

Regarding the assumptions stated previously, the origin of the stress field in a fuselage lap joint is related to the ground-air-ground (GAG) fuselage pressurization cycles, the inertia loads (due to fuselage weight) and the aerodynamic loads (specifically the ones created by the horizontal stabilizer). Fuselage pressurization is the primary fatigue load on a fuselage lap-splice, it gives rise to a combination of hoop tension (membrane stress), longitudinal tension and out of plane bending [102]. The hoop tension and out of plane bending are predominant in fatigue life determination; while after the initial fatigue cracks in the macro size range are formed the main parameter governing the crack growth is the membrane stress in the skin and the rivet reaction force [77]. For multiple crack growth, and due to the dominant membrane stress, a local two-dimensional model containing pin-loaded holes has been reported adequate for multiple crack propagation of fuselage joints [77, 102]; and the MSD model proposed in section 3.3 is used here for crack propagation.

As cracks grow towards other cracks, the Swift criterion [103] (or ligament yield criterion) is employed in this work for crack link-up. This criterion has been compared to other five different crack link-up criteria and demonstrated to be the most accurate for panels with MSD [104]. According to Swift [103], link-up of a lead crack and a MSD crack would occur when the intact ligament stress between them reaches the yield strength of the material (plane stress condition – thin sheets), i.e, when the two plastic zones ahead of the crack tip touch each other as schematically illustrated in Figure 4.2.1.

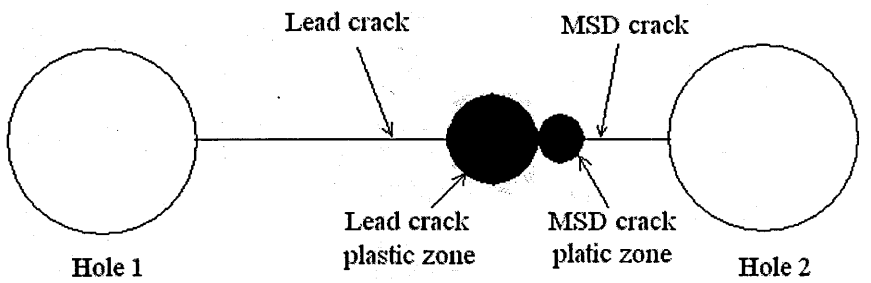

Figure 4.2.1: Schematic of Swift link-up criterion for a lead and a MSD cracks.

The same intuitive link-up criterion, as proposed by Swift, has been investigated experimentally and via FE analysis but for the case of a crack approaching an undamaged hole, as schematically illustrated in Figure 4.2.2, demonstrating good agreement [31].

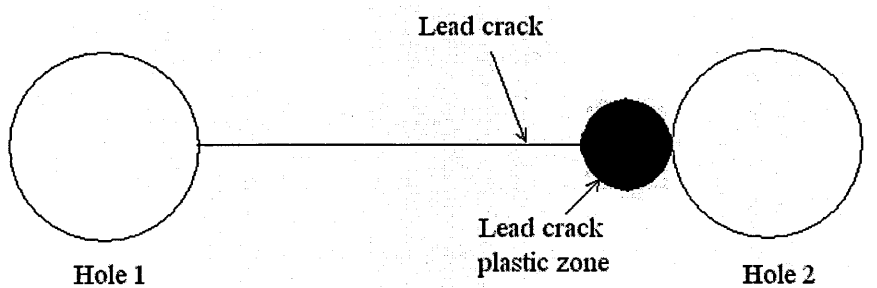

Figure 4.2.2: Schematic of link-up criterion for a lead crack and an undamaged hole.

The ligament yield criterion adopted in this work for link-up calculation is usually represented by the link-up stress expression [105] as follows,

$$\sigma_{LU} = \sigma_{YS}\sqrt{\frac{2L}{a_{lead}(\beta_{lead})^2 + a_{msd}(\beta_{msd})^2}} \qquad 4.2.1$$

Where σ_{LU} is the link-up stress necessary to link-up the lead crack (a_{lead} length) and the MSD crack (a_{msd} length) when the crack tips are separated by the ligament length L. σ_{YS} is the yield strength of the material, β_{lead} is the geometrical correction factor for the lead crack and β_{msd} is the geometrical correction factor for the MSD crack.

The riveted joint from Figure 3.3.1 has been analysed and the results obtained for stress intensity factors for the lead crack and the MSD crack, respectively, presented in Tables 3.3.1 and 3.3.2 (chapter 3). Using the SIF values from Tables 3.3.1 and 3.3.2, the definitions of a_{lead}, a_{msd} and the experimental values obtained for σ_{LU} from Cope [99] for the lap joint geometry from Figure 3.3.1; the comparison of the link-up stresses obtained with the DTD code [87] and the corresponding test values are presented in Figure 4.2.3.

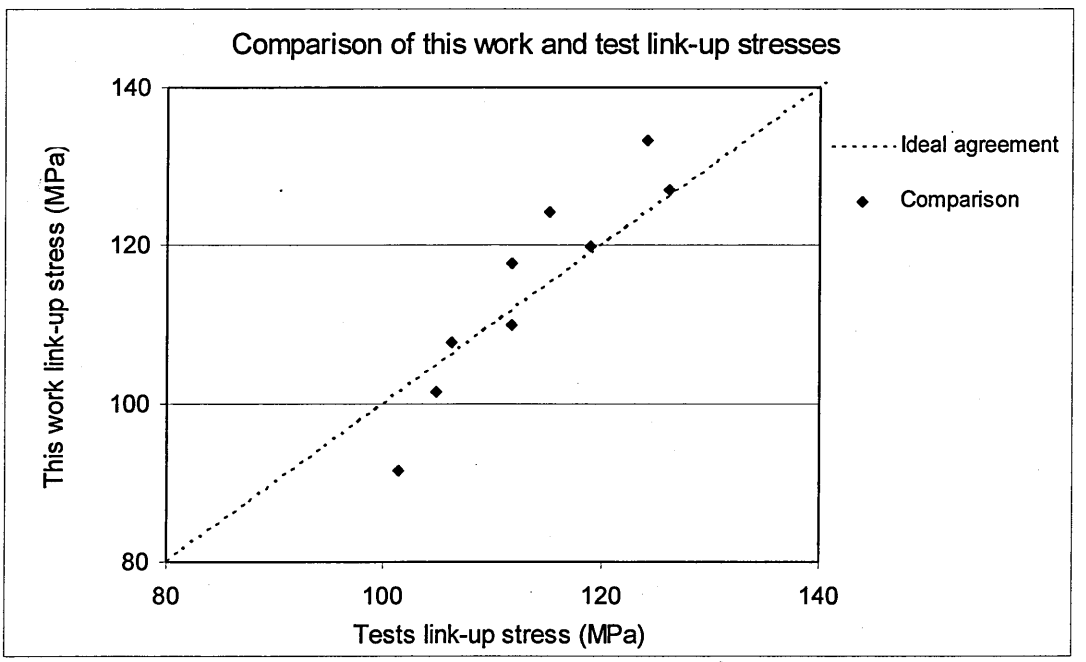

Figure 4.2.3: Link-up stress prediction from this work.

From Figure 4.2.3, the differences between the calculated values and the test ones for σ_{LU} are in a range of – 9.7 % to + 7.4 %, with a mean difference value of 1 %. Comparing the difference range for σ_{LU} from Figure 4.2.3 with other published work from the literature [104-106] which applies the Swift criterion, as well as other link-up criteria, it can be realized that σ_{LU} predictions within ± 10 % are considered good correlation to experimental work.

After link-up takes place, as illustrated in Figures 4.2.1 and 4.2.2, continuing damage assumption [76] is employed in this work as illustrated in Figure 4.2.4.

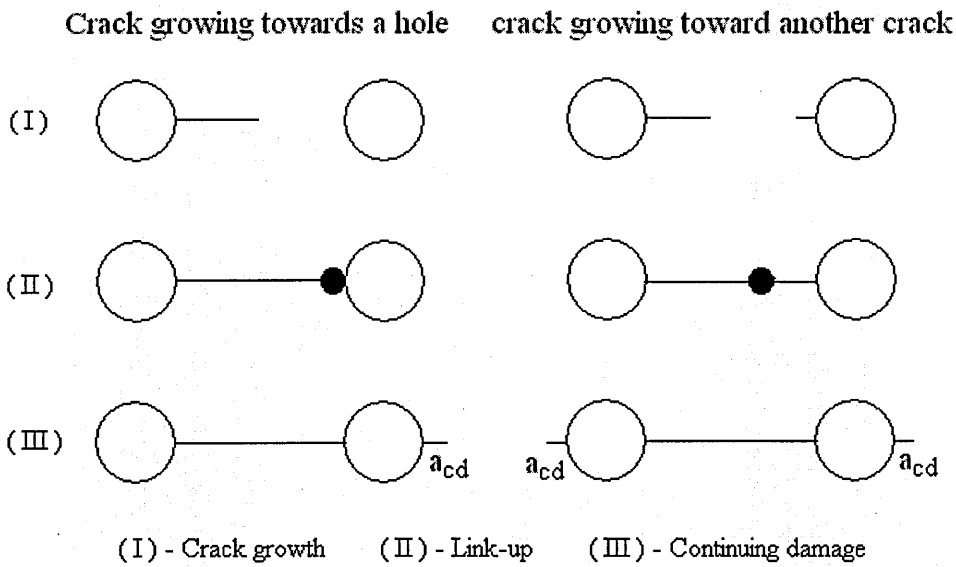

Figure 4.2.4: Continuing damage assumption illustration.

The continuing damage, as described by Gallagher [76] (recommended by the USAF), is intended to provide an orderly and progressive path for a crack that may cause structural failure, i.e, a crack size a_{cd} = 0.127 mm (0.005 in) is assumed to start from the opposite hole border to where link-up took place, as illustrated in Figure 4.2.4. In his work, Gallagher refers to a 0.127 mm corner crack size. In this work, the continuing damage is performed by a through-the-thickness crack size a_{cd} = 0.127 mm.

The MSD probabilistic models reported in chapter 2 use a damage accumulation technique, opposed to continuing damage assumption from this model, to re-initiate crack growth after crack link-up has taken place, as sketched in Figure 4.2.5.

From Figure 4.2.5, it can be seen that a lead crack 'a_{lead}' starts to grow in (1) and it links-up in (2). Before or after link-up takes place, some possible situations for re-initiation of fatigue crack growth are illustrated in, respectively, (3) and (4). In models that use a damage accumulation technique, as a_{lead} grows (by adding pre-defined crack increment sizes 'Δa') the stress level a point 'a' changes at each different Δa value added; and consequently the initial fatigue life allocated for point 'a' has to be updated. In order to update the initial fatigue life at point 'a', Miner rule for damage

accumulation calculation [107] is widely employed. If (2) is achieved, then (4) can occur where 'a_1' and 'a_3' enter the crack propagation model via Miner rule as well.

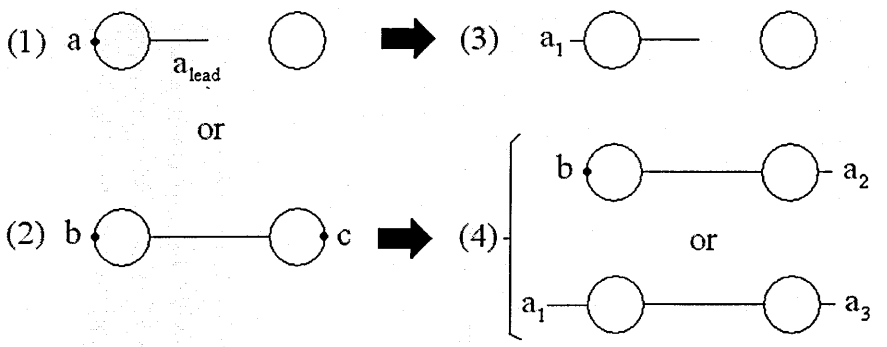

Figure 4.2.5: Sketch of a damage accumulation technique for crack growth re-initiation.

In the case of multiple crack growth analysis via probabilistic MSD assessment models, the use of a damage accumulation technique, as illustrated in Figure 4.2.5, increases considerably the analysis burden if the analyst has to stop at each crack increment size to consider changes in stress levels at undamaged FCLs such as points 'a', 'b' and 'c'. Therefore, the use of a damage accumulation technique for re-initiation of fatigue cracks can only justify itself in case it can be automatically taken into account by a step-routine incorporated into computer codes employed for crack growth analysis. In case a step-routine for continuing damage calculation cannot be incorporated, continuing damage assumption is a simplifying alternative.

4.3. Probabilistic Fatigue Crack Propagation

Possibly the first work to demonstrate the probabilistic nature of crack growth was presented by Virkler [51] by means of sixty eight replicate constant amplitude crack propagation tests conducted on 2024-T3 aluminium alloy (Figure 4.3.1). Virkler verified that fatigue crack propagation process presents a scatter, and so does the crack growth rate (Figure 4.3.2).

From the results presented in Figure 4.3.1, Virkler observed that if a 'test started out slow it tended to remain slow for most of the test'. From Figure 4.3.1, it can also be stated the opposite situation: tests that start out fast tend to remain fast.

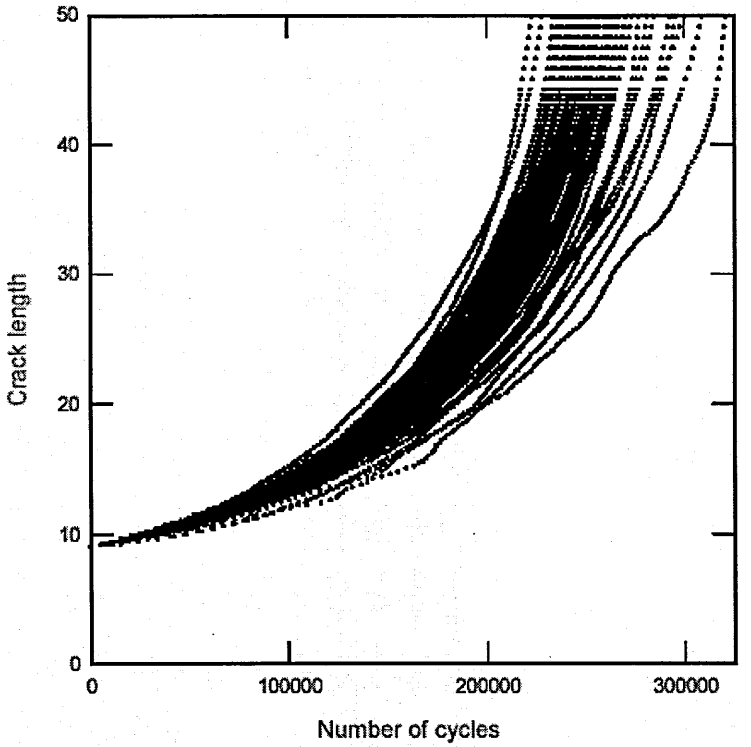

Figure 4.3.1: Trajectories of the stochastic crack growth from Virkler [51].

In order to represent the probabilistic nature of fatigue crack growth in this work, the Xing [108] formulation will be used to couple Monte Carlo simulation to the deterministic numerical technique for crack propagation presented in section 4.2. Considering the modified Paris equation (3.1.3), reproduced here as follows,

$$\frac{da}{dN} = C\left(\Delta K_{eff}\right)^{n} \tag{4.3.1}$$

Taking the logarithm on both sides of equation 4.3.1 it follows,

$$\log\frac{da}{dN} = \log C + n\log\left(\Delta K_{eff}\right) \tag{4.3.2}$$

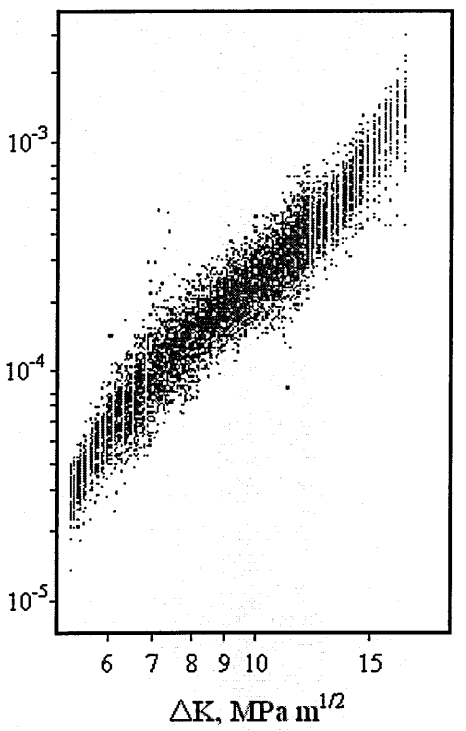

Figure 4.3.2: Crack propagation rate dispersion from Virkler [51].

To represent the stochastic nature of crack propagation, a normally distributed variable $Z \sim N(0,\sigma_z^{\,2})$ is added to the logarithm of the fatigue crack growth equation 4.3.2,

$$\log\frac{da}{dN} = \log C + n\log\left(\Delta K_{eff}\right) + Z \qquad 4.3.3$$

Considering the properties of the standard normal distribution [$N(0,1)$], the probability that a measurement will fall in a range $Z \le Z_p$ is given by $P(Z \le Z_p) = p$, and Z_p can be written as,

$$Z_p = \alpha_p \sigma_z \qquad 4.3.4$$

When the probability 'p' is given, α_p can be obtained from the standard normal distribution. For example, when $p = 50\%$, $\alpha_p = 0$, leading $Z_p = 0$ in equation 4.3.4, and equation 4.3.3 becomes equation 4.3.2 which becomes equation 4.3.1 which is the deterministic average fatigue crack growth rate. The probabilistic crack growth rate,

represented by equation 4.3.3, can be simplified if the value of 'n' is assumed as a mean constant value and the probabilistic character of crack growth is attributed to 'C', assumed as a lognormal distribution. The assumption of considering 'n' constant and varying 'C' as a lognormal distribution is enough to adequately describe the crack propagation rate and its statistical feature [17, 60]; and it has been widely employed by the MSD models presented in chapter 2, when probabilistic crack growth is considered. Therefore, equations 4.3.3 and 4.3.4 can be re-arranged as,

$$\log\left(\frac{da}{dN}\right)_p = \log C_p + n\log\left(\Delta K_{eff}\right) \qquad 4.3.5$$

Where $\log C_p = \log C + \alpha_p \sigma_z$ is now a random variable normally distributed with mean $\log C$ and variance σ_z^2. Considering the equality from equation 4.1.2, equation 4.3.5 can be re-written as,

$$\frac{da}{dN} = [C\exp(\ln 10.\alpha_p.\sigma_z)](\Delta K_{eff})^n = \overline{C}(\Delta K_{eff})^n \qquad 4.3.6$$

At the original work from Xing [108], equation 4.3.6 is derived from equation 4.3.1 as presented in this section, but taking the natural logarithm both sides from equation 4.3.1 which leads equation 4.3.6 to be written as,

$$\frac{da}{dN} = [C\exp(\alpha_p.\sigma_z)](\Delta K_{eff})^n = \overline{C}(\Delta K_{eff})^n \qquad 4.3.7$$

The difference between equations 4.3.6 and 4.3.7 is because in the former the value of σ_z is given in log-scale and in the latter it is given in natural-log-scale. As values of σ_z are more commonly found in the literature in log-scale, in this work equation 4.3.6 is adopted for probabilistic crack growth analysis.

For a given value of α_p, the number of cycles N_f to grow a crack from an initial crack size 'a_0' up to a crack size 'a_f' is obtained from direct integration of equation 4.3.6,

$$N_f = \frac{1}{\overline{C}} \int_{a_0}^{a_f} \frac{da}{(\Delta K_{eff})^n} \qquad 4.3.8$$

Based on Virkler findings described in the beginning of this section, it is assumed in this work that each initial damage scenario generated by Monte Carlo simulation (section 4.1) has a unique α_p value in equation 4.3.6, i.e., in practice each damage scenario is assigned a random '$\overline{C}$' value so that deterministic crack propagation can be performed as described in section 4.2.

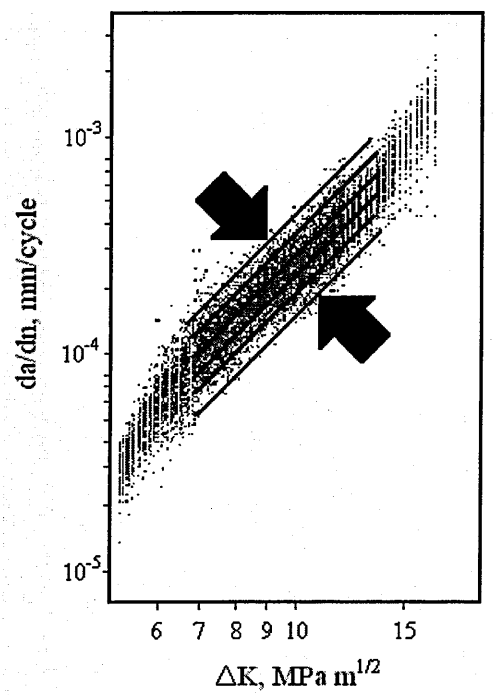

Figure 4.3.3: Various crack propagation rate curves for constant 'n' and variable 'C'.

The effect of considering 'n' constant and 'C' varying as a lognormal distribution is illustrated in Figure 4.3.3; where it can be seen that parallel crack growth rate curves are created to describe the scatter from Figure 4.3.2.

4.4. Failure Criterion

To check for residual strength during the crack growth period, the fracture toughness criterion is employed in this work for each crack existing in a cracked lap joint scenario.

The fracture toughness criterion states that the residual strength of a structural element will be lost when, for example, mode I stress intensity factor 'K_I' equals or surpass the material fracture toughness value K_C (plane stress conditions in the case of this work since thin sheets are considered),

$$K_I \geq K_C \qquad 4.4.1$$

Figure 4.4.1 illustrates an example of residual strength monitoring using the DTD code [87] for the lap joint configuration illustrated in Figure 4.1.1 where five cracks are present; represented by tips 1, 2, 3, 4 and 5.

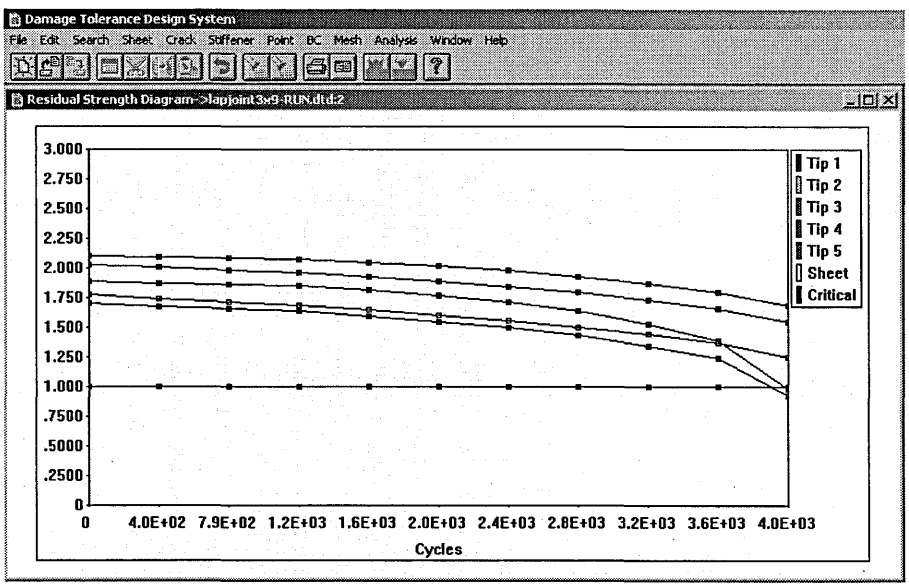

Figure 4.4.1: Residual strength monitoring with the DTD code [87].

The y-axis is plotted as K_C/K_I. The horizontal line y = 1 represents $K_I = K_C$ value for the lap joint analysed. The x-axis shows the number of cycles for crack propagation. It can be seen that as cracks grow, the corresponding K_I values for each crack tip

increases, causing crack tips 1, 2, 3, 4 and 5 curves to decrease values until one of these curves crosses y = 1, leading to failure due to the fracture toughness criterion.

4.5. Summary

In this chapter, a probabilistic MSD assessment model was proposed where both fatigue crack initiation and fatigue crack propagation were considered as random variables. The MSD assessment model developed was presented in three separate parts: fatigue crack initiation, deterministic crack growth and probabilistic crack growth up to failure. Continuing damage assumption was incorporated into the proposed MSD assessment model as a simplifying alternative to a damage accumulation technique present in MSD models reported in the literature (chapter 2). Fatigue crack initiation was calculated based on a lognormal distribution of lives, given by Monte Carlo simulation, to achieve a through-the-thickness crack size (macro crack range). Previous MSD simulations using dual boundary element models have used deterministic crack growth for open hole geometries in their analysis [39]. In this work, MSD analysis is performed in a row of pin-loaded holes and the probabilistic nature of crack propagation is considered. Crack propagation was based on the dual boundary element model presented in chapter 3 for lap joints subjected to MSD. Firstly, deterministic crack propagation is performed to each damage scenario generated from the crack initiation stage of the model. As cracks grow, the Swift criterion [103] is used to define link-up and the continuing damage assumption [76] is incorporated after link-up. Secondly, based on observations of the experimental work from Virkler [51], the probabilistic nature of crack propagation was incorporated into the model using a formulation proposed by Xing [108]. To check for the residual strength of a cracked lap joint, the fracture toughness criterion is employed as presented in section 4.4.

In the chapters to come, the proposed MSD assessment model is verified by comparison to another MSD model (to check for the continuing damage assumption) considering the same lap joint geometrical configuration and loading conditions; to experimental work from the literature and to in-service findings originated from teardown inspections of fuselage panels.

Chapter 5

5. EXPERIMENTAL WORK PROCEDURES

In this chapter the procedures for the experimental work performed are described. The objective of the experimental work was to determine fatigue life mean and scatter (standard deviation) values for typical riveted lap joint samples manufactured with different rivet squeeze force levels; and use these values to address, by means of Monte Carlo simulation, its implications to MSD behaviour, which has not been addressed yet (chapter 2).

As presented in chapter 2, recent publications from the literature have already highlighted the importance of high squeeze force on the improvement of mean time to initiation of fatigue cracks, but no concern to changes in scatter and its implication to MSD behaviour has been reported. Workers have been focusing the comparison of the mean time to crack initiation considering different squeeze force values applied to various material types, geometrical configurations and loading conditions for riveted joints; and the quantity of fatigue tests performed has frequently ranged from 2 to 5 for each joint configuration analysed.

In order to a test sample distribution demonstrate a good approximation to a normal one, the execution of at least twenty one tests is recommended [109]. In the next sections a strap lap joint test specimen, manufactured with three different squeeze force values, is presented. The testing procedures for twenty one fatigue tests, performed for each test specimen configuration, are described.

5.1. Specimen Description and Manufacturing Procedures

The lap joint geometrical configuration tested is of a strap containing 3 rows of rivets and 1 rivet per row. Countersunk rivets (NAS1097AD5-5 of aluminium 2117) were used to attach the sheets mechanically and there was no bonding or sealant between the mating sheets, i.e., the assembly was dry. The lap joint sheet material is Al2024-T351

Clad L-T direction and the dimensions of the test specimen are presented in Table 5.1.1 and Figures 5.1.1 and 5.1.2.

Table 5.1.1: Lap joint test specimen dimensions.

Description	Dimension (mm)	Reference
Length (l)	250 ± 0.050	Figure 5.1.1
Clamping length (c)	40 ± 0.050	Figure 5.1.1
Edge distance (e)	10 ± 0.025	Figure 5.1.1
Pitch (p)	20 ± 0.025	Figure 5.1.1
Width (W)	20 ± 0.050	Figure 5.1.1
Thickness (t)	1.6	Figure 5.1.1
Hole diameter (d_0)	Reamed to 4	Figure 5.1.2
Countersink (A)	0.94 ± 0.025	Figure 5.1.2

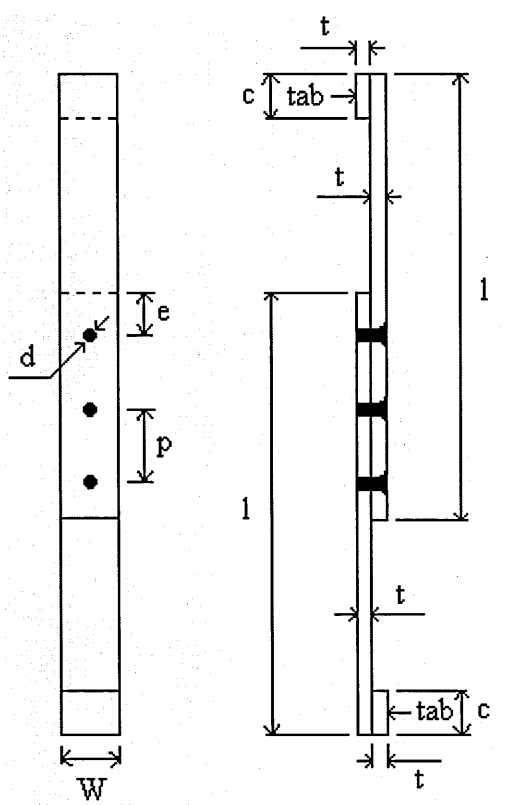

Figure 5.1.1: Lap joint test specimen geometry.

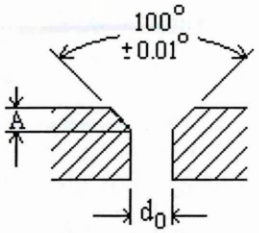

Figure 5.1.2: Hole countersink detail from Figure 5.1.1.

From Figure 5.1.1 it can be seen that there are two tabs (Al2024-T351 Clad) placed at the extremes of the lap joint assembly. The tabs are glued to the base sheets by means of araldite 420A resin mixed with araldite 420B hardener in a proportion of, respectively, 5:2. The resin and hardener mixture is cured at 50 ^{0}C during four hours. The purpose of the tabs is to keep the load applied to the centre line of the lap joint assembly.

In order to rivet the samples sketched in Figure 5.1.1, a controlled compressive force riveting process was performed by using a hydraulic testing machine INSTRON 8500 (50 KN capacity), as illustrated in Figure 5.1.3. Each rivet was squeezed separately using a compressive load rate of 10 KN per minute up to the specified value.

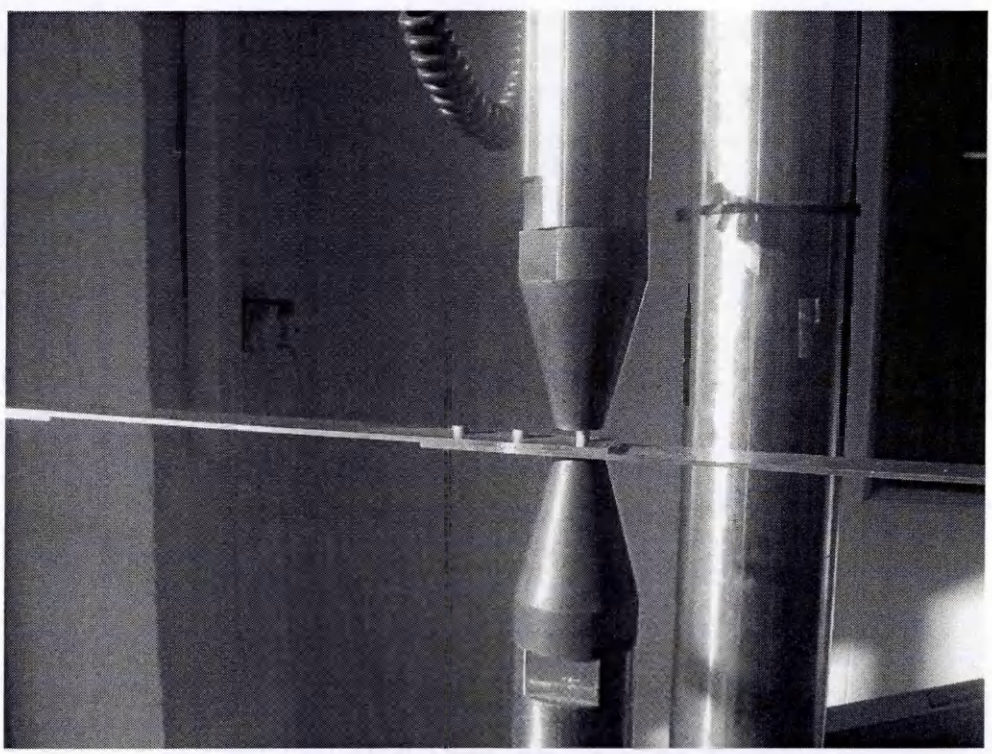

Figure 5.1.3: Riveting controlled compressive force.

The amount of compressive squeeze force load 'F_{sq}' and measured displacement '$\Delta h = h_0 - h$' to form different ratios 'd/d_0', as sketched in Figure 5.1.4, are presented in Table 5.1.2.

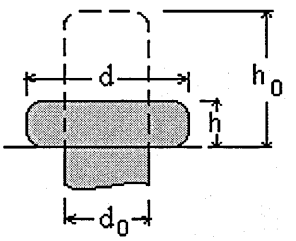

Figure 5.1.4: Rivet formed head.

Table 5.1.2: Rivet squeeze force and correspondent d/d_0 ratio.

F_{sq} (KN)	Δh x 10^{-3} m	d x 10^{-3} m	d/d_0 ratio
0	---	4.00	1.00
2	0.16	4.00	1.00
4	0.57	4.11	1.03
6	1.13	4.33	1.08
8	1.71	4.81	1.20
10	2.16	5.19	1.30
12	2.49	5.49	1.37
14	2.70	5.73	1.43
16	2.96	6.07	1.52
18	3.13	6.29	1.57
20	3.28	6.51	1.63
21	3.32	6.57	1.64
22	3.45	6.71	1.68
23	3.49	6.73	1.68
24	3.52	6.83	1.71
25	3.58	6.91	1.73

Figure 5.1.5 (a), (b) and (c) illustrates the case of different rivet formed head ratios 'd/d_0' due to, respectively, the application of 10, 16 and 24 KN squeeze force values from Table 5.1.2.

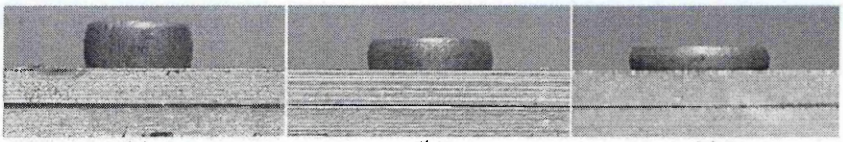

Figure 5.1.5: Different rivet formed heads due to 10, 16 and 24 KN squeeze forces.

5.2. Testing Procedures

The testing procedures consist of fatigue testing to failure the strap lap joint illustrated in Figure 5.1.1 under two different stress levels (100 and 120 MPa), with constant amplitude loading ($R = S_{min}/S_{max} = 0.1$) and 20 Hz frequency; according to the test matrix presented in Table 5.2.1. As it can be seen from Table 5.2.1, three different rivet squeeze force values 'F_{sq}' were considered: 10, 16 and 24 KN. For each testing configuration 21 samples were tested.

Table 5.2.1: Testing matrix for the sample from Figure 5.1.1.

Testing configuration	Maximum stress (MPa)	R (S_{min}/S_{max})	F_{sq} (KN)	d/d_0*	No. tests
1	100	0.1	10	1.30	21
2			16	1.52	21
3			24	1.71	21
4	120	0.1	10	1.30	21
5			16	1.52	21
6			24	1.71	21

* Values from Table 5.1.2

The criterion for choosing the squeeze force values from Table 5.2.1 was based on findings from previous workers, such as Muller [79] and Chiarelli [53], where 10, 16 and 24 KN are considered, respectively, low, mean and high squeeze force values. The mean squeeze force values are typical manufacturing procedure adopted in the aeronautical industry for riveted fuselage panels; and they form rivet heads [Figure 5.1.5 (b)] around a 'd/d_0' ratio equal to 1.5 (Table 5.1.2).

The fatigue tests, presented in Table 5.2.1, were conducted by a hydraulic testing machine INSTRON DARTEC M9500 series (10 KN capacity), and the samples (Figure 5.1.1) were placed in the testing machine as illustrated in Figure 5.2.1. Figure 5.2.1 (a) shows an overview of the testing machine (left) and its control panel (right). Figure 5.2.1 (b) shows the sample itself gripped in the testing machine.

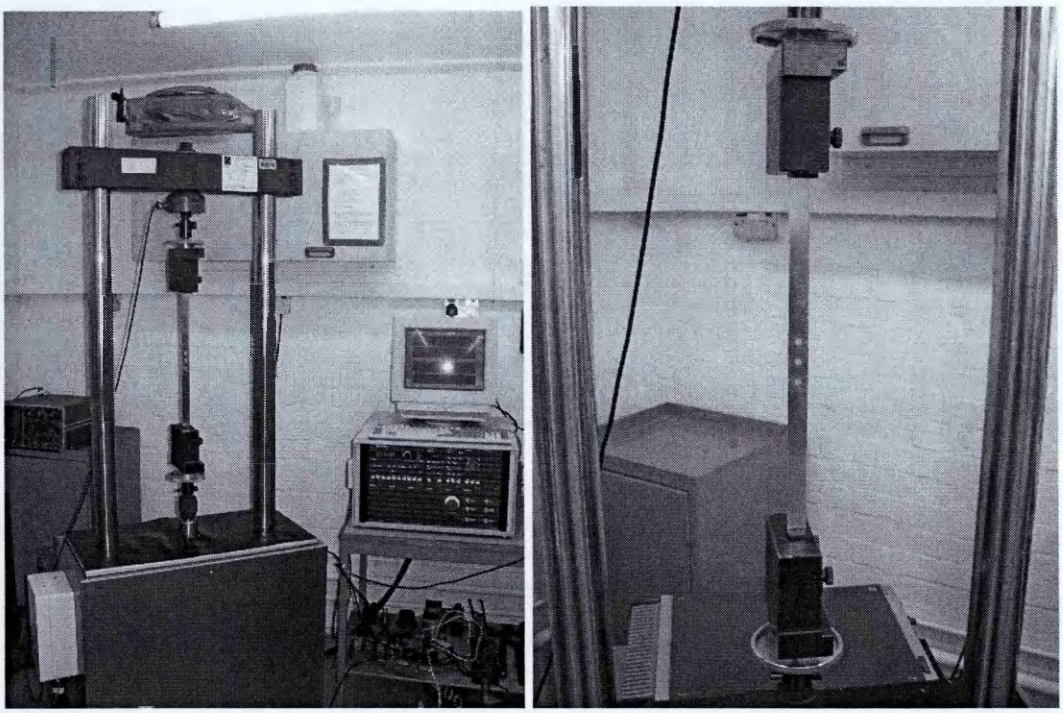

(a) (b)

Figure 5.2.1: Testing rig.

The tensile loads 'P_i' applied, considering the stress levels presented in Table 5.2.1, and R = 0.1 are obtained as follows:

$$P_i = S_i \,.\, A \qquad 5.2.1$$

Where: 'P_i' is the tensile load;

'S_i' is the tensile stress; and

'A' is the cross section area 'W.t' (Figure 5.1.1).

The values obtained for P_i are presented in Table 5.2.2 as P_{max} and P_{min}, and they represent, respectively, the maximum and the minimum load values corresponding to each maximum stress value and R = 0.1.

Table 5.2.2: Testing loads according to Table 5.2.1.

Maximum stress (MPa)	A x 10^{-6} (m^2)	P_{max} (N)	P_{min} (N)
100	32	3,200	320
120		3,840	384

The experimental work data, derived from the test matrix presented in Table 5.2.1, regards the number of fatigue cycles to fail the specimens from Figure 5.1.1. In the following chapter, this data will be reduced to fatigue crack initiation data for a pre-defined crack size value. Afterwards, the mean time to crack initiation and the corresponding scatter values are derived, for each testing configuration from Table 5.2.1, to serve as input variables to the MSD assessment model, presented in chapter 4, so that MSD behaviour can be addressed due to changes in rivet squeeze force.

5.3. Summary

In this chapter, the experimental work objective, the test specimen configuration, manufacturing details and testing procedures were presented. It has been highlighted the need for establishing the effect that changes in rivet squeeze force may cause to MSD behaviour, via Monte Carlo simulation, which has not been addressed yet.

The results from the experimental work procedures described in this chapter are presented in chapter 6; and its implications to MSD discussed in chapter 7.

Chapter 6

6. RESULTS

6.1. Experimental Work

As presented in chapter 5, the testing procedures consist of fatigue testing to failure the strap lap joint illustrated in Figure 5.1.1 according to the test matrix presented in Table 5.2.1, which is repeated here as Table 6.1.1. Three different rivet squeeze force values 'F_{sq}' were considered: 10, 16 and 24 KN which represents a low, a medium and a high squeeze force values.

Table 6.1.1: Testing matrix for the sample from Figure 5.1.1.

Testing configuration	Maximum stress (MPa)	R (S_{min} /S_{max})	F_{sq} (KN)	d/d_0*	No. tests
1	100	0.1	10	1.30	21
2			16	1.52	21
3			24	1.71	21
4	120	0.1	10	1.30	21
5			16	1.52	21
6			24	1.71	21

* Values from Table 5.1.2

The fatigue life to failure as a function of maximum stress level (100 and 120 MPa) for each test specimen from Table 6.1.1 is plotted in Figure 6.1.1. The notation 'F_{sq}' in the legend denotes squeeze force. For the case of the testing configuration number 3 (Table 6.1.1), the fatigue tests were interrupted at 2,200,000 cycles due to the high number of cycles obtained, and 5 test points fall into this situation.

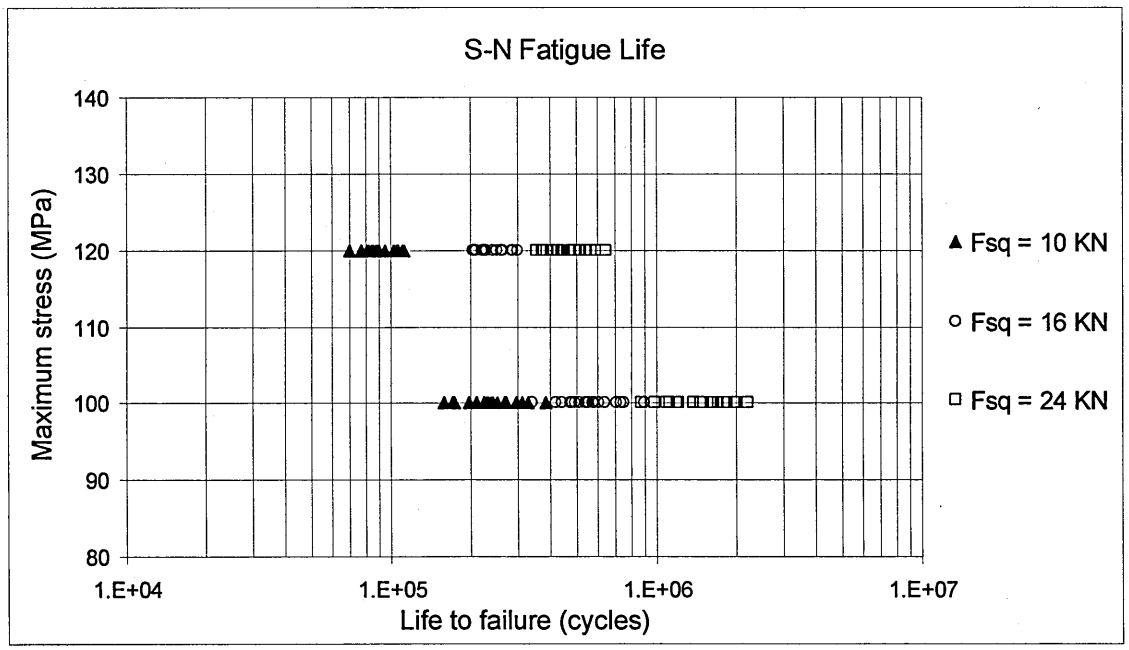

Figure 6.1.1: Fatigue life to failure for each test specimen from Table 6.1.1.

Considering that n observations $N_1, N_2, ..., N_n$ form a sample distribution randomly selected from a normal distribution of mean μ and standard deviation σ, the sample distribution mean $\bar{x}$ and the standard deviation s are the estimates of, respectively, μ and σ given by [109],

$$\bar{x} = \frac{\sum_{i=1}^{n} N_i}{n} \qquad 6.1.1$$

$$s = \sqrt{\frac{\sum_{i=1}^{n} (N_i - \bar{x})^2}{n-1}} \qquad 6.1.2$$

When μ and σ are the mean and the standard deviation of $\log(N)$, and N is the number of cycles to failure, the best estimates of μ and σ are, respectively, given by substituting N_i by $\log(N_i)$ in equations 6.1.1 and 6.1.2 [20].

The parameters μ and σ are enough by themselves to define the normal distribution, but sometimes the coefficient of variation v is also employed. Any two of the three parameters μ, σ and v can be used to define the normal distribution, and the expression for the coefficient of variation is given by [109],

$$v = \frac{\sigma}{\mu} \qquad 6.1.3$$

In this work, the estimated coefficient of variation is given by,

$$v' = \frac{s}{\bar{x}} \qquad 6.1.4$$

The values for $\bar{x}$, s and v' for each testing configuration from Table 6.1.1 are presented in Table 6.1.2. The $\bar{x}$ and s values are given in both cycles and log (cycles), according to equations 6.1.1 and 6.1.2. The v' value is given by equation 6.1.4 for the values of $\bar{x}$ and s in log (cycles). The values presented in Table 6.1.2 are also illustrated from Figures 6.1.2 to 6.1.7.

From Figure 6.1.2 it can be seen the effect of rivet squeeze force on the mean time to failure (cycles) for the 6 testing configurations from Table 6.1.1. For both stress levels (100 and 120 MPa) the increase of squeeze force increases $\bar{x}$, with the greater stress range producing the smallest lives. In the case of 100 MPa stress level, the increase of $\bar{x}$ (cycles) for squeeze forces varying from 10 to 16 KN, 16 to 24 KN and 10 to 24 KN are, respectively, by factors of 2.4, 2.9 and 6.9. In the case of 120 MPa stress level, the increase of $\bar{x}$ (cycles) for squeeze forces varying from 10 to 16 KN, 16 to 24 KN and 10 to 24 KN are, respectively, by factors of 2.6, 1.9 and 5.0.

Figures 6.1.3 and 6.1.4 show the same results as in Figure 6.1.2 but with the associated standard deviation value (cycles) for, respectively, 100 and 120 MPa stress levels. For both stress levels the increase of squeeze force increases the s values, with the greater

stress range producing the smallest scatters. In the case of Figure 6.1.3, the increase of s for squeeze forces from 10 to 16 KN, 16 to 24 KN and 10 to 24 KN are, respectively, by factors of 2.3, 3.4 and 7.7. In the case of Figure 6.1.4, the increase of s for squeeze forces varying from 10 to 16 KN, 16 to 24 KN and 10 to 24 KN are, respectively, by factors of 2.4, 2.7 and 6.7.

Table 6.1.2: Fatigue life to failure parameters from Table 6.1.1.

Testing configuration	F_{sq} (KN)	$\bar{x}$ (cycles)	s (cycles)	$\bar{x}$ log (cycles)	s log (cycles)	v'
1	10	238,079	57,849	5.3650	0.1029	0.0192
2	16	573,893	133,096	5.7478	0.1005	0.0175
3	24	1,652,713	447,697	6.2014	0.1274	0.0205
4	10	92,377	11,822	4.9622	0.0555	0.0112
5	16	244,396	28,805	5.3853	0.0508	0.0094
6	24	461,954	78,856	5.6588	0.0718	0.0127

Notation:

F_{sq}: Rivet squeeze force;

$\bar{x}$: Estimated mean fatigue life;

s : Estimated standard deviation; and

v' : Estimated coefficient of variation.

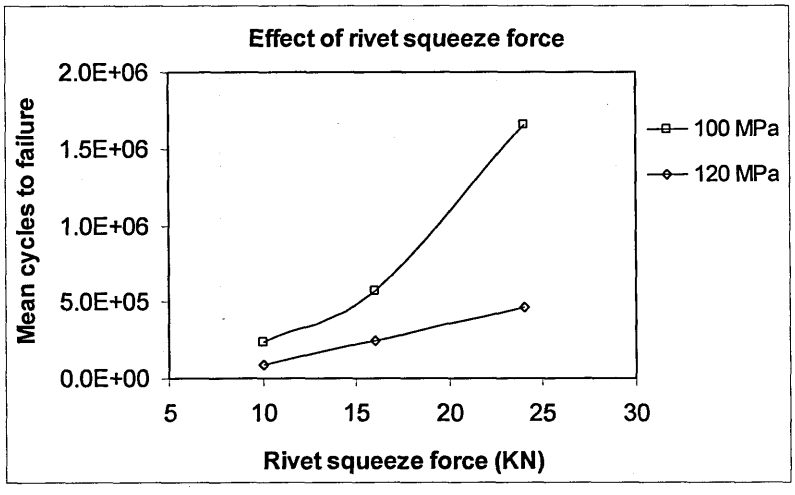

Figure 6.1.2: Effect of rivet squeeze force on the mean cycles to failure.

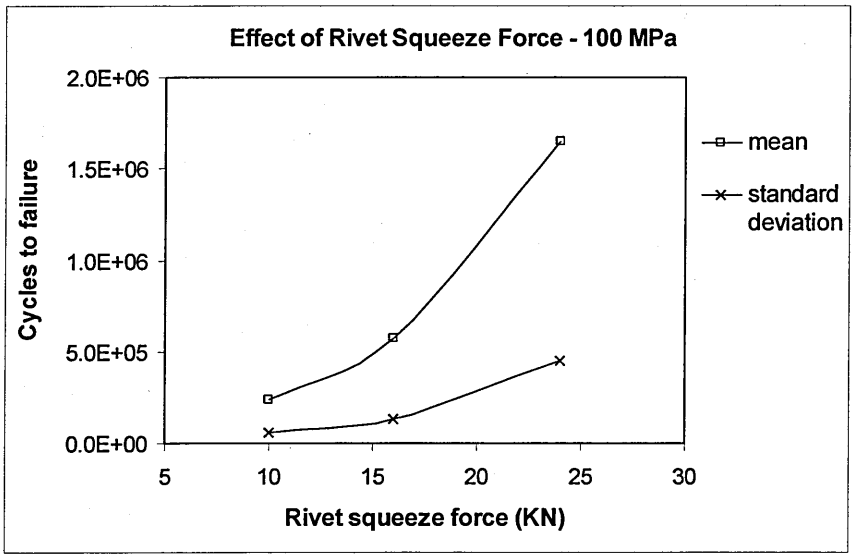

Figure 6.1.3: Rivet squeeze force effect on mean cycles to failure and corresponding standard deviation at 100 MPa.

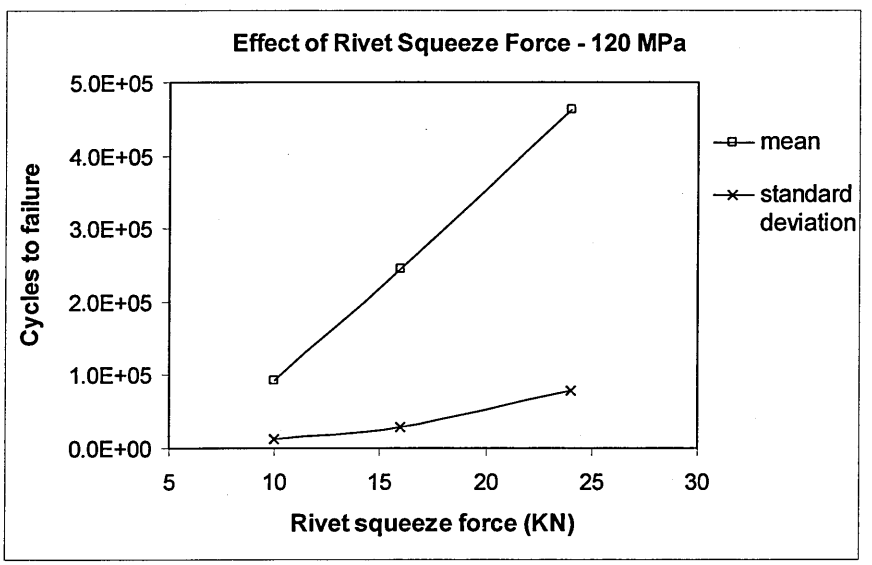

Figure 6.1.4: Rivet squeeze force effect on mean cycles to failure and corresponding standard deviation at 120 MPa.

From Figures 6.1.2 to 6.1.4, the high squeeze force value (24 KN) produced the biggest fatigue lives to failure and the biggest standard deviation values.

Figure 6.1.5 shows the same results as in Figure 6.1.1 but with fatigue life to failure in log (cycles) with the corresponding standard deviation value for each rivet squeeze

force and at both 100 MPa and 120 MPa stress levels. From Figure 6.1.5, as observed from Figures 6.1.2 to 6.1.4, for the same stress level the high squeeze force value (24 KN) produced the biggest fatigue lives to failure and the biggest standard deviation values. It can also be seen that an increase in the stress level leads to a reduction of the standard deviation values for similar fatigue lives, no matter the squeeze force value adopted.

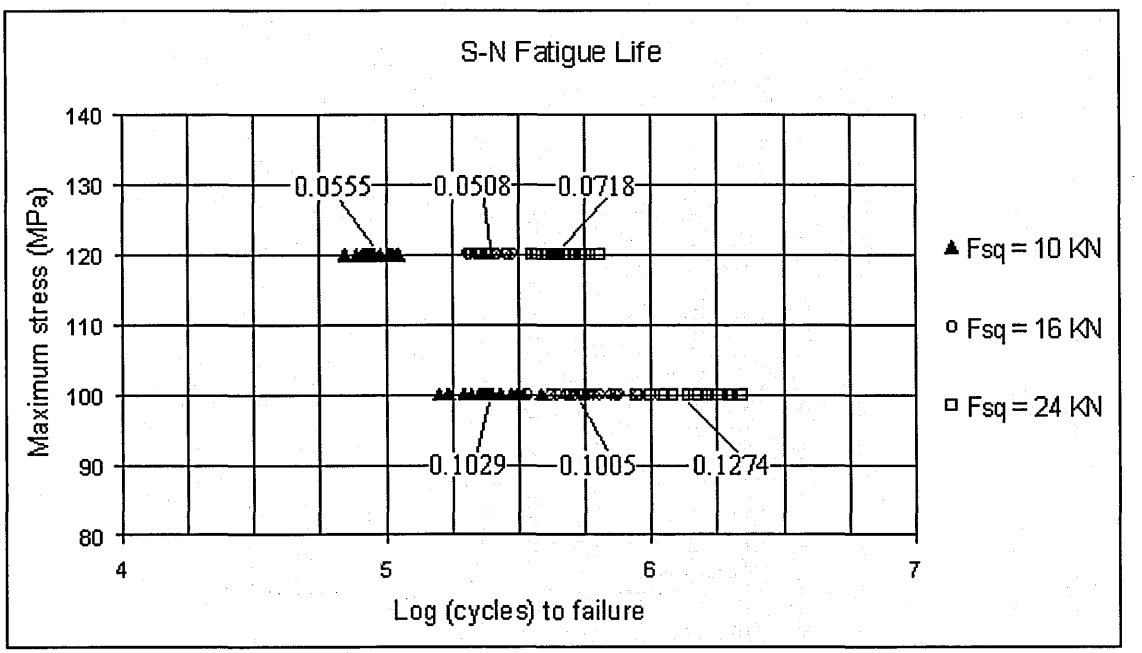

Figure 6.1.5: Fatigue life to failure for each test specimen from Table 6.1.1.

Another parameter that can be used to define a log-normal distribution is the coefficient of variation v', as in equation 6.1.4. The data from Table 6.1.2 for the values of v' as a function of rivet squeeze force and number of log (cycles) to failure are presented in Figures 6.1.6 and 6.1.7.

Figure 6.1.6 shows that at the stress of 120 MPa, v' values are between 0.0094 and 0.0127. At the smaller stress of 100 MPa, v' values are between 0.0175 and 0.0205. The largest values of v' are associated with the highest squeeze forces and smallest stresses. At each stress value, the highest squeeze force always has the greatest v' and the intermediate squeeze force the smallest v'.

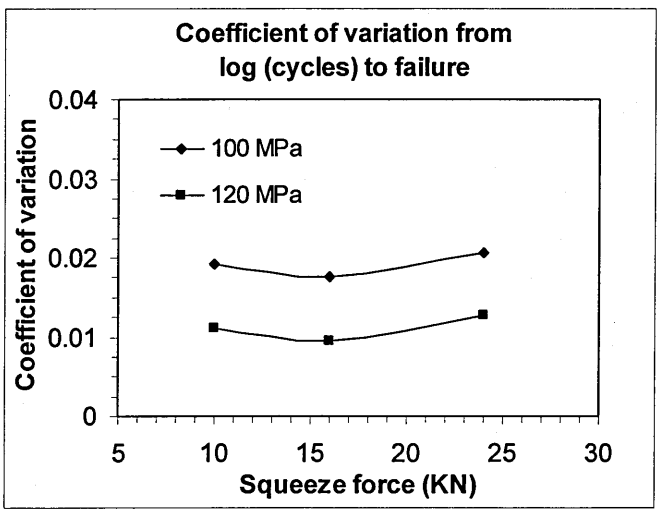

Figure 6.1.6: Coefficient of variation as a function of squeeze force.

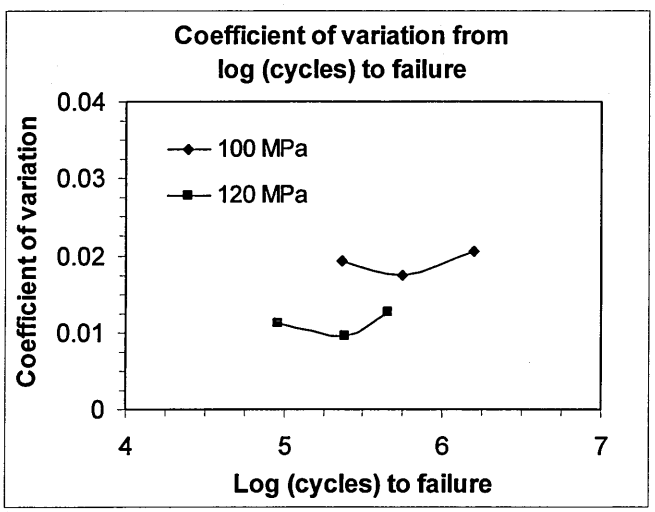

Figure 6.1.7: Coefficient of variation as a function of log (cycles) to failure.

It needs to be established whether squeeze force influences v' at similar values of life to failure. Figure 6.1.7 shows a plot of v' derived from mean values of lives in log (cycles) for tests at 100 and 120 MPa. It can be seen from Figure 6.1.7 that, at lives between 5.3 and 5.7 log (cycles), specimens at 100 MPa have greater values of v' than those at 120 MPa, irrespective of the squeeze force.

From Figures 6.1.6 and 6.1.7 it can be seen that largest values of v' are associated with smallest stresses, long lives and large squeeze forces; and the smallest values of v' are associated with the highest stresses and intermediate lives and squeeze forces.

Regarding the fracture surface of the test specimens from the testing matrix presented in Table 6.1.1, Figure 6.1.8 shows a typical crack detected from a 16 KN squeeze force test specimen at approximately the 9 o'clock position of the hole border. The crack length is of 1.0 mm detected by visual inspection.

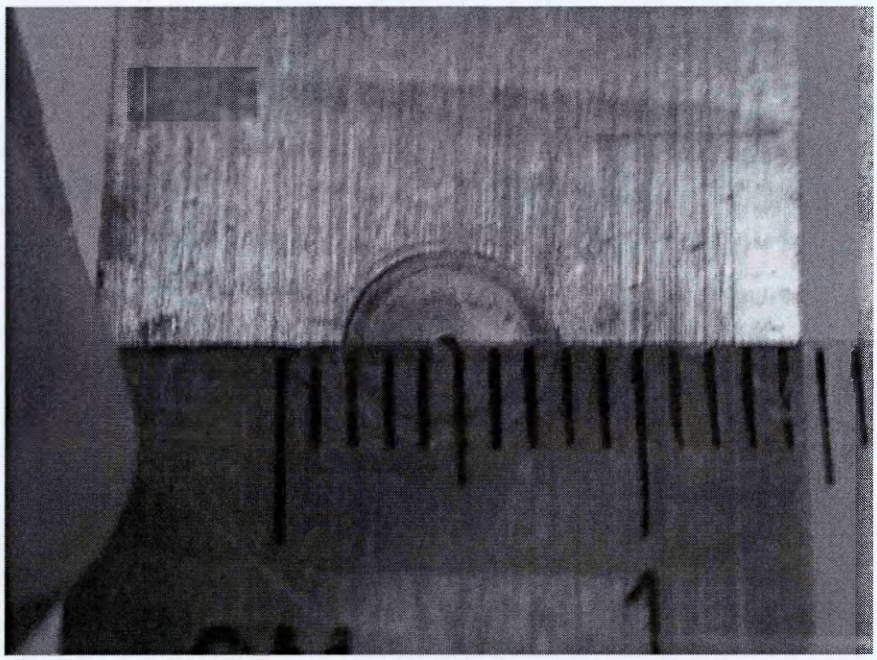

Figure 6.1.8: Visual inspection crack detection.

Figures 6.1.9 and 6.1.10 show, respectively, typical lateral and front view from fracture surfaces of 10 KN squeeze force test specimens at 100 MPa maximum stress level (Table 6.1.1). Figures 6.1.11 and 6.1.12 show the same information but for 16 KN squeeze force test specimens and Figures 6.1.13 and 6.1.14 for 24 KN squeeze force test specimens.

From Figures 6.1.9, 6.1.11 and 6.1.13 some shaded surfaces can be clearly observed which increase in area as the squeeze force increases. These shaded surfaces are possibly fretting regions created by friction between both sheets, during constant amplitude fatigue testing, due to the clamping forces originated from the riveting process. Figures 6.1.10, 6.1.12 and 6.1.14 show crack fronts which resemble an elliptical shape in all cases.

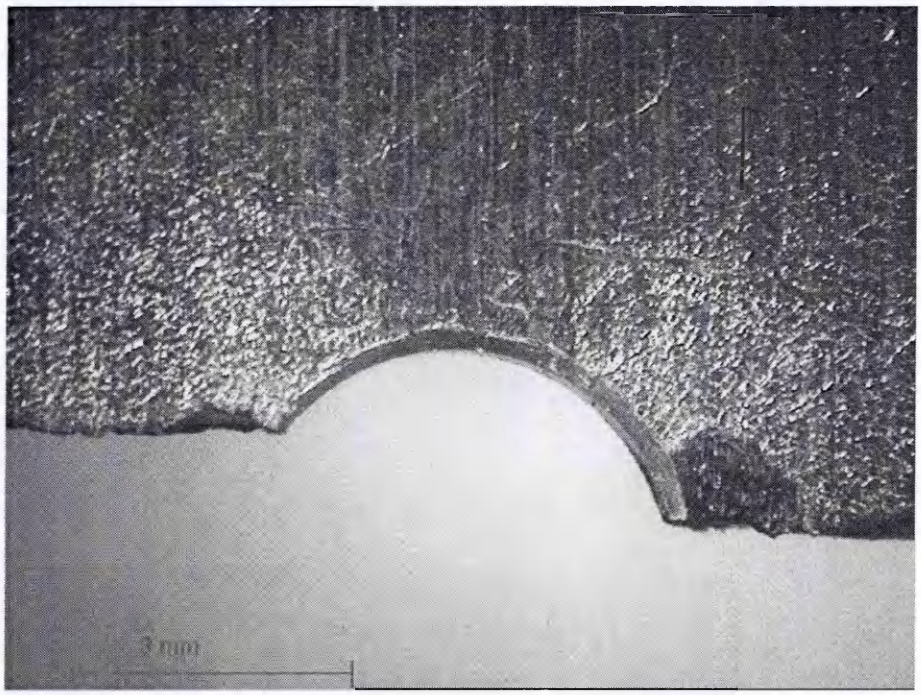

Figure 6.1.9: Lateral fracture surface from testing configuration 1 (Table 6.1.1)

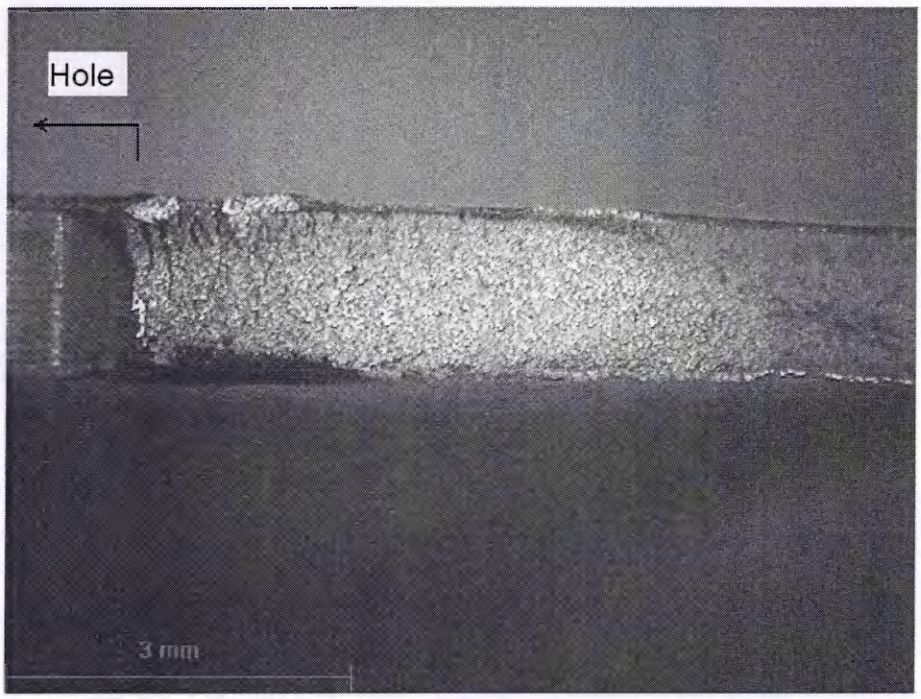

Figure 6.1.10: Front fracture surface from testing configuration 1 (Table 6.1.1)

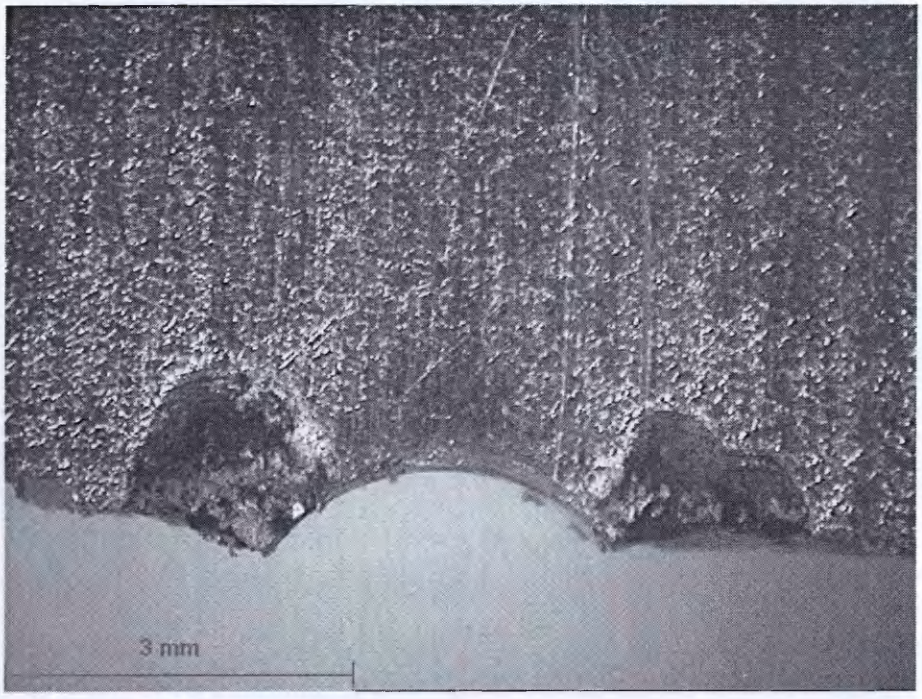

Figure 6.1.11: Lateral fracture surface from testing configuration 2 (Table 6.1.1)

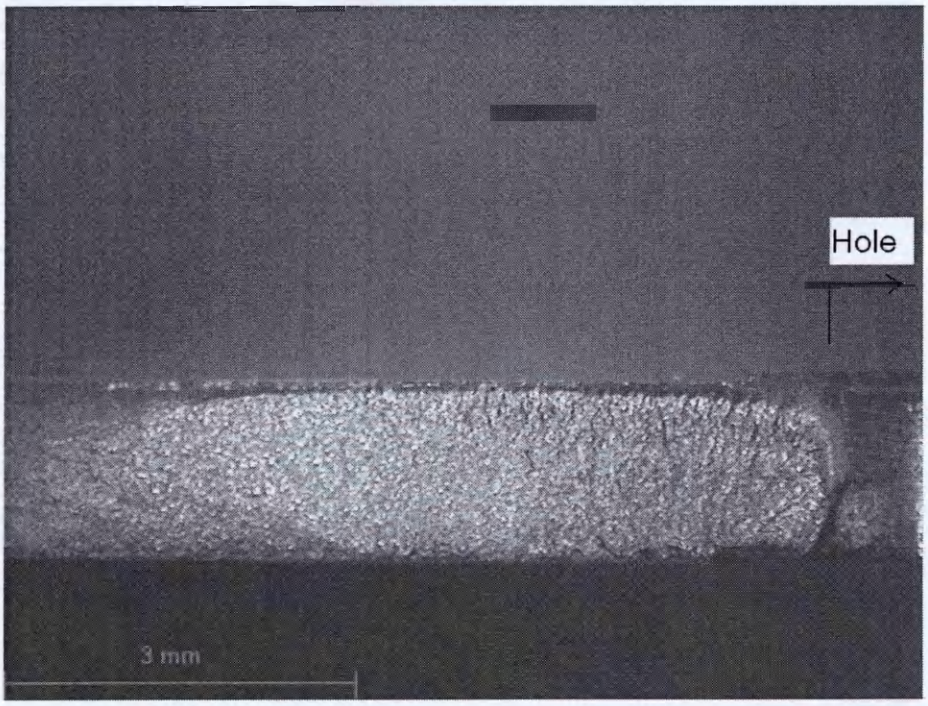

Figure 6.1.12: Front fracture surface from testing configuration 2 (Table 6.1.1)

Figure 6.1.13: Lateral fracture surface from testing configuration 3 (Table 6.1.1)

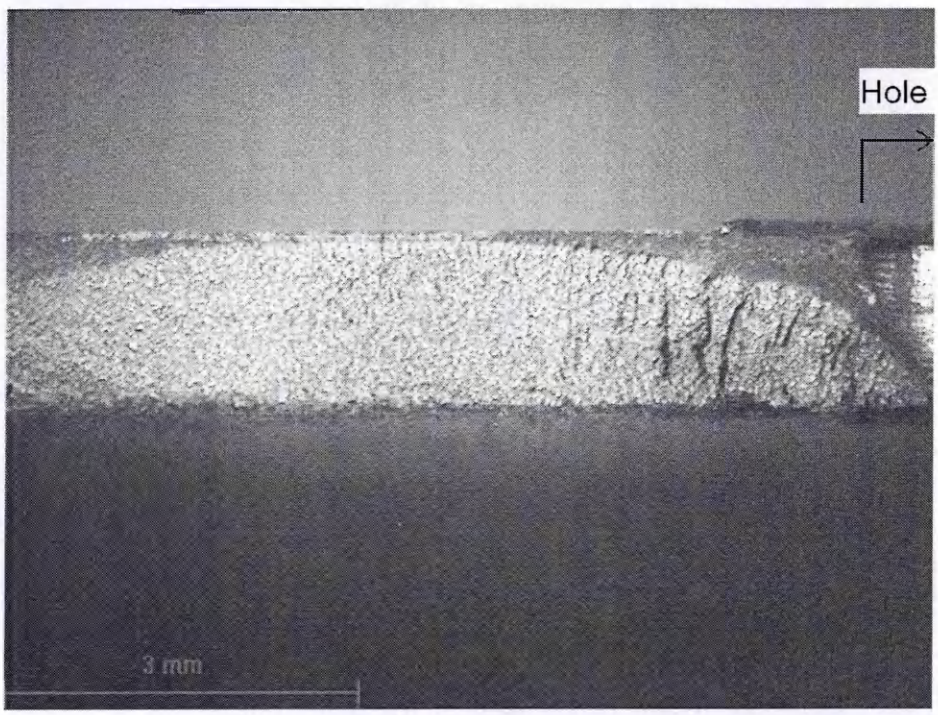

Figure 6.1.14: Front fracture surface from testing configuration 3 (Table 6.1.1)

Figure 6.1.15 shows a sketch of a segment of hole border and a fretting region (as in Figures 6.1.9, 6.1.11 and 6.1.13) where 'p' is the approximate mean point for fatigue crack initiation measured with the help of an optical microscope, 'D', 'h' and 'r' are distances measured from the centre '0' of the hole and θ is the angle formed by 'r' and 'D' with centre in '0'. AA' is a centre line that crosses the 3 and 9 o'clock positions and the middle of the hole '0'. Table 6.1.3 presents the mean values of 'D', 'h', 'r' and θ measured from all testing configurations 1, 2 and 3 (Table 6.1.1).

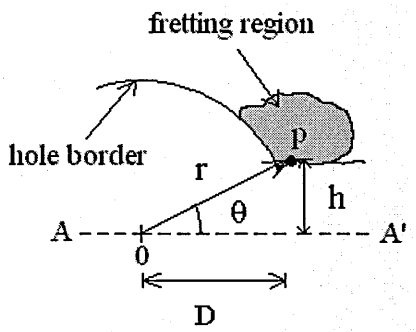

Figure 6.1.15: Mean fatigue crack initiation site coordinates.

Table 6.1.3: Mean crack initiation sites for configurations 1, 2 and 3 (Table 6.1.1).

Mean fatigue crack initiation site coordinates				
Squeeze Force (KN)	D (mm)	h (mm)	r (mm)	θ (degrees)
10	1.8	0.9	2.0	26.6
16	1.6	1.6	2.3	45.0
24	1.4	2.0	2.4	55.0

As it can be observed from Table 6.1.3, the coordinate 'r' is a vector that changes its value (given by changes in 'D' and 'h') and direction (given by changes in θ). For the 10 KN squeeze force the values of 'r' and θ are the smallest ones and for the 24 KN squeeze force the biggest ones. In the case of the 10 KN squeeze force the value of 'r' is practically the same as the hole radius (2.0 mm), indicating that in average cracks nucleate at the hole border or extremely close to it. As the squeeze force increases to 16 KN and to 24 KN, the mean values of 'r' and θ increase indicating that cracks tend to nucleate further away from the hole border.

In general, the fracture surface pictures review that as the squeeze force increases the mean crack nucleation sites move further away from the centre of the hole '0' and from the centre line AA' (Figure 6.1.15).

6.2. Methodology Application

6.2.1. Comparison to Experimental Work from the Literature

Regarding the MSD methodology proposed in chapter 4, the MSD assessment model is employed to analyse the lap joint configuration presented in Fig. 4.1.1, reproduced here as Figure 6.2.1.1, and the results compared to experimental work from the literature for validation of the approach. Appendix A presents the rough cracking chronology for 6 unstiffened riveted lap joints (Figure 6.2.1.1) from Santgerma [31].

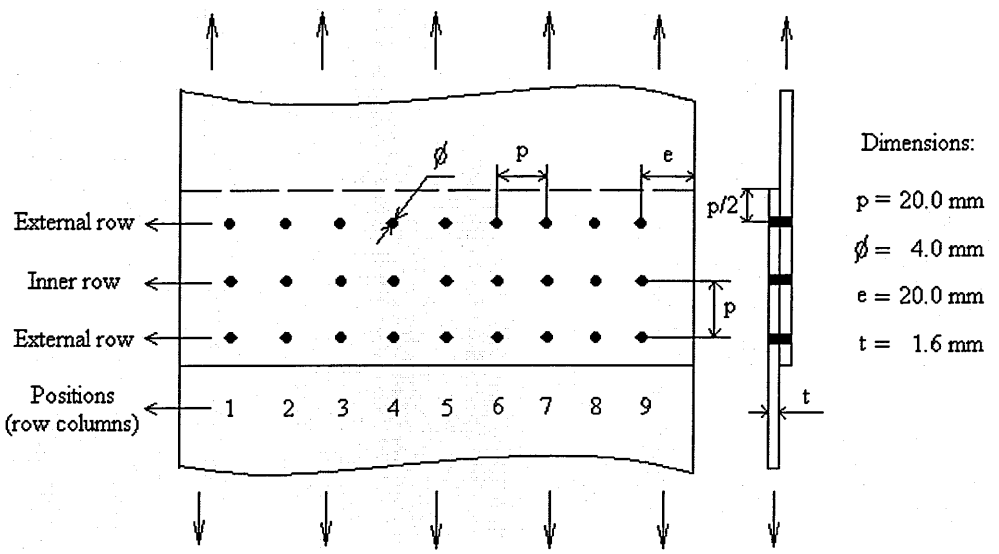

Figure 6.2.1.1: Riveted lap-splice joint configuration.

The geometry selected (Figure 6.2.1.1) is of a typical fuselage lap joint section. The material is Al2024-T3 Clad T-L and the material properties employed are σ_{UTS} = 448 MPa, σ_{YS} = 331 MPa and K_{1C} = 32 MPa $m^{1/2}$. Material constants for deterministic crack growth C and n values (equation 3.1.3) are C = 6.09E-11 and n = 2.6, obtained from Salgado [87]; and $\sigma_z[\log] = 0.043$ has been assumed, following Proppe [40], for

probabilistic crack growth (equation 4.3.6). The lap joint configuration is subjected to a cyclic tensile stress of 100 MPa and R = 0.1. It has to be highlighted that the value of K_{1C} from the DTD code (32 MPa $m^{1/2}$) for Al2024-T3 is set automatically for plane strain condition showing that the author of the code [87] chose a conservative approach when calculating critical crack size values via the fracture toughness failure criterion

For the geometrical configuration from Figure 6.2.1.1, the S-N fatigue curve is given by reference [31] and the number of cycles 'N' is obtained as a function of the theoretical local elastic stress 'S' (from FE analysis [31]) existing at both 3 and 9 o'clock positions of each hole for the external rows of the lap joint from Figure 6.2.1.1. The value of the local elastic stresses 'S' for each FCL (18 FCLs corresponding to 9 holes) calculated by the DTD code [87] is presented in Figure 6.2.1.2; and these values are within ± 5 % from the corresponding ones obtained by the elastic FE analysis [31].

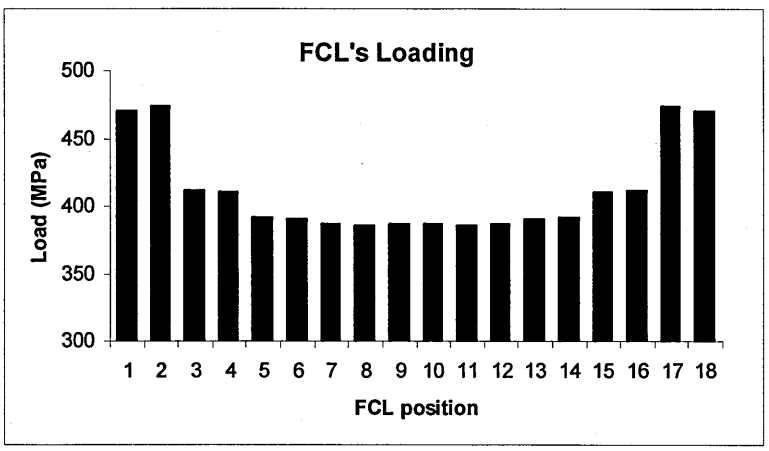

Figure 6.2.1.2: Calculated local elastic stresses at 3 and 9 o'clock positions for an external row from Figure 6.2.1.1 – elastic analysis.

From Figure 6.2.1.2, it can be seen that the FCLs '1 and 2' (corresponding to, respectively, the 9 and 3 o'clock positions for row column no. 1 at the external rows – Figure 6.2.1.1) and '17 and 18' (corresponding to, respectively, the 9 and 3 o'clock positions for row column no. 9 at the external rows – Figure 6.2.1.1) are the highest stressed locations. This fact is due to FCLs 1, 2, 17 and 18 are located at the pin-loaded holes by the free edges of the lap joint (holes 1 and 9 - Figure 6.2.1.1). While for the inner holes (from 2 to 8 – Figure 6.2.1.1) there is a pair of adjacent pin-loaded holes to

re-distribute the far field load applied, for the case of holes 1 and 9 (Figure 6.2.1.1) there is only one adjacent hole each case plus a free edge distance equal to one pitch ('e' from Figure 6.2.1.1) causing holes 1 and 9 (Figure 6.2.1.1) to be overloaded compared to the other ones.

From the experimental results presented in appendix A [31], the first and the last holes (corresponding to, respectively, FCLs '1 and 2' and '17 and 18' – Figure 6.2.1.2) were riveted with 60 μ m interference to avoid crack nucleation at these sites [31]; although it did not happen to all test specimens (Figures A1, A4 and A5 – appendix A), and, therefore, in this work cracks were allowed to nucleate at the first and last holes (corresponding to, respectively, FCLs '1 and 2' and '17 and 18' – Figure 6.2.1.2) to simulate what was observed from appendix A. The values of the local stresses at FCLs '1 and 2' and '17 and 18' (9 and 3 o'clock positions for, respectively, row columns no. 1 and no. 9 at the external rows – Figure 6.2.1.1) were arbitrarily assumed as in Figure 6.2.1.3, i.e., as the smallest stress value presented in Figure 6.2.1.2 (386.3 MPa).

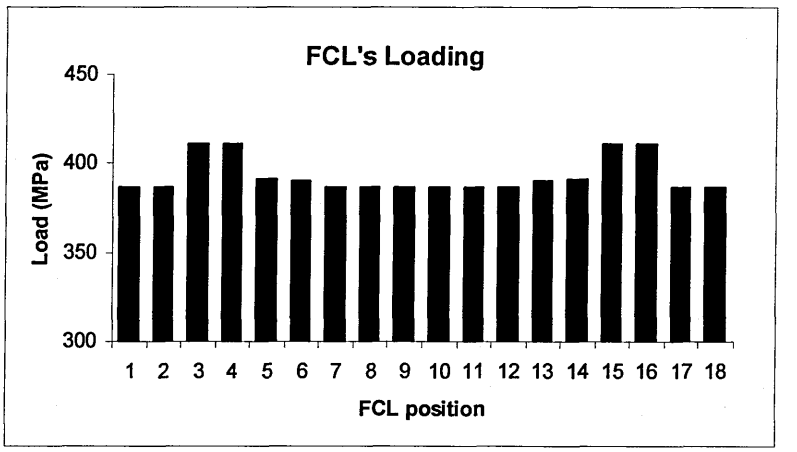

Figure 6.2.1.3: Assumed local elastic stresses at 3 and 9 o'clock positions for an external row from Figure 6.2.1.1.

The values of the mean fatigue life 'μ' for crack nucleation and the corresponding standard deviation 'σ' for the lap joint geometry presented in Figure 6.2.1.1 are given by [31],

$$\mu = \log 10^5 \left(\frac{S - 11.5}{494.5 - 11.5} \right)^{-6.2} \qquad 6.2.1.1$$

$$\sigma = \frac{14018}{S^2} + \frac{2.76}{S} + 0.11 \qquad 6.2.1.2$$

Where S is the local elastic stress value for each FCL assumed as in Figure 6.2.1.3. It has to be noted that equation 6.2.1.2 has no physical meaning since it is not dimensionally balanced. The initial crack size 'a_0' for the S-N curve defined by equations 6.2.1.1 and 6.2.1.2 is equal to 1.0 mm. The initial crack size 'a_0' was obtained by normalizing the rough experimental data (as presented in Appendix A) to achieve a fatigue life corresponding to a crack length of 1.0 mm. The normalized test data, used for comparison purposes in this section, is reproduced in Table 6.2.1.1 and it comes from Santgerma [31]; where TTCI is the time to crack initiation, TCP is the time for crack propagation and N_f is the number of cycles to failure (TTCI + TCP) for the 6 test specimens.

Table 6.2.1.1: Experimental fatigue test data from Santgerma [31].

Specimen no.	TTCI (cycles) a_0 = 1.0 mm	TCP (cycles)	N_f = TTCI + TCP (cycles)
1	280,900	85,200	366,100
2	281,950	85,111	367,061
3	201,700	36,200	237,900
4	201,950	68,150	270,100
5	200,000	85,368	285,368
6	97,000	45,827	142,827
Mean	210,583	67,642	278,226

Figures 6.2.1.4 and 6.2.1.5 present plots for, respectively, equations 6.2.1.1 and 6.2.1.2. As is can be seen from these figures, both the mean TTCI (μ) and the corresponding standard deviation (σ) vary as the local elastic stress S assumes different values. For the case of local elastic stresses presented in Figure 6.2.1.3, the values of μ and σ range from, respectively, 5.51 to 5.68 log (cycles) and 0.20 to 0.21 log (cycles).

The DBEM lap joint model which has been idealized to analyze the lap joint configuration from Figure 6.2.1.1 is presented in Appendix B.

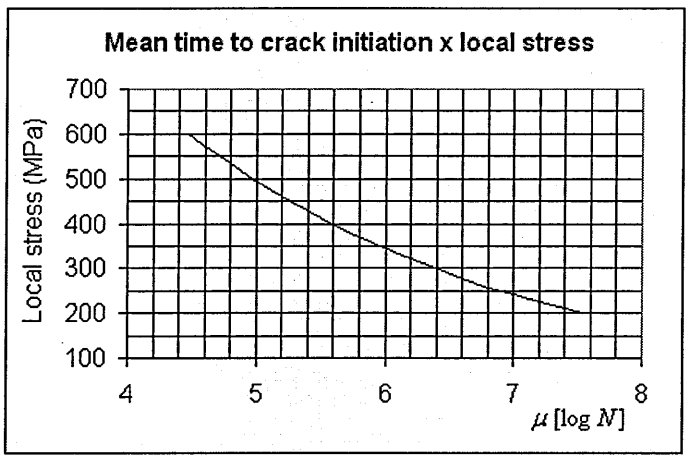

Figure 6.2.1.4: Plot of equation 6.2.1.1.

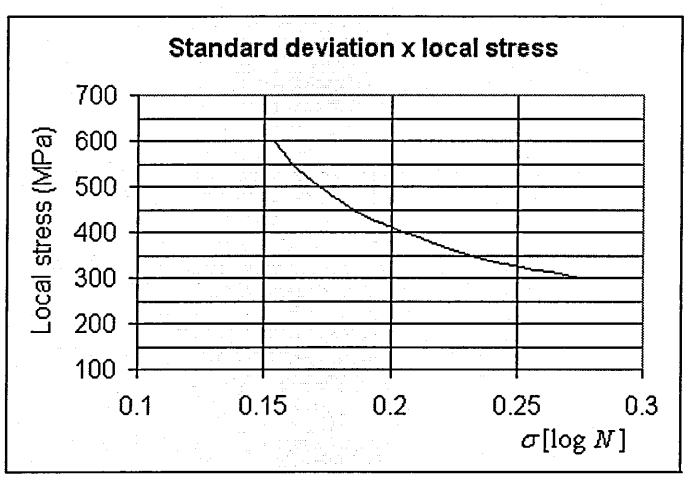

Figure 6.2.1.5: Plot of equation 6.2.1.2.

Figure 6.2.1.6 sketches the MSD development for one damage scenario. From Figure 6.2.1.6, the whole MSD simulation sequence can be seen, i.e., crack nucleation, crack growth, link-up, continuing damage and failure. In this scenario, the 1st crack nucleated with 129,609 cycles at the right side of hole no. 8, and the 2nd crack nucleated with 137,197 cycles at the right side of hole no. 5. The number of cycles to crack initiation (section 4.1), crack propagation (section 4.2) and failure (section 4.4) always refer to the first crack nucleated (the lead crack) in each damage scenario.

Figure 6.2.1.7 presents an excel worksheet idealized for random fatigue crack initiation calculation, which in this case refers to the scenario sketched in Figure 6.2.1.6; where Sce # is the scenario number, FCL is the fatigue critical location (18 FCLs corresponding to 9 holes), S is the local elastic stress for each FCL from Figure 6.2.1.3, MeanTTCI is the mean time to crack initiation (log-scale) for each FCL given by equation 6.2.1.1, Stdeva is the standard deviation value (log-scale) given by equation 6.2.1.2, Ran # is a random number assigned to each FCL obtained from Hudson [101], TTCI is the random time to crack initiation (log-scale) assigned to each FCL given by equation 4.1.1 and TCI is the random time to crack initiation (cycles) assigned to each FCL given by equation 4.1.3.

From column H of Figure 6.2.1.7 it can be seen the attributed random initial fatigue lives assigned to each FCL for scenario 94. The smallest fatigue life for crack initiation is the one from cell H18, which corresponds to FCL 16 (right side of hole no. 8 – Figure 6.2.1.6) where the lead crack enters the model to start crack propagation. The lead crack is then inserted in the DBEM model (Appendix B) and it is propagated by the DTD code [87] to create a file of crack size versus number of cycles for crack propagation.

The second crack to enter the model is the one from cell H12 (right side of hole no. 5 – Figure 6.2.1.6) because it has the second smallest initial fatigue life (Figure 6.2.1.7). The difference between the first and the second smallest fatigue lives is 7,288 cycles (137,197 – 129,909 cycles). From the crack size versus number of cycles file for propagation of the lead crack generated by the DTD code [87], when 7,288 cycles is reached the lead crack has an approximate length of 2.3 mm (Figure 6.2.1.6). At this stage of the model, the second crack is inserted in the DBEM model (as sketched in Figure 6.2.1.6) where the lead crack length is set to be 2.3 mm. Both cracks are then propagated simultaneously by the DTD code [87] (Figure 6.2.1.8 illustrates an example of crack propagation starting at the second continuing damage stage from Figure 6.2.1.6), and from Figure 6.2.1.6 it can be seen that the total time for crack propagation is 52,201 cycles (182,110 – 129,909 cycles), when failure occurs at 182,110 cycles (fracture toughness criterion). From Figure 6.2.1.7, it can be seen that the third smallest initial fatigue life assigned to an FCL is the one from cell H16 (182,407 cycles); but as

failure occurred at 182,110 cycles (Figure 6.2.1.6) a third crack is not placed into the scenario from Figure 6.2.1.6, which had two nucleated cracks only.

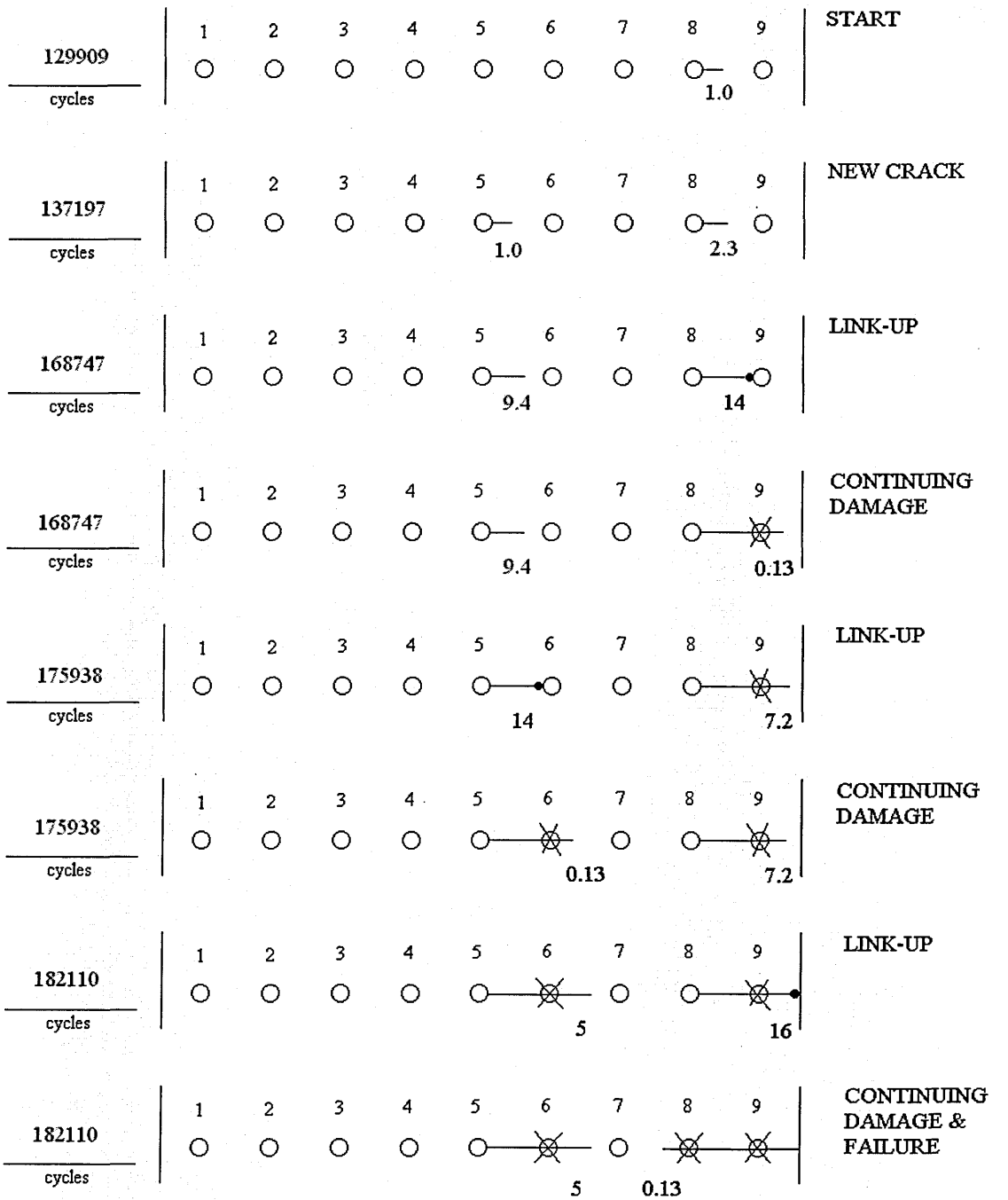

Figure 6.2.1.6: Example of MSD simulation sequence for one damage scenario.

	A	B	C	D	E	F	G	H	I
1									
2	Sce #	FCL	S	MeanTTCI	Stdeva	Ran #	TTCI (log)	TCI (cycles)	
3	94	1	386.3	5.682915	0.211082	0.348414	5.756459	562336	
4		2	386.3	5.682915	0.211082	0.899543	5.872792	734849.7	
5		3	411.4	5.508374	0.199533	0.984861	5.704886	499437.3	
6		4	410.7	5.513091	0.199827	0.994882	5.711895	507554.3	
7		5	391.2	5.647941	0.208654	0.350136	5.720998	518292.3	
8		6	390.5	5.652909	0.208995	0.322082	5.720223	517369.2	
9		7	386.5	5.681478	0.210981	-1.81339	5.298888	196308.3	
10		8	386.3	5.682915	0.211082	-0.84522	5.504503	315009.5	
11		9	386.7	5.680043	0.21088	-1.45307	5.37362	233124.2	
12		10	386.7	5.680043	0.21088	-2.54611	5.14312	137197.4	
13		11	386.3	5.682915	0.211082	0.268246	5.739537	540870	
14		12	386.5	5.681478	0.210981	0.763388	5.842539	685455.4	
15		13	390.5	5.652909	0.208995	-1.18529	5.40519	250681.1	
16		14	391.2	5.647941	0.208654	-1.82592	5.266955	182407.1	
17		15	410.7	5.513091	0.199827	0.015401	5.516168	323575.4	
18		16	411.4	5.508374	0.199533	-1.94949	5.119386	129908.8	
19		17	386.3	5.682915	0.211082	-0.65585	5.544476	345343.8	
20		18	386.3	5.682915	0.211082	-1.65336	5.33392	212780.5	

Figure 6.2.1.7: Example of a worksheet for random fatigue crack initiation calculation.

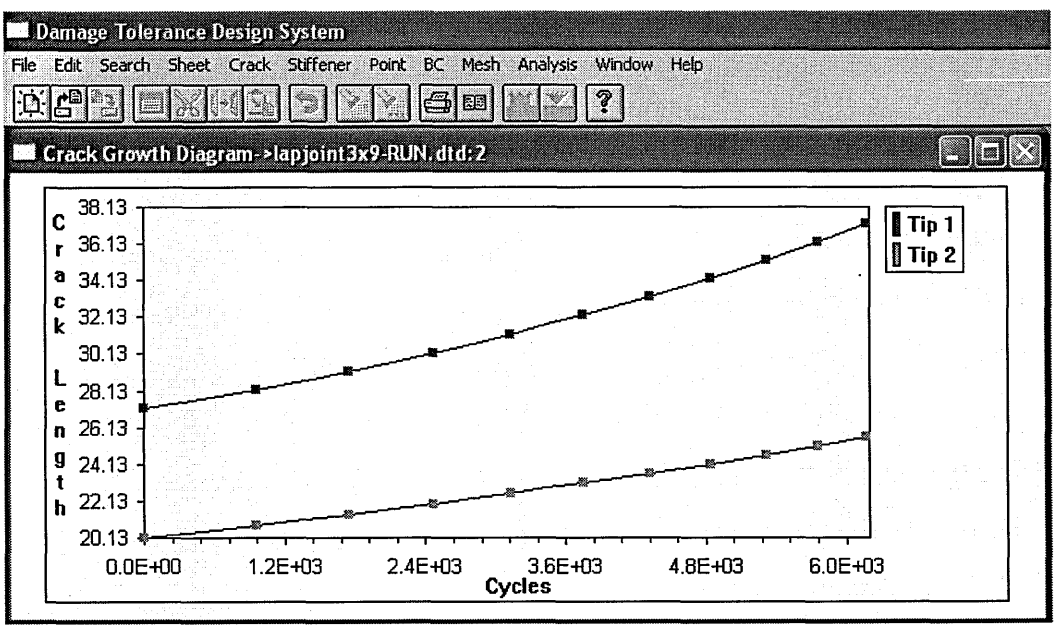

Figure 6.2.1.8: Example of simultaneous crack propagation performed with the DTD code [87] for the damage scenario from Figure 6.2.1.6.

The procedure described previously for the MSD simulation of scenario 94 is repeated for each damage scenario, as many times as necessary, by employing an excel worksheet for random fatigue life crack initiation and the DTD code [87] for deterministic crack propagation up to failure.

The result of 400 Monte Carlo simulations (400 damage scenarios), represented by black dots, is presented in Figure 6.2.1.9 together with the 6 experimental test points from Table 6.2.1.1. In Figure 6.2.1.9, each black dot is one damage scenario where the x-axis presents the TTCI and the y-axis the TCP for the lead crack.

From Figure 6.2.1.9 it can be seen that lives to failure are dominated by crack initiation, with mean initiation life equal to 176,455 cycles and the mean propagation life equal to 54,286 cycles, i.e., the initiation phase represents 76.5 % of the mean failure process (TTCI + TCP = 176,455 + 54,286 cycles = 230,741 cycles). Total initiation life varies from 55,758 to 352,684 cycles, whereas propagation lives are between 24,206 to 88,382 cycles. From Table 6.2.1.1 it can be seen that the spread of the six experimental test points are enclosed by the range of 400 Monte Carlo simulations presented in Figure 6.2.1.9 at both initiation and propagation axis. The mean initiation and propagation lives of the simulations are, respectively, 16.2 % and 19.7 % smaller than the one from the experimental data; leading, consequently, to the mean failure life of the simulations (230,741 cycles) being 17.1 % smaller than the 6 experimental test points (278,226 cycles).

Figures 6.2.1.10 and 6.2.1.11 show the convergence behaviour of, respectively, the mean life to failure and the associated standard deviation values as a function of the number of Monte Carlo simulations related to the results from Figure 6.2.1.9. As it can be seen from Figure 6.2.1.10, the minimum number of Monte Carlo simulations necessary to stabilize the mean number of cycles to failure is around 280; while from Figure 6.2.1.11 the same value for the associated standard deviation is 250.

The reason for checking for the minimum necessary number of simulations for life to failure and its corresponding standard deviation is that the results from Figure 6.2.1.9 can also be presented in terms of cumulative distributions of failure (TTCI + TCP). In order to plot such distributions, it is necessary to estimate the unbiased mean and standard deviation values to failure; and these estimators are obtained when convergence is achieved from Monte Carlo simulations.

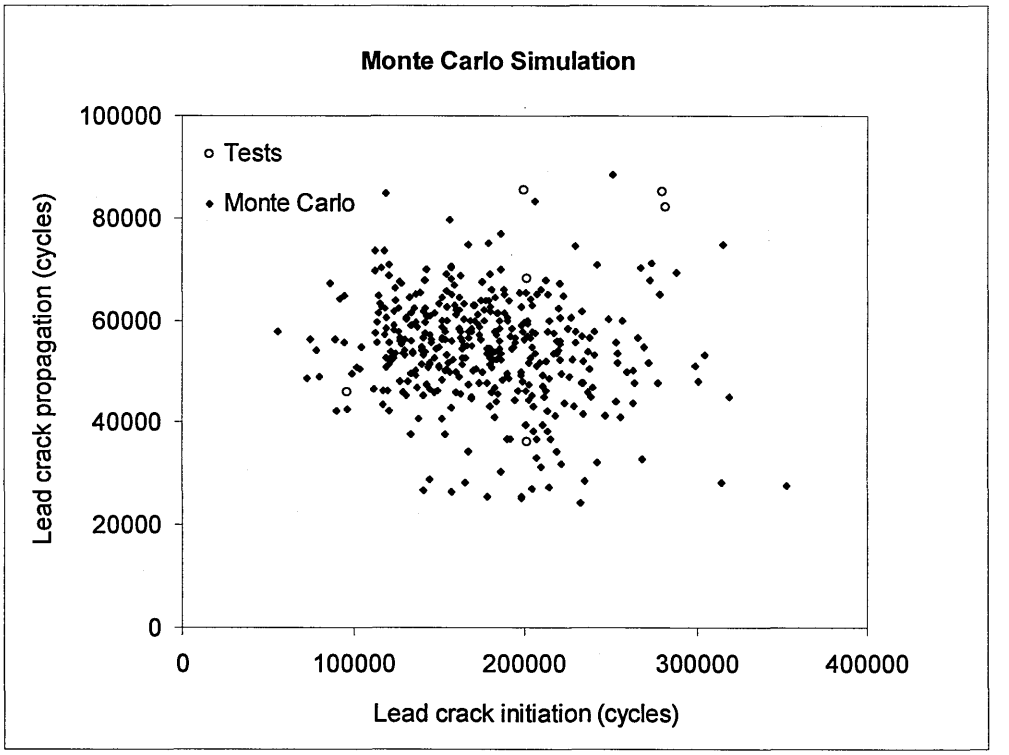

Figure 6.2.1.9: Monte Carlo simulation comparison to experimental data from Table 6.2.1.1 [31] – standard deviation for TTCI (log) = 0.21, non-uniform pin-loading and 100 MPa (R = 0.1) cyclic tensile stress.

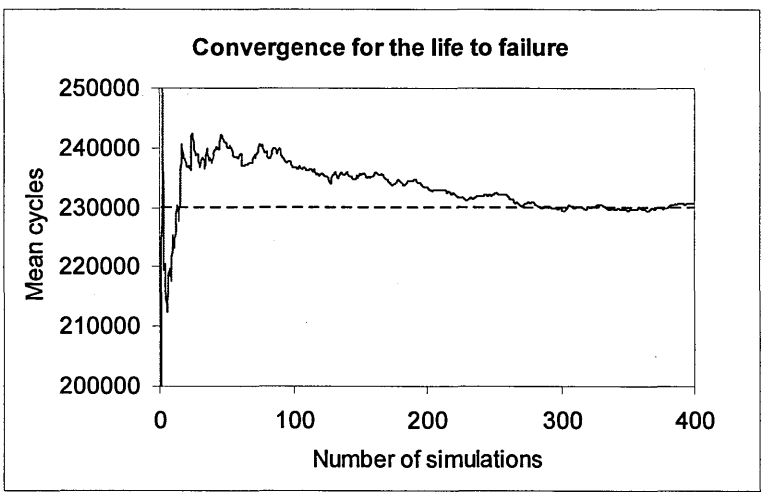

Figure 6.2.1.10: Convergence of mean number of cycles to failure as a function of number of Monte Carlo simulations.

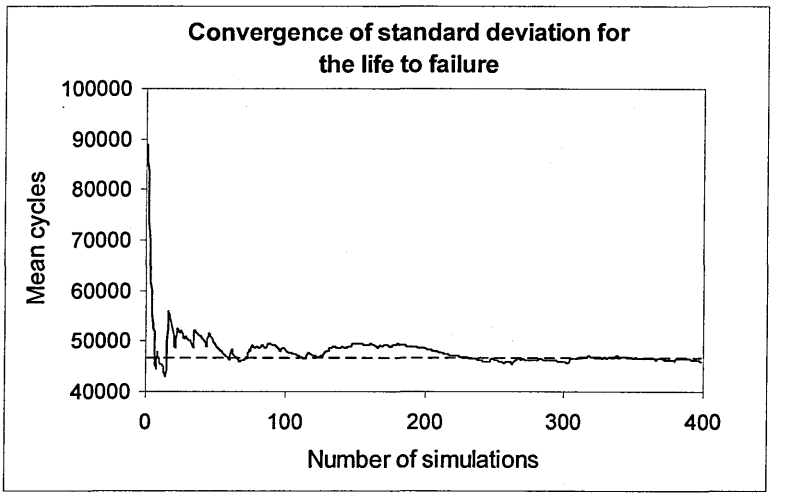

Figure 6.2.1.11: Convergence of mean number of cycles of the standard deviation to failure as a function of number of Monte Carlo simulations.

Figure 6.2.1.12 shows the cumulative probability distribution of failure from the results presented in Figure 6.2.1.9 together with the theoretical cumulative normal distribution. The x-axis shows the number of cycles to failure and the y-axis the corresponding cumulative probabilities from 0 to 1 (0 to 100%). The theoretical distribution is plotted by using an excel function called NORMDIST with the same mean and corresponding standard deviation values for failure from Monte Carlo simulations (converged values from Figures 6.2.1.10 and 6.2.1.11). From Figure 6.2.1.12, the 0.5 cumulative probability of failure corresponds to 230,741 cycles which represents the mean failure behaviour given by the Monte Carlo simulation results from Figure 6.2.1.9. With the mean number of cycles to failure established, the ISP and the SMP are calculated as, respectively, 76,914 cycles and 115,371 cycles; considering, respectively, factors 3 and 2 as recommended in reference [3].

From the results shown in Figure 6.2.1.9, two interesting outcomes to be investigated are the ones related to the crack nucleation positioning generated by the Monte Carlo simulations and also the number of cracks present in each single scenario. Figure 6.2.1.13 presents the percentage of lead crack nucleation sites for the external row of holes from Figure 6.2.1.9. As it can be seen hole positions 2 and 8 (Figure 6.2.1.1) present a clear tendency for crack nucleation compared to the other positions; and this fact should be expected considering the pin-loading from Figure 6.2.1.3.

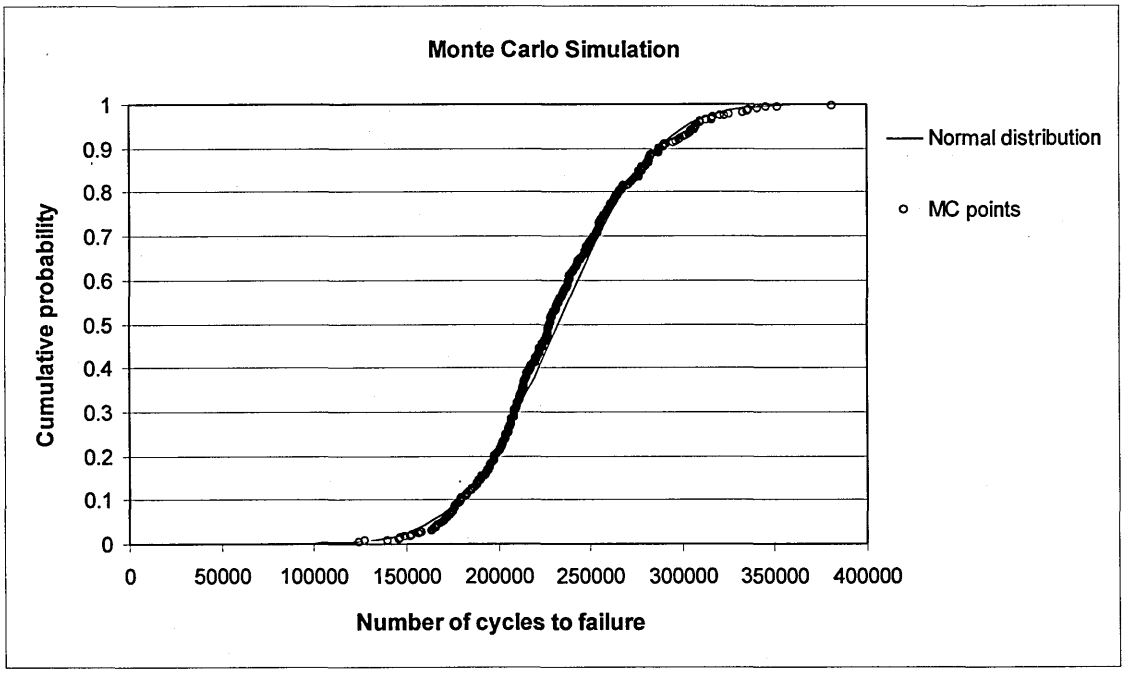

Figure 6.2.1.12: Cumulative probability distribution of failure from Figure 6.2.1.9.

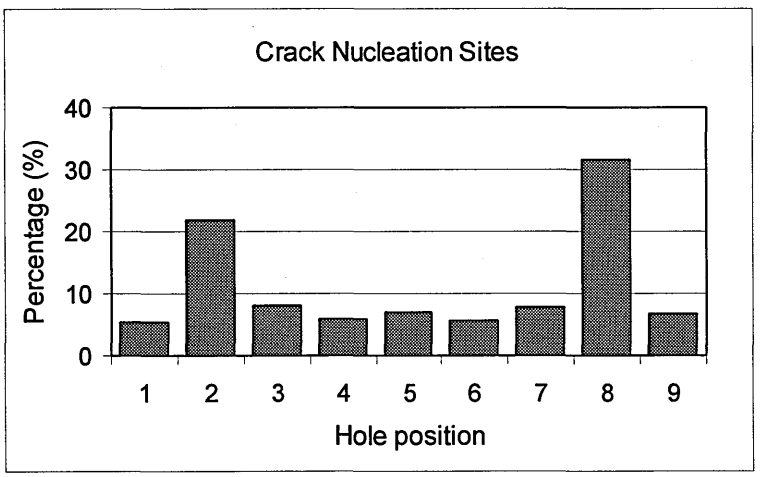

Figure 6.2.1.13: Percentage of lead crack nucleation sites for the external row of holes from Figure 6.2.1.9.

Figure 6.2.1.14 shows the percentage of scenarios which developed 1, 2, 3, 4 and 5 cracks related to the 400 simulations from Figure 6.2.1.9. It can be seen that damage scenarios which developed only one crack represent a bit more than 40 % of the cases and the maximum number of cracks developed were 5, which represents less than 0.5 % of the simulations.

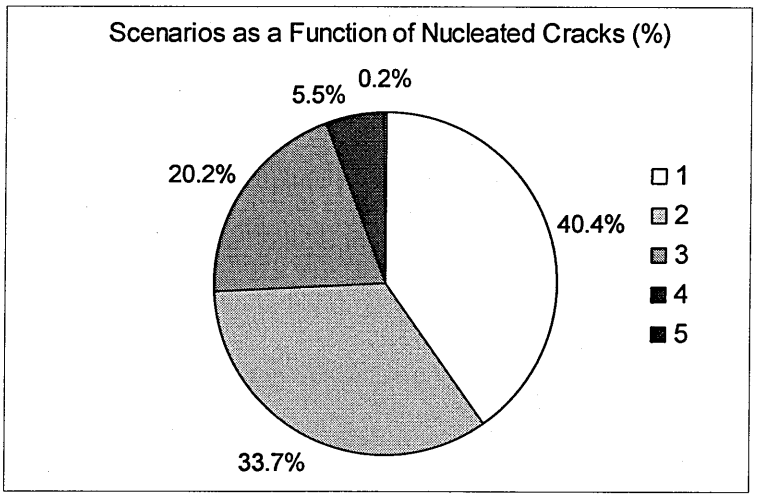

Figure 6.2.1.14: Percentage of scenarios as a function of number of nucleated cracks from Figure 6.2.1.9.

6.3. Parametric Study

In this section, the MSD assessment model presented in chapter 4 is employed to perform a parametric study to investigate variables influencing MSD assessment. These variables are the standard deviation for fatigue crack initiation (section 6.3.1), hole pin-loading (section 6.3.2), nominal stress level (section 6.3.3) and high rivet squeeze force (section 6.3.4). 400 simulations were performed for all Monte Carlo data presented in the next sections; and the minimum number of simulations for convergence of lives to failure, checked as in Figures 6.2.1.10 and 6.2.1.11, ranged from 260 to 280.

6.3.1. Effect of Change in Standard Deviation on MSD Assessment

In order to evaluate the effect of change in scatter (standard deviation) on the MSD assessment results presented in Figure 6.2.1.9, the scatter value for fatigue crack initiation (column E from Figure 6.2.1.7) is the only one variable that is changed from the model, everything else is kept the same for all damage scenarios.

Figure 6.3.1.1 presents the same results as in Figure 6.2.1.9 but the standard deviation value (log) input is set as 0.09 for crack initiation of all damage scenarios.

As observed in Figure 6.2.1.9, from Figure 6.3.1.1 it can be seen that lives to failure are dominated by crack initiation, with mean initiation life equal to 257,773 cycles and the mean propagation life equal to 51,974 cycles, i.e., the initiation phase represents 83.2 % of the mean failure process (TTCI + TCP = 257,773 + 51,974 cycles = 309,747 cycles). Total initiation life varies from 144,960 to 370,530 cycles, whereas propagation lives are between 22,469 to 74,794 cycles.

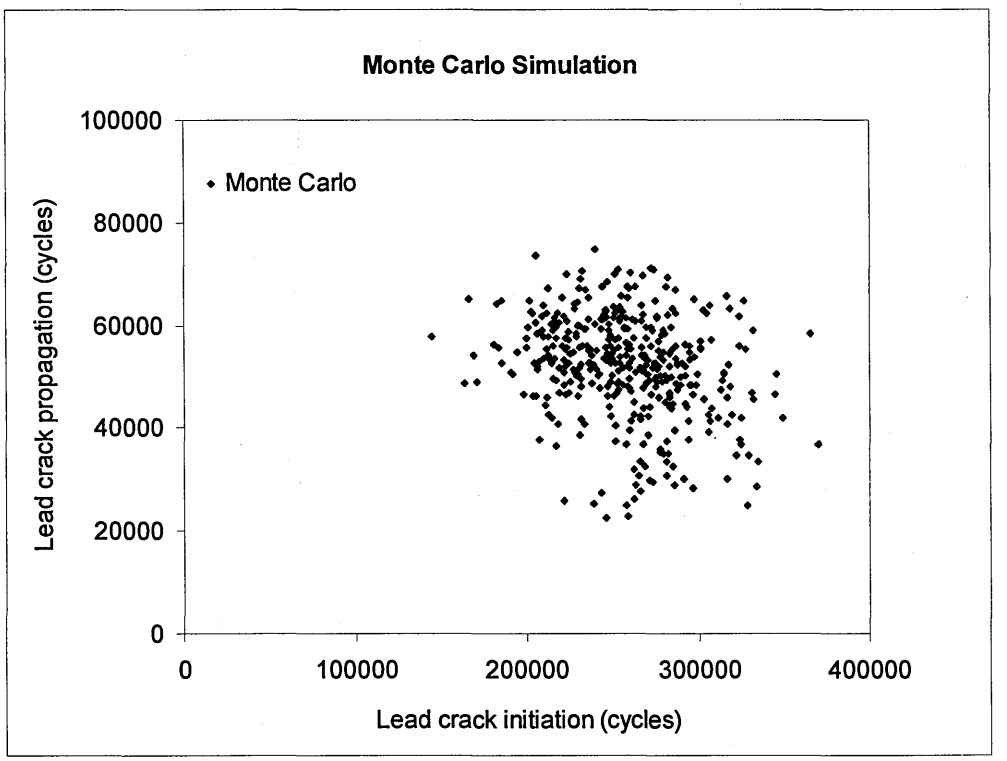

Figure 6.3.1.1: Monte Carlo simulations – standard deviation for TTCI (log) = 0.09, non-uniform pin-loading and 100 MPa (R = 0.1) cyclic tensile stress.

Comparing the results from Figure 6.3.1.1 to the ones from Figure 6.2.1.9, it can be seen that the mean initiation life has increased by 46.1 %, while the mean time for crack propagation life has decreased by 4.3 %; leading to the mean failure process to increase by 34.2 %.

As in Figure 6.2.1.12, Figure 6.3.1.2 shows the cumulative probability distribution of failure from the results presented in Figure 6.3.1.1 together with the theoretical cumulative normal distribution. The x-axis shows the number of cycles to failure and

the y-axis the corresponding cumulative probabilities from 0 to 1 (0 to 100%). From Figure 6.3.1.2, the 0.5 cumulative probability of failure corresponds to 309,747 cycles which represents the mean failure behaviour given by the Monte Carlo simulation results from Figure 6.3.1.1. With the mean number of cycles to failure established, the ISP and the SMP are calculated as, respectively, 103,249 cycles and 154,874 cycles; considering, respectively, factors 3 and 2 as recommended in reference [3].

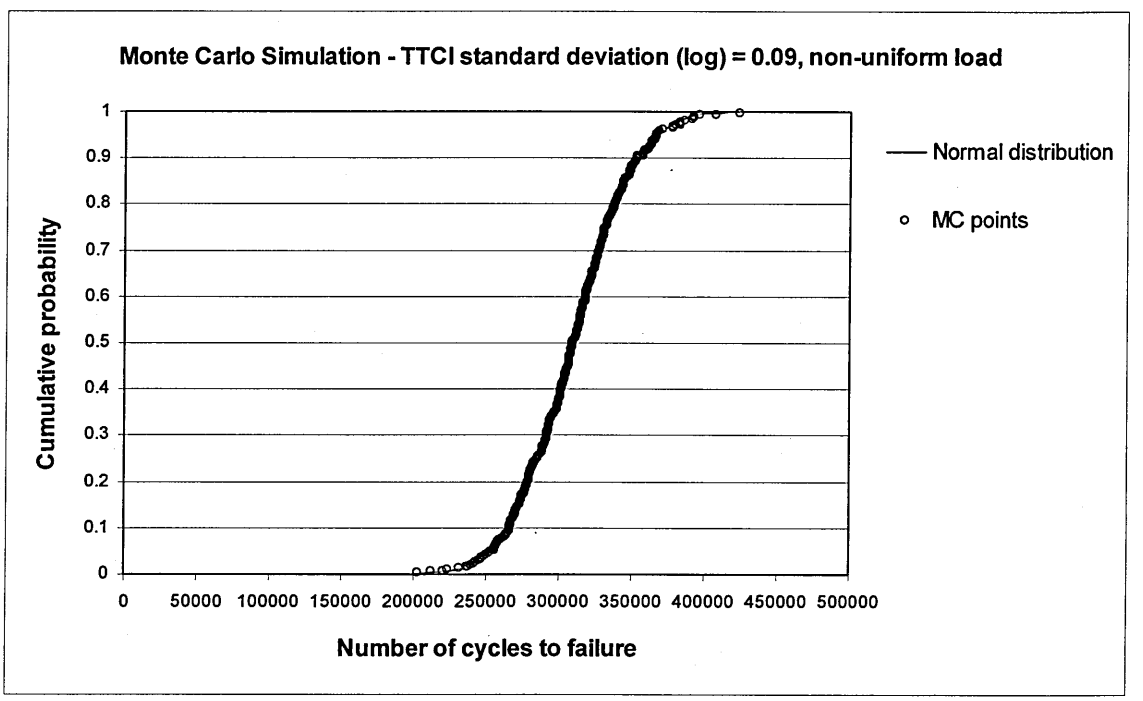

Figure 6.3.1.2: Cumulative probability distribution of failure from Figure 6.3.1.1.

Comparing the ISP and SMP values from Figure 6.3.1.1 to the ones from Figure 6.2.1.9, it can be seen that the ISP and the SMP have increased by 34.2 %, due to an increase in the mean failure process by 34.2 %.

Figure 6.3.1.3 shows the percentage of lead crack nucleation positioning for the simulations from Figure 6.3.1.1. From Figure 6.3.1.3 it can be seen that there is a clear tendency for cracks to nucleate at hole positions 2 and 8 (Figure 6.2.1.1); while the percentage of crack nucleation at hole positions 1, 3, 4, 5, 6, 7 and 9 (Figure 6.2.1.1) are quite similar; as in Figure 6.2.1.13.

Comparing the tendency for crack nucleation at positions 2 and 8 from Figure 6.3.1.3 to the one from Figure 6.2.1.13, it can be seen that lead crack nucleation at positions 2 and 8 (Figure 6.2.1.1) has been increased, while the lead crack nucleation at positions 1, 3, 4, 5, 6, 7 and 9 (Figure 6.2.1.1) has been diminished demonstrating that a decrease in scatter for fatigue crack initiation tends to concentrate crack nucleation sites at the high stressed locations (Figure 6.2.1.3).

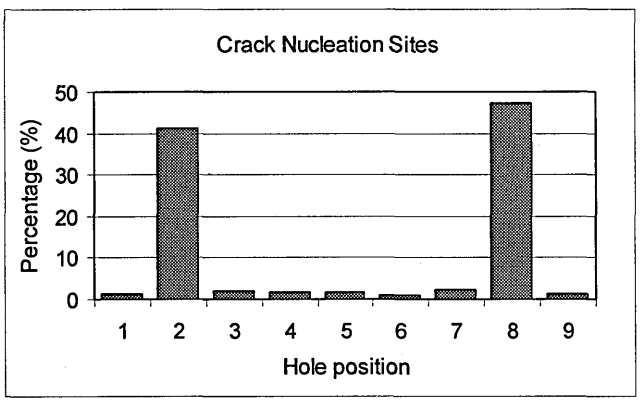

Figure 6.3.1.3: Percentage of lead crack nucleation sites for the external row of holes from Figure 6.3.1.1.

Figure 6.3.1.4 shows the percentage of scenarios which developed 1, 2, 3, 4, 5 and 6 cracks related to the 400 simulations from Figure 6.3.1.1. It can be seen that damage scenarios which developed only one crack represent a bit less than 30 % of the cases and the maximum number of cracks developed were 6, which represents less than 0.5 % of the simulations.

Comparing the results from Figure 6.3.1.4 to the ones from Figure 6.2.1.14, it can be seen that the number of scenarios that initiated a single crack as decreased from 40.4 % (Figure 6.2.1.14) to 29.5 % (Figure 6.3.1.4) for the simulations. The decrease in the number of mono-crack scenarios from Figure 6.3.1.4 reflects an increase in the percentage of scenarios that developed more than one crack, without exception, when compared to figure 6.2.1.14. From Figure 6.3.1.4 it can also be noted that scenarios containing 6 cracks have entered the model, increasing the number of MSD-like scenarios, while from Figure 6.2.1.14 the maximum number of cracks developed by one possible damage scenario was 5.

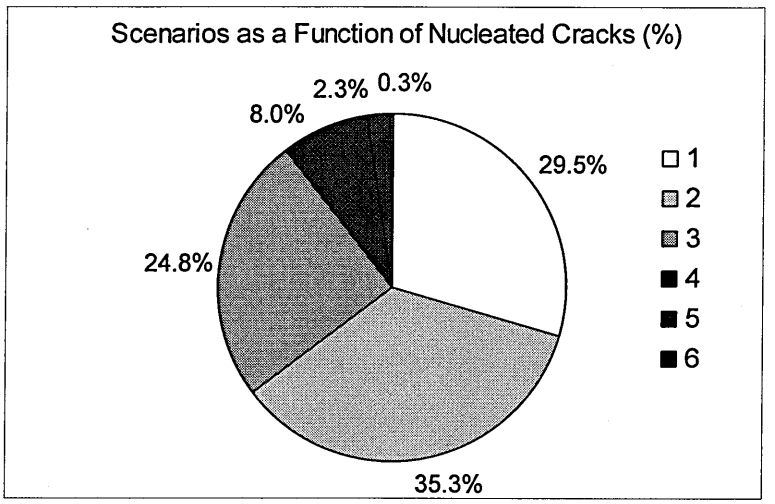

Figure 6.3.1.4: Percentage of scenarios as a function of number of nucleated cracks from Figure 6.3.1.1.

6.3.2. Effect of Change in Pin-Loading on MSD Assessment

To simulate MSD behaviour of a lap joint in a frame-bay, MSD assessment models consist of a row of 8 to 10 uniformly pin-loaded holes. The reason for the small number of holes, and the pin-loading distribution, is well summarized by Horst [30] where he notes that in stiffened lap joints a nearly quadratic stress distribution is found within one frame-bay and the maximum of this distribution is located in the centre of the bay (Figure 6.3.2.1). Therefore, MSD models usually present 8 to 10 holes uniformly loaded in such a manner that the fatigue life can be very similar compared to the one, for example, in the centre of the bay from Figure 6.3.2.1.

As it can be seen from Figures 6.2.1.4 and 6.2.1.5, the mean time for fatigue crack initiation and the corresponding standard deviation values are a function of the local elastic stress values adopted for each FCL (Figure 6.2.1.3), i.e., as far as there is a non-uniform pin-loading distribution, different initial fatigue life properties are assigned to each FCL. From the MSD assessment models presented in chapter 2, this approach was employed by Santgerma [31]; while other MSD models employ equal pin-loading (uniform pin-loading) in a row of pin-loaded holes.

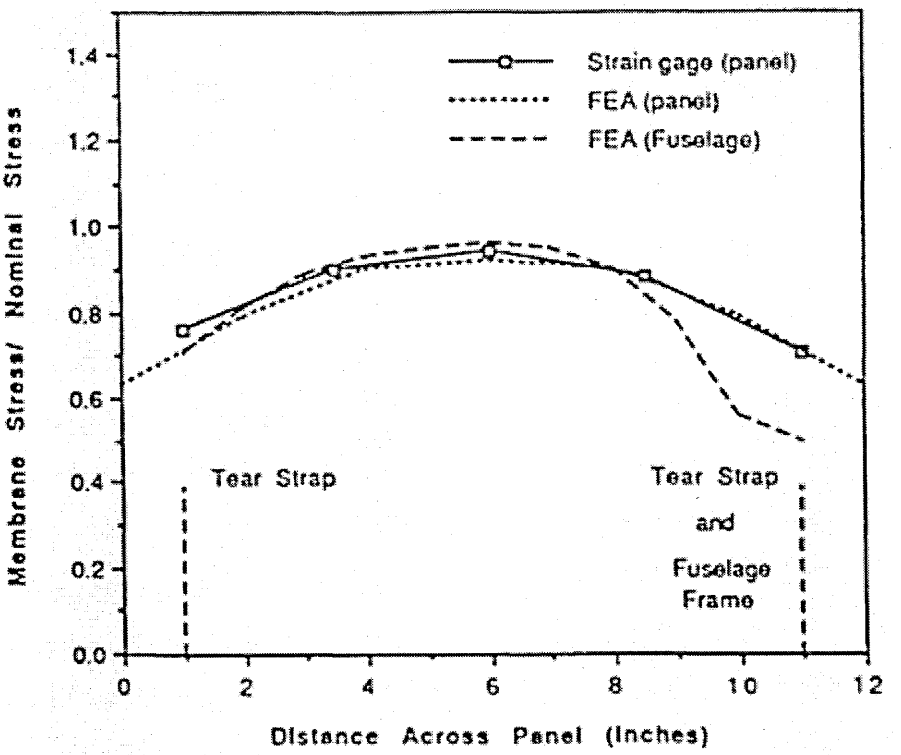

Figure 6.3.2.1: Stress distribution in 12-inch panel [2].

In this section, MSD assessment for the lap joint from Figure 6.2.1.1 is performed using a row of uniformly pin-loaded holes (as in Figure 6.3.2.2, where the FCL loading is a mean value from Figure 6.2.1.3) to establish the difference between the non-uniform pin-loading distribution employed in section 6.2.1 and the uniform pin-loading distribution on MSD assessment.

In order to compare the differences that a uniform pin-loading distribution produces in the whole MSD assessment, the results from Figure 6.2.1.9 are repeated here but with the pin-loading from Figure 6.3.2.2, instead of the one from Figure 6.2.1.3, for fatigue crack initiation of all damage scenarios. According to equations 6.2.1.1 and 6.2.1.2, the new values for μ and σ are, respectively, equal to 5.6071 and 0.2059; and the results of the simulations are presented in Figure 6.3.2.3.

As observed in Figure 6.2.1.9, from Figure 6.3.2.3 it can be seen that lives to failure are dominated by crack initiation, with mean initiation life equal to 178,662 cycles and the mean propagation life equal to 54,208 cycles, i.e., the initiation phase represents 76.7 %

of the mean failure process (TTCI + TCP = 178,662 + 54,208 cycles = 232,870 cycles). Total initiation life varies from 69,691 to 320,566 cycles, whereas propagation lives are between 21,568 to 86,247 cycles.

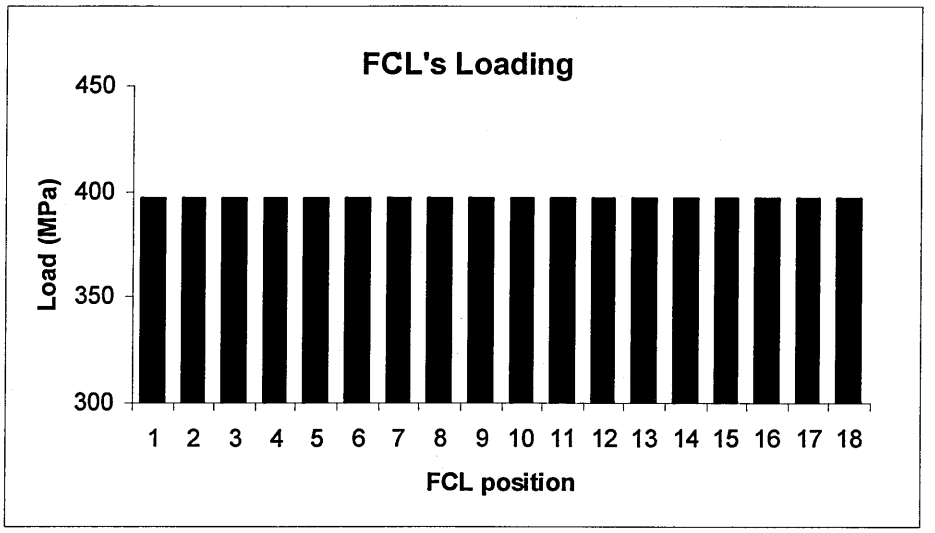

Figure 6.3.2.2: Mean local stresses at 3 and 9 o'clock positions for an external row from Figure 6.2.1.3 – uniform pin-loading distribution.

Comparing the results from Figure 6.3.2.3 to the ones from Figure 6.2.1.9, it can be seen that the mean initiation life has increased by 1.3 %, while the mean time for crack propagation life has decreased by 0.1 %; leading to the mean failure process to increase by 0.9 %.

As in Figure 6.2.1.12, Figure 6.3.2.4 shows the cumulative probability distribution of failure from the results presented in Figure 6.3.2.3 together with the theoretical cumulative normal distribution. The x-axis shows the number of cycles to failure and the y-axis the corresponding cumulative probabilities from 0 to 1 (0 to 100%). From Figure 6.3.2.4, the 0.5 cumulative probability of failure corresponds to 232,870 cycles which represents the mean failure behaviour given by the Monte Carlo simulation results from Figure 6.3.2.3. With the mean number of cycles to failure established, the ISP and the SMP are calculated as, respectively, 77,623 cycles and 116,435 cycles; considering, respectively, factors 3 and 2 as recommended in reference [3].

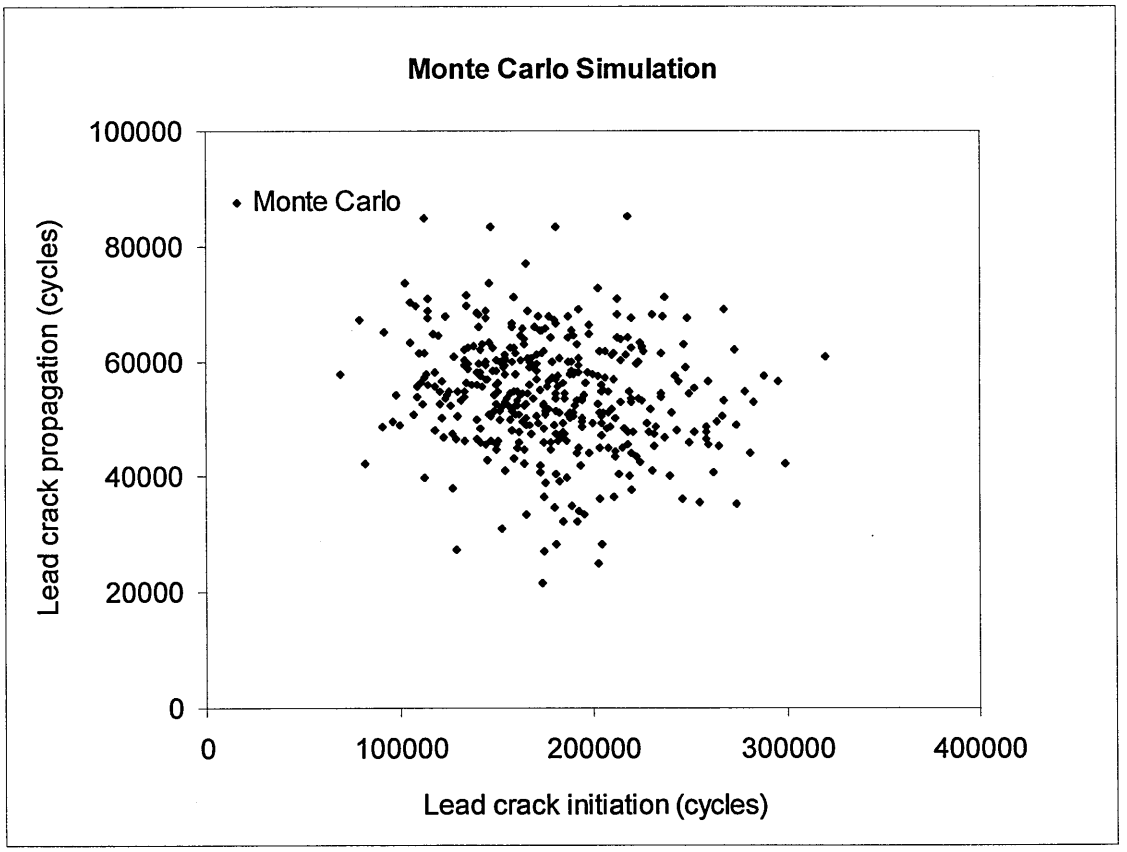

Figure 6.3.2.3: Monte Carlo simulations - standard deviation for TTCI (log) = 0.21, uniform pin-loading and 100 MPa (R = 0.1) cyclic tensile stress.

Comparing the ISP and SMP values from Figure 6.3.2.3 to the ones from Figure 6.2.1.9, it can be seen that the ISP and the SMP have increased by 0.9 %, due to an increase in the mean failure process by 0.9 %.

Figure 6.3.2.5 shows the percentage of lead crack nucleation positioning for the simulations from Figure 6.3.2.3. From Figure 6.3.2.5 it can be seen that there is no specific tendency for cracks to nucleate at any hole positions (Figure 6.2.1.1).

Comparing the crack nucleation pattern from Figure 6.3.2.5 to the one from Figure 6.2.1.13, it can be seen that the uniform pin-loading distribution (Figure 6.3.2.2) has given the lead crack a fairly smooth crack nucleation site distribution, which does not occur in the case of Figure 6.2.1.13.

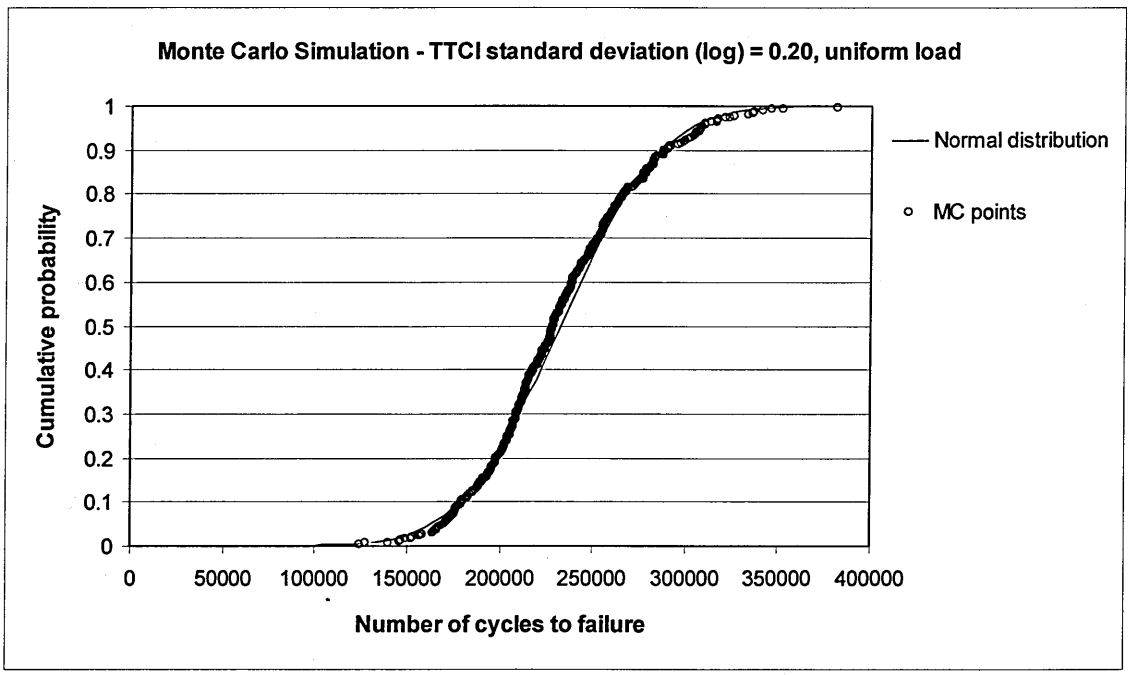

Figure 6.3.2.4: Cumulative probability distribution of failure from Figure 6.3.2.3.

Figure 6.3.2.6 shows the percentage of scenarios which developed 1, 2, 3, 4, 5 and 6 cracks related to the simulations from Figure 6.3.2.3. It can be seen that damage scenarios which developed only one crack represent 34 % of the cases and the maximum number of cracks developed were 6, which represents less than 0.5 % of the simulations.

Comparing the results from Figure 6.3.2.6 to the ones from Figure 6.2.1.14, it can be seen that the number of scenarios that initiated a single crack as decreased from 40.4 % (Figure 6.2.1.14) to 34 % (Figure 6.3.2.6). The decrease in the number of mono-crack scenarios from Figure 6.3.2.6 reflects an increase in the percentage of scenarios that developed more than one crack, without exception, when compared to figure 6.2.1.14; and scenarios that developed 6 cracks have entered the model.

Considering the case of Figure 6.3.1.1 (standard deviation for TTCI of 0.09 and non-uniform pin-loading), the same results are presented in Figure 6.3.2.7 but for uniform pin-loading from Figure 6.3.2.2 instead of the one from Figure 6.2.1.3.

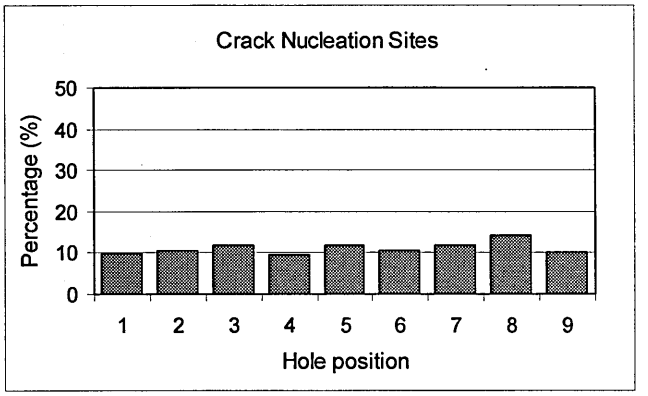

Figure 6.3.2.5: Percentage of lead crack nucleation sites for the external row of holes from Figure 6.3.2.3.

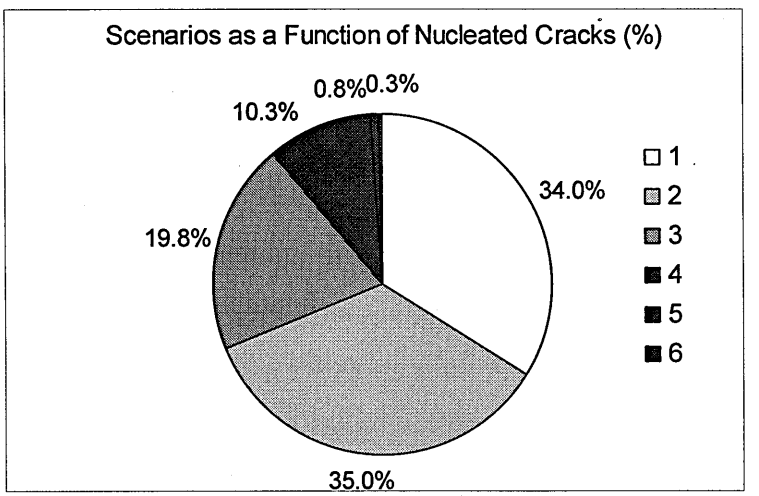

Figure 6.3.2.6: Percentage of scenarios as a function of number of nucleated cracks from Figure 6.3.2.3.

As observed in Figure 6.3.1.1, from Figure 6.3.2.7 it can be seen that lives to failure are dominated by crack initiation, with mean initiation life equal to 275,935 cycles and the mean propagation life equal to 52,182 cycles, i.e., the initiation phase represents 84.1 % of the mean failure process (TTCI + TCP = 275,935 + 52,182 cycles = 328,117 cycles). Total initiation life varies from 181,921 to 361,507 cycles, whereas propagation lives are between 22,011 to 84,759 cycles.

Comparing the results from Figure 6.3.2.7 to the ones from Figure 6.3.1.1, it can be seen that the mean initiation life has increased by 7.0 %, while the mean time for crack

propagation life has increased by 0.4 %; leading to the mean failure process to increase by 5.9 %.

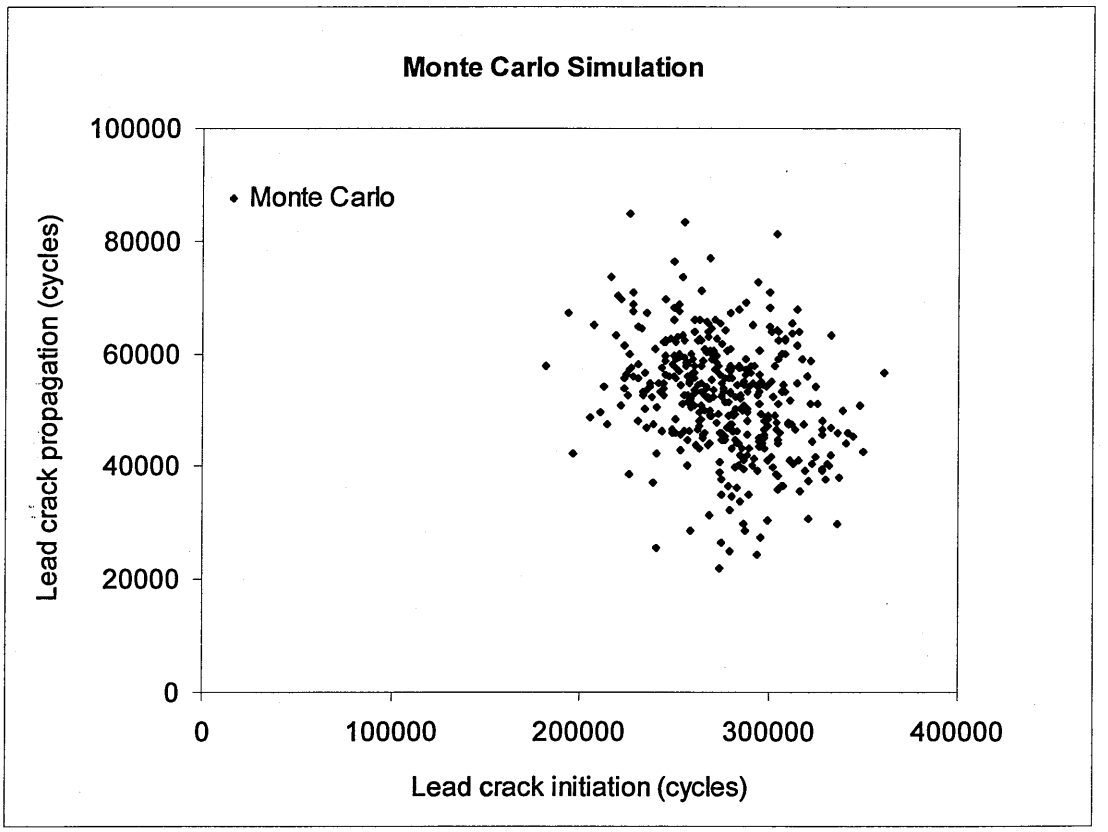

Figure 6.3.2.7: Monte Carlo simulations - standard deviation for TTCI (log) = 0.09, uniform pin-loading and 100 MPa (R = 0.1) cyclic tensile stress.

As in Figure 6.3.1.2, Figure 6.3.2.8 shows the cumulative probability distribution of failure from the simulations in Figure 6.3.2.7 together with the theoretical cumulative normal distribution. The x-axis shows the number of cycles to failure and the y-axis the corresponding cumulative probabilities from 0 to 1 (0 to 100%). From Figure 6.3.2.8, the 0.5 cumulative probability of failure corresponds to 328,117 cycles which represents the mean failure behaviour given by Figure 6.3.2.7. With the mean number of cycles to failure established, the ISP and the SMP are calculated as, respectively, 109,372 cycles and 164,059 cycles; considering, respectively, factors 3 and 2 as recommended in reference [3].

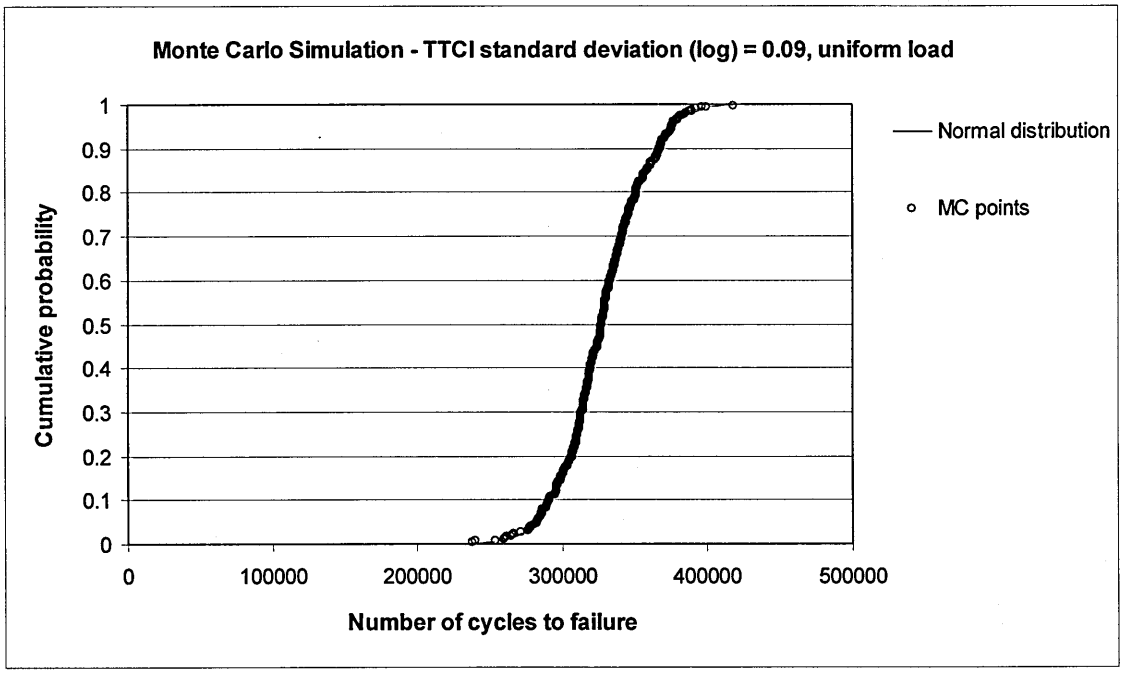

Figure 6.3.2.8: Cumulative probability distribution of failure from Figure 6.3.2.7.

Comparing the ISP and SMP values from Figure 6.3.2.7 to the ones from Figure 6.3.1.1, it can be seen that the ISP and the SMP have increased by 5.9 %, due to an increase in the mean failure process by 5.9 %.

Figure 6.3.2.9 shows the percentage of lead crack nucleation positioning for the simulations from Figure 6.3.2.7. From Figure 6.3.2.9 it can be seen that there is no specific tendency for cracks to nucleate at any hole positions (Figure 6.2.1.1).

Comparing the crack nucleation pattern from Figure 6.3.2.9 to the one from Figure 6.3.1.3, it can be seen that the uniform pin-loading distribution (Figure 6.3.2.2) has given the lead crack a fairly smooth crack nucleation site distribution, which does not occur in the case of Figure 6.3.1.3.

Figure 6.3.2.10 shows the percentage of scenarios which developed 1, 2, 3, 4, 5, 6 and 7 cracks related to the simulations from Figure 6.3.2.7. It can be seen that damage scenarios which developed only one crack represent 19.3 % of the cases and the maximum number of cracks developed were 7, which represents 0.5 % of the simulations.

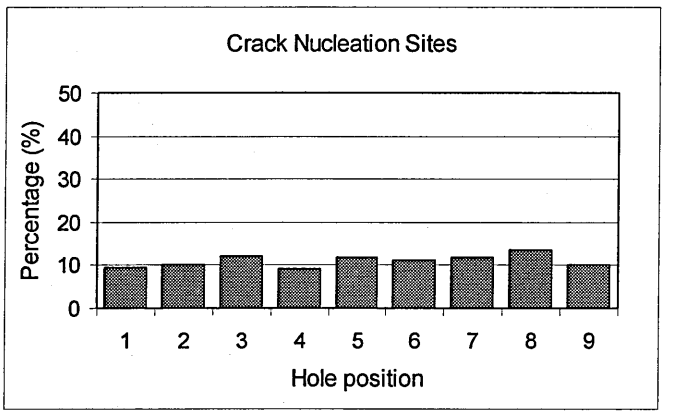

Figure 6.3.2.9: Percentage of lead crack nucleation sites for the external row of holes from Figure 6.3.2.7.

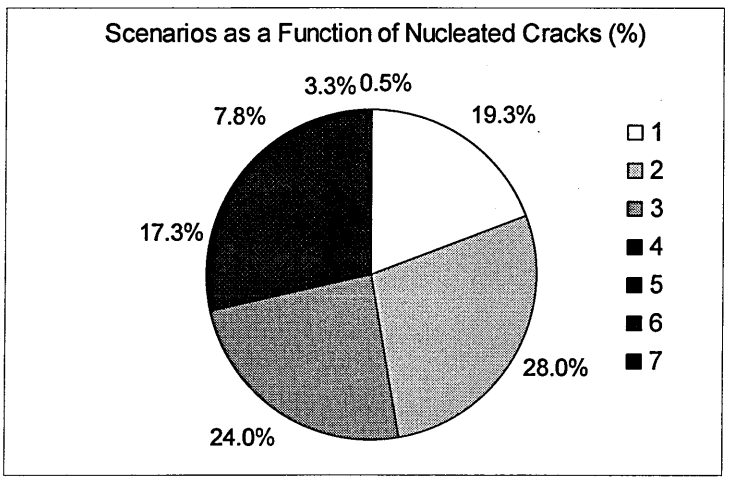

Figure 6.3.2.10: Percentage of scenarios as a function of number of nucleated cracks from Figure 6.3.2.7

Comparing the results from Figure 6.3.2.10 to the ones from Figure 6.3.1.4, it can be seen that the number of scenarios that initiated a single crack as decreased from 29.5 % (Figure 6.3.1.4) to 19.3 % (Figure 6.3.2.10) for the Monte Carlo simulations. The decrease in the number of mono-crack scenarios from Figure 6.3.2.10 reflects an increase in the percentage of scenarios that developed 4, 5 and 6 cracks, when compared to figure 6.3.1.4. It can also be noted that scenarios that developed 7 cracks have entered the model.

6.3.3. Effect of Change in Stress Level on MSD Assessment

In the present section, a change in the remote applied stress level from 100 to 120 MPa is performed to establish the differences on MSD assessment.

The lap joint configuration analysed is the same from Figure 6.2.1.1 and the pin-loading condition considered is the uniform one, as in Figure 6.3.2.2 for the case of 100 MPa, but with a mean value of 508.4 MPa for each FCL loading considering 120 MPa. The value of 508.4 MPa for the local stresses was calculated by the DTD code [87] via elastic analysis, as in sections 6.2.1 and 6.3.2, but for nominal stress level of 120 MPa applied to the lap joint configuration from Figure 6.2.1.1.

Figure 6.3.3.1 shows the experimental results from Figure 6.1.5 but normalized to achieve a fatigue life corresponding to an initial through-the-thickness crack size of 1.0 mm. The procedure adopted to normalize the data presented in Figure 6.3.3.1 was subtracting the number of cycles to grow an initial crack size of 1.0 mm up to failure from the number of cycles to failure from Figure 6.1.5. To perform this procedure; a DBE strap lap joint model was built, as idealized in section 3.2, but to represent the test specimen configuration from Figure 5.1.1 at both 100 and 120 MPa stress levels.

From equations 6.2.1.1 and 6.2.1.2, and considering a local stress level equal to 508.4 MPa for each FCL, the values of μ and σ are, respectively, equal to 4.9236 and 0.1697 to initiate a 1.0 mm fatigue crack. From Figure 6.3.3.1, for a crack initiation life of 4.9236, at 120 MPa stress level, the corresponding standard deviation value is close to 0.05; which is much smaller than 0.1697 obtained from equation 6.2.1.2. As presented in sections 6.3.1 and 6.3.2, a reduction in the standard deviation value [log(cycles)] produces a decrease in the number of mono-crack scenarios and, therefore, for the parametric study presented in this section a standard deviation value of 0.05 is adopted to force the development of more MSD-like damage scenarios.

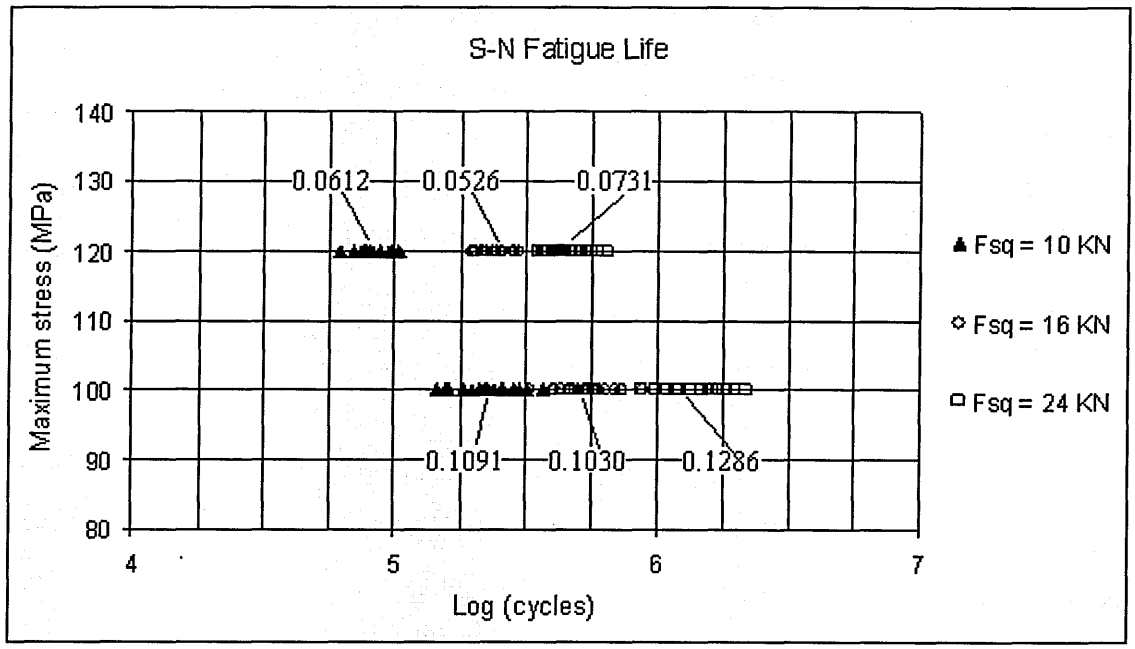

Figure 6.3.3.1: Fatigue life to achieve an initial crack size of 1.0 mm for each test specimen calculated from Figure 6.1.5.

Before presenting the results from the MSD assessment model for 120 MPa nominal stress level, a comparison between the results from Figure 6.3.2.3 (μ = 5.6071 and σ = 0.2059, for uniform pin-loading) and 6.3.3.2 (μ = 5.6071 and σ = 0.05, for uniform pin-loading), both at 100 MPa nominal stress level, is presented.

As observed in Figure 6.3.2.3, from Figure 6.3.3.2 it can be seen that lives to failure are dominated by crack initiation, with mean initiation life equal to 324,560 cycles and the mean propagation life equal to 47,830 cycles, i.e., the initiation phase represents 87 % of the mean failure process (TTCI + TCP = 324,560 + 47,830 cycles = 372,390 cycles). Total initiation life varies from 257,877 to 377,658 cycles, whereas propagation lives are between 20,564 to 84,746 cycles.

Comparing the results from Figure 6.3.3.2 to the ones from Figure 6.3.2.3, it can be seen that the mean initiation life has increased by 81.7 %, while the mean time for crack propagation life has decreased by 11.8 %; leading to the mean failure life to increase by 59.9 %.

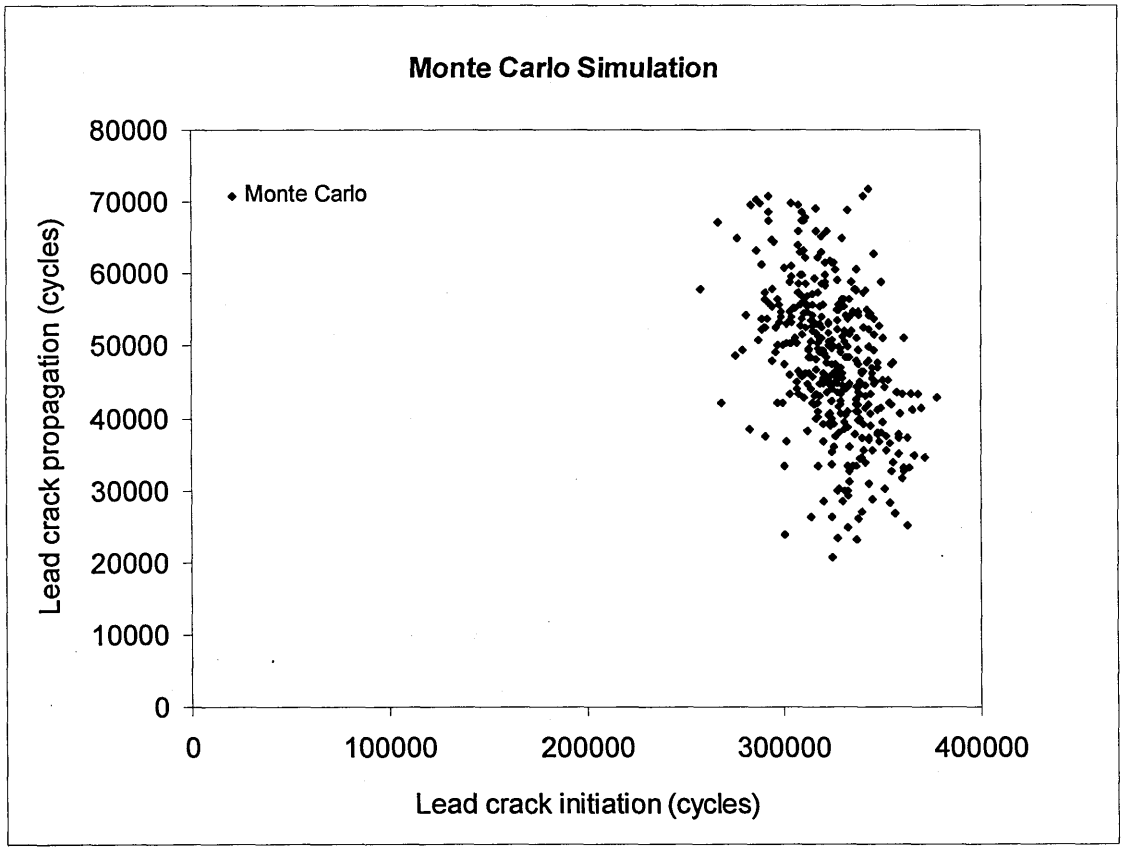

Figure 6.3.3.2: Monte Carlo simulations from Figure 6.3.2.3 - standard deviation for TTCI (log) = 0.05, uniform pin-loading and 100 MPa (R = 0.1) cyclic tensile stress.

As in Figure 6.3.2.4, Figure 6.3.3.3 shows the cumulative probability distribution of failure from the results presented in Figure 6.3.3.2 together with the theoretical cumulative normal distribution. The x-axis shows the number of cycles to failure and the y-axis the corresponding cumulative probabilities from 0 to 1 (0 to 100%). From Figure 6.3.3.3, the 0.5 cumulative probability of failure corresponds to 372,390 cycles which represents the mean failure life given by the simulations from Figure 6.3.3.2. With the mean number of cycles to failure established, the ISP and the SMP are calculated as, respectively, 124,130 and 186,195 cycles; considering, respectively, factors 3 and 2 as recommended in reference [3]. Comparing the ISP and SMP values from Figure 6.3.3.2 to the ones from Figure 6.3.2.3, it can be seen that the ISP and the SMP have increased by 59.9 %, due to an increase in the mean failure process by 59.9 %.

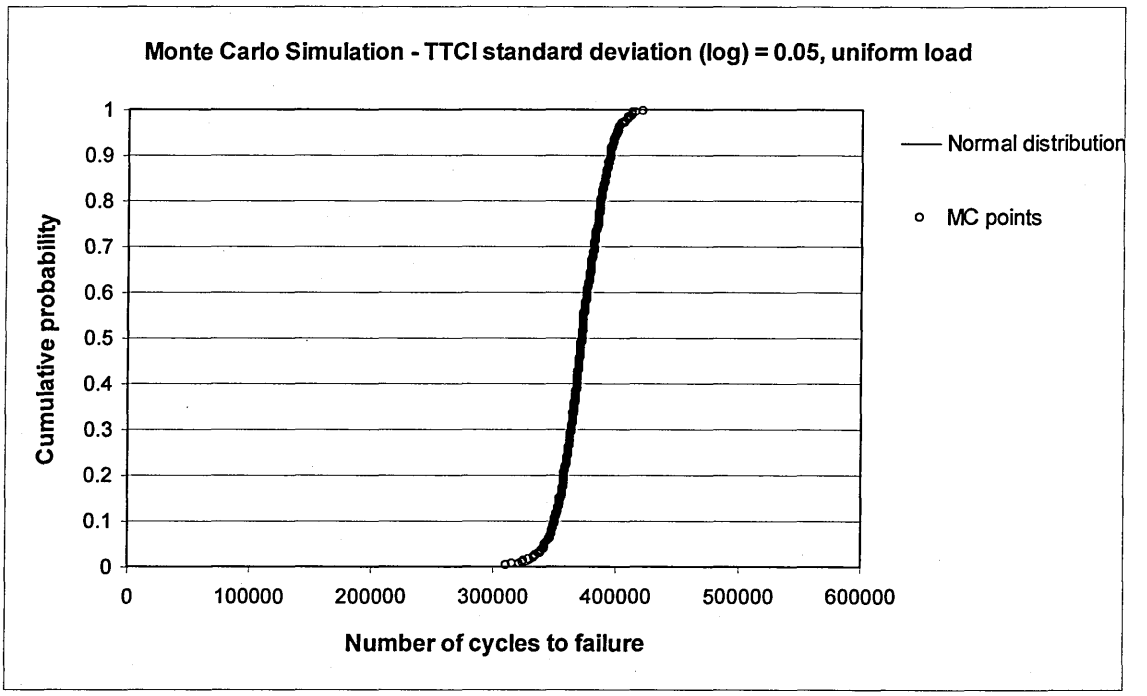

Figure 6.3.3.3: Cumulative probability distribution of failure from Figure 6.3.3.2.

Figure 6.3.3.4 shows the percentage of scenarios which developed 1, 2, 3, 4, 5, 6, 7 and 8 cracks related to the simulations from Figure 6.3.3.2. It can be seen that damage scenarios which developed only one crack represent 4.3 % of the cases, and the maximum number of cracks developed per damage scenario was 8. This case represents less than 1.3 % of the simulations.

Comparing the results from Figure 6.3.3.4 to the ones from Figure 6.3.2.6, it can be seen that the number of scenarios that initiated a single crack has decreased from 34 % (Figure 6.3.2.6) to 4.3 % (Figure 6.3.3.4). The decrease in the number of mono-crack scenarios from Figure 6.3.3.4 reflects an increase in the percentage of scenarios that developed 3, 4, 5 and 6 cracks, when compared to Figure 6.3.2.6. It can also be noted that scenarios that developed 7 and 8 cracks have entered the model.

As in Figure 6.3.3.2 (μ = 5.6071 and σ = 0.05, for uniform pin-loading), Figure 6.3.3.5 (μ = 4.9236 and σ = 0.05, for uniform pin-loading) presents the same results but for a remote applied stress level of 120 MPa. Therefore, the difference between the

results from both figures consist only in a change of the nominal stress applied (or the mean time to crack initiation) variable.

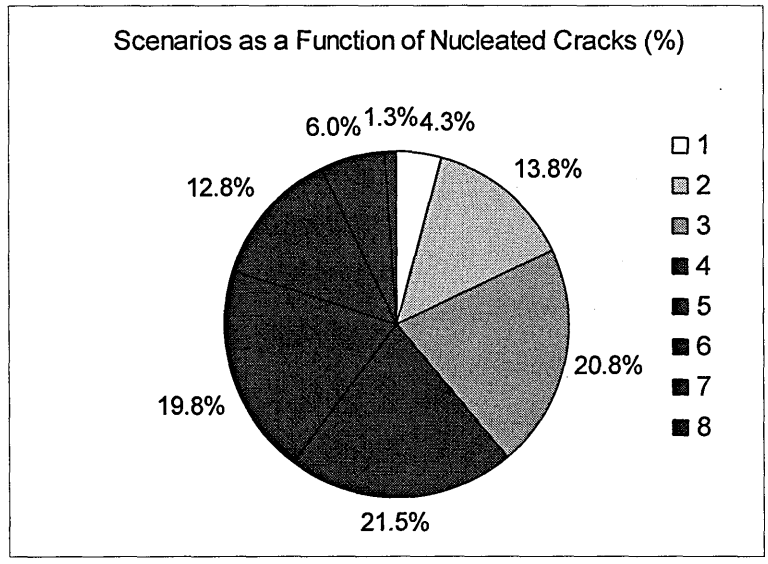

Figure 6.3.3.4: Percentage of scenarios as a function of nucleated cracks from Figure 6.3.3.2.

As observed in Figure 6.3.3.2, from Figure 6.3.3.5 it can be seen that lives to failure are dominated by crack initiation, with mean initiation life equal to 67,382 cycles and the mean propagation life equal to 19,493 cycles, i.e., the initiation phase represents 87 % of the mean failure process (TTCI + TCP = 67,382 + 19,493 cycles = 86,875 cycles). Total initiation life varies from 53,538 to 78,406 cycles, whereas propagation lives are between 11,016 to 32,546 cycles.

Comparing the results from Figure 6.3.3.5 to the ones from Figure 6.3.3.2, it can be seen that the mean initiation life has decreased by 79.2 %, while the mean time for crack propagation life has decreased by 59.2 %; leading to the mean failure process to decrease by 76.7 %.

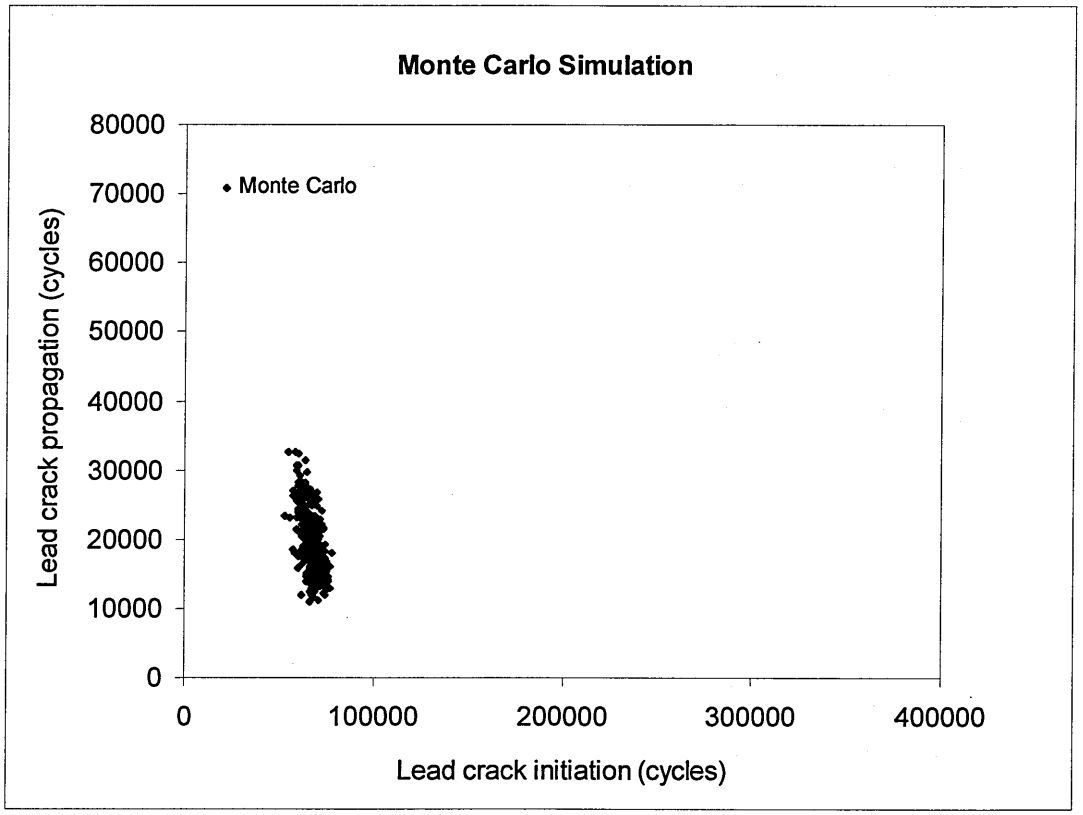

Figure 6.3.3.5: Monte Carlo simulations from Figure 6.3.3.2 - standard deviation for TTCI (log) = 0.05, uniform pin-loading and 120 MPa (R = 0.1) cyclic tensile stress.

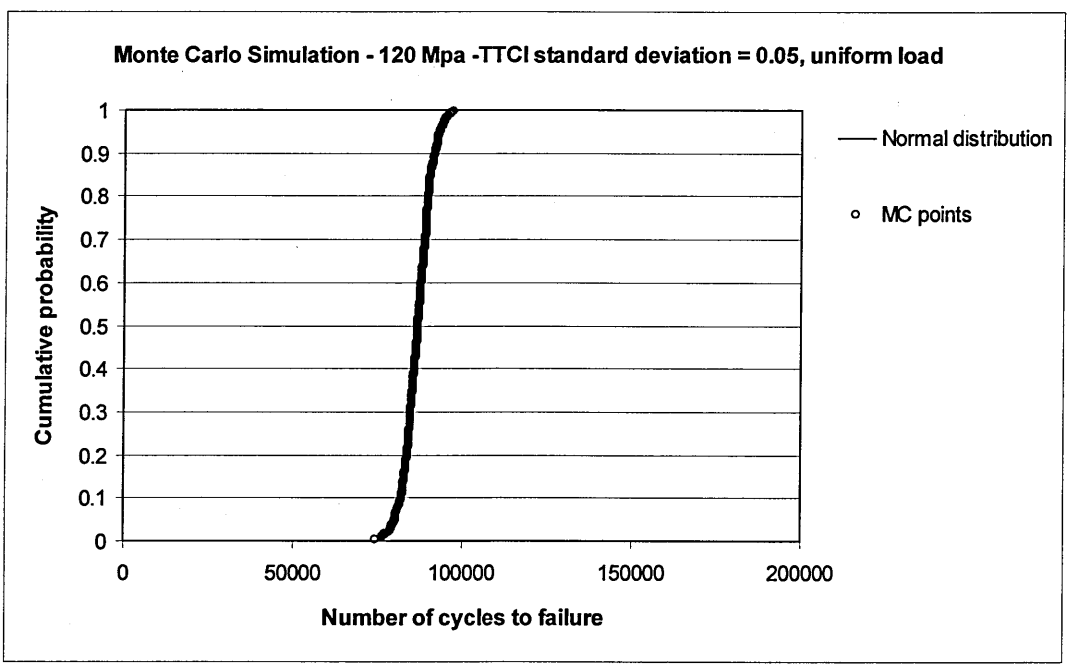

Figure 6.3.3.6: Cumulative probability distribution of failure from Figure 6.3.3.5.

As in Figure 6.3.3.3, Figure 6.3.3.6 shows the cumulative probability distribution of failure from the results presented in Figure 6.3.3.5 together with the theoretical cumulative normal distribution. The x-axis shows the number of cycles to failure and the y-axis the corresponding cumulative probabilities from 0 to 1 (0 to 100%). From Figure 6.3.3.6, the 0.5 cumulative probability of failure corresponds to 86,875 cycles which represents the mean failure behaviour given by the simulations from Figure 6.3.3.5. With the mean number of cycles to failure established, the ISP and the SMP are calculated as, respectively, 28,958 cycles and 43,438 cycles; considering, respectively, factors 3 and 2 as recommended in reference [3].

Comparing the ISP and SMP values from Figure 6.3.3.5 to the ones from Figure 6.3.3.2, it can be seen that the ISP and the SMP have decreased by 76.7 %, due to a decrease in the mean failure process by 76.7 %.

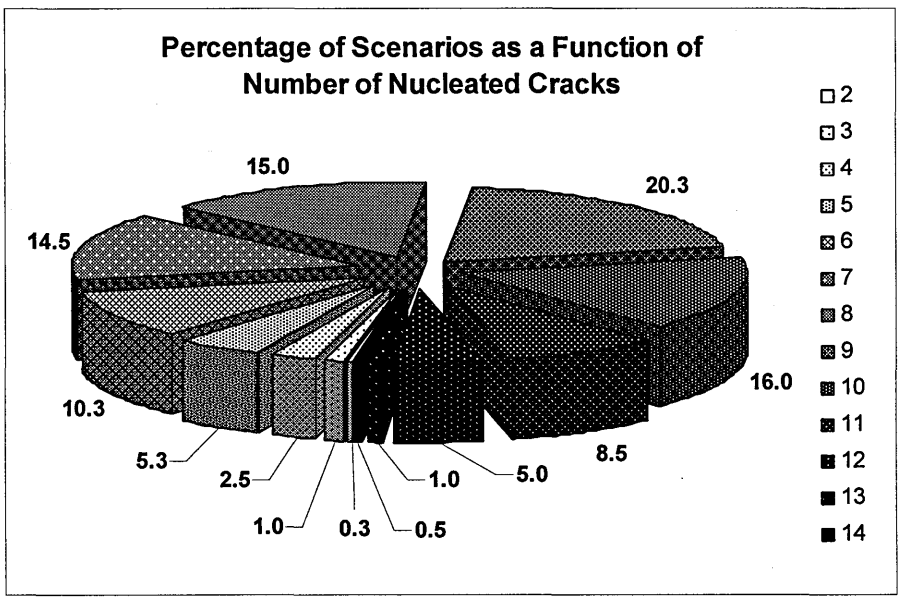

Figure 6.3.3.7: Percentage of scenarios as a function of nucleated cracks from Figure 6.3.3.5.

Figure 6.3.3.7 shows the percentage of scenarios which developed from 2 to 14 cracks related to the simulations from Figure 6.3.3.5. It can be seen that damage scenarios which developed only one crack do not exist anymore and scenarios with the smallest

number of cracks represent 0.3 % of the cases with 2 cracks. The maximum number of cracks developed was 14, which represents 0.5 % of the simulations.

Comparing the results from Figure 6.3.3.7 to the ones from Figure 6.3.3.4, it can be seen that the number of scenarios that initiated a single crack as decreased from 4.3 % (Figure 6.3.3.4) to 0 % (Figure 6.3.3.7). The absence of mono-crack scenarios from Figure 6.3.3.7 reflects an increase in the percentage of scenarios that developed 7 and 8 cracks, when compared to Figure 6.3.3.4. It can also be noted that scenarios that developed 9 to 14 cracks have entered the model, where scenarios with 9 cracks represent 20.3 % of the simulations.

6.3.4. Effect of High Rivet Squeeze Force on MSD Assessment

In order to study the effect of high rivet squeeze force on MSD assessment, the case of 24 KN squeeze force at 100 MPa stress level from Figure 6.3.3.1 is used as input data for the MSD assessment model from this work.

For the 100 MPa stress level from Figure 6.3.3.1, it can be seen that the 24 KN squeeze force produces the highest mean time for crack initiation (6.1976) and standard deviation (0.1286) values compared to the 10 and 16 KN squeeze forces.

Considering the values of μ = 6.1976 and σ = 0.1286 as input variables for the uniform pin-loaded MSD assessment model from section 6.3.2, the Monte Carlo simulations are presented in Figure 6.3.4.1.

From Figure 6.3.4.1 it can be seen that lives to failure are dominated by crack initiation, with mean initiation life equal to 919,481 cycles and the mean propagation life equal to 57,750 cycles, i.e., the initiation phase represents 94.1 % of the mean failure process (TTCI + TCP = 919,481 + 57,750 cycles = 977,231 cycles). Total initiation life varies from 505,211 to 1,347,769 cycles, whereas propagation lives are between 35,986 to 85,247 cycles.

Figure 6.3.4.2 shows the cumulative probability distribution of failure from the results presented in Figure 6.3.4.1 together with the theoretical cumulative normal distribution. The x-axis shows the number of cycles to failure and the y-axis the corresponding cumulative probabilities from 0 to 1 (0 to 100%). From Figure 6.3.4.2, the 0.5 cumulative probability of failure corresponds to 977,231 cycles, which represents the mean failure life given by Figure 6.3.4.1. With the mean number of cycles to failure established, the ISP and the SMP are calculated as, respectively, 325,744 cycles and 488,616 cycles; considering, respectively, factors 3 and 2 as recommended in reference [3].

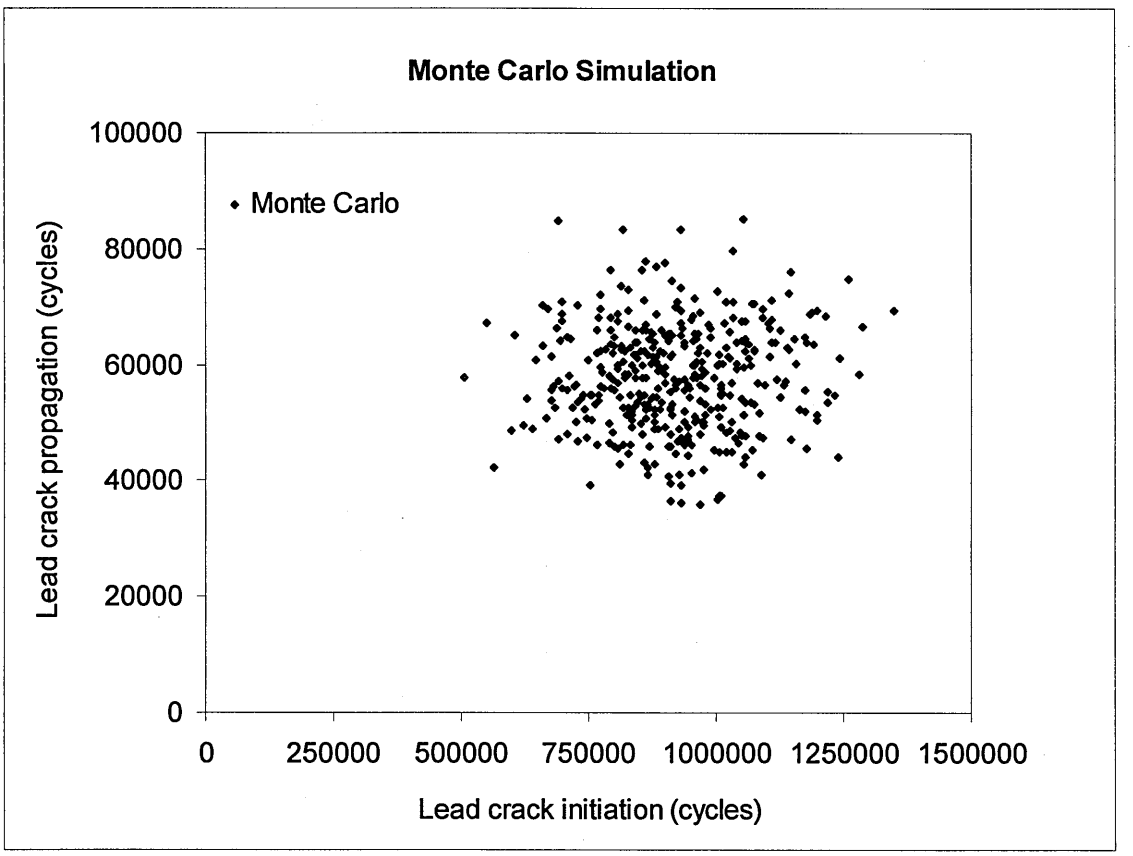

Figure 6.3.4.1: Monte Carlo simulations for 24 KN squeeze force - standard deviation for TTCI (log) = 0.13, uniform pin-loading and 100 MPa (R = 0.1) cyclic tensile stress.

Figure 6.3.4.3 shows the percentage of scenarios which developed 1, 2, 3 and 4 cracks related to the simulations from Figure 6.3.4.1. It can be seen that damage scenarios which developed only one crack represent 72 % of the cases and the maximum number

of cracks developed were 4, which represents 0.5 % of the simulations; showing that the majority of the damage scenarios generated were mono-crack ones.

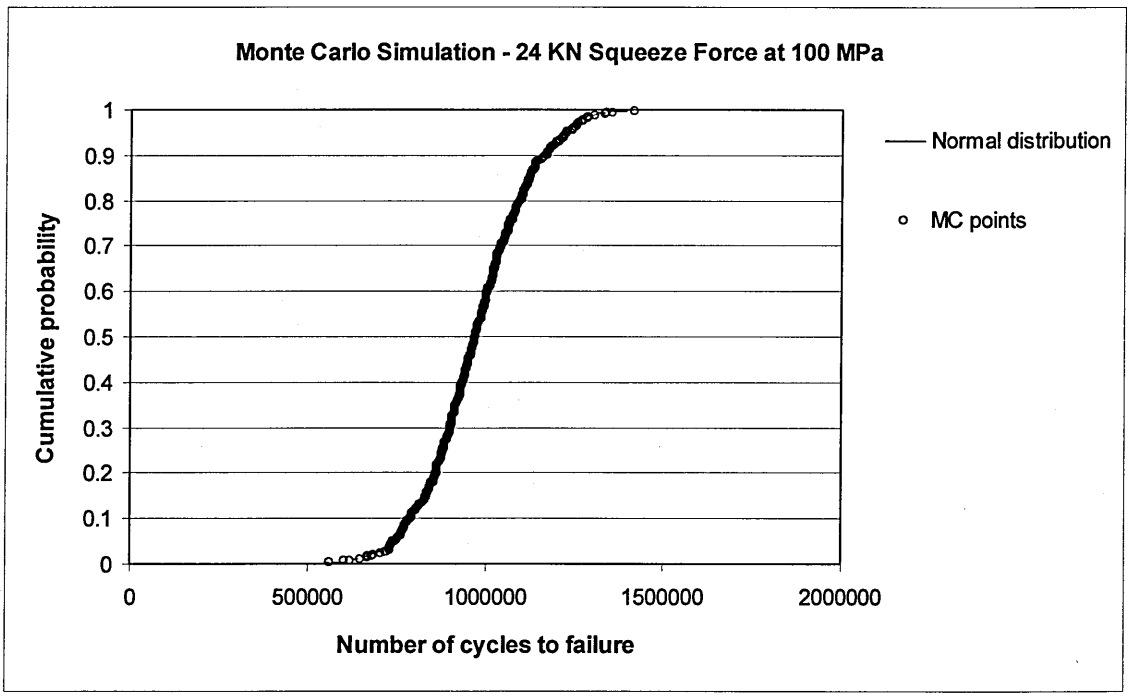

Figure 6.3.4.2: Cumulative probability distribution of failure from Figure 6.3.4.1.

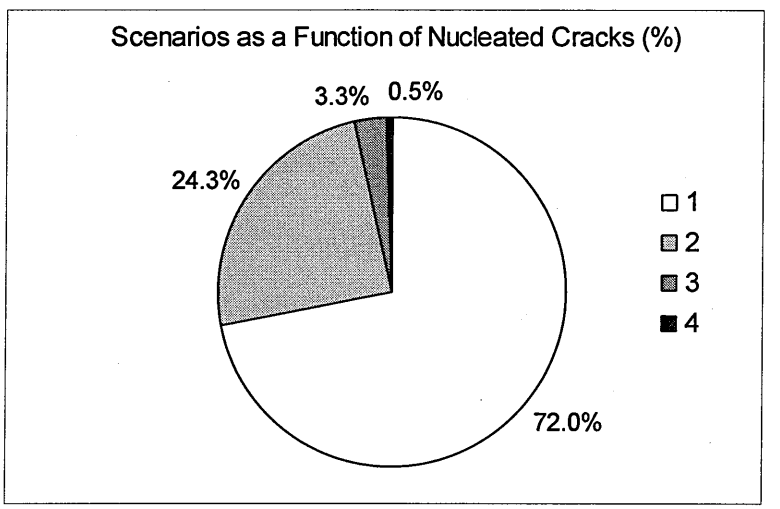

Figure 6.3.4.3: Percentage of scenarios as a function of nucleated cracks from Figure 6.3.4.1.

6.4. Summary of the Results from Sections 6.2 and 6.3

In this section, a summary of the results from sections 6.2 (methodology application) and 6.3 (parametric study) is presented from Tables 6.4.1 to 6.4.6.

Table 6.4.1 presents the list of figures and corresponding variables which have been analysed for MSD assessment. These variables are the standard deviation for fatigue crack initiation, hole pin-loading, nominal stress level and high rivet squeeze force. Tables 6.4.2 to 6.4.6 present the results themselves.

In Table 6.4.1 the 'standard deviation' value for the case of Figure 6.2.1.9 (which varies from 0.1995 to 0.2111) is presented as 0.21; for the case of Figure 6.3.2.3 (which is 0.2059) is presented as 0.21; and for the case of Figure 6.3.4.1 (which is 0.1286) is presented as 0.13. The same simplifying notation is valid for Tables 6.4.2 to 6.4.6.

For Tables 6.4.1 to 6.4.6 the meaning of 'NU' is for 'non-uniform pin-loading'; 'U' is for 'uniform pin-loading'; '$\overline{TTCI}$' is for 'mean time to crack initiation of the lead crack'; '$\overline{TCP}$' is for 'mean time for crack propagation of the lead crack'; '$\overline{N_f}$' is for '$\overline{TTCI}+\overline{TCP}$', and 'MSD-like scenarios' is for 'damage scenarios that nucleated more than one crack'.

Table 6.4.1: Index of figures and corresponding variables analysed.

Figure #	Standard deviation log (cycles)				Pin-load		Stress (MPa)		High squeeze force
	0.21	0.13	0.09	0.05	NU	U	100	120	
6.2.1.9	✓				✓		✓		
6.3.1.1			✓		✓		✓		
6.3.2.3	✓					✓	✓		
6.3.2.7			✓			✓	✓		
6.3.3.2				✓		✓	✓		
6.3.3.5				✓		✓		✓	
6.3.4.1		✓				✓	✓		✓

Table 6.4.2: Influence of standard deviation on MSD parameters (100 MPa)

Standard deviation log (cycles)	Pin-load type	$\overline{TTCI}$ (cycles)	$\overline{TCP}$ (cycles)	$\overline{N_f}$ (cycles)	ISP (cycles)	SMP (cycles)	MSD-like scenarios (%)
0.21	NU	176,455	54,286	230,741	76,914	115,371	59.6
0.09	NU	257,773	51,974	309,747	103,249	154,874	70.5

Table 6.4.3: Influence of standard deviation on MSD parameters (100 MPa)

Standard deviation log (cycles)	Pin-load type	$\overline{TTCI}$ (cycles)	$\overline{TCP}$ (cycles)	$\overline{N_f}$ (cycles)	ISP (cycles)	SMP (cycles)	MSD-like scenarios (%)
0.21	U	178,662	54,208	232,870	77,623	116,435	66.0
0.09	U	275,935	52,182	328,117	109,372	164,059	80.7
0.05	U	324,560	47,830	372,390	124,130	186,195	95.7

Table 6.4.4: Influence of pin-loading on MSD parameters (100 MPa)

Standard deviation log (cycles)	Pin-load type	$\overline{TTCI}$ (cycles)	$\overline{TCP}$ (cycles)	$\overline{N_f}$ (cycles)	ISP (cycles)	SMP (cycles)	MSD-like scenarios (%)
0.21	NU	176,455	54,286	230,741	76,914	115,371	59.6
0.21	U	178,662	54,208	232,870	77,623	116,435	66.0
0.09	NU	257,773	51,974	309,747	103,249	154,874	70.5
0.09	U	275,935	52,182	328,117	109,372	164,059	80.7

Table 6.4.5: Influence of stress level on MSD parameters (scatter TTCI (log) = 0.05)

Stress (MPa)	Pin-load type	$\overline{TTCI}$ (cycles)	$\overline{TCP}$ (cycles)	$\overline{N_f}$ (cycles)	ISP (cycles)	SMP (cycles)	MSD-like scenarios (%)
100	U	324,560	47,830	372,390	124,130	186,195	95.7
120	U	67,382	19,493	86,875	28,958	43,438	100.0

Table 6.4.6: Influence of high squeeze force on MSD parameters (100 MPa)

Standard deviation log (cycles)	Pin-load type	$\overline{TTCI}$ (cycles)	$\overline{TCP}$ (cycles)	$\overline{N_f}$ (cycles)	ISP (cycles)	SMP (cycles)	MSD-like scenarios (%)
0.13	U	919,481	57,750	977,231	325,744	488,616	28.0

6.5. MSD Assessment Comparison to Teardown Inspections from In-Service Data

In this section the MSD assessment model presented in chapter 4 is employed to compare its output to teardown data from in-service fuselage lap joints of aging aircraft.

The lap joint geometrical configuration analysed is presented in Figure 6.5.1 and it is from a Boeing 727 aircraft [15]. The fuselage skin is of aluminium 2024-T3, the outer and inner skins thicknesses are, respectively, 1.6 mm and 1.0 mm; and they are connected by 3 rows of NAS1097D6 aluminium rivets of diameter 4.76 mm, row spacing of 22.9 mm and pitch distance between rivets of 28.6 mm. The frame spacing is of 508 mm and 17 rivet holes are present within one frame bay, excluding the ones from the frames. The lap joint configuration is subjected to a nominal hoop stress of 103.4 MPa at fuselage skin mid-frame bay due to pressurization.

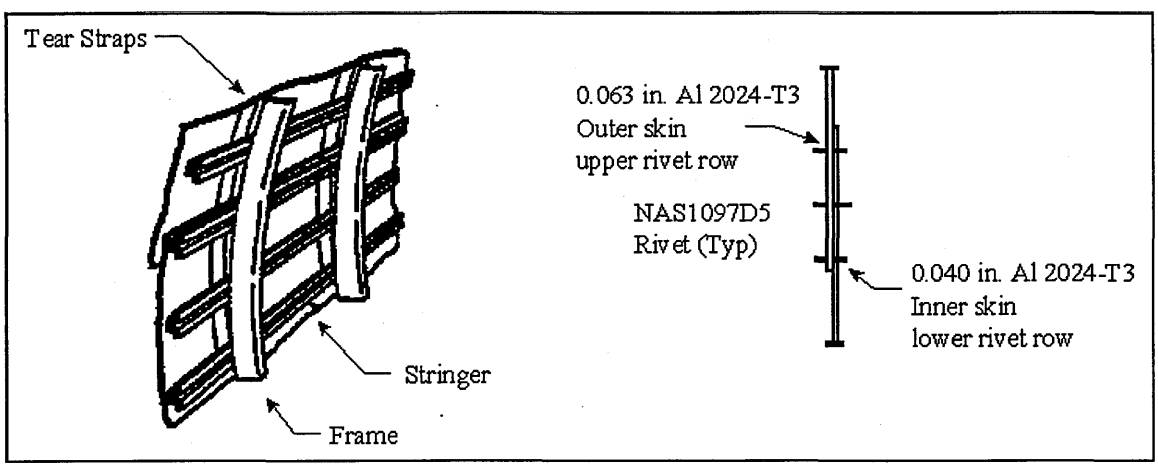

Figure 6.5.1: Fuselage lap joint configuration for Boeing 727 aircraft [15].

According to Steadman [15], MSD was detected at the inner fuselage skin at the rivet lower row (Figure 6.5.1) and cracks nucleated basically at holes from the centre of the bay. The DBE model idealized to analyse the inner skin of the lap joint configuration from Figure 6.5.1 is presented in Figure 6.5.2.

The DBE model from Figure 6.5.2 consists of one rectangular sheet of aluminium 2024-T3; 1000 mm long and 314.4 mm wide; discretized by 182 boundary elements and 364

nodes; with a central row of 11 pin-loaded holes; lateral constraint (D_x) in the x direction to simulate a wider joint, top and bottom constraint (D_x) in the x direction and lateral constraint (D_y) in the y direction where no displacements are expected due to symmetry; gross stress (T_y) applied in the top of the model and bypass stress (T_y) applied in the bottom of the model. The hole diameter, pitch distance between holes and sheet thickness are the same as illustrated in Figure 6.5.1 for the inner skin.

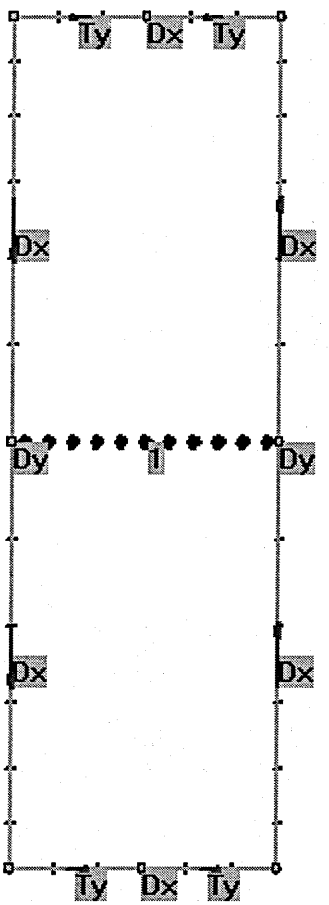

Figure 6.5.2: DBE model for the lap joint inner skin lower row from Figure 6.5.1.

The bypass stress (σ_{bp} = 66.7 MPa) and the bearing stress (σ_{br} = 220.2 MPa) for the DBE model from Figure 6.5.2 was obtained considering a gross stress σ_{gross} = 103.4 MPa applied to a strap lap joint subjected to load equilibrium, as in section 3.2 (Figure 3.2.2), but with width of 28.6 mm (one pitch distance) and all remaining dimensions as from Figure 6.5.1 inner skin. All the 11 holes from Figure 6.5.2 have the same pin-

loading (uniform pin-loading) and they represent the inner skin lower row of rivet holes present in the central part of the fuselage bay from Figure 6.5.1.

Figure 6.5.3 presents S-N fatigue data [100] for cycles to failure of a loose fit/open hole strap specimens of aluminium 2024-T3, which is adopted in this section for the fatigue crack initiation part of the MSD assessment model. The material and dimensions of the strap specimen used to generate the S-N data from Figure 6.5.3 are the same as for the inner skin from Figure 6.5.1, but the specimen width is of 31.8 mm.

As it can be seen, Figure 6.5.3 presents the S-N data as a function of the gross stress (σ_{gross}) and the stress ratio $\sigma_{br}/\sigma_{gross}$. For the calculated loading conditions used in this section σ_{gross} = 103.4 MPa (15 ksi) and $\sigma_{br}/\sigma_{gross}$ = 2.13, the fatigue life to failure of the strap specimen is equal to 42,000 cycles. The value of 42,000 cycles to failure has to be normalized to achieve a fatigue life corresponding to an initial crack size to serve as input variable for the crack initiation part of the MSD assessment model. In his work Steadman [15] presents a cumulative distribution function for fatigue crack initiation corresponding to an initial crack size of 1.27 mm (0.05 inches), which is adopted in this section.

To normalize the 42,000 cycles to failure to a fatigue life corresponding to an initial crack size of 1.27 mm; a DBE strap lap joint model was built, as idealized in section 3.2, but to represent the strap specimen configuration at the top right from Figure 6.5.3. The loading condition was a maximum tensile stress of 103.4 MPa and R = 0. The number of cycles to propagate an initial crack size of 1.27 mm up to failure from the DBE strap model was 6,300 cycles, which subtracted from 42,000 cycles to failure gives a mean time to crack initiation of 35,700 cycles or 4.5527 in log (cycles). With the mean time to crack initiation defined, the corresponding standard deviation value has to be established. As from Figure 6.5.3 no information about scatter is provided, it is assumed a standard deviation of 0.15 (log-scale) to be a typical value for fatigue testing of aluminium alloy 2024 components under constant amplitude loading [110].

Figure 6.5.4 presents cumulative probability distributions from the detailed results of teardown inspections on 24 fuselage bays calculated by Steadman [15]. The x-axis presents life in terms of percent of DSG (Design Service Goal), where 100 % DSG is equal to 60,000 flight cycles. The y-axis presents the cumulative probabilities from 0 to 1 (0 to 100 %). In the legends, 'Initiation' is the cumulative distribution for initiation of fatigue cracks with a crack length of 1.27 mm; 'Detectable' is the cumulative distribution to detect a crack length of 5.1 mm with 66 % probability; and 'Failure' is the cumulative distribution for the link-up of adjacent MSD cracks.

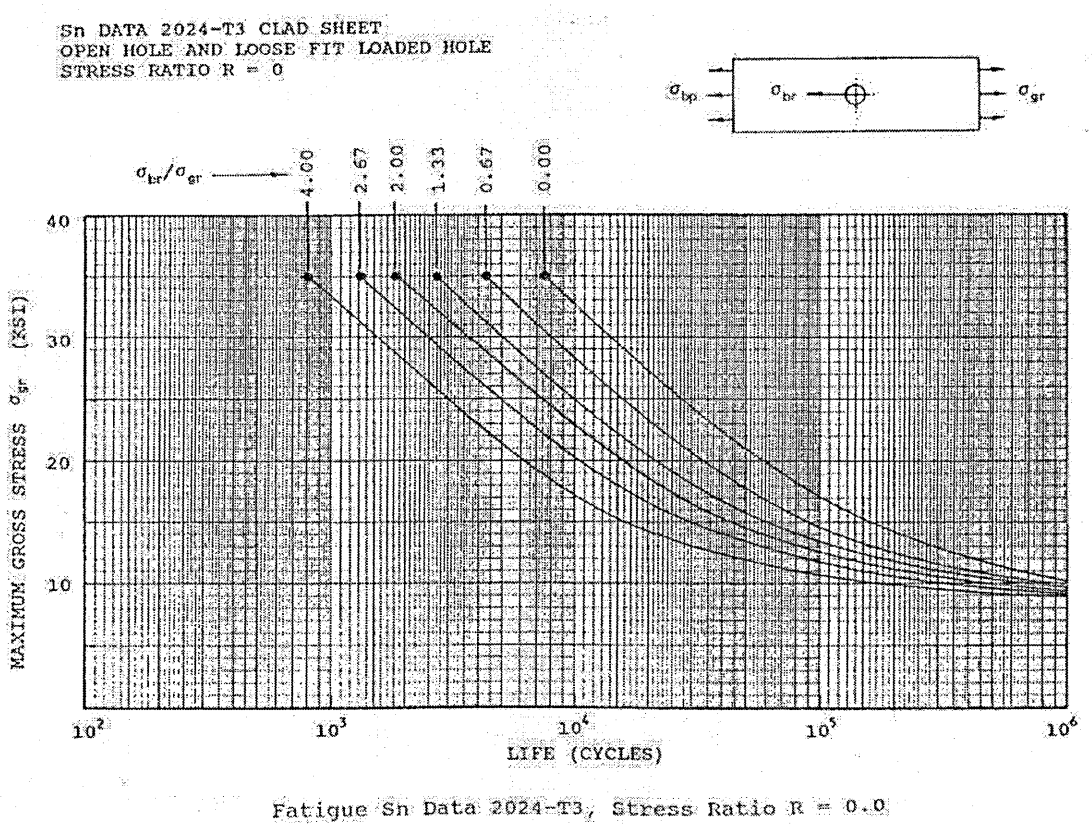

Figure 6.5.3: S-N fatigue data for inner skin lower rivet hole from Figure 6.5.1 [100].

In this section failure is defined as the first crack link-up, i.e., crack propagation is performed considering an initial crack size of 1.27 mm, as defined in previous paragraph, up to the link-up of a crack with another crack to compare with the results from Figure 6.5.4.

To check for crack propagation obtained with the DBE model from Figure 6.5.2; Figure 6.5.5 presents fleet crack growth data for Boeing 737 and 727 aircraft [111] together with 'This work' deterministic crack propagation data. From Figure 6.5.5, Jones [111] highlights one crack growth region between the horizontal lines that cross the 4 and 11 mm crack length axis. It can be seen that, within the region defined, the crack propagation time ranges from, approximately, 16,000 to 45,000 flight cycles for several B-737 and B-727 aircraft. The crack growth data plotted as 'This work' indicates a number of, approximately, 26,000 cycles to grow a single crack from 4 up to 11 mm; which demonstrates that the number of cycles obtained for 'This work' is within the range of the data measured from real aircraft fuselage panels.

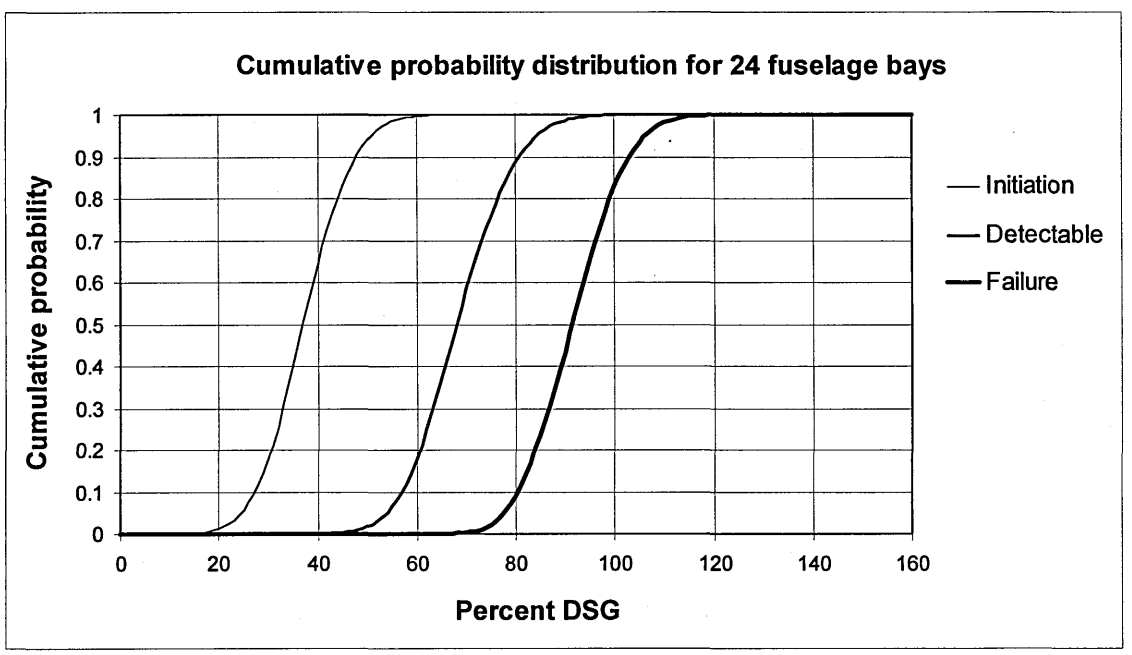

Figure 6.5.4: Cumulative probability distributions from teardown inspections [15].

The result of Monte Carlo simulations regarding 11 central holes for the idealized inner skin lower row of rivets from Figure 6.5.1 is presented in Figure 6.5.6. It can be seen that lives to failure are dominated by crack propagation, with mean initiation life equal to 18,655 cycles (31.1 % DSG) and the mean propagation life equal to 23,890 cycles (39.8 % DSG), i.e., the propagation phase represents 56.2 % of the mean failure process (TTCI + TCP = 18,655 + 23,890 cycles = 42,545 cycles = 70.9 % DSG). Total initiation

life varies from 9,536 to 28,780 cycles, whereas propagation lives are between 13,614 to 43,007 cycles.

Figure 6.5.7 shows the cumulative probability distribution comparison for crack initiation from the results presented in Figures 6.5.6 (Monte Carlo simulations) and 6.5.4 (teardown inspection data). The x-axis shows life as a function of percentage of DSG and the y-axis the corresponding cumulative probabilities from 0 to 1 (0 to 100%). In the legends, 'Initiation' refers to the teardown data (Figure 6.5.4) while 'Initiation MC' to the Monte Carlo simulations (Figure 6.5.6).

From Figure 6.5.7, the 0.5 cumulative probabilities for initiation of fatigue cracks from the teardown data and from Monte Carlo simulations are, respectively, 36.9 % DSG (22,140 cycles) and 31.1 % DSG (18,665 cycles); with the Monte Carlo simulation results being 15.7 % smaller than the teardown inspection results.

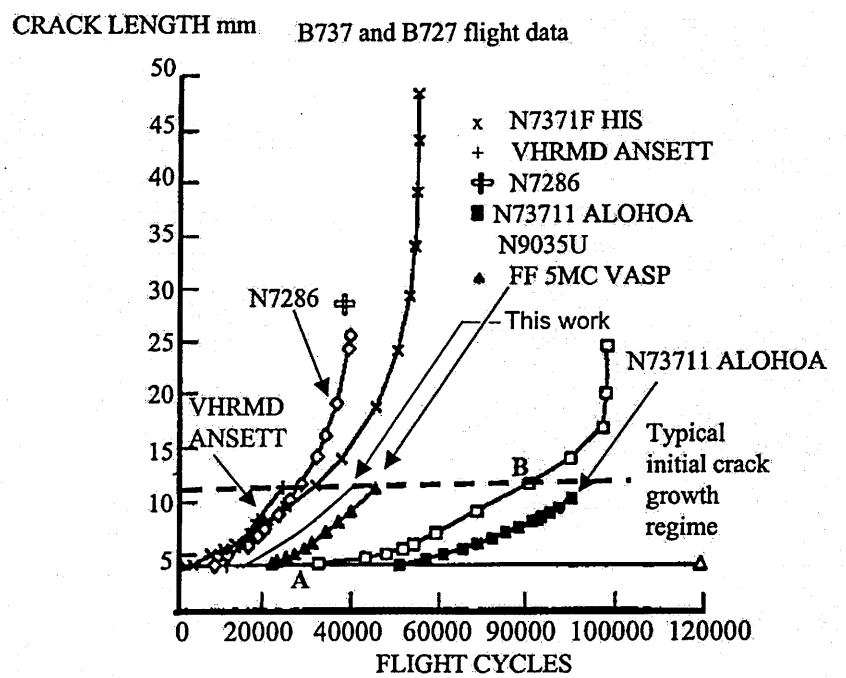

Figure 6.5.5: Fleet crack growth data for B-737 and B-727 aircraft [111] comparison to deterministic crack growth from this work.

Figure 6.5.8 shows the cumulative probability distribution comparison for crack detection. The results for Monte Carlo simulation from Figure 6.5.8 were obtained from

the results presented in Figure 6.5.7 (initiation of fatigue cracks) but adding the number of cycles to grow the corresponding lead cracks probabilistically from 1.27 mm to 5.1 mm (detectable crack length considered in Figure 6.5.4).

From Figure 6.5.8, the x-axis shows life as a function of percentage of DSG and the y-axis the corresponding cumulative probabilities from 0 to 1 (0 to 100%). In the legends, 'Detectable' refers to the teardown data (Figure 6.5.4) while 'Detectable MC' to the Monte Carlo simulation results.

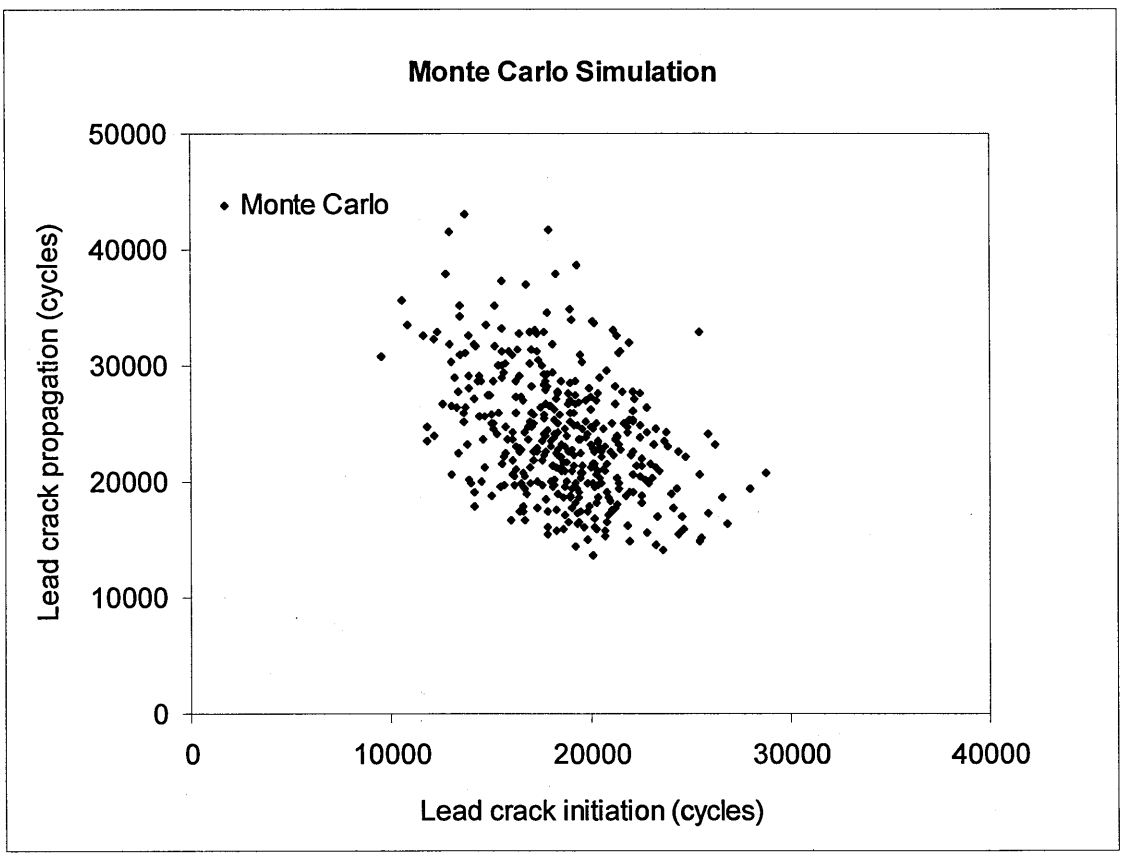

Figure 6.5.6: Monte Carlo simulation for teardown inspection comparison.

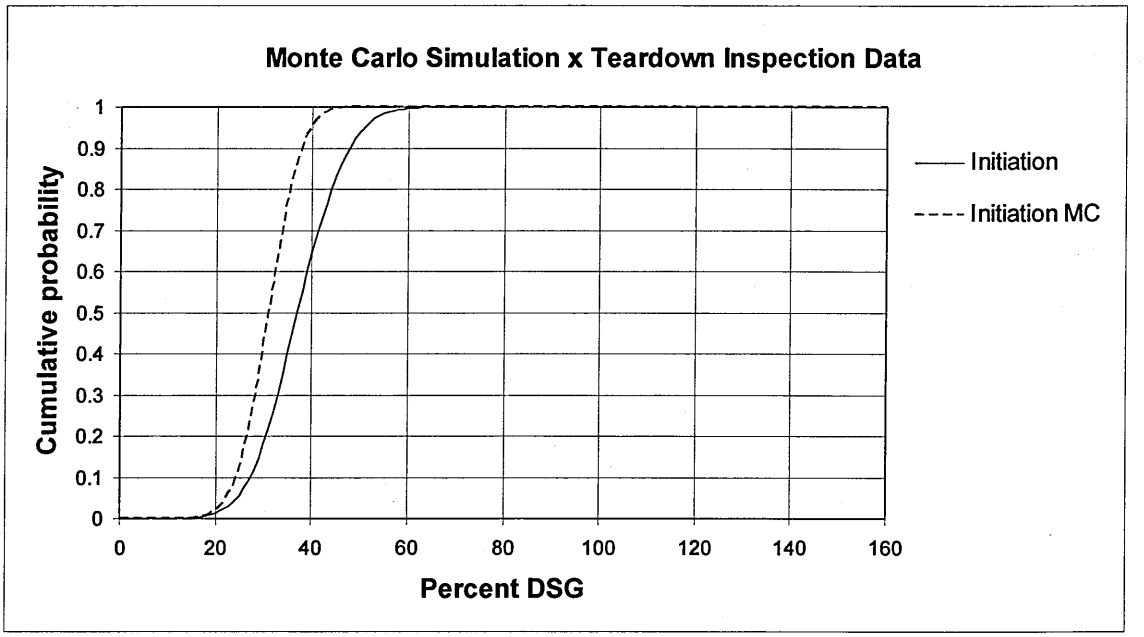

Figure 6.5.7: Cumulative probability distribution for initiation of fatigue cracks comparison to teardown inspection data.

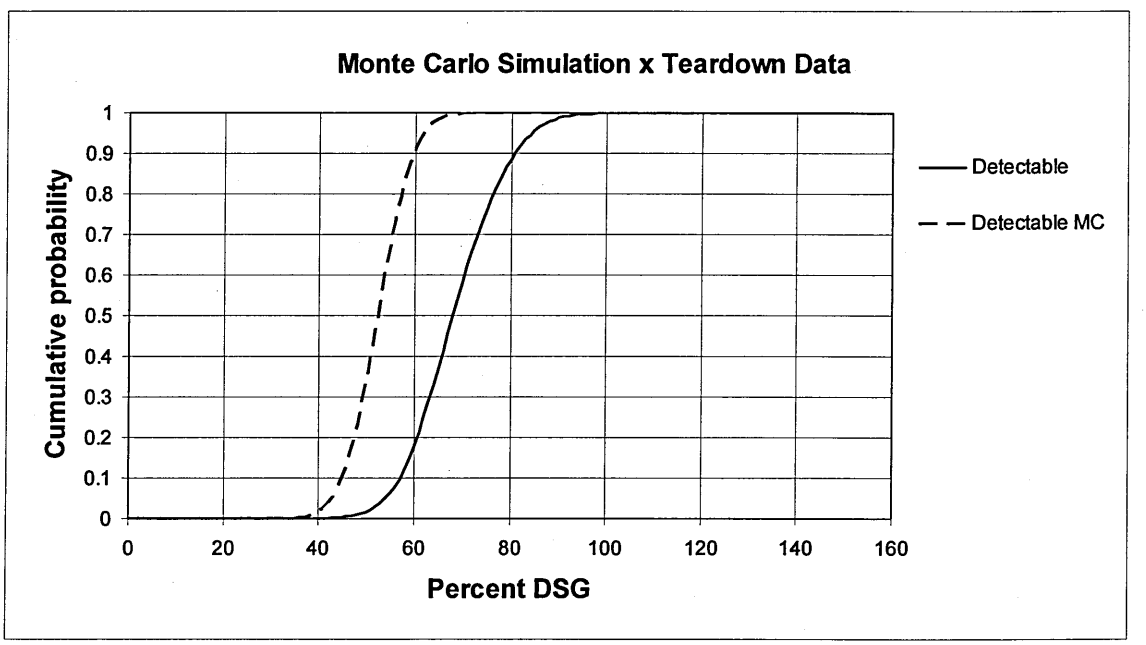

Figure 6.5.8: Cumulative probability distribution for detection of fatigue cracks comparison to teardown inspection data.

From Figure 6.5.8, the 0.5 cumulative probabilities for detection of fatigue cracks from the teardown data and from Monte Carlo simulations are, respectively, 68 % DSG

(40,800 cycles) and 52.3 % DSG (31,380 cycles); with the Monte Carlo simulation results being 23.1 % smaller than the teardown inspection results.

Figure 6.5.9 shows the cumulative probability distribution comparison for failure, defined as first crack link-up, from the results presented in Figure 6.5.6 (Monte Carlo simulation) and Figure 6.5.4 (teardown inspection data). The x-axis shows life as a function of percentage of DSG and the y-axis the corresponding cumulative probabilities from 0 to 1 (0 to 100%). In the legends, 'Failure' refers to the teardown data (Figure 6.5.4) while 'Failure MC' to the Monte Carlo simulations (Figure 6.5.6).

From Figure 6.5.9, the 0.5 cumulative probabilities for failure from the teardown data and from Monte Carlo simulations are, respectively, 91.5 % DSG (54,900 cycles) and 70.9 % DSG (42,540 cycles); with the Monte Carlo simulation results being 22.5 % smaller than the teardown inspection results. With the mean number of cycles to failure established by Monte Carlo simulation, the ISP and the SMP are calculated as, respectively, 14,180 cycles (23.6 % DSG) and 23,270 cycles (35.5 % DSG); considering, respectively, factors 3 and 2 as recommended in reference [3]. The ISP and the SMP values for the Monte Carlo simulations from Figure 6.5.6 are 22.5 % smaller than the same values from the teardown data presented in the same figure.

Figure 6.5.10 shows the percentage of scenarios which developed from 8 to 21 cracks related to the simulations from Figure 6.5.6. It can be seen that damage scenarios which developed only one crack do not exist, and scenarios with the smallest number of cracks represent 0.3 % of the cases with 8 cracks. The maximum number of cracks developed was 21, which represents 1.3 % of the simulations. Considering that the DBE model from Figure 6.5.2 has 11 holes (22 fatigue critical locations), for scenarios containing 21 cracks (Figure 6.5.10) all holes are cracked before failure (first link-up).

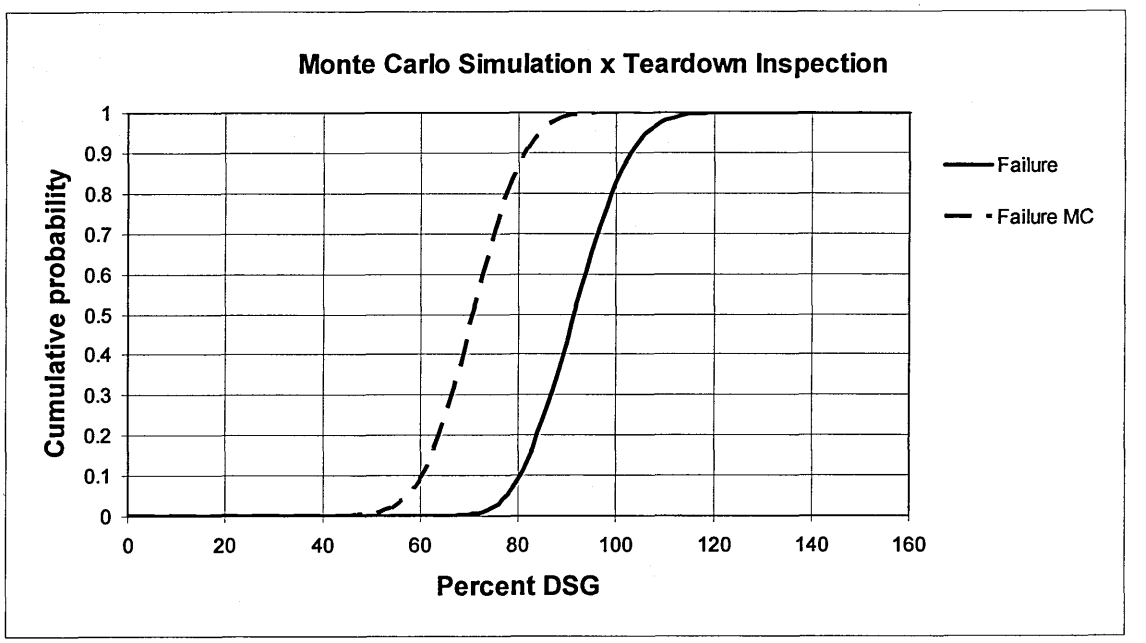

Figure 6.5.9: Cumulative probability distribution for failure comparison to teardown inspection data.

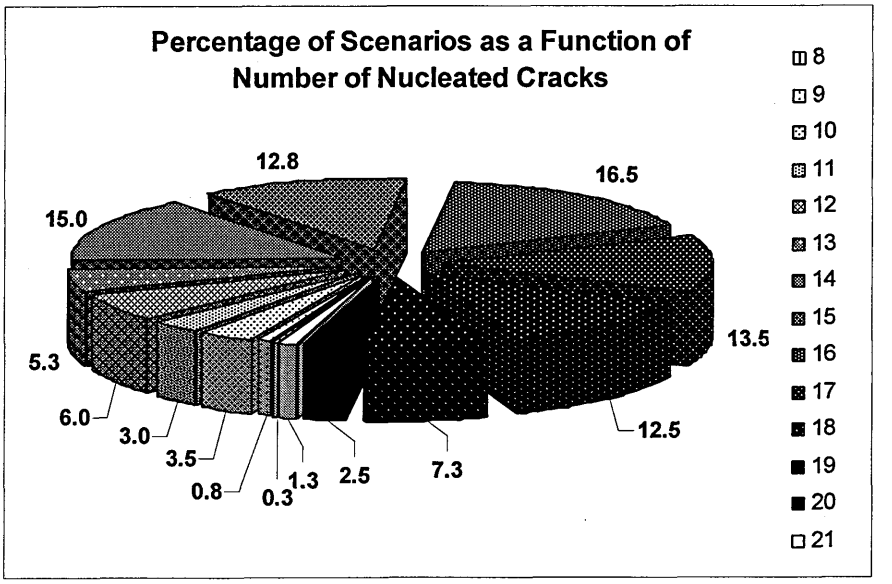

Figure 6.5.10: Percentage of scenarios as a function of nucleated cracks from Figure 6.5.6.

Chapter 7

7. DISCUSSION

In this chapter the discussion given follows the same order as for the results presented in chapter 6, whenever possible.

7.1. Experimental Work

The objective of the experimental work presented in section 6.1 was to generate fatigue crack initiation data to assess the effect of high squeeze force on MSD development via the application of the MSD model presented in chapter 4; and high squeeze force is one of the variables studied in this work regarding MSD behaviour. The purpose of the discussion presented in this section is to provide a general explanation to the results presented in section 6.1 and, mainly, to compare the fatigue data obtained to published work from the literature in order check its validity.

The fatigue test data from Figure 6.1.1 is presented in Figure 7.1.1 together with the corresponding theoretical cumulative probability of failure curves, and the data shows a good fit to the normal distribution. As found in other published work [53, 79, 80, 83-85], the testing configurations from Table 6.1.1 show that the mean time to failure (cycles) increases when the squeeze force varies from a low to a high value, despite the stress level employed; and with the smallest stress range producing the biggest lives (Figure 6.1.2).

The reason for why fatigue lives are consistently improved when squeeze force is increased is explained by Harish [83, 85] and Muller [79]; and a brief summary is presented here. When high rivet squeeze force values are employed, an expansion of the hole in the material sheet occurs due to the rivet expansion inside the hole. This expansion causes an interference fit between rivet and hole which leads to beneficial compressive residual stresses in radial and tangential directions in the vicinity of the hole. As the compressive tangential stresses increase, there is a reduction on the local

stresses at the boundary of the hole during fatigue loading; and if a small crack is present at the hole edge the stress intensity factor is reduced and more crack closure occurs. Also, the squeeze force produces a clamping pressure on the mating surfaces of both sheets, especially pronounced, around the vicinity of the hole border. The clamping pressure causes part of the load transmitted by the rivet to be taken up by the sheets due to interfacial friction. The higher the clamping pressure the greater is the interfacial frictional load, and the smaller is the load transmitted by the rivet. This complex stress distribution results in lower peak stress values at the rivet/skin interface leading to higher fatigue crack nucleation lives and, consequently, fatigue life improvement.

For example, if the 10 KN squeeze force test specimens at 100 MPa stress from Figure 6.1.1 are considered, it can be seen that the mean fatigue life is equal to 238,079 cycles (Table 6.1.2); when the squeeze force and stress level are increased to, respectively, 16 KN and 120 MPa, the mean fatigue life obtained (Table 6.1.2) is 244,396 cycles (which is practically the same as for the case of 10 KN squeeze force at 100 MPa). This example shows that an increase in squeeze force makes the fatigue critical location to behaves as if it was subjected to a lower nominal stress than it actually is due to changes in the local stress field around the hole border.

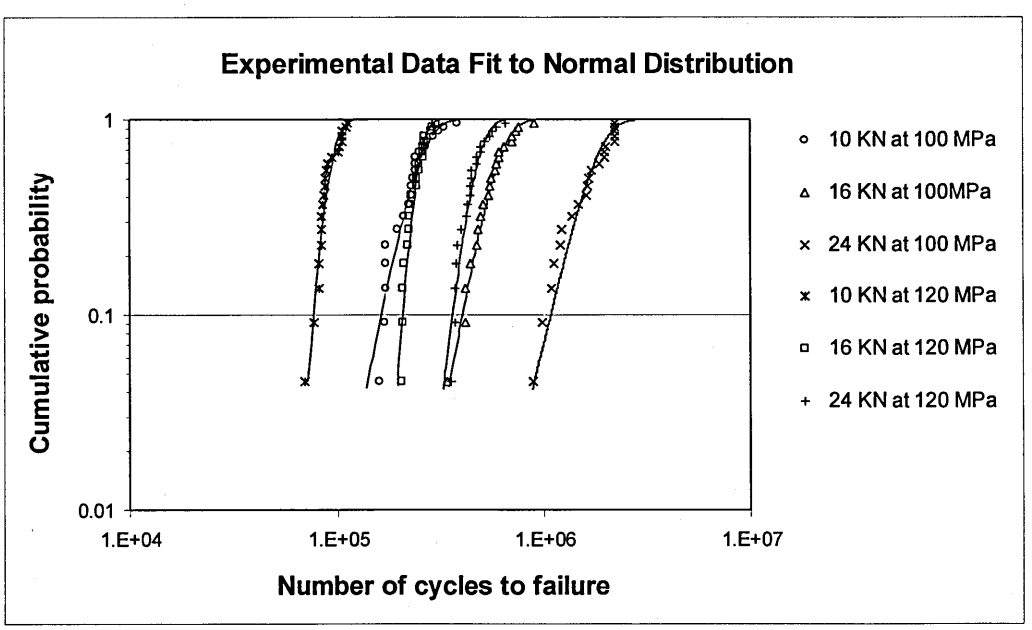

Figure 7.1.1: Experimental data fit to theoretical cumulative probability distribution. and 100 MPa (R = 0.1) cyclic tensile stress.

Figures 6.1.3 and 6.1.4 show the results from Figure 6.1.2 but with the corresponding standard deviation values. From both figures it can be seen that not only the mean fatigue life is increased when squeeze force increases, but also the corresponding standard deviation values (cycles) regardless of the stress level considered. A direct comparison of changes in scatter due to changes in squeeze force from this work to other published data is not straightforward. As presented in chapter 2, research on different rivet squeeze forces has been concentrated in comparison of the mean fatigue life to failure of strap joint specimens. This comparison was usually done by performing only 3 to 5 fatigue tests; and a comparison of the scatter data from this work, where 21 fatigue tests were performed, with 3 to 5 fatigue tests from other publications becomes quite questionable.

What is clear from Figures 6.1.3 and 6.1.4 is that when squeeze force increases the mean fatigue life improves, and it is well known from the literature that scatter varies when the mean fatigue life changes. For constant amplitude fatigue tests, the fatigue life distribution generally depends on the stress level, where longer fatigue lives and greater scatters are obtained as the stress amplitude is reduced [112]; and this statement can be confirmed observing the differences on the mean fatigue lives and corresponding scatter values for the same squeeze forces from Figures 6.1.3 and 6.1.4.

The main question here is why different squeeze forces produce different scatters for the same stress level. As explained previously, as the squeeze force increases beneficial residual compressive stresses and high clamping pressures are created. These stress state acts reducing the stress concentration at the fatigue critical location leading to longer fatigue lives and, consequently, bigger scatter values in fatigue life would be expected even at the same stress levels.

As a general trend, it can be stated that as the squeeze force increases, fatigue life is improved and bigger scatter values are obtained for the same stress level; although this statement is not always true. For example, Ofsthun [86] verified that squeeze force can not be increased infinitely because at some point the fatigue life degrades instead of

improving. Stagg [20] showed that the life – scatter relationship is not linear and that for some loading conditions scatter tends to level off.

Considering Figures 6.1.6 and 6.1.7, it can be seen that the COV values range from 0.0094 to 0.0127 at 120 MPa and from 0.0175 to 0.0205 at 100 MPa. These values are in accordance to what has been reported by Stagg [20] for riveted aluminium joints for fatigue lives varying from 5 to 6.5 in log (cycles). What calls the attention in Figures 6.1.6 and 6.1.7 is that there is a point of minimum for the intermediate lives in log (cycles) corresponding to the intermediate squeeze force (16 KN). From Figure 6.1.5 it can also be seen that, not only the COV (Figures 6.1.6 and 6.1.7), but the scatter values in log (cycles) are smaller at intermediate lives at both stress levels.

Raikher [113, 114] and Stagg [20] investigated scatter behaviour out of thousands of aluminium alloy coupons and structural elements by gathering a comprehensive fatigue test data from many sources to compare them. A typical plot of scatter 'S (logX)' versus mean time to fatigue crack initiation '$\overline{X}$', both in log (cycles), is presented in Figure 7.1.2 [114].

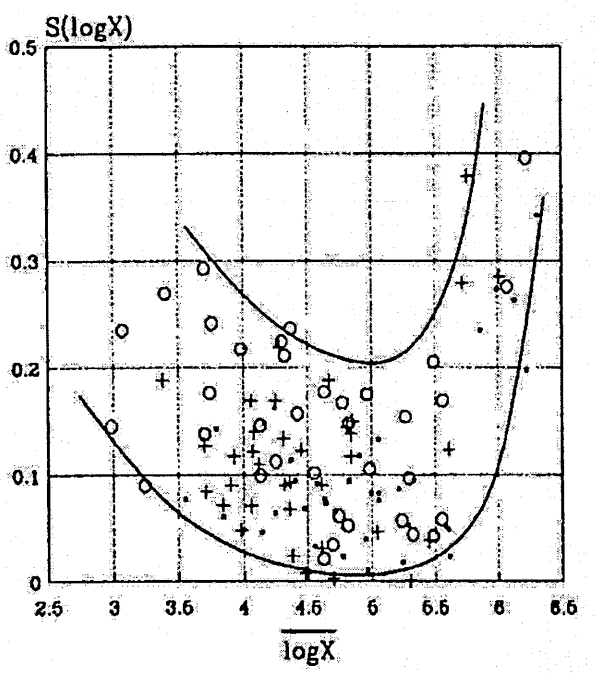

Figure 7.1.2: Influence of mean life on scatter [114].

As it can be seen from Figure 7.1.2, scatter does not always increase with increasing life, as observed in Figure 6.1.5. Raikher [113, 114] and Stagg [20] concluded that scatter increases for both high and low lives, and that there is a region of minimum scatter which can be found between these lives; and the same trend is observed for a plot of COV versus mean fatigue life in log (cycles) (see Stagg [20]). Therefore, the results presented in Figures 6.1.5 and 6.1.7 are in accordance to Raikher and Stagg, but an explanation to why scatter, and COV, behaves such as in Figure 7.1.2 is not clear from the literature.

Beyond of the improvement in fatigue life caused by high squeeze force values, Harish [83, 85] and Muller [79] also showed, by means of FE analysis and thermal imaging measurements of riveted joints, that crack nucleation sites change for different squeeze force values due to changes in the residual stress distribution patterns in the vicinity of the hole. For low squeeze force values, the crack nucleation sites are close to the 3 and 9 o'clock positions of the hole and mainly at its border. For large squeeze force values the boundary of the hole is not critical anymore, with crack nucleation taking place away from the 3 and 9 o'clock positions and from the hole border. The previous findings from Harish and Muller are in accordance to the experimental results from this work, reported in Table 6.1.3, regarding changes on the mean fatigue crack initiation site coordinates for increasing squeeze force values.

From Table 6.1.3 it can be seen that for the low squeeze force value crack nucleation takes place mainly at the hole border. When the squeeze force is increased from a small to an intermediate or high values, crack nucleation moves further away from the hole border; and fatigue crack nucleation away from hole border has also been confirmed by teardown inspections from in-service riveted lap joint fuselage panels [115].

Regarding the fatigue crack initiation mechanism in fuselage riveted joints, it has been verified that fretting is the main cause for fatigue crack nucleation in aging aircraft [29]. Figures 6.1.9, 6.1.11 and 6.1.13 show darker areas that are evidences of fretting. It can be noted that as the squeeze force increases, the dark areas increase as well. This behaviour can be explained by the clamping forces originated from the riveting process.

As the squeeze force increases, clamping increases as well and it is expected that friction contact areas (possibly the dark areas) increase. From Figures 6.1.10, 6.1.12 and 6.1.14, it can be observed that the fracture surfaces resemble an elliptical shape; and these results are in accordance to Fawaz [81]. Fawaz showed that the crack propagation front at riveted joints is elliptical and, therefore, elliptical-like fracture surfaces are expected.

From the discussion given previously, it can be seen that the fatigue test results presented in section 6.1 demonstrate good agreement to what has been reported in the literature. Therefore, the fatigue data generated can be considered valid as input variable for the MSD assessment model from this work for future MSD behaviour investigation.

7.2. MSD Assessment Model Comparison to Experimental Work and Other Models from the Literature

In this section a discussion on the MSD assessment results from Figure 6.2.1.9 (Monte Carlo simulations and 6 experimental test data) and on a comparison to other MSD models from the literature is provided. The purpose of this discussion is to verify if the MSD methodology from this work can be used as an engineering tool for MSD assessment.

As found in other published simulations for MSD assessment, for instance Santgerma [31], Proppe [40], Kebir [39] and Cavallini [17], Figure 6.2.1.9 shows that lives to failure are dominated by the crack initiation phase. It can be noted that for the Monte Carlo simulations the total initiation life varies from 55,758 to 352,684 cycles, whereas propagation lives are between 24,206 to 88,382 cycles. Considering the 6 experimental test points, the total initiation life varies from 97,000 to 281,950 cycles, whereas propagation lives are between 36,200 to 85,368 cycles and, therefore, the spread of predicted lives encloses the scatter of the experimental lives for both initiation and propagation stages. It can also be seen that the 6 experimental test points demonstrate a spread comparable to the 400 Monte Carlo simulations in both initiation and propagation axis. This observation is found in the majority of previous comparisons of

Monte Carlo simulations to experimental MSD data from the literature (Figures 7.2.1 to 7.2.4), despite of the geometry and loading conditions of the experimental data used for comparison. In the case of Figure 6.2.1.9, it is possible that were 400 experiments to be performed the observed scatter could be greater than the current simulations data set; but this issue can not be addressed here due to the small number of test points. What can be stated from Figure 6.2.1.9 is that the simulations were able to enclose and, therefore, to represent the experimental test data used for comparison purposes, demonstrating its effectiveness.

Figures 7.2.1 to 7.2.4 present typical MSD assessment analysis from, respectively, Santgerma [31], Proppe [40], Kebir [39] and Cavallini [17] (refer to section 2.3 for a detailed description of these methodologies). Santgerma analysed the same configuration as from Figure 6.2.1.1, Proppe and Kebir analysis is for a row of 14 open holes and Cavallini analysis is for a butt joint of 14 holes. The results from Figures 7.2.1 to 7.2.4 serve as good comparison basis to the ones presented in Figure 6.2.1.9, since both fatigue crack initiation and propagation phases are plotted, in the case of Cavallini initiation and failure (initiation + propagation).

As the results presented in Figure 6.2.1.9, it can be seen from Figures 7.2.1 to 7.2.4 that the test points demonstrate a spread comparable to the MC simulations and that they are reasonably enclosed by them, but in the case of Figure 7.2.4 for the total life axis (initiation + propagation). The discrepancies between the experimental data and MC simulations from Cavallini [17] have been explained as an incorrect evaluation of the time to crack initiation as a consequence of different riveting processes while manufacturing the test specimens. Cavallini explanation coincides with what can be observed from Table 6.1.2. It can be seen that if test samples are manufactured with different rivet squeeze forces, they will demonstrate a different behaviour regarding the mean time to crack initiation and, therefore, present different fatigue life distributions.

When compared to MSD experimental test data, it is clear from Figures 7.2.1 to 7.2.4 and 6.2.1.9 that MSD assessment is feasible when its probabilistic nature is taken into account. The probabilistic nature of MSD can be explained based on Schijve [116], who

states that a quantitative prediction of fatigue properties (deterministic fatigue life predictions) cannot yet be given because of the qualitative understanding of the complexity of fatigue damage accumulation.

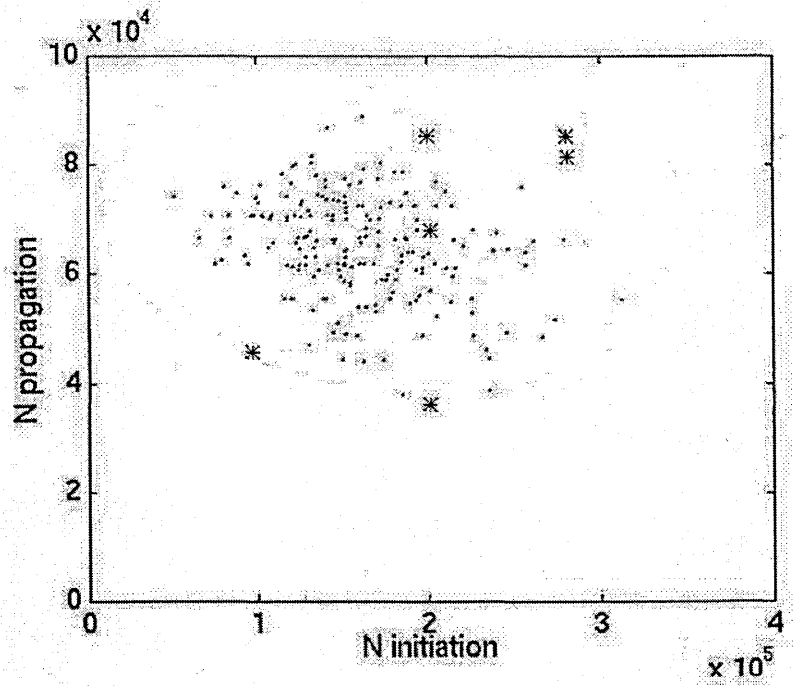

Figure 7.2.1: MSD assessment and comparison to experimental work [31].

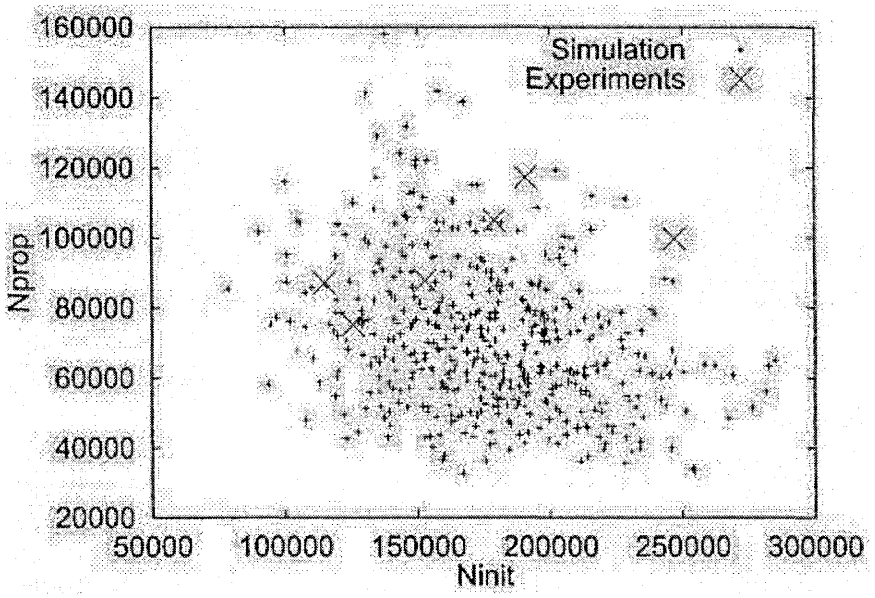

Figure 7.2.2: MSD assessment and comparison to experimental work [40].

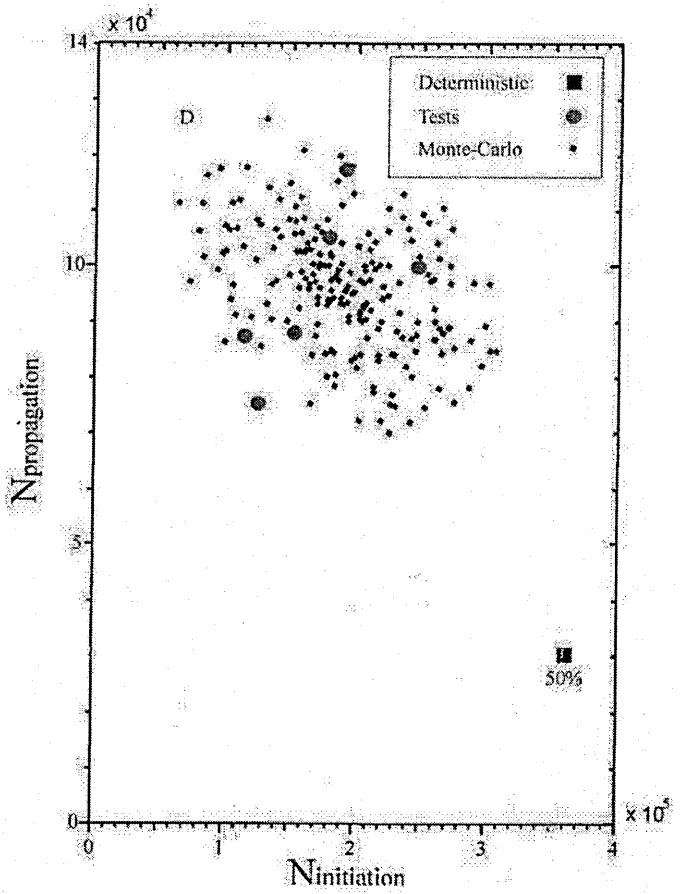

Figure 7.2.3: MSD assessment and comparison to experimental work [39].

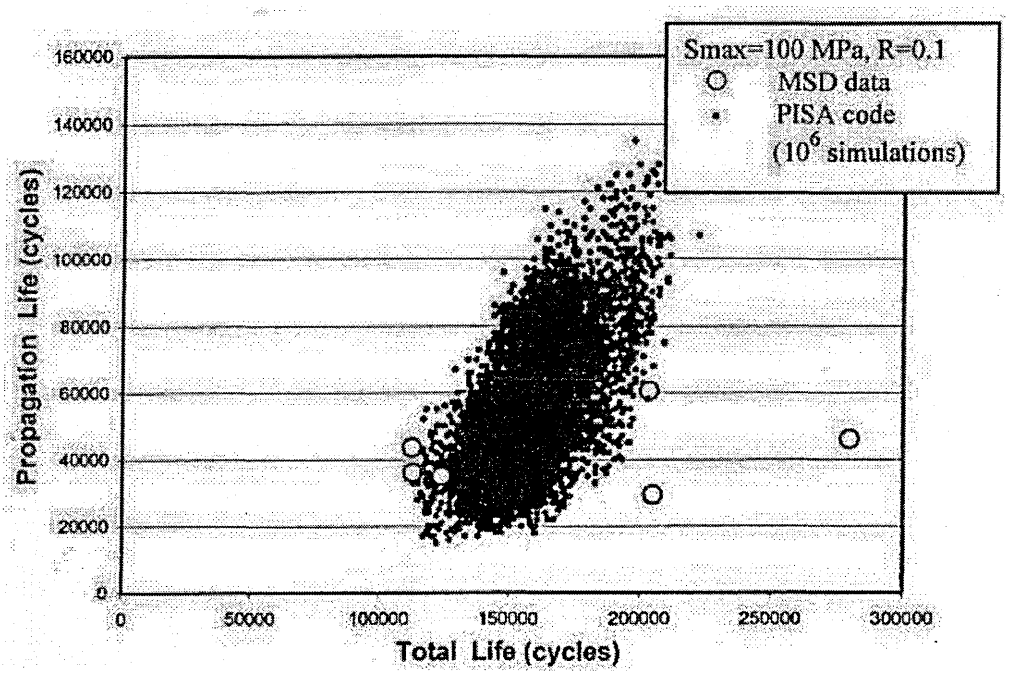

Figure 7.2.4: MSD assessment and comparison to experimental work [17].

Regarding the MSD models themselves, it can be noticed by visual inspection from Figures 7.2.1 to 7.2.4 and 6.2.1.9 that different models produce similar outputs. Although MSD models have differed in their built-in assumptions and in their calculation techniques; they also have some assumptions in common. One assumption that is common to the models reported (chapter 2) is the use of a damage accumulation technique for calculating re-initiation of fatigue cracks opposed to continuing damage assumption, as described in section 4.2. The use of continuing damage assumption in probabilistic based models for MSD assessment has been reported only by Garcia [117, 118]; but the difference between modelling with a damage accumulation technique or continuing damage assumption has not been established. To establish this difference, the MSD assessment results from Santgerma [31], presented in Figure 7.2.1, are used as a comparison basis since the same lap joint configuration under the same loading conditions was analysed.

In the case of Santgerma [31], the lap joint configuration analysed is the one from Figure 6.2.1.1 subjected to the same loading conditions (100 MPa cyclic tensile stress and R = 0.1). The fatigue crack initiation phase is modelled exactly the same as in this work, where the same S-N fatigue data and its scatter come from, respectively, equations 6.2.1.1 and 6.2.1.2 to achieve a distribution of lives corresponding to an initial crack size of 1.0 mm via Monte Carlo simulation applied to a lognormal distribution (equation 4.1.1). Regarding the crack propagation phase, Santgerma [31] performs deterministic crack growth via a FE based computer code and the Swift criterion [103] for crack link-up (as in section 4.2). FE analysis for local stress calculation and Miner rule [107] are used to establish fatigue damage accumulation at crack-free FCLs. The crack propagation phase stops when residual strength is lost by net section yielding.

From the MSD methodology by Santgerma [31], it can be realized that the differences to the one from this work are concentrated in the crack propagation phase. In order to establish a comparison basis between the continuing damage assumption from this work and the damage accumulation technique from Santgerma, the crack propagation analysis from the results presented in Figure 6.2.1.9 is kept deterministic and the new results are

presented in Figure 7.2.5. Before comparing the results from Figure 7.2.5 to Santerma (Figure 7.2.1) a comparison between Figures 7.2.5 and 6.2.1.9 is presented.

Comparing the results from Figure 7.2.5 to the ones from Figure 6.2.1.9, it can be clearly seen a change in the crack propagation life distributions, but no changes are observed for the crack initiation lives. While the distribution of lives for crack initiation remains the same, the mean time for crack propagation is now equal to 54,213 cycles with the propagation lives varying from 23,524 to 65,510 cycles. From Figure 6.2.1.9 the corresponding values for mean time for crack propagation is 54,286 cycles with the propagation lives varying from 24,206 to 88,382 cycles. It can be noticed that the mean time for crack propagation of the deterministic analysis and the probabilistic one are basically the same, with a difference of 0.1 %. This small difference, or no difference at all, is expected since the probabilistic crack growth treatment (section 4.3) applied to the deterministic crack propagation output (section 4.2) uses the random Gaussian distribution from Figure 4.1.2 (which is fairly centred around zero), i.e., each deterministic crack propagation life from Figure 7.2.5 is randomly modified either to a bigger or to a smaller value when probabilistic crack growth is considered, but the mean of the modified lives is not supposed to suffer any big change when a minimum number of Monte Carlo simulations is performed for convergence; and this behaviour is shown by the small difference between the mean crack propagation lives from Figures 7.2.5 and 6.2.1.9.

Another difference in the crack propagation axis from Figures 7.2.5 and 6.2.1.9 is that while in Figure 7.2.5 it can be noticed some clear straight lines, in Figure 6.2.1.9 these lines disappear giving place to a smoother distribution of lives for crack propagation. The straight lines from Figure 7.2.5 represent single-crack scenarios that, although assigned different crack initiation lives, had the lead crack nucleation at the same FCL and, since deterministic crack growth is considered, the number of cycles for crack propagation does not change. From Figure 6.2.1.14 it can be seen that scenarios that developed a single crack represent 40.4 % of the cases, i.e., 162 out of 400 simulations. As for the lap joint configuration analysed (Figure 6.2.1.1) there are only 18 FCLs for the external row of holes, what can be invariably concluded is that among the 162

single-crack scenarios some of them can have the same time for crack propagation. On the other hand, when the probabilistic crack growth treatment (section 4.3) is applied to the scenarios from Figure 7.2.5, the number of cycles for crack propagation of each damage scenario moves up or down; determining a smoother crack propagation distribution (Figure 6.2.1.9) with an enlarged life range. In fact, differences in the crack propagation lives from Figures 7.2.5 and 6.2.1.9 are mostly concentrated in the crack propagation range (max. TCP – min. TCP). While in Figure 7.2.5 propagation lives range is 41,986 cycles, in Figure 6.2.1.9 the same value is 64,176 cycles. The main implication of this difference is that while in Figure 6.2.1.9 the experimental data set scatter could be enclosed by the Monte Carlo simulations in the crack propagation axis, the same fact is not true for the case of Figure 7.2.5, where continuing damage assumption is employed with deterministic crack propagation. From Figure 7.2.5 it can be seen that 4 out of 6 experimental points are not enclosed by the crack propagation lives from the simulations. This result shows that when continuing damage assumption is employed with deterministic crack propagation, conservative crack growth life ranges are obtained compared to the results from Figure 6.2.1.9 (continuing damage assumption + probabilistic crack growth) and to the experimental data as well.

Considering the results from Santgerma [31], Figure 7.2.1 shows that the mean initiation life is 162,075 cycles and the mean propagation life is 65,264 cycles, with a mean failure process of 227,339 cycles. If these values are compared to the ones from Figure 7.2.5 (continuing damage assumption + deterministic crack growth), it can be seen that the mean initiation life from Figure 7.2.5 is 8.9 % bigger than the one from Figure 7.2.1, while the corresponding mean propagation life is 16.9 % smaller, leading to a mean failure process 1.5 % bigger than the one from Figure 7.2.1. The difference obtained for the mean time to crack initiation can be explained by differences on the FCLs loading from this work (Figure 6.2.1.3) and the one adopted by Santgerma [31]. Since the crack initiation stage for both models are the same (given by equations 4.1.1, 6.2.1.1 and 6.2.1.2 for the same lap joint configuration); were the values for each FCL loading calculated by Santgerma [31] utilized in this work, as well as the same random numbers for fatigue crack initiation, then the mean time to crack initiation would be exactly the same.

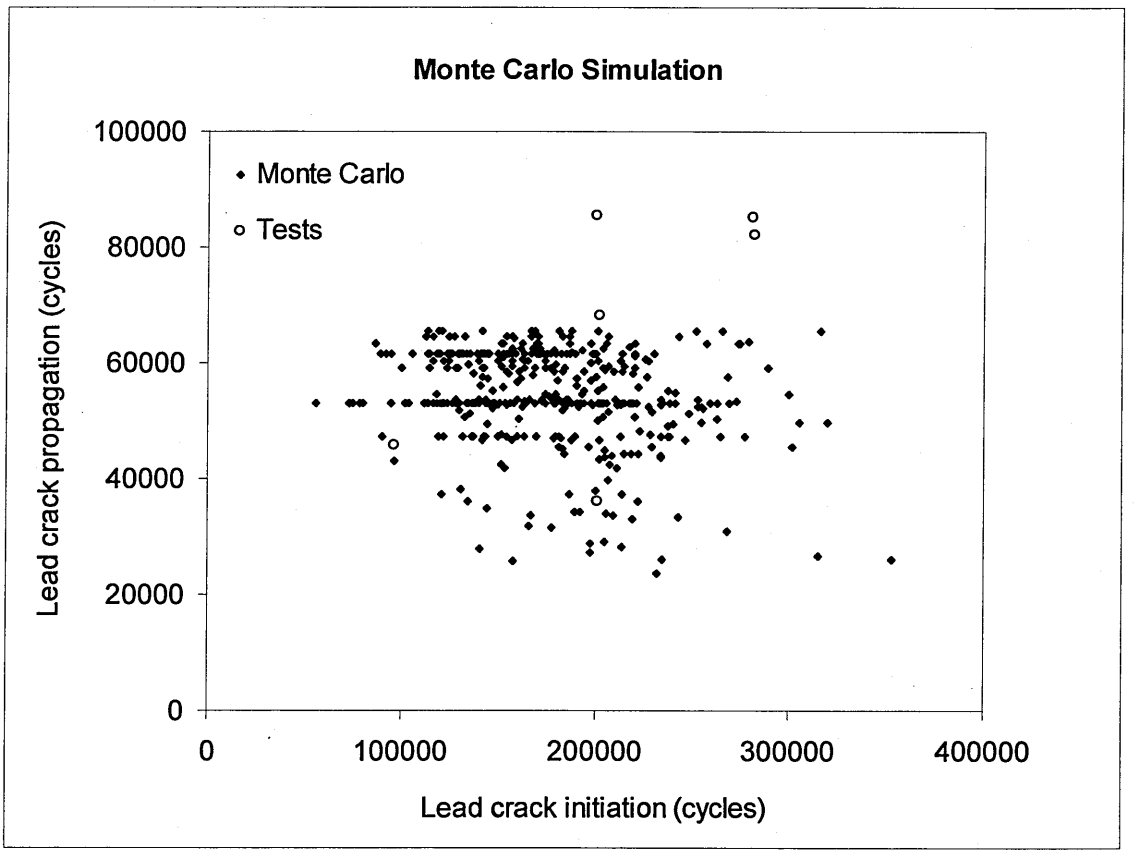

Figure 7.2.5: Results from Figure 6.2.1.9 but with deterministic crack growth.

While the difference arising from the crack initiation stage between this work and Santgerma [31] is relatively simple to explain, the same does not occur for the crack propagation lives. Differences in the mean time for crack propagation can be attributed to factors which are difficult to separate and quantify each one's influence in the whole context of the crack propagation stage. Despite continuing damage assumption and a damage accumulation technique, other factors related to differences in crack propagation modelling assumptions exist. For instance, while Santgerma [31] employs the Paris equation (equation 2.2.5.1) for crack propagation, this work employs a modified version of it which takes into account the effective stress intensity factor (equation 3.1.3). Differences in the lap joint modelling from Figure 6.2.1.1 also occur since Santgerma [31] used an FE code and in this work the same configuration is modelled by a DBE code (Appendix B); and these modelling differences can be translated by, for example, different pin-loading and bypass loading values and

boundary conditions assumed (constraints in x and y directions); which lead to differences in stress intensity factors calculation, as shown in section 3.3 for example.

For the reasons stated in the previous paragraph, a direct comparison of Figures 7.2.1 and 7.2.5, for establishing the contributions that continuing damage assumption and a damage accumulation technique have on the whole crack propagation stage is not an easy task; but some interesting discussion can be given if the results from Figure 6.2.1.9 are considered to compare Figures 7.2.1 and 7.2.5 for general trends.

Observing Figures 6.2.1.9 (continuing damage assumption + probabilistic crack growth) and 7.2.1 (damage accumulation technique + deterministic crack growth), it can be seen that the results from the Monte Carlo simulations are quite similar to each other considering the scatter bands on both crack propagation and initiation axis when compared to the experimental data set, showing a good agreement between both models outcome. Therefore, it can be realized that continuing damage assumption and probabilistic crack growth can be used as a valid option to a damage accumulation technique and deterministic crack growth as an engineering approach to MSD models. Also, for the reasons presented in section 4.2, continuing damage assumption represents a simplifying assumption compared to a damage accumulation technique when it comes to model MSD on probabilistic basis.

On the other hand, when the crack propagation scatter from Figures 7.2.1 (damage accumulation technique + deterministic crack growth) and 7.2.5 (continuing damage assumption + deterministic crack growth) are compared, while in Figure 7.2.1 the experimental data set scatter could be reasonably enclosed by the Monte Carlo simulations in the crack propagation axis, the same is not true for the case of Figure 7.2.5 and, therefore, continuing damage assumption + deterministic crack growth is not an appropriate approach to represent the scatter inherent to crack propagation. Also, the mean time for crack propagation from Figure 7.2.5 is 15.6 % smaller than the one from Figure 7.2.1 showing that, as a general trend, deterministic crack propagation performed with continuing damage assumption gives conservative crack propagation lives compared to the ones from deterministic crack propagation performed with a damage

accumulation technique; and this is readily verified by observing Figures 7.2.1 and 7.2.5.

7.3. MSD Assessment Model Limitations

The purpose of this section is to present the author point of view about some limitations, as well as possible solutions to overcome them, concerning the MSD methodology from this work.

Regarding the minimum number of Monte Carlo simulations performed for MSD assessment, what can be realized from the literature is that this number varies among authors. For example, Santgerma [31] reported 150 simulations for a row of open 14 holes and 200 simulations for a row of 9 pin-loaded holes; Kebir [39] reported 200 simulations for a row of 14 open holes (same configuration as in [31]); Balzano [16] reported from 100 to 150 simulations for a row of 14 open holes (same configuration as in [31]); Shkarayev [41] reported 100 to 200 simulations for a row of 3 and 6 open holes; Horst [30] reported 250 simulations for a row of 8 pin-loaded holes; and in this work (chapter 6) it has been reported from 260 to 280 simulations for a row of 9 pin-loaded holes (same configuration as in [31]).

Horst [30] verified that if real mathematical convergence is needed then millions of simulations are necessary, but for engineering applications only a few hundreds of simulations are enough to stabilize the results from Monte Carlo simulations. As observed by Horst [30], Figure 6.2.1.10 shows, for example, that failure lives vary at the beginning but after 280 simulations the differences are no longer large if compared to uncertainties inherit to the model itself. In fact, the importance of convergence in MC simulations relies on the need for having unbiased estimators (mean fatigue life and corresponding standard deviation) in order to use statistical tools, such as cumulative distribution functions or confidence regions, to extrapolate the results from a limited number of simulations.

The reason for why the minimum number of simulations varies among different MSD models, even when the same geometrical configuration and loading conditions is analysed, is not clear for the author; and it may be connected to modelling assumptions and calculations inherit to each model. The literature (chapter 2) brings no answer for this question, but it is clear from Figure 7.2.4 that if the right input variables are not employed in probabilistic MSD models, then even 10^6 simulations are not enough to represent the test data accordingly.

At this point, the need for performing at least a minimum number of Monte Carlo simulations is clear; but what is the desired maximum number of simulations to be performed is not. For example, if 1,000 simulations were presented in Figure 6.2.1.9 instead of 400 then both ranges for crack initiation and propagation lives would be possibly enlarged due to new damage scenarios. In fact, what can be realized is that probabilistic MSD assessment models, like the one from this work, that perform a few hundreds of simulations have its limitations. For MSD assessment models that use FE or BE based computer codes for crack propagation calculation it is feasible to perform a few hundreds of simulations; but millions of simulations, for example, is out of question. To overcome this limitation, Horst [30] and Santgerma [31] used confidence regions together with their simulations.

The use of confidence regions is, in fact, a statistical treatment applied to the limited number of Monte Carlo simulations; as far as this limited number of simulations is enough for achieving convergence. While Horst [30] used confidence regions (also called joint confidence sets) that resemble a skewed bell-like shape, Santgerma [31] used an elliptical one. Differences and comparison among 5 different joint confidence sets, including the ones from Horst and Santgerma, can be found in Arnold [119]. In this work, the elliptical confidence set is employed for simplicity and the procedure to plot this type of confidence set comes from Press [21]. The difference of the elliptical confidence regions from this work and Santgerma relies on the fact that in this work the elliptical confidence boundaries have been corrected according to Arnold [119]; so that a finite number of simulations can produce the same confidence region size as the theoretical infinite number. The Monte Carlo simulations from Figure 6.2.1.9 are

presented in Figure 7.3.1 together with a 99 and 99.97 % confidence regions for all possible outcomes from Monte Carlo simulations.

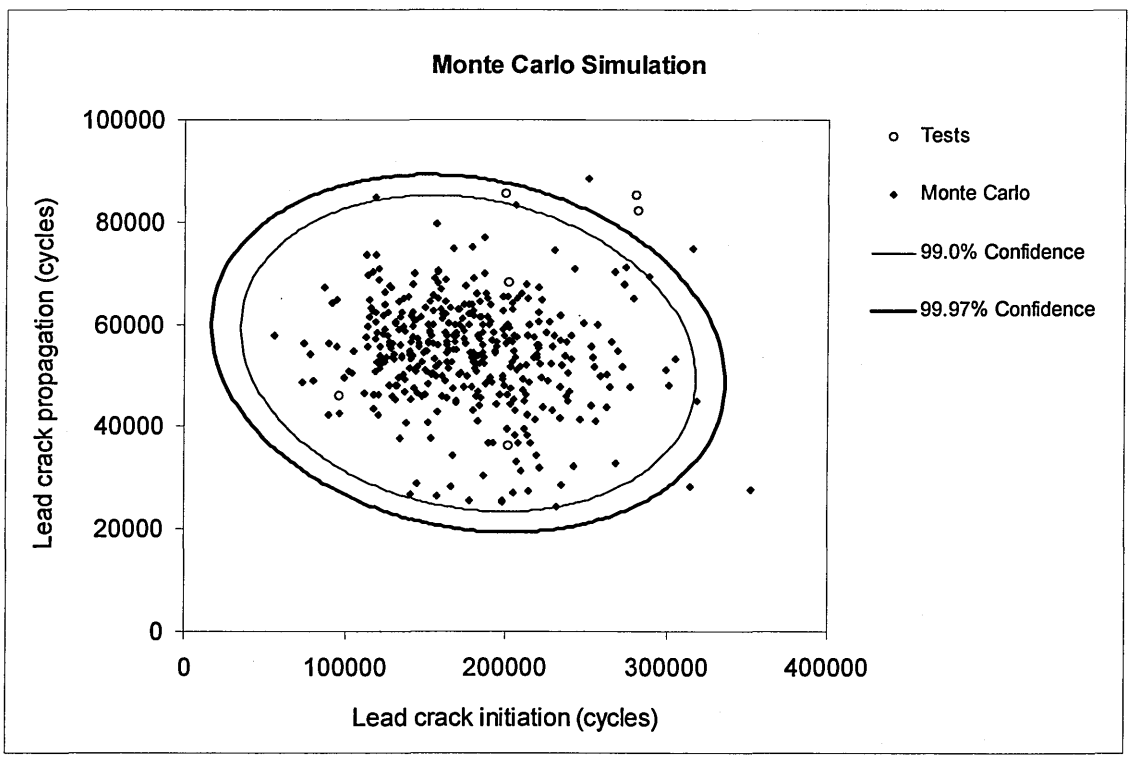

Figure 7.3.1: Results from Figure 6.2.1.9 with 99 and 99.97 % confidence intervals.

From Figure 7.3.1, it can be seen that 2 experimental points fall out of the 99.97 % confidence region. The reason for this fact does not seem to rely on scatter of the simulations (considering both crack initiation and propagation axis) since the scatter of the 6 experimental test points are enclosed by them, while the mean value obtained for fatigue crack initiation of the simulations is 176,455 cycles when compare to the same value from the experimental data being 210,583 cycles. If the fatigue crack initiation values for each simulation is added by a fixed number of cycles so that the mean time to crack initiation has the same value from the experimental test points (210,583 cycles), then the results from Figure 7.3.1 become the ones from Figure 7.3.2. From Figure 7.3.2 it can be seen that now only one experimental point falls outside the 99.97 % confidence zone, and it may be that this point is really out of it, showing that best agreement of the simulations is obtained when the mean time to crack initiation matches the one from the test data. From this example, it can be realized that the mean time to

crack initiation is an important parameter and the most correctly it is calculated the best MSD simulations output will be.

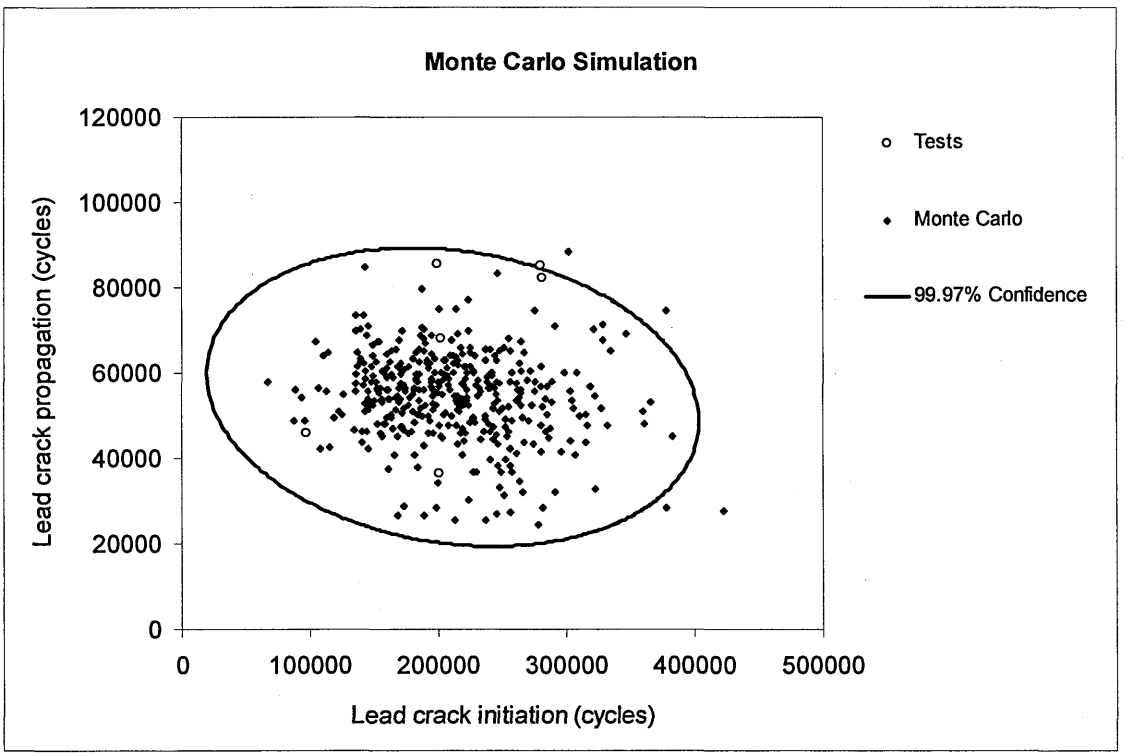

Figure 7.3.2: Results from Figure 7.3.1 with simulations mean time to crack initiation modified to the one from experimental test data.

Another interesting interpretation can be given to, for example, the 99.97 % confidence region from Figure 7.3.1, which is presented alone in Figure 7.3.3. This confidence region, or any other confidence region used, can be interpreted as a crack initiation and crack propagation envelop where the points A, B, C and D indicate its extreme values. If the corresponding crack initiation and propagation lives from points A, B, C and D are added then the failure lives are, respectively, 76,418; 239,660; 385,096; 221,734 cycles; i.e., the point represented by A has the smallest failure life.

From section 6.2.1, the ISP and the SMP have been established by the Monte Carlo simulations from Figure 7.3.1 (former 6.2.1.9) and these values are, respectively, 76,941 and 115,371 cycles. If the number of cycles to failure from point A (Figure 7.3.3) is considered, it can be seen that this number is very close to the ISP one (76,941 cycles).

At this stage it would be interesting to check whether the number of cycles to failure given by the point A or by the ISP is so close to each other. To perform this comparison, the cumulative probability distribution of failure from Figure 7.3.5 is employed, but before some considerations have to be made about the approximations adopted.

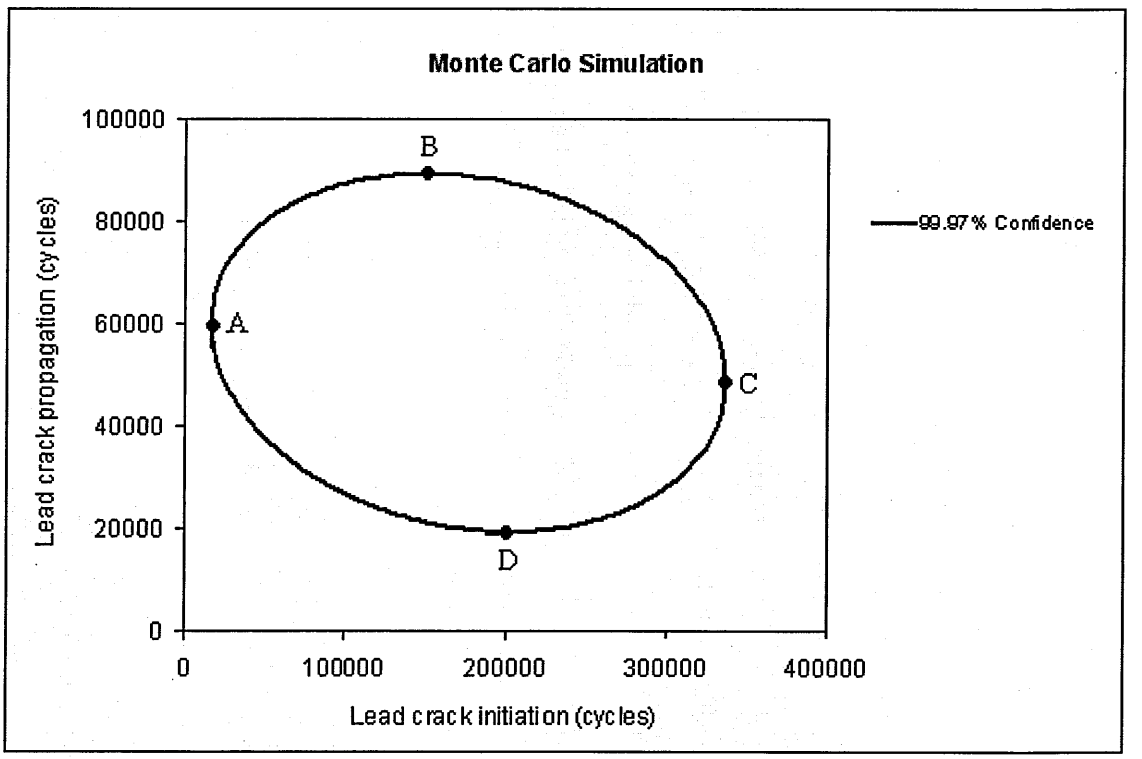

Figure 7.3.3: 99.97% confidence region from Figure 7.3.1.

Figures 7.3.4 and 7.3.5 show the same results with different scales in the y-axis, where the simulation points from Figure 7.3.1 are plotted with the theoretical normal cumulative probability distributions of failure. The theoretical distributions have the same mean and corresponding standard deviation values from the simulations.

As observed from other authors [17, 31], Figures 7.3.4 and 7.3.5 show that the simulation points demonstrate a reasonable fit with the theoretical normal cumulative distributions, with the largest differences at the tail (Figure 7.3.5); and the simulations approximation to the theoretical case can be considered acceptable for the extrapolation

of its results to compute low probabilities of occurrence, not covered by the simulations itself.

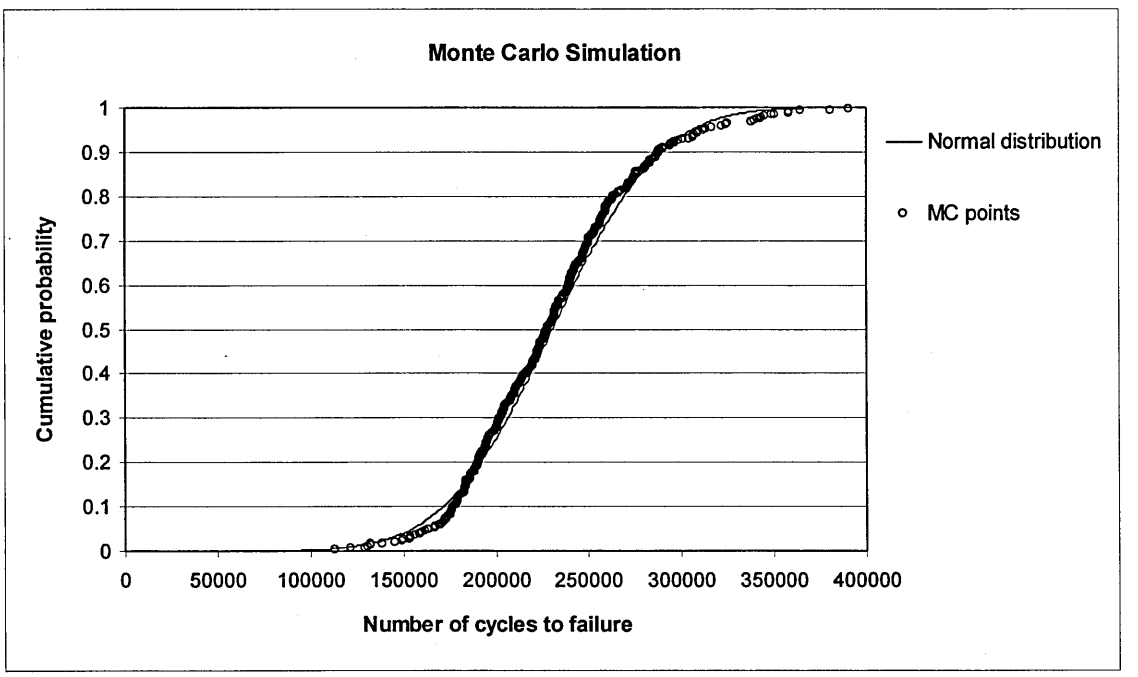

Figure 7.3.4: Cumulative probability distribution comparison.

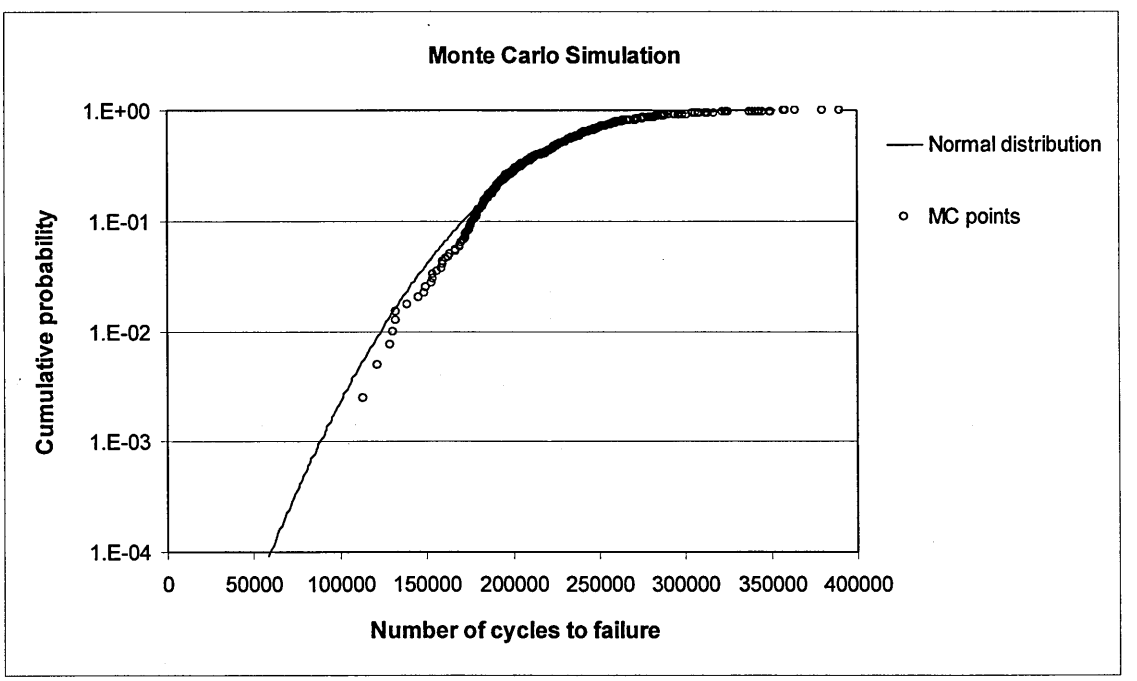

Figure 7.3.5: Cumulative probability distribution comparison.

Regarding the number of cycles to failure of point A (76,418 cycles) from Figure 7.3.3, it can be seen from Figure 7.3.5 that for 76,418 cycles the corresponding cumulative probability of failure is approximately 4E-4. According to Gallagher [75], the USAF adopts the criterion that if a single flight probability of failure is less than 1E-7 then the risk is acceptable for long term operation of aircraft structure. If the 1E-7 single flight probability of failure is computed in terms cumulative probability of failure then this value is equal to 1E-3 [48]. The equivalent 1E-3 cumulative probability of failure from Figure 7.3.5 is approximately 89,000 cycles, which is a bit more than 12,000 cycles from the ones established by point A and by the ISP. From these results it can be realized that the ISP is well established and, in fact, the confidence level of 99.97 % from Figure 7.3.1 (from which point A originated – Figure 7.3.3) is quite high and can be reduced.

On the other hand, if the SMP value (115,371 cycles), established by the simulations from Figure 7.3.1, is considered, then it can be seen from Figure 7.3.5 that its cumulative probability of failure would be approximately 6E-3; and this value is bigger than what is recommended by the USAF criterion [75] for adequate long-term operation of the structure! This result is quite interesting because it shows that the factor of 2, recommended for establishing the SMP [3], does not provide an acceptable cumulative probability of failure according to the USAF criterion [75]; and a value of 2.6 should be used instead for a cumulative failure risk of 1E-3. It is worthwhile to note that the ISP and the SMP are established based on a unique point of the cumulative failure distribution: the 50 % one; and no other parameters are taken into account.

From the results presented in the previous paragraph regarding the SMP, it is noticeable that the establishment of this point, according to the recommendations from the AAWG [3], is in conflict with the USAF criterion [75]. This conflict suggests that the establishment of the SMP can be reviewed; and this issue is discussed in section 7.5.

In order to finalize the discussions of this section, the establishment of inspection intervals from MSD analysis needs some considerations., If the Monte Carlo simulations are considered solely from Figure 7.3.1, it can be seen that the smallest time

for crack propagation is 24,206 cycles. If the 99.97 % confidence region is considered, for example, the same value is 19,323 cycles. If the smallest time for crack propagation from Monte Carlo simulations (24,206 cycles) is employed to establish the inspection intervals instead of the one from the 99.97 % confidence region, then different answers are obtained; and the reason for this difference is explained as follows.

The main reason for MSD assessment models existence is the establishment of the Inspection Starting Point (ISP) and the Structural Modification Point (SMP), used to define the monitoring period [3]. The ISP and the SMP are calculated by dividing the mean time to failure by typical factors of 3 and 2 respectively [3]. For the Monte Carlo simulations from Figure 7.3.1 the ISP and the SMP values are respectively, 76,914 cycles and 115,371 cycles.

Repeat inspection intervals (I_{WFD}) are established based on time from a detectable crack size initiation up to the SMP, divided by a factor (F_{WFD}) which must lead to several opportunities for crack detection [3]. Considering the chosen initial crack size value of 1.0 mm as the detectable crack length, the total Inspection Period (IP) is defined as the number of cycles between the ISP and the SMP [3], i.e., equal to 38,457 cycles (115,371 – 76,914 cycles). From the Monte Carlo simulations from Figure 7.3.1 the smallest time for crack propagation is 24,206 cycles. According to traditional damage tolerance analysis [76], if the smallest time for crack propagation (24,206 cycles) is divided by a typical factor of 3 it will lead to an inspection period of 8,067 cycles. Dividing the IP by 8,067 cycles, a factor $F_{WFD} = 4.8$ is obtained and, consequently, a factor of 5 (or greater) is more likely to be employed. Therefore, the repeat inspection intervals can be defined, at least, as $I_{WFD} = IP/F_{WFD} = 38,457/5 = 7,691$ cycles which can be approximated to $I_{WFD} = 7,600$ cycles. If the previous calculation is repeated but considering the smallest time for crack propagation from the 99.97 % confidence region from Figure 7.3.1 (19,323 cycles), then the I_{WFD} will be equal to 6,400 cycles, which is 1,200 cycles smaller than the 7,600 cycles obtained by considering so lonely the Monte Carlo simulations from Figure 7.3.1.

As it can be seen from the previous calculations, if a limited number of simulations is employed, a bigger inspection interval is obtained compared to the one from the confidence region, and this fact can lead to fatigue cracks missing during the inspection period. Therefore, the establishment of repeat inspection periods obtained from MSD models that perform a limited number of simulations should be faced with care; and to overcome this limitation, the use of confidence regions is recommended.

7.4. Parametric Study

In section 6.3, the MSD assessment model (presented in chapter 4) was used to investigate variables that might influence MSD assessment via a parametric study. These variables were the standard deviation for fatigue crack initiation, uniform and non-uniform hole pin-loadings, nominal stress level and high rivet squeeze force.

From the literature review regarding the MSD methodologies presented in chapter 2, workers have concentrated in proposing their own MSD models and comparing its output to experimental work for validation. One fact that amazes the author is the almost complete lack of information when it comes to employ the proposed MSD methodologies to perform a parametric study for investigation of variables influencing MSD. The only exception found by the author belongs to Horst [18, 30, 33-35] who, among other variables not analysed in this work, has also investigated the influence of standard deviation for fatigue crack initiation on MSD behaviour; but all the other variables analysed in this work have no comparison basis to any other probabilistic MSD assessments. Therefore, the reader shall not be surprised with the reduced comparison of the parametric study results from this work to other workers from the literature, this might be expected.

7.5. Effect of Change in Standard Deviation on MSD Assessment

In order to evaluate the effect of scatter (standard deviation) on MSD behaviour, the scatter value for the initiation of fatigue cracks was changed, and the effect of such a

change on MSD parameters was presented in Table 6.4.2 for the case of non-uniform pin-loading.

Scatter in crack initiation has been reported as one of the major factors to control the MSD phenomenon [16]. Rather than being a purely theoretical situation, different scatter values for approximately the same mean value of fatigue life for crack initiation is feasible to happen. For example, for the lap joint configuration from Figure 6.2.1.1, the values of mean cycles to crack initiation μ and corresponding standard deviation σ come from equations 6.2.1.1 and 6.2.1.2 [31] and they vary from $5.51 \leq \mu \leq 5.68$ and $0.20 \leq \sigma \leq 0.21$ (Figure 6.2.1.7). From Liao [47], for $5.51 \leq \mu \leq 5.68$ the scatter values recommended are $0.09 \leq \sigma \leq 0.15$. Hoggard [120] recommends the value of $\sigma = 0.20$ for general design of aluminium structures. From Nesterenko [121] the typical values of scatter for zero-to-tension loads in aluminium alloys are $\sigma \leq 0.15$. The results from the fatigue tests presented in Figure 6.1.5 indicate that σ is approximately 0.10 for $5.51 \leq \mu \leq 5.68$ for the lap joint configuration from Figure 6.2.1.1.

The explanation for this great variability in σ values is not the aim of this work, but it is possible that the manufacturing process quality makes a significant contribution [30]. While hand-riveted samples may exhibit large scatter values for initiation of fatigue cracks, because of non-homogeneity of hole filling, the opposite situation can possibly be related to samples manufactured under tight control where holes are reamed to the desired diameter value; which gives a much proper expansion of the hole due to better rivet interference fit. The effect of proper hole interference fit and its improvement to the mean fatigue life is reported by Swift [100]; although manufacturing process is not the only one variable that could influence scatter values, and a deep scientific study of scatter as a research target has been acknowledged [113].

From the point of view of aeronautical safety regulators, a main concern would be how different scatter values adopted for MSD assessment can change the establishment of the ISP and the SMP. Observing Table 6.4.2, it can be seen that when the scatter was varied from 0.21 to 0.09 the mean time to crack initiation of the lead crack ($\overline{TTCI}$) is

increased by 46.1 % and the mean time for crack propagation of the lead crack ($\overline{TCP}$) is decreased by 4.3 %; leading both the ISP and the SMP to increase by 34.2 %. As it can be seen, the establishment of the ISP and the SMP points are quite sensitive to changes in scatter. Horst [35] reached the same conclusion by using theoretical examples.

The variation of the ISP and SMP values is a good reason for the regulators concern, since both scatter values from Table 6.4.2 (0.21 and 0.09) could be justified by data from the literature [31] or by in-house fatigue tests (Figure 6.1.5) for the same geometrical configuration under the same loading conditions analysed (Figure 6.2.1.1).

Figure 7.5.1 presents the simulation points from Figures 6.2.1.9 and 6.3.1.1 (results presented in Table 6.4.2) and the corresponding theoretical cumulative probability distributions of failure (c.p.d. Fig. 6.2.1.9 and c.p.d. Fig. 6.3.1.1, respectively). In section 7.3, it was shown that the SMP point (Figure 7.3.5) had an unacceptable probability of failure, according to the USAF criterion [75], when established with the coefficient 2. From Table 6.4.2, for the case of the standard deviation equal to 0.09, the ISP and the SMP are, respectively, 103,249 and 154,874 cycles. From Figure 7.5.1 it can be seen that the cumulative probability of failure for the SMP from Figure 6.3.1.1 is smaller than 1E-3; demonstrating that this point is conservatively established according to the USAF criterion [75]. On the other hand, the USAF criterion [75] shows that there would be no safety risk for structural functioning until 203,000 cycles (1E-3 cumulative failure probability); which is in conflict to the point of SMP (154,874 cycles) established according to recommendations from the AAWG [3]!

The results from Figure 7.5.1 show that when the large standard deviation value is considered for fatigue crack initiation, the SMP point (given by the AAWG recommendations [3]) is non-conservatively established according to the USAF criterion [75]; and when the small standard deviation value is considered for fatigue crack initiation, the limit to proper structural functioning (given by the USAF criterion [75]) is non-conservatively established according to the AAWG recommendations [3]. The literature review presented in chapter 2 brings no similar example where, via a

possible situation (Figure 7.5.1), these two safety criteria would diverge from each other.

Despite the merits from both safety criteria [3, 75], what seems clear to the author is that there is a conflict between them both and, therefore, a third criterion is proposed in Figure 7.5.2 to overcome this issue.

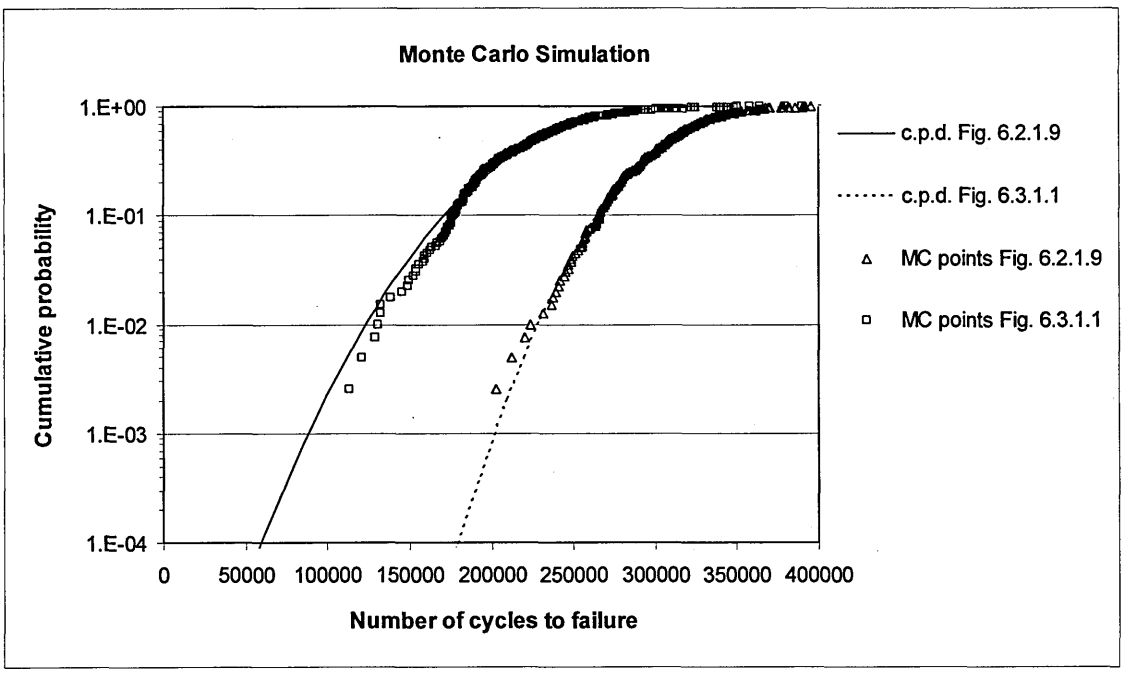

Figure 7.5.1: Cumulative probability of failure distributions from Figures 6.2.1.9 [standard deviation for TTCI (log) = 0.21] and 6.3.1.1 [standard deviation for TTCI (log) = 0.09] with non- uniform pin-loading at 100 MPa (R = 0.1) cyclic tensile stress.

From Figure 7.5.2 it can be seen that the SMP and the limit to proper structural functioning (LPSF) are both established from the cumulative probability of failure distribution from MSD analysis. While the SMP is derived from the mean MSD failure behaviour divided by the recommended coefficient 2 [3], the LPSF is derived from the 1E-3 cumulative probability of failure [75]. The proposed structural safety criterion from this work is presented in the shaded boxes. The basic idea is to compare both the SMP and the LPSF in such a way that: if the SMP $\leq$ LPSF then the SMP and the ISP are established according to the AAWG recommendations [3]. If the SMP > LPSF then

the SMP is assumed as the LPSF and the ISP is established based on 2/3 of the LPSF value.

In fact, the proposed structural safety criterion from Figure 7.5.2 is simply establishing a lower boundary for the SMP, based on the AAWG recommendations [3] and USAF criterion [75] for structural safety; and, when SMP > LPSF, it defines the SMP equal to the LPSF (based on a cumulative probability of failure equal to 1E-3) instead of deriving it from the mean MSD failure behaviour.

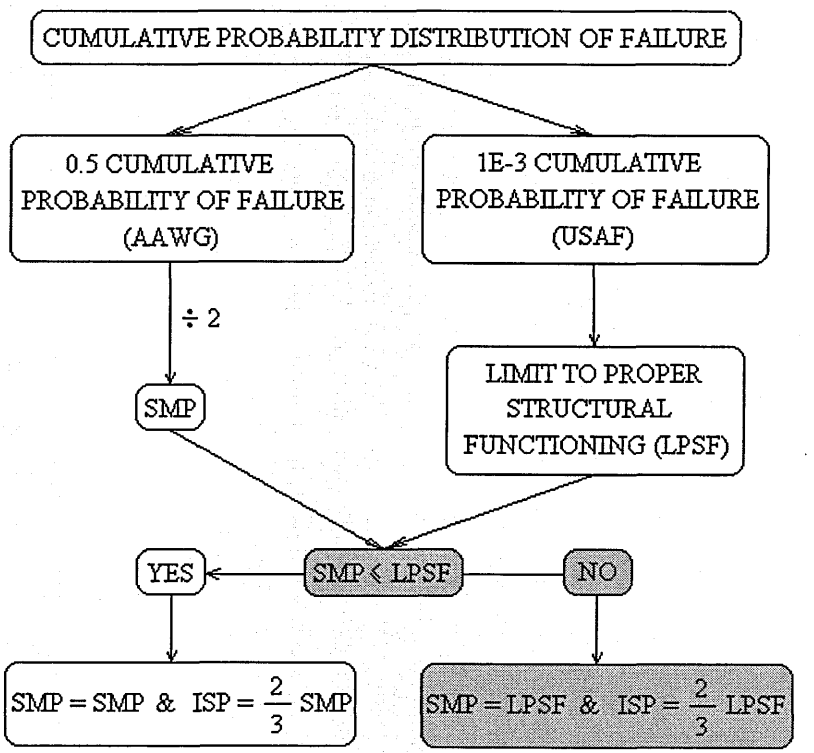

Figure 7.5.2: Proposed structural safety criterion.

When it comes to comparing the simulation results from Figures 6.2.1.9 and 6.3.1.1, not only differences in the ISP and the SMP occur. From Table 6.4.2 it can be seen that these differences come from the fact that $\overline{N_f}$ is changed due to changes in the $\overline{TTCI}$ and $\overline{TCP}$. The changes in $\overline{TTCI}$ can be explained from equation 4.1.1, which is repeated as equation 7.5.1.

$$\log(N_0) = \mu + \alpha.\sigma \qquad 7.5.1$$

From equation 7.5.1, it can be seen that changes in N_0 can occur due to changes in μ, α or σ. Table 7.5.1 presents an example where it can be observed how N_0 changes by changing σ for some values of α. The 'FCL' column presents 4 hypothetical fatigue critical locations, the 'Differences' column represents the differences of lives (cycles) from FCL2 – FCL1 and FCL4 – FCL3 (given by column N_0). In this example, only negative values of α are considered due to the fact that a FCL is assigned to the smallest fatigue life; and α is likely to be negative, as it can be observed from Figure 6.2.1.7 where α is presented in the column Ran #.

Table 7.5.1: Changes in N_0 due to changes in σ.

FCL	μ log (cycles)	σ log (cycles)	α	$Log\ (N_0)$	N_0 (cycles)	Differences (cycles)
1	5.00	0.20	-1.0	4.80	62,318	16,115
2	5.00	0.20	-0.5	4.90	78,433	
3	5.00	0.10	-1.0	4.90	78,433	9,559
4	5.00	0.10	-0.5	4.95	87,992	

From Table 7.5.1 it can be seen that, for the same α values, when σ is decreased the corresponding N_0 lives increase. This result explains why the $\overline{TTCI}$ increases in Figure 6.3.1.1 compared to Figure 6.2.1.9 (see Table 6.4.2), since the same Gaussian random numbers (α values) have been used for both analyses. It can also be noted that when σ is decreased the differences in lives (cycles) between FCLs '4 and 3' and '2 and 1' decrease. This result shows that fatigue cracks are allowed to nucleate closer in time (cycles) from different FCLs, leading to a possible increase in the number of MSD-like scenarios; and, in fact, this is what column 'MSD-like scenarios' from Table 6.4.2 is demonstrating (as well as Figures 6.2.1.14 and 6.3.1.4). As the MSD-like scenarios increase with decreasing σ values, crack interaction effects tend to augment and it is expected that $\overline{TCP}$ is reduced, as actually can be seen from Table 6.4.2. An increase in crack interaction effects has been verified from Garcia [122] when the number of cracks per damage scenario increases. What can also be noted from Table 6.4.2 is that the dominant part of the whole failure process belongs to $\overline{TTCI}$, and as the $\overline{TTCI}$ is

considerably increased compared to the reduction in the $\overline{TCP}$, the final result is that $\overline{N_f}$ increases leading the ISP and the SMP to increase when σ decreases.

The same trends regarding changes on the $\overline{TTCI}$, the $\overline{TCP}$ and the number of MSD-like scenarios, as a result of changes in σ from Table 6.4.2, have also been reported by Horst [30, 33], though Horst did not quantify the number (or percentage) of MSD-like scenarios from his simulations. The agreement to Horst results [30, 33] applies not only for Table 6.4.2 but to any other result from this work, which is presented in sections to come, regarding changes in scatter values.

Concerning the results from sections 6.2.1 and 6.3.1 (resumed in Table 6.4.2), the lead crack nucleation differences from Figures 6.2.1.13 and 6.3.1.3 can be explained with the help of, respectively, Figures 7.5.3 and 7.5.4; where 'Stdeva' in the legend means standard deviation. In these figures, FCLs 1 and 3 are used as an example for having, respectively, the smallest and the biggest loads (Figure 6.2.1.7).

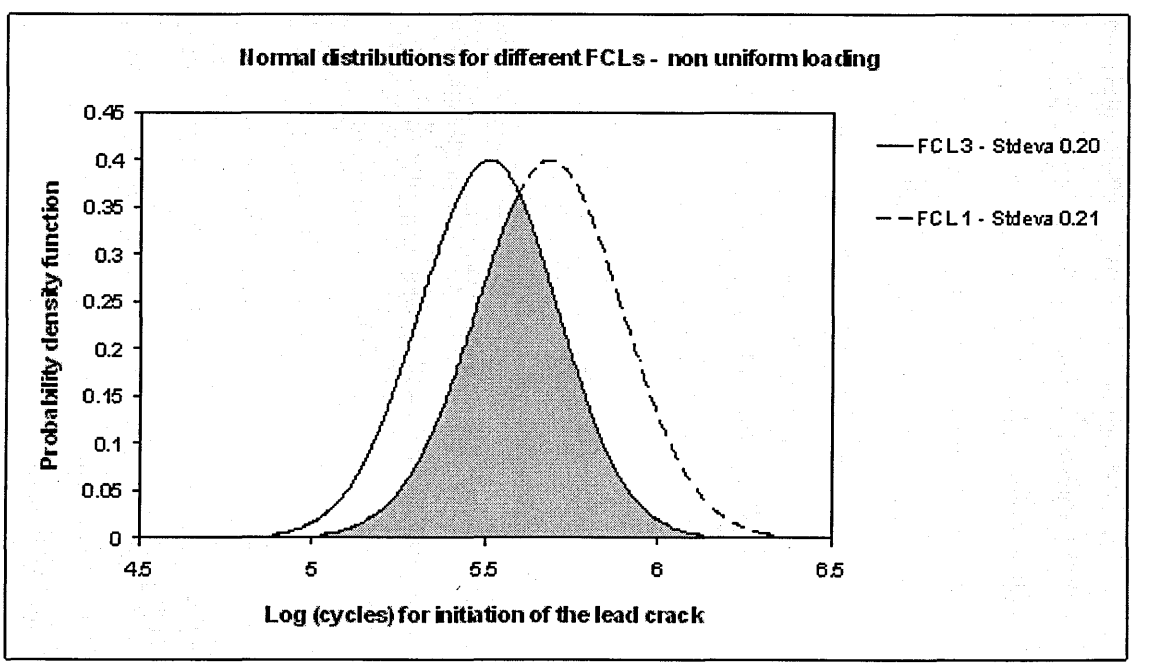

Figure 7.5.3: FCLs 1 and 3 (Figure 6.2.1.7) normal distributions for fatigue crack initiation lives.

The non-uniformity of pin-loading from Figure 6.2.1.3 causes the crack nucleation of the lead crack to be forced into hole positions 2 and 8 (Figure 6.2.1.1 - which contains the FCLs with the highest loads such as FCL 3); as it can be seen from Figures 6.2.1.13 and 6.3.1.3. The reason for this crack nucleation behaviour is that different fatigue life distributions are assigned to each FCL due to differences in pin-loading.

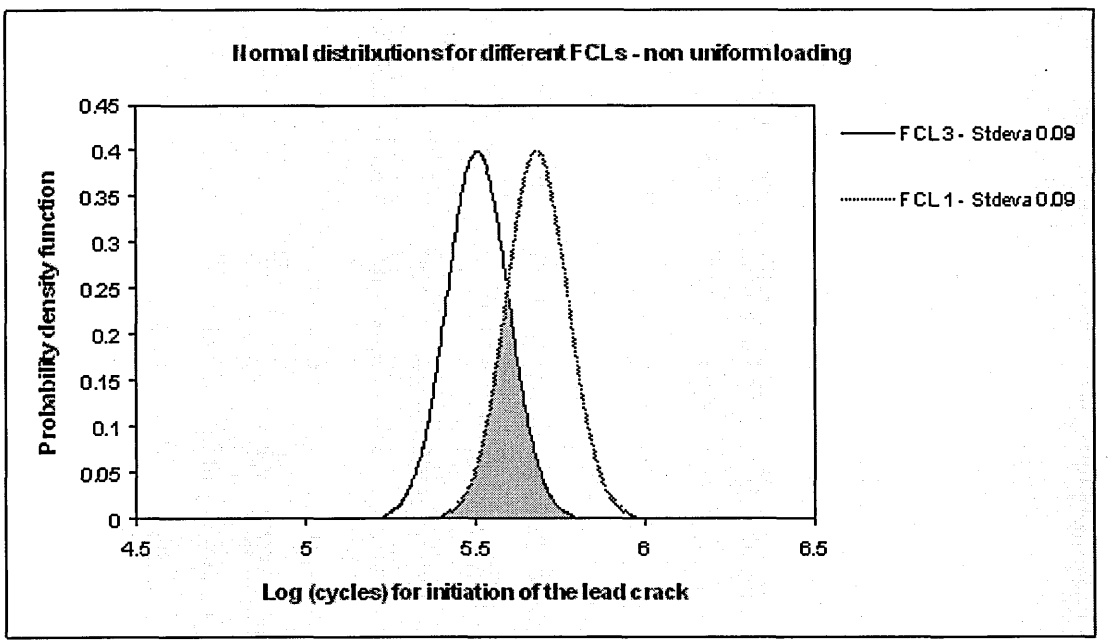

Figure 7.5.4: FCLs 1 and 3 (Figure 6.2.1.7, but with 'Stdeva' equal to 0.09) normal distributions for fatigue crack initiation lives.

From Figures 7.5.3 and 7.5.4, it can be seen that the lead crack will clearly tend to nucleate from FCL 3, instead of FCL 1, because the fatigue crack initiation distributions are situated in a region of smaller lives. The shaded areas indicate a common fatigue crack initiation life region (overlap region) where both FCLs 1 and 3 can have the lead crack nucleation. As the standard deviation decreases to 0.09 (from Figure 7.5.3 to 7.5.4), the corresponding overlap region diminishes and, therefore, it is expected that the lead crack nucleation be exacerbated in FCL 3. This exacerbated tendency can be verified from Figure 6.3.1.3, compared to Figure 6.2.1.13, where the lead crack nucleation takes place mostly at holes with the highest pin-loadings (see Figure 6.2.1.3). In Figure 6.2.1.13, although the lead crack nucleation tendency is clear, crack nucleation pattern is not as exacerbated as in Figure 6.3.1.3. It is easy to verify, with the

help of Figures 7.5.3 and 7.5.4, that if the standard deviation keeps on decreasing, for example if it tends to zero, then the normal distributions will become more and more narrower and they will tend to a vertical line passing through the corresponding means; and in this case the fatigue crack initiation life of the lead crack will be the deterministic one and crack nucleation will always start from the highest FCLs such as FCL 3, in the case of this example.

7.6. Effect of Change in Pin-Loading on MSD Assessment

In section 6.3.2, the uniform pin-loading adopted in this work for MSD assessment of the lap joint from Figure 6.2.1.1 is presented in Figure 6.3.2.2; and the load is a mean value from the non-uniform pin-loading distribution from Figure 6.2.1.3. The main purpose of this section is to discuss what changes in the establishment of MSD parameters, mainly the ISP and the SMP, when different pin-loadings are employed and how these changes can possibly affect airworthiness.

From the analyst point of view, uniform pin-loading is a simplifying assumption used to represent a nearly quadratic stress distribution in the centre of a fuselage bay (Figure 6.3.2.1) because it avoids the need for assigning different fatigue crack initiation life distributions for each FCL. The results from section 6.3.2 are resumed in Table 6.4.3 and Table 6.4.4 (where the corresponding non-uniform pin-loading cases are presented for comparison purposes).

From Table 6.4.3 it can be noted that the biggest differences occur when the standard deviation values are smaller. Starting from $\overline{TTCI}$ and MSD-like scenarios columns, it can be seen that for decreasing values of standard deviation both $\overline{TTCI}$ and MSD-like scenarios increase for the U pin-loads can be observed. The explanation for this behaviour is the same as for the NU pin-loads from section 7.5.

When $\overline{TTCI}$ (Table 6.4.4) from NU and U pin-loads are compared, it can be seen that U pin-loads show bigger values. Figure 7.6.1 presents the same distributions as in Figure 7.5.4 but added by the normal distribution for fatigue crack initiation for the U pin-

loading case (All FCL – U pin-load – Stdeva 0.09). As it can be seen from Figure 7.6.1, fatigue crack initiation of the lead crack will tend to nucleate first in the case of NU pin-loading because one of the distributions is situated in a region of smaller lives; and this fact is confirmed from the results presented in Table 6.4.4. The U pin-loading fatigue crack initiation distribution is enclosed by the two extreme distributions from the NU pin-loads (representing the highest and smallest pin-loads); and this is expected since mean values of pin-loads are employed for the U pin-loading distribution (Figure 6.3.2.2).

When MSD-like scenarios (Table 6.4.4) from NU and U pin-loads are compared, it can be seen that U pin-loads show bigger percentage values. As the U pin-loading employs only one fatigue crack initiation distribution to all FCLs, cracks tend to nucleate closer in time when compared to the NU pin-loads case (where more than one fatigue crack initiation distribution is employed), and without any crack nucleation positioning tendency, as verified from Figures 6.3.2.5 and 6.3.2.9.

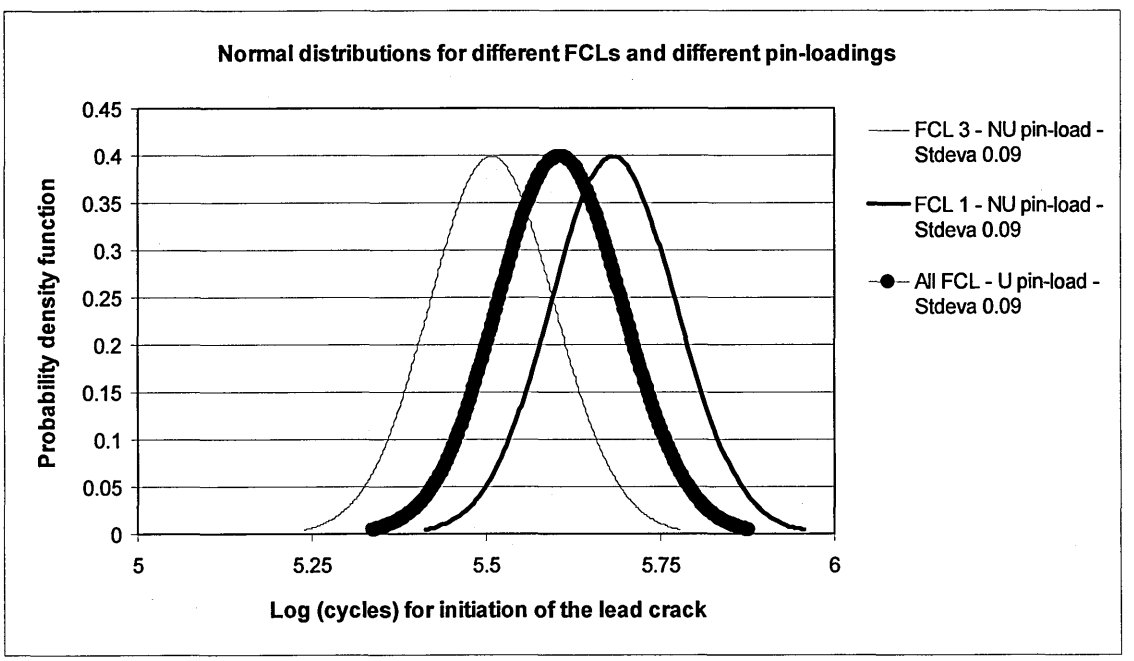

Figure 7.6.1: Normal distributions for fatigue crack initiation lives for different pin-loading conditions.

Regarding the $\overline{TCP}$ parameter for the U pin-loading results (Table 6.4.3), it can be seen that the mean time for crack propagation of the lead crack decreases with increasing percentages of MSD-like scenarios; for the same reasons as presented in section 7.5 for the case of NU pin-loading. When comparing the $\overline{TCP}$ from U and NU pin-loads (Table 6.4.4), it can be seen that $\overline{TCP}$ values are within ± 0.5 % difference. What is curious from these results is that an increase in the percentage of MSD-like scenarios seems not to be the only reason for decreasing the $\overline{TCP}$, and other reasons may exist. As it can be seen from Table 6.4.4, all U pin-loading cases present a bigger percentage of MSD-like scenarios compared to the corresponding NU pin-loading ones; although it is not necessarily leading to smaller $\overline{TCP}$ values. In order to provide a possible explanation for these results, a separate discussion is presented in section 7.8.

From Table 6.4.3 it can be noted that the $\overline{N_f}$, and, consequently, the ISP and the SMP, increase with decreasing standard deviation values. This result is explained by the increase on $\overline{TTCI}$ values, which dominate the whole failure process, despite of the decrease on $\overline{TCP}$ values. Comparing the values of the ISP and the SMP (Table 6.4.4) for the U and NU pin-loadings, it can be seen that for the larger standard deviation the U pin-loading distribution gave ISP and SMP values 0.9 % bigger than the NU pin-loading ones; while for the smaller standard deviation these values were 5.9 % bigger. These differences seem not so large, but it has to be noted that the ISP and the SMP are established according to the recommendations from the AAWG [3] based so lonely on a single point of the cumulative failure distribution: the 50 % one.

Figure 7.6.2 presents the simulation points from Figures 6.3.2.3 and 6.3.2.7 (U pin-loading cases – Table 6.4.3) demonstrating a reasonable fit to the corresponding theoretical cumulative probability distributions.

Figure 7.6.3 presents the cumulative probability distributions for the pin-loading models from Table 6.4.4. In the legend, 'c.p.d.' means cumulative probability distribution; 'U. load and N.U. load' mean, respectively, U and NU pin-loading distributions; and '0.21 and 0.09' mean 0.21 and 0.09 standard deviation values in log (cycles).

From Figure 7.6.3, it can be seen that the differences between the cumulative failure distributions for the U and NU pin-loading cases (Table 6.4.4) tend to distance from each other as the cumulative probabilities of failure decrease. Considering the case of the smaller standard deviation (0.09), for the 1E-3 cumulative probability of failure (USAF structural safety criterion [75]), the U and NU pin-loading distributions indicate that the limit for proper structural functioning (LPSF) would be, respectively, 241,000 and 203,000 cycles; and the U pin-loading number of cycles for the LPSF is 18.7 % bigger than the one for the NU pin-loading case. If the safety structural criterion recommended by the AAWG [3] is considered for the standard deviation value of 0.09, then differences in the SMP are of 5.9 % (Table 6.4.4).

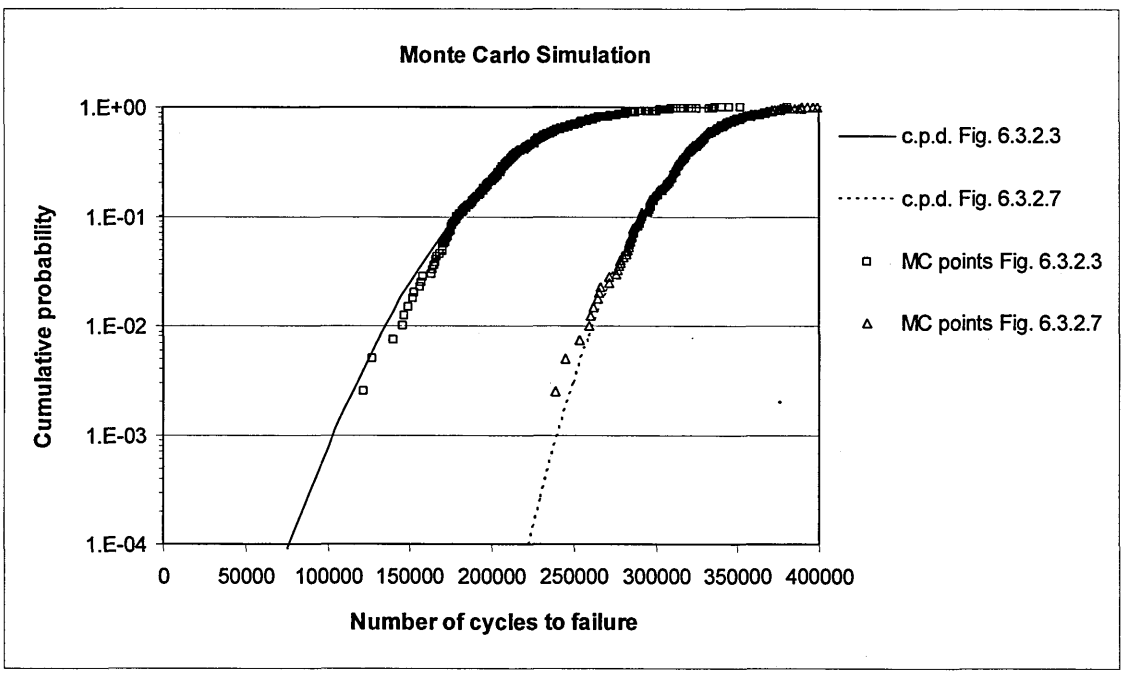

Figure 7.6.2: Cumulative probability of failure distributions from Figures 6.3.2.3 [standard deviation for TTCI (log) = 0.21] and 6.3.2.7 [standard deviation for TTCI (log) = 0.09] with uniform pin-loading at 100 MPa (R = 0.1) cyclic tensile stress.

From the previous paragraph, it can be realized that the U pin-loading distribution, when implemented with mean pin-loading values (Figure 6.3.2.2) from NU pin-loading distributions (Figure 6.2.1.3), results to non-conservatism for establishing structural safety parameters such as the SMP and, more noticeably, the LPSF which is based on

low cumulative probabilities of failure. Therefore, if uniform pin-loading is used for MSD assessment it is recommended that the biggest pin-load be assumed, which will lead to conservative establishment of the SMP and LPSF, instead of assuming mean pin-loading ones, as in Figure 6.3.2.2.

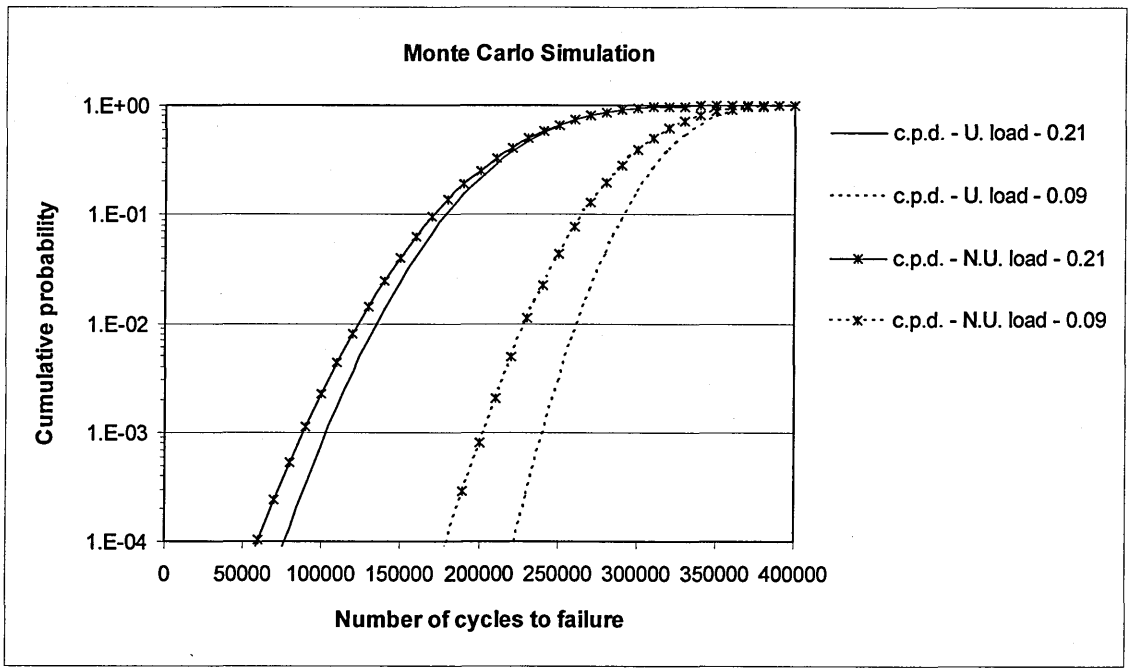

Figure 7.6.3: Cumulative probability of failure distributions from Figures 6.2.1.9, 6.3.1.1, 6.3.2.3 and 6.3.2.7 at 100 MPa (R = 0.1) cyclic tensile stress.

7.7. Effect of Change in Stress Level on MSD Assessment

From Table 6.4.5 it can be seen the effect that an increase of 20 % in nominal stress value causes on the MSD parameters presented. It can be noted that when the stress level is increased from 100 to 120 MPa the $\overline{TTCI}$ is decreased by 79.2 %. This difference is considerable, and the first issue that has to be verified is whether it is reasonable or not.

The mean fatigue crack initiation life (μ) for each FCL from the lap joint configuration analysed (Figure 6.2.1.1) was established according to equation 6.2.1.1 [31]; and μ is derived as function of the local elastic stress 'S'. As presented in section 6.3.3, the value

of S determined by the DTD code [87] was 508.4 MPa corresponding to a nominal stress of 120 MPa. If this value is inserted in equation 6.2.1.1 then μ is assigned a value of 4.9236 in log (cycles), which is equivalent to 82,809 cycles (50 % S-N fatigue life for crack initiation). Considering the nominal stress of 100 MPa, the corresponding μ is equivalent to 398,865 cycles. Therefore, μ is decreased by 78.8 % when the nominal stress level is increased by 20 %; and the physical meaning of this reduction for μ needs to be checked. From Figure 6.3.3.1, derived from the experimental data presented in Figure 6.1.1, when the stress level was increased by 20 % the reductions (calculated in cycles) for μ corresponding to the 10, 16 and 24 KN squeeze forces were, respectively, by 62.6 %, 57.9 % and 72.3 %; performing a mean reduction of 64.3 %. These values demonstrate that a reduction (cycles) in μ by 78.8 %, calculated via equation 6.2.1.1 and the local stress S obtained from the DTD code [87], is reasonable; and μ, corresponding to the nominal stress of 120 MPa, can be considered as a valid input data for the MSD assessment analysis presented in section 6.3.3. As presented in section 6.3.3, the standard deviation for fatigue crack initiation was assumed as 0.05 in log (cycles), based on the data from Figure 6.3.3.1.

The changes in $\overline{TTCI}$ (Table 6.4.5) can be explained with the help of equation 7.5.1. From equation 7.5.1, it can be seen that changes in N_0 can occur due to changes in μ, α or σ. Table 7.7.1 presents an example where it can be observed how N_0 changes by changing μ for some values of α. The 'FCL' column presents 4 hypothetical fatigue critical locations, the 'Differences' column represents the differences of lives (cycles) from FCL2 – FCL1 and FCL4 – FCL3 (given by column N_0).

Table 7.7.1: Changes in N_0 due to changes in μ.

FCL	μ log (cycles)	σ log (cycles)	α	$Log\ (N_0)$	N_0 (cycles)	Differences (cycles)
1	5.6071	0.05	-1.0	5.5571	355,518	21,042
2	5.6071	0.05	-0.5	5.5821	376,559	
3	4.9236	0.05	-1.0	4.8736	73,812	4,369
4	4.9236	0.05	-0.5	4.8986	78,181	

From Table 7.7.1 it can be seen that, for the same α values, when μ is decreased the corresponding N_0 lives decrease. This result explains why the $\overline{TTCI}$ decreases in Figure 6.3.3.5 compared to Figure 6.3.3.2 (see Table 6.4.5), since the same Gaussian random numbers (α values) have been used for both analyses. It can also be noted that when μ is decreased the differences in lives (cycles) between FCLs '4 and 3' and '2 and 1' decrease. This result shows that fatigue cracks are allowed to nucleate closer in time (cycles) from different FCLs, leading to a possible increase in the number of MSD-like scenarios; and, in fact, this is what column 'MSD-like scenarios' from Table 6.4.5 is demonstrating (as well as Figures 6.3.3.4 and 6.3.3.7). As the MSD-like scenarios increase with decreasing μ values, crack interaction effects tend to augment and it is expected that $\overline{TCP}$ is reduced, as verified by Garcia [122]. What can also be noted from Table 6.4.5 is that both the $\overline{TTCI}$ and $\overline{TCP}$ are decreased; and the final result is that the $\overline{N_f}$, the ISP and the SMP decrease when μ decreases.

Figure 7.7.1 presents a comparison of the cumulative probabilities of failure obtained from Figures 6.3.2.3 (100 MPa nominal stress and 0.21 standard deviation for fatigue crack initiation), 6.3.3.2 (100 MPa nominal stress and 0.05 standard deviation for fatigue crack initiation) and 6.3.3.5 (120 MPa nominal stress and 0.05 standard deviation for fatigue crack initiation). In the legend, 'Normal distributions' refer to the corresponding theoretical normal distributions, 'MC points' refer to Monte Carlo simulation points, 100 and 120 MPa refer to nominal stress levels, and 0.05 and 0.21 refer to the standard deviation for initiation of fatigue cracks.

An interesting outcome from Figure 7.7.1 is regarded to the cumulative failure distribution inclinations. A decrease in inclination is related to a more severe MSD condition. Small inclinations lead to a decrease in the range of number of cycles to failure; and once MSD starts, the probabilities of failure increase much faster in time (cycles) than for the case of large cumulative distribution inclinations. The increase in MSD severity can also be verified by the increase in MSD-like scenarios from Tables 6.4.3 and 6.4.5, for the corresponding distributions plotted in Figure 7.7.1.

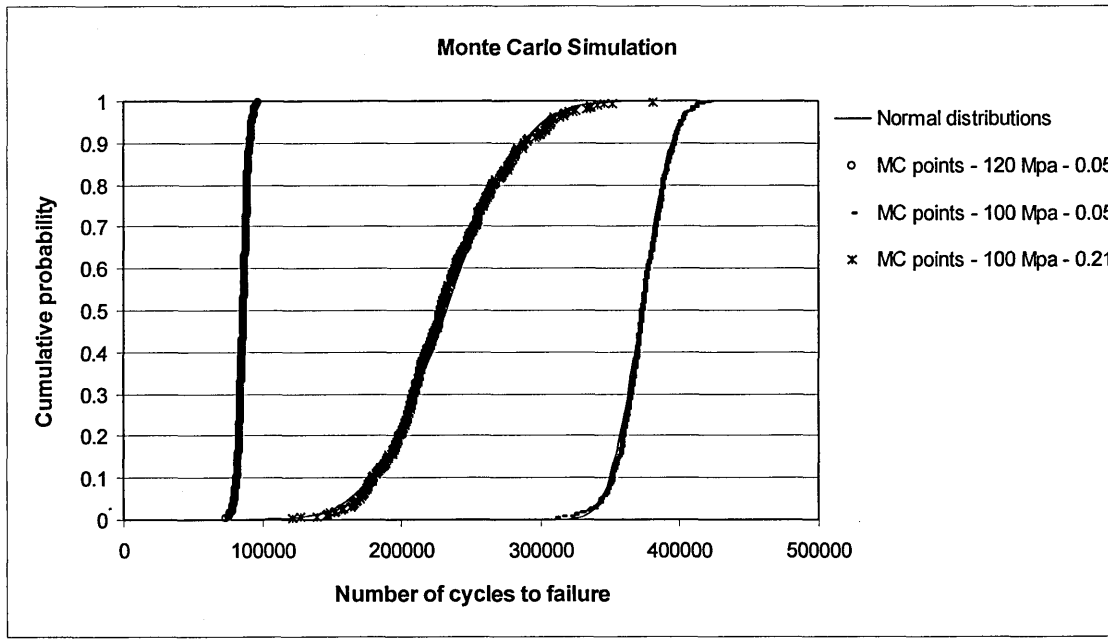

Figure 7.7.1: Comparison of cumulative probabilities of failure for different nominal stress levels and standard deviation values.

From Figure 7.7.1, if the failure distribution 'MC points – 100 MPa – 0.21' is compared to the 'MC points – 100 MPa – 0.05', when the standard deviation is decreased by 76.2 % (from 0.21 to 0.05) the MSD behaviour becomes more severe; although the mean failure process is increased by 59.9 % (from 232,870 to 372,390 cycles). Comparing the 'MC points – 100 MPa – 0.21' to the 'MC points – 120 MPa – 0.05', when the stress level is increased by 20 % (from 100 to 120 MPa), the MSD behaviour becomes even more severe and the mean failure process is anticipated by 62.7 % (from 232,870 to 86,875 cycles). Comparing the distributions 'MC points – 120 MPa – 0.05' to 'MC points – 100 MPa – 0.05', it can be seen that when the stress level is increased by 20 % (from 100 to 120 MPa), the MSD behaviour becomes more severe and the mean failure process is anticipated by 76.7 % (from 232,870 to 86,875 cycles).

What can be realized from the previous paragraph is that MSD-like behaviour is aggravated to an increase in nominal stress level (decrease in mean time to fatigue crack initiation) and to a decrease in standard deviation value for fatigue crack initiation; being more sensitive to changes in stress level than in standard deviation values. Mean time to crack initiation has been reported [5] to be the most important parameter that

can be randomly varied for MSD assessment, but no analysis, as the one from Figure 7.7.1, was shown to support this statement.

Figure 7.7.2 shows the Monte Carlo simulation points from Figures 6.3.3.2 and 6.3.3.5 ('MC points – 100 MPa' and 'MC points – 120 MPa', respectively), a 99 % confidence region for Figure 6.3.3.5 ('99 % confidence – 120 MPa') and a single point ('Determ. MSD – 120 MPa') plotted for the deterministic analysis of MSD. The 'Determ. MSD – 120 MPa' crack initiation life is determined from the 50 % S-N data (82,809 cycles), where σ = 0 from equation 7.5.1 and, therefore, all FCLs initiate a 1.0 mm fatigue crack simultaneously. The crack propagation phase performed for simultaneous equal sized crack growth from all FCLs, calculated by means of the DTD code [87], gives a number of cycles equal to 7,653.

From Figure 7.7.2, the 'MC points – 100 MPa' and the 'MC points – 120 MPa' are plotted together in order to visualize the big difference between those results due to an increase of 20 % in nominal stress level. As it can be seen, the MC points from both analyses do not overlap, as can also be noted from Figure 7.7.1. The results related to the simulations from 'MC points – 120 MPa' (Figure 7.7.2) presented in Figure 6.3.3.7 show, for the first time since the beginning of this chapter, that no mono-crack scenarios are present; and situations where all holes were cracked are encountered from the corresponding simulations. At this point two issues have to be discussed, the first is related to the mono-crack scenarios and the second is related to whether or not the simulations from 'MC points – 120 MPa' can predict the deterministic MSD failure, i.e., simultaneous fatigue crack initiation and propagation from all FCLs.

Considering the results for the 'MSD-like scenarios' columns from Tables 6.4.2 to 6.4.5, it has been shown that the number of mono-crack scenarios decrease (MSD-like scenarios increase) with a decrease in standard deviation for fatigue crack initiation, with change from NU to U pin-loading and with a decrease in the nominal stress value. From these results, and as the fatigue crack initiation lives for each FCL is assigned from equation 7.5.1, it can be realized that there is a limitation from the MSD model from this work; since mono-crack scenarios are not representative of MSD-like

situations. The occurrence of mono-crack scenarios is intrinsic to random fatigue crack initiation modelling from equation 7.5.1; and mono-crack scenarios are feasible to occur given the values of μ and σ employed in this equation. Unfortunately, almost no information about number of cracks per damage scenario can be found in the literature for the MSD models reported in chapter 2, apart from Santgerma [31] and Garcia [117]. In the case of Santgerma and Garcia for the lap joint configuration analysed (Figure 6.2.1.1), it has been reported, respectively, almost 60 % and 40.4 % (100 % – 59.6 %, Table 6.4.2 for 0.21 standard deviation) occurrence of mono-crack scenarios indicating that this work is not the only one that has a limitation regarding the occurrence of mono-crack scenarios.

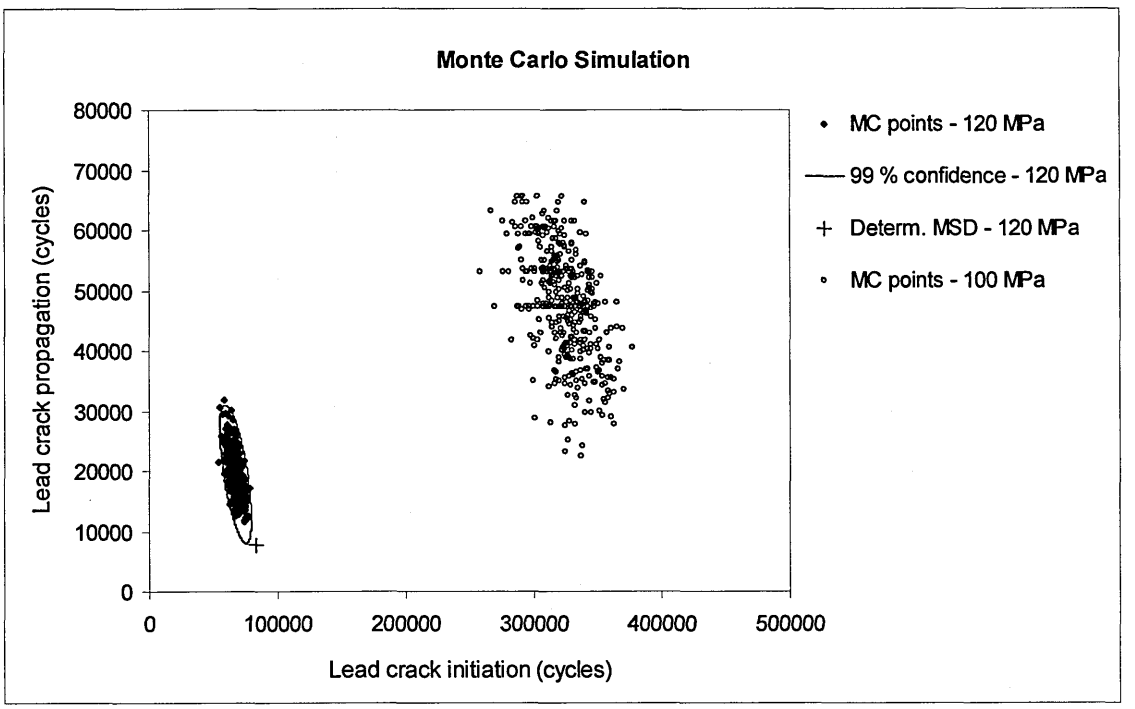

Figure 7.7.2: Monte Carlo simulation points from Figures 6.3.3.2 [100 MPa (R = 0.1) cyclic tensile stress] and 6.3.3.5 [120 MPa (R = 0.1) cyclic tensile stress] and the deterministic MSD case [120 MPa (R = 0.1) cyclic tensile stress] with standard deviation for TTCI (log) = 0.05 and uniform pin-loading

Regarding the deterministic MSD ('Determ. MSD – 120 MPa' from Figure 7.7.2), it has to be established how close the MSD assessment results, for the 120 MPa stress level, can predict it or not. From Figure 7.7.2, the time to crack initiation from the 'Determ.

MSD – 120 MPa' (82,809 cycles) is bigger than the ones from the '99 % confidence – 120 MPa'. The smallest time for crack propagation from the '99 % confidence – 120 MPa' is equal to 8,026 cycles; which is only 4.9 % bigger than the case of 'Determ. MSD – 120 MPa' (7,653 cycles)! The number of cycles to failure from the 'Determ. MSD – 120 MPa' is equal to 90,462 cycles; which is bigger than the mean failure behaviour $\overline{N_f}$ (86,875 cycles – Table 6.4.5) obtained from the simulations ('MC points – 120 MPa). From Table 6.4.5 (120 MPa stress level), it can also be seen that the ISP and the SMP are, respectively, equal to 28,958 and 43,438 cycles; demonstrating that these points are established before the 'Determ. MSD -120 MPa' and, therefore, the simulations demonstrate its effectiveness to prevent the deterministic MSD occurrence.

The results from the previous paragraph show that the failure behaviour from the deterministic MSD (simultaneous fatigue crack initiation and propagation from all FCLs) is very close to the mean failure value from the simulations and that it can be safely prevented. At this point, it is interesting to check if other simulations (which contained mono-crack scenarios – Tables 6.4.2 to 6.4.5) can also predict the failure life from the corresponding deterministic MSD; and these results are presented in Table 7.7.2.

Table 7.7.2: Deterministic MSD failure lives comparison to MSD simulations.

MSD simulation from Figure #	$\overline{N_f}$ (cycles)	ISP (cycles)	SMP (cycles)	Deterministic MSD failure (cycles)
6.2.1.9	230,741	76,914	115,371	344,106
6.3.1.1	309,747	103,249	154,874	344,106
6.3.2.3	232,870	77,623	116,435	410,745
6.3.2.7	328,117	109,372	164,059	410,745
6.3.3.2	372,390	124,130	186,195	410,745

From Table 7.7.2, it can be seen that, with no exception, the deterministic MSD failure behaviour is far from $\overline{N_f}$; and both the ISP and SMP parameters are established before any structural risk can occur. Therefore, even for the MSD simulations where mono-crack scenarios were present, the MSD assessment models demonstrated that

deterministic MSD failure (simultaneous fatigue crack initiation and propagation from all FCLs) can be prevented.

7.8. The Role of Number of Cracks and Crack Nucleation Positioning on MSD Assessment Modelling

From section 7.6, a question was raised when comparing the $\overline{TCP}$ from U (uniform) and NU (non-uniform) pin-loads for the standard deviation equal to 0.09 (Table 6.4.4). From Table 6.4.4, it can be seen that $\overline{TCP}$ values are within ± 0.5 % difference. The U pin-loading cases presents a bigger percentage of MSD-like scenarios, compared to the corresponding NU pin-loading ones, but it is not necessarily leading to a smaller $\overline{TCP}$ value. The curiosity about these results is that an increase in the percentage of MSD-like scenarios seems not to be the only reason for decreasing the $\overline{TCP}$; although this tendency is clear and applies to the majority of the results from Tables 6.4.2 to 6.4.5.

In order to investigate another possible reason for decreasing the $\overline{TCP}$, than increasing the number of MSD-like scenarios, this section is concerned to establish whether the number of nucleated cracks per damage scenario or the crack nucleation sequence plays the most important role in decreasing $\overline{TCP}$. Before starting this investigation, different crack nucleation sequences need to be defined. In this work, two cases are assumed: 'case 1' and 'case 2'. Figure 7.8.1 presents examples of what is defined as 'case 1'.

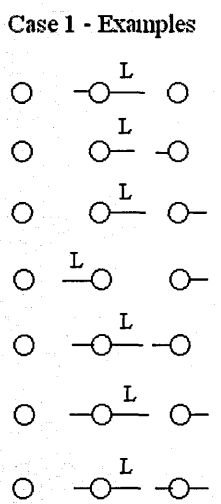

Figure 7.8.1: Crack nucleation sequence for 'case 1' definition examples.

Whenever there is at least a second crack which nucleates at the same hole or at an adjacent hole to where the lead crack (represented by 'L' in Figure 7.7.1) nucleation took place, and before the lead crack links-up for the first time, then these damage scenarios are defined as 'case 1'. All other damage scenarios not defined as 'case 1' are named as 'case 2'.

Starting with the number of nucleated cracks per damage scenarios; Figures 7.8.2, 7.8.3, 7.8.4 and 7.8.5 present the Monte Carlo simulation points from, respectively, Figures 6.3.2.3, 6.3.2.7, 6.3.3.2 and 6.3.3.5 but with the number of nucleated cracks per damage scenarios indicated by the legends.

From Figures 7.8.2 to 7.8.5 it can be realized that the damage scenarios are quite mixed and it is not easy to visualize any possible influence that an increase in the number of cracks per damage scenario might have on the mean time for crack propagation.

It is worthwhile to note from Figures 7.8.2 to 7.8.5 that due to the probabilistic crack propagation modelling, situations where, for example, damage scenarios containing two nucleated cracks can present a bigger time for crack propagation than damage scenarios containing only one nucleated crack is feasible to happen.

Figures 7.8.6, 7.8.7, 7.8.8 and 7.8.9 present the same results from, respectively, Figures 7.8.2, 7.8.3, 7.8.4 and 7.8.5 but plotted as 'case 1' and 'case 2' damage scenarios. From Figures 7.8.6 to 7.8.9, it can be clearly observed that 'case 1' damage scenarios present a mean time for crack propagation smaller than 'case 2' damage scenarios. These results indicate that when cracks nucleate at the same hole or at adjacent holes, before the lead crack links-up for the first time, then the mean time for crack propagation is decreased when compared to damage scenarios where cracks nucleate in holes placed more than one pitch distance from each other. This conclusion coincides with Garcia [122]: 'as close two crack tips are positioned (in the same hole and/or at adjacent holes) as pronounced crack interaction effects will be. As cracks nucleation positioning among cracks increase, the influence that crack tips exert on each other tends to vanish'. And, of course, crack propagation time decreases with an increase in crack interaction [122].

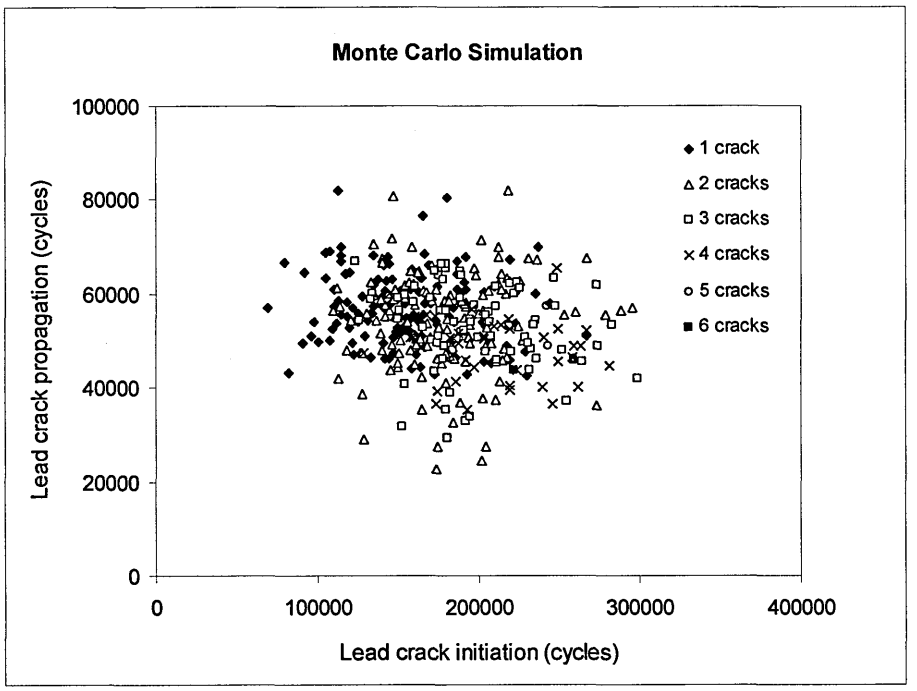

Figure 7.8.2: Number of nucleated cracks per damage scenario from Figure 6.3.2.3 - standard deviation for TTCI (log) = 0.21, uniform pin-loading at 100 MPa (R = 0.1) cyclic tensile stress.

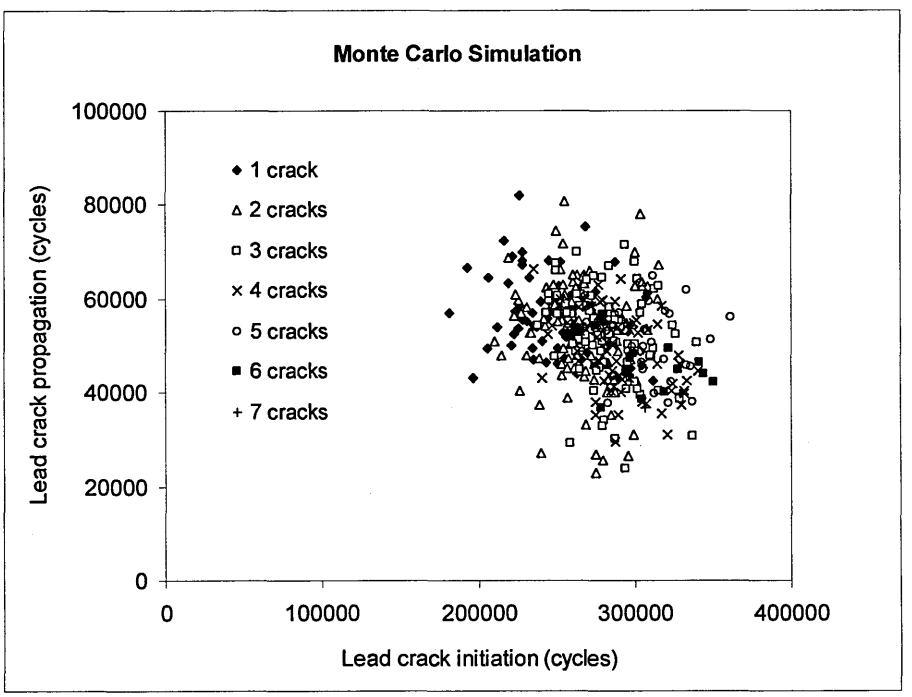

Figure 7.8.3: Number of nucleated cracks per damage scenario from Figure 6.3.2.7. - standard deviation for TTCI (log) = 0.09, uniform pin-loading at 100 MPa (R = 0.1) cyclic tensile stress.

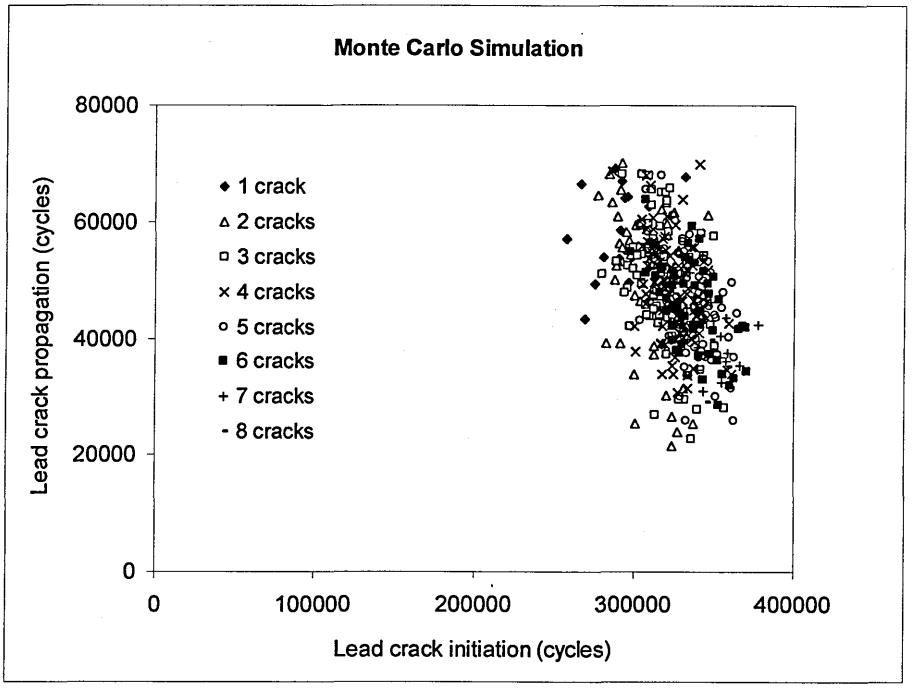

Figure 7.8.4: Number of nucleated cracks per damage scenario from Figure 6.3.3.2 - standard deviation for TTCI (log) = 0.05, uniform pin-loading at 100 MPa (R = 0.1) cyclic tensile stress.

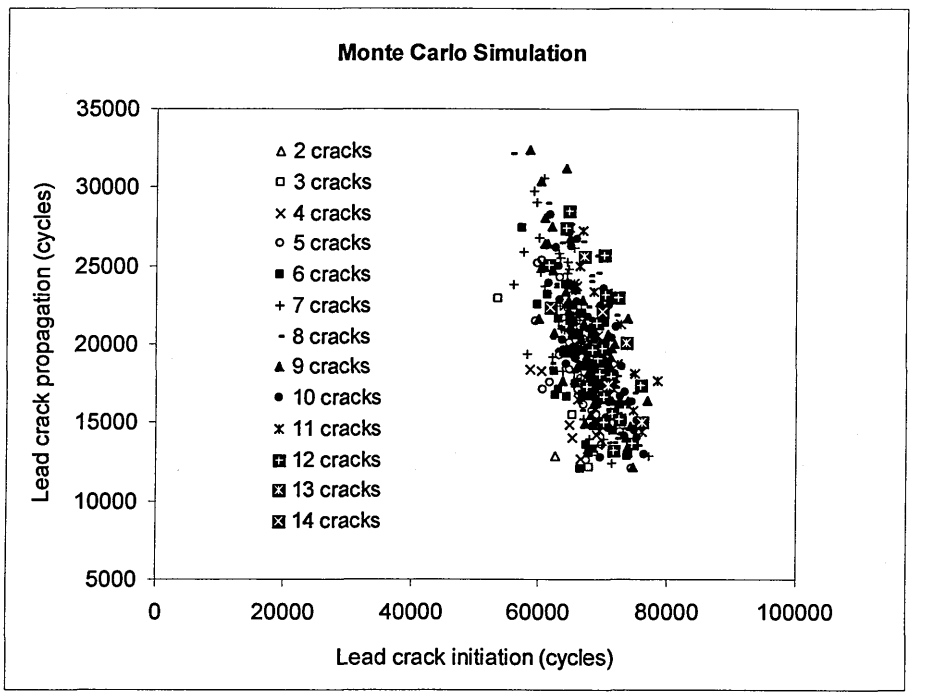

Figure 7.8.5: Number of nucleated cracks per damage scenario from Figure 6.3.3.5 - standard deviation for TTCI (log) = 0.05, uniform pin-loading at 120 MPa (R = 0.1) cyclic tensile stress.

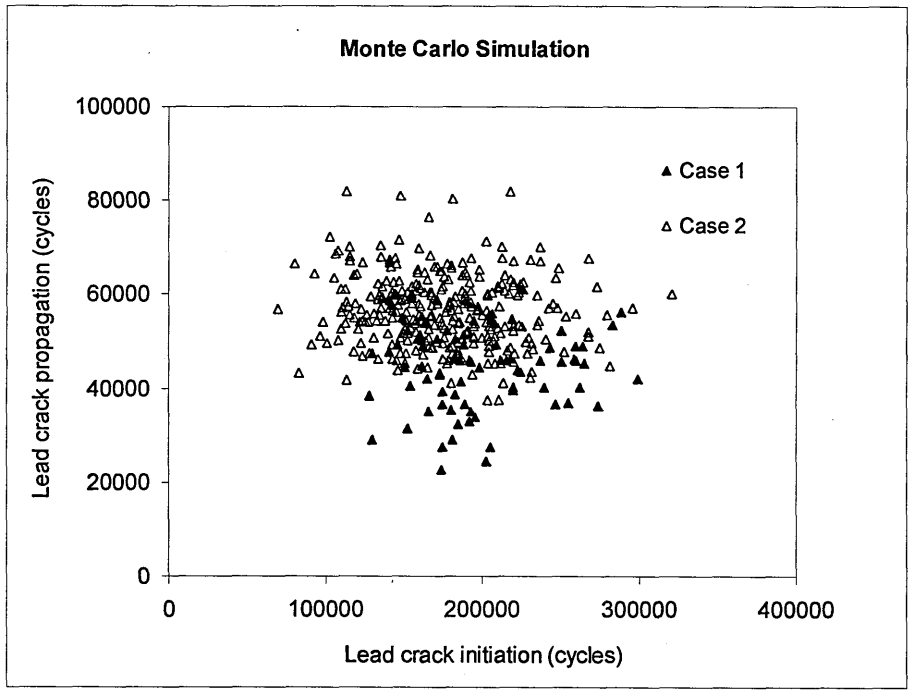

Figure 7.8.6: Crack nucleation sequence 'case 1' and 'case 2' from Figure 7.8.2 - standard deviation for TTCI (log) = 0.21, uniform pin-loading at 100 MPa (R = 0.1) cyclic tensile stress.

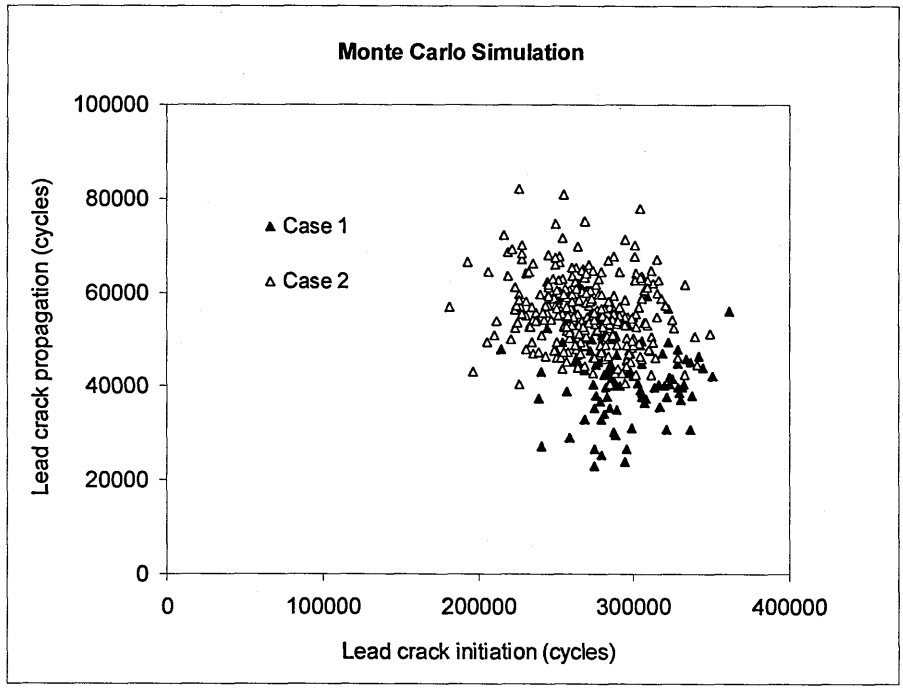

Figure 7.8.7: Crack nucleation sequence 'case 1' and 'case 2' from Figure 7.8.3 - standard deviation for TTCI (log) = 0.09, uniform pin-loading at 100 MPa (R = 0.1) cyclic tensile stress.

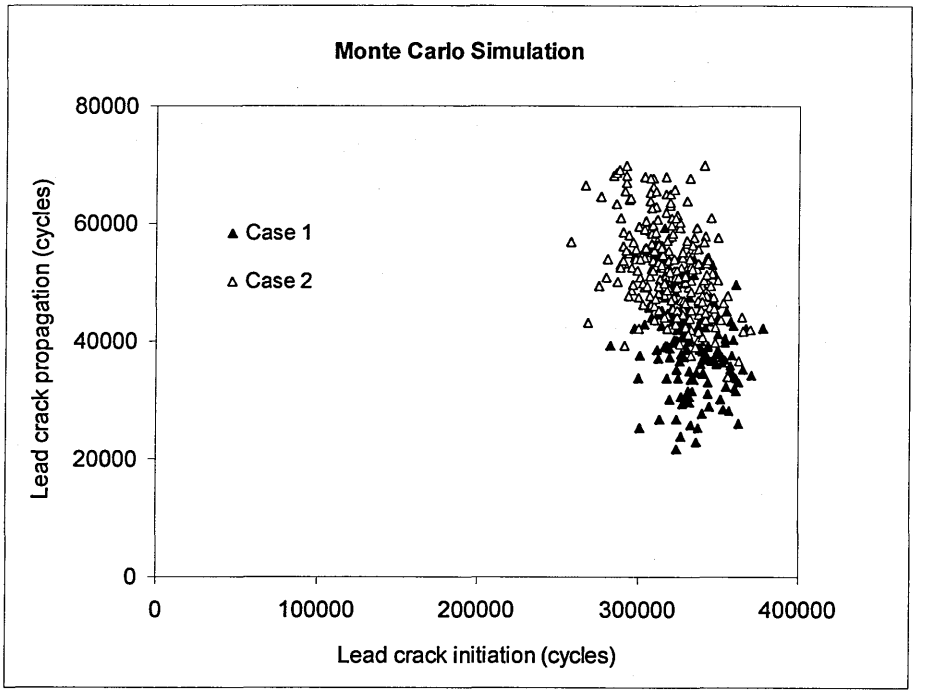

Figure 7.8.8: Crack nucleation sequence 'case 1' and 'case 2' from Figure 7.8.4 - standard deviation for TTCI (log) = 0.05, uniform pin-loading at 100 MPa (R = 0.1) cyclic tensile stress.

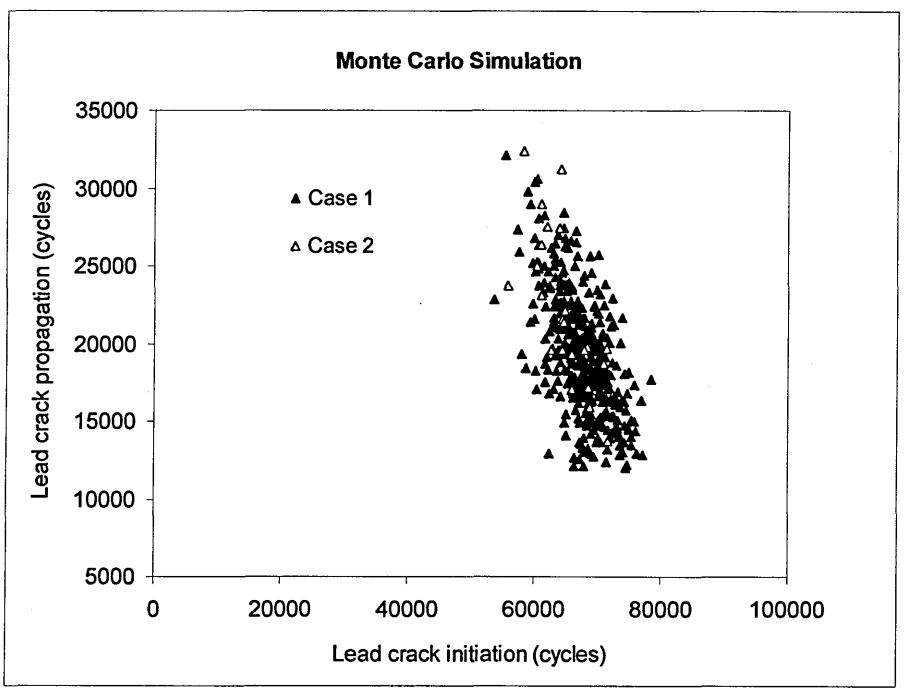

Figure 7.8.9: Crack nucleation sequence 'case 1' and 'case 2' from Figure 7.8.5 - standard deviation for TTCI (log) = 0.05, uniform pin-loading at 120 MPa (R = 0.1) cyclic tensile stress.

Figures 7.8.10, 7.8.11, 7.8.12 and 7.8.13 present a comparison of the mean time for crack propagation given by damage scenarios with the same number of nucleated cracks ('scenarios with same number of cracks') and the crack nucleation sequence ('case 1' scenarios). By definition 'case 1' scenarios have a constant mean time for crack propagation; and this is the reason why its value does not change in the x-axis ('number of nucleated cracks per damage scenario').

As it can be seen from Figures 7.8.10 to 7.8.13, opposed to Figures 7.8.2 to 7.8.5, there is a clear tendency, indicated by the trend lines, that the mean time for crack propagation is decreased as the number of MSD-like scenarios increase; but not always a bigger number of nucleated cracks per damage scenario gives the smallest time for crack propagation (see, for example, the mean time for crack propagation from Figure 7.8.11 for the case of 4 and 5 nucleated cracks per damage scenario). It can also be noted that the mean time for crack propagation of 'case 1' scenarios is always smaller than the value for any other group of damage scenarios regardless of the number of nucleated cracks; but for the case of Figure 7.8.13.

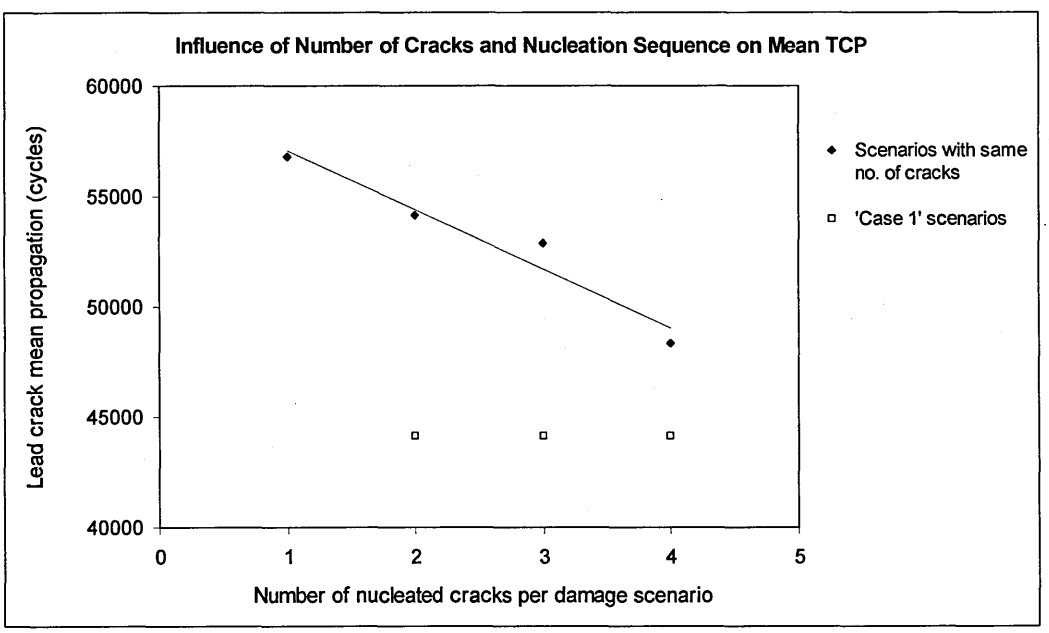

Figure 7.8.10: Mean lead crack time for crack propagation comparison from Figures 7.8.2 and 7.8.6 - standard deviation for TTCI (log) = 0.21, uniform pin-loading at 100 MPa (R = 0.1) cyclic tensile stress.

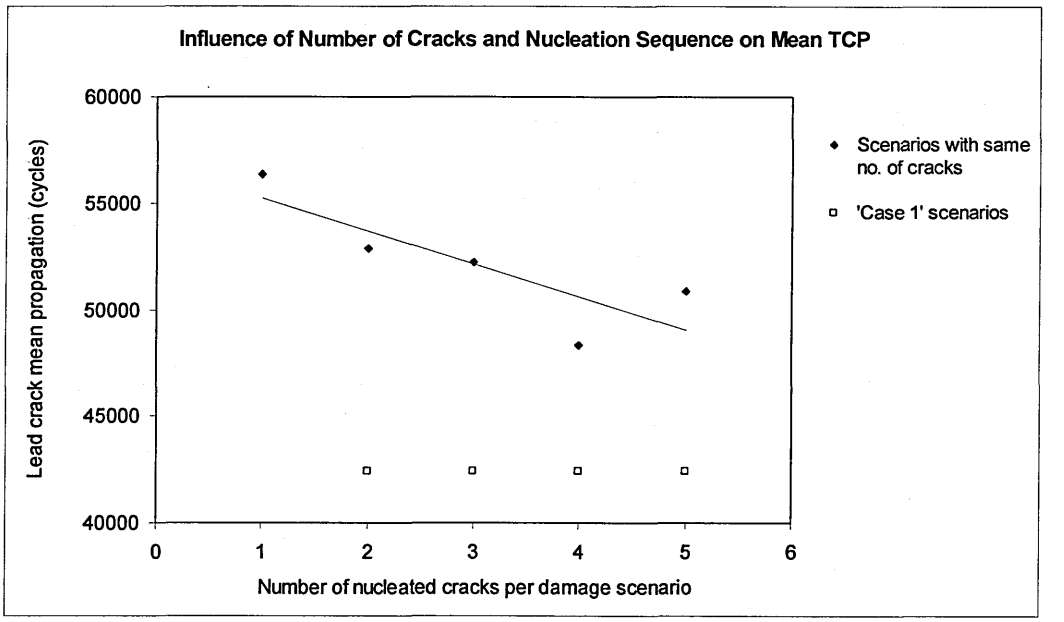

Figure 7.8.11: Mean lead crack time for crack propagation comparison from Figures 7.8.3 and 7.8.7 - standard deviation for TTCI (log) = 0.09, uniform pin-loading at 100 MPa (R = 0.1) cyclic tensile stress.

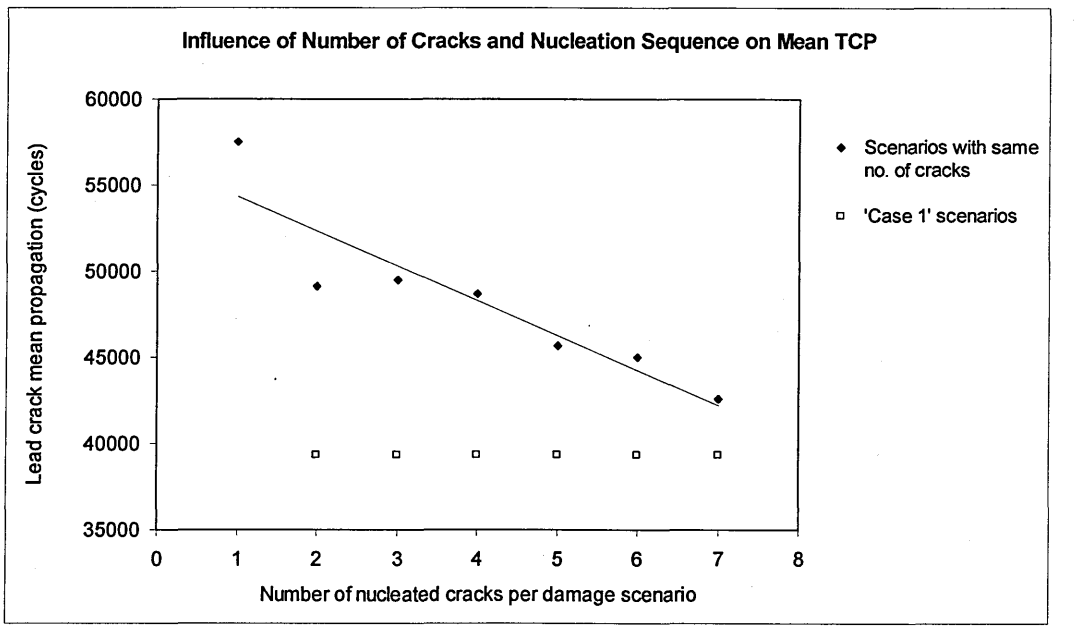

Figure 7.8.12: Mean lead crack time for crack propagation comparison from Figures 7.8.4 and 7.8.8 - standard deviation for TTCI (log) = 0.05, uniform pin-loading at 100 MPa (R = 0.1) cyclic tensile stress

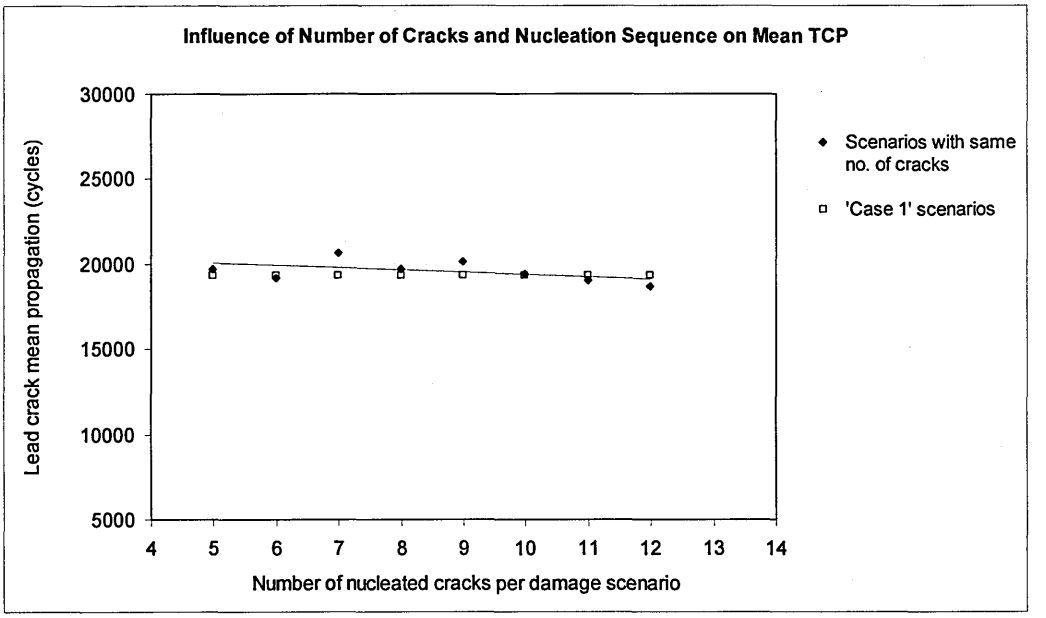

Figure 7.8.13: Mean lead crack time for crack propagation comparison from Figures 7.8.5 and 7.8.9 - standard deviation for TTCI (log) = 0.05, uniform pin-loading at 120 MPa (R = 0.1) cyclic tensile stress.

From Figure 7.8.13, it can be seen that the mean time for crack propagation of 'scenarios with same no. of cracks' is, in fact, very similar to 'case 1' scenarios. The explanation for this behaviour relies on the fact that 92 % of the damage scenarios from Figures 7.8.5 and 7.8.9 fall into the definition of 'case 1' scenarios and, therefore, no big differences are expected for the mean time for crack propagation, as it can be seen from Figure 7.8.13.

Regarding the question in the beginning of this section, and from the discussion presented, it can be concluded that the crack nucleation sequence plays the most important role in decreasing $\overline{TCP}$ compared to the number of nucleated cracks per damage scenario. This statement means that when cracks nucleate at the same hole or at adjacent holes, before the lead crack links-up for the first time, the mean time for crack propagation is smaller compared to damage scenarios where cracks nucleate more than one pitch distance from each other. Also, the results presented in this section show that there is a clear tendency for decreasing the mean time for crack propagation with the increase of MSD-like scenarios; but this tendency is not always true since damage scenarios with bigger number of nucleated cracks can present a bigger time for crack

propagation compared to damage scenarios containing a smaller number of nucleated cracks.

It is interesting to notice that the results from this section can be used to indirectly compare differences between different MSD methodologies for crack propagation. From chapter 2, a methodology that forces crack nucleation to start at adjacent holes, i.e., crack nucleation is not allowed randomly in a row of holes, is the one from Delta Airlines, which is presented in reference [3]. If the results from the simulations presented in, for example, Figure 6.3.2.7 were analysed by forcing crack nucleation in adjacent holes, then the final $\overline{TCP}$ from Table 6.4.3 (52,182 cycles) would be likely to resemble the 'case 1' mean time for crack propagation from Figure 7.8.7 (42,394 cycles); and a direct consequence of this change is that $\overline{N_f}$ would be reduced from 328,117 cycles (Table 6.4.3) to 318,329 cycles, leading to early establishment of the ISP and the SMP. This example is interesting from the point of view of aeronautical safety regulators because, as intuitively it could be imagined, forcing the crack nucleation sequence to adjacent holes do lead to a more conservative establishment of the monitoring period (given by the ISP and the SMP [3]).

7.9. Effect of High Squeeze Force on MSD Assessment

In section 6.3.4, the MSD simulations for the case of high squeeze force was presented, and the input data for that analysis came from Figure 6.3.3.1. To compare the effect of high squeeze force on MSD assessment, the 16 KN rivet squeeze force data from Figure 6.3.3.1 (μ = 5.7371 and σ = 0.1030) is used and the results from the simulations are presented in Table 7.9.1 and Figure 7.9.1, together with the corresponding results from Table 6.4.6 and Figure 6.3.4.2.

Table 7.9.1 shows that $\overline{TTCI}$ is increased by a factor of 2.6 when the squeeze force is increased from 16 to 24 KN; and the benefits of high rivet squeeze force on time to fatigue crack initiation life improvement has been discussed in section 7.1.

Table 7.9.1: Comparison of intermediate and high squeeze forces at 100 MPa stress.

Squeeze Force (KN)	Standard deviation log (cycles)	Pin-load type	$\overline{TTCI}$ (cycles)	$\overline{TCP}$ (cycles)	$\overline{N_f}$ (cycles)	ISP (cycles)	SMP (cycles)	MSD-like scenarios (%)
16	0.10	U	353,139	53,450	406,589	135,530	203,295	70.2
24	0.13	U	919,481	57,750	977,231	325,744	488,616	28.0

From equation 7.5.1, it can be seen that changes in N_0 can occur due to changes in μ, α or σ. Table 7.9.2 presents an example where it can be observed how N_0 changes by changing both μ and σ (considering the values of the 16 and 24 KN squeeze forces) for the same values of α. The 'FCL' column presents 4 hypothetical fatigue critical locations, the 'Differences' column represents the differences of lives (cycles) from FCL2 – FCL1 and FCL4 – FCL3 (given by column N_0).

From Table 7.9.2 it can be seen that, for the same α values, when μ and σ are increased the corresponding N_0 lives increase. This result explains why the $\overline{TTCI}$ increases from Table 7.9.1 when the squeeze force is increased from 16 to 24 KN. It can also be noted that when μ and σ are increased the differences in lives (cycles) between FCLs '4 and 3' and '2 and 1' increase. This result shows that fatigue cracks are allowed to nucleate more separate in time (cycles) from different FCLs, leading to a possible decrease in the number of MSD-like scenarios; and, in fact, this is what column 'MSD-like scenarios' from Table 7.9.1 is demonstrating. As the MSD-like scenarios decrease, crack interaction effects tend to diminish and it is expected that $\overline{TCP}$ is increased, as actually can be seen from Table 7.9.1 and from Garcia [122]. What can also be noted from Table 7.9.1 is that the $\overline{TTCI}$ and the $\overline{TCP}$ are both increased when the rivet squeeze force is increased; and the final result is that $\overline{N_f}$ increases.

Table 7.9.2: Changes in N_0 due to changes in μ and σ.

FCL	μ log (cycles)	σ log (cycles)	α	$Log\ (N_0)$	N_0 (cycles)	Differences (cycles)
1	5.7371	0.1030	- 1.0	5.6341	424,399	53,368
2	5.7371	0.1030	- 0.5	5.6856	477,768	
3	6.1976	0.1286	- 1.0	6.0690	1,153,948	183,923
4	6.1976	0.1286	- 0.5	6.1333	1,337,871	

Figure 7.9.1 shows in the legend 'Normal distributions' corresponding to the theoretical cumulative failure distributions, 'MC points – 24 KN' and 'MC points – 16 KN' which represent, respectively, the Monte Carlo simulation points for the 24 and 16 KN rivet squeeze forces.

From Figure 7.9.1, it can be seen that the cumulative failure distribution inclination from the 'MC points – 16 KN' is smaller than the one from the 'MC points – 24 KN'. A decrease in inclination is related to a more severe MSD condition. Small inclinations lead to a decrease in the range of number of cycles to failure; and once MSD starts, the probabilities of failure increase much faster in time (cycles) than for the case of large cumulative distribution inclinations. The increase in MSD severity can also be verified by the increase in MSD-like scenarios from Table 7.9.1 for the intermediate rivet squeeze force (16 KN).

The results from Figure 7.9.1 and Table 7.9.1 show that high rivet squeeze, beyond retarding the whole failure process, also lead to a decrease in MSD-like scenarios. The direct conclusion from these results is that high rivet squeeze force is extremely beneficial for MSD prevention since it helps to decrease the number of nucleated cracks in the same row of holes. Unfortunately the use of different squeeze force input values (μ and σ - equation 7.5.1) and its effect on MSD failure behaviour has not been reported from the literature (chapter 2), and no comparison to the results from this section can be done.

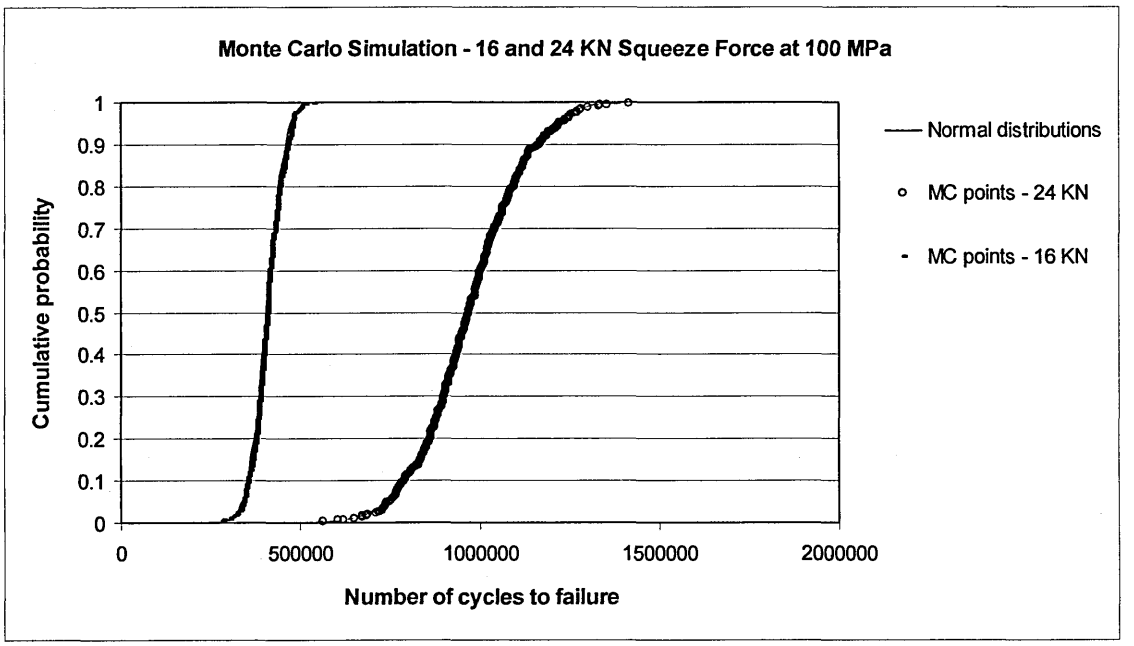

Figure 7.9.1: High and intermediate squeeze force MSD assessment comparison.

7.10. MSD Assessment Comparison to Teardown Inspections from In-Service Data

In section 6.5, an MSD assessment analysis was presented to compare its output to teardown data obtained from in-service fuselage panels of aging aircraft (Figures 6.5.7 to 6.5.9) published by Steadman [15]. Before comparing the results themselves, it is worthwhile to discuss, firstly, the hypothesis assumed in the MSD model that led to the differences obtained.

Starting from the initiation part of the MSD assessment model, it was assumed an open-hole quality S-N fatigue data (Figure 6.5.3) for fatigue crack initiation. As the lap joint configuration analysed (Figure 6.5.1) is riveted, this choice must be justified.

From the MSD models presented in chapter 2, for example Schmidt [5], it is a common practice to use strap flat fatigue test specimens, manufactured using aircraft standards (material, rivets and assembly techniques), to derive S-N fatigue data for MSD assessment comparison to laboratory fatigue tests of flat fuselage panel sections. The MSD models, such as the ones discussed in section 7.2 (including the one from this work), compared their outputs to pristine sections of flat fuselage panels. Of course,

these comparisons are valid to demonstrate the effectiveness of the methodologies since the models output represents what is intended for comparison. A direct consequence of this issue is that MSD models can be describing the MSD behaviour of flat lap joints in laboratory environment, and not real aircraft structures [117].

Real aircraft fuselage lap joints are subjected to bi-axial loads such as circumferential and axial stresses caused by pressurization, bending and torsion caused by aerodynamic loads, inertia loads and landing, not to mention environmental issues such as corrosion. In his work, Okada [123] compares the fatigue lives for initiation of 1 mm cracks from flat panel specimens and one-third scale-models of a B-737 fuselage structure subjected to pressurization and bending loads. If the fatigue life for crack initiation obtained from the scale-model specimens is divided by the corresponding value from flat panel specimens, a mean coefficient of 0.42 is obtained. This coefficient means that the fatigue life for crack initiation is reduced by 58 % when curved panel test specimens are considered. It has to be highlighted that the mean coefficient of 0.42, derived by the author from Okada [123] experimental work, was calculated based on two flat lap joint and two scale-model fatigue test specimens; which cannot represent the statistical dispersion inherent to a wider number of fatigue tests. But, certainly, Okada [123] experiments give a clear indication that there are significant differences from both fatigue test specimens as a source for input data for Monte Carlo simulations.

Another indication that pristine and good quality riveted flat lap joint test specimens are possibly not indicated to generate S-N fatigue data for MSD assessment of real fuselage panels comes from Wanhill [124], Bakuckas [125] and Steadman [15]. Wanhill [124] presents the service histories of pressurized fuselage lap splices from five different in-service aircraft types where MSD cracking was detected. By the time MSD was identified, the number of flights varied from 34,470 to 75,158. From Bakuckas [125] it is also reported MSD occurrence, detected by current methods for field inspections, from a retired Boeing 727 containing 59,497 flight cycles. Steadman [15] findings were already presented in Figure 6.5.4 and MSD initiation was reported even before 20 % DSG (12,000 flight cycles). These numbers are showing that MSD occurrence, from in-service or retired fuselage panels, happens in a range of 1E+4 to 1E+5 flight cycles;

while fatigue lives to crack initiation from S-N tests of pristine and good quality strap lap joints are commonly reported to be higher than 1E+5 cycles at typical loads around 100 MPa and R ratios ranging from 0 to 0.1 (see, for example, Table 6.1.2).

Another complicating factor, when assessing real fuselage panels for MSD behaviour via fatigue data from flat lap joint specimens, is corrosion. Corrosion occurrence has been reported from retired and in-service aircraft fuselage joints [126]. Concerning S-N fatigue data itself, a comparison between fatigue tests from pristine and corroded flat lap joint samples showed that corrosion can easily degrade the fatigue life for visible crack initiation by 40 % [127]; and, therefore, pristine test specimens seem not to be adequate to approach real aircraft fuselage panels if corrosion is considered.

For some of the reasons and examples described in the previous paragraphs, the applicability of fatigue crack initiation data obtained from pristine and good quality riveted flat lap joint test specimens for MSD assessment of real aircraft fuselage panels is questioned by the author.

From the literature review on MSD methodologies presented in chapter 2, the only positive indication that flat riveted lap joint test specimens could be used for comparison to full-scale fatigue tests (which mostly resembles in-service fuselage panels) comes from Horst [30]. From his MSD simulations, Horst could predict a full-scale fatigue test result at the border of his 99.7 % confidence region where the smallest fatigue lives were obtained from the simulations. It has to be highlighted that Horst [30] employed a poor quality deep countersunk riveted joint to force early fatigue crack initiation because, according to his arguments, good quality riveted samples would be inadequate for comparison purposes with the full-scale test due to the high fatigue lives obtained from those samples. The result from the full-scale fatigue test [30] presented a detectable crack with fatigue life around 80,000 pressurization cycles and, as observed from in-service fuselage panels, a fatigue life in the range of 1E+4 to 1E+5 cycles.

For the lap joint configuration analysed in section 6.5, S-N fatigue data obtained from good quality riveted flat lap joint test specimens can be found in Swift [100]; and the

mean time to crack initiation is approximately 1E+6 cycles. If a typical standard deviation value of 0.15 in log (cycles) is assumed for fatigue crack initiation of Al 2024-T3 riveted panels [121], the results from Monte Carlo simulations will give a mean time to crack initiation of the lead crack equal to 536,250 cycles; with the smallest and biggest lives equal to, respectively, 266,088 and 835,761 cycles. At this stage, it is quite clear that MSD assessment of real aircraft fuselage panels, when performed with input S-N fatigue life data from good quality riveted flat lap joint samples, is destined to a terrible non-conservatism. For the example given, this statement is easily verified if lives to MSD occurrence from aging aircraft pressurized fuselage panels (34,470 to 75,158 cycles [124]; 59,497 cycles [125]; 12,000 cycles [15]) are compared to the fatigue crack initiation lives generated by the Monte Carlo simulations (266,088 to 835,761 cycles).

For the reasons discussed so far, the author decided to assume open hole quality S-N fatigue data input (Figure 6.5.3) for the fatigue crack initiation part of the MSD assessment model. This assumption seems logical since it can be observed that the open hole S-N data used, for the lap joint configuration from Figure 6.5.1, falls in the range of 1E+4 to 1E+5 cycles for fatigue crack initiation and, therefore, it is likely to resemble lives to MSD occurrence from in-service findings [15, 124, 125]. As no information for the standard deviation value is available from Figure 6.5.3, a value of 0.15 in log (cycles) was assumed.

From Figure 6.5.7, it can be seen that the cumulative probabilities for fatigue crack initiation of the lead crack from the simulations is surprisingly close to the one from in-service data, more noticeably for low probabilities of occurrence. It can also be noted that the inclination of the distribution from the simulations is smaller than the one from in-service data, indicating that in reality a bigger standard deviation value should be used. If the mean times to crack initiation from the distributions are compared, then it can be seen that the value from the simulations is 15.7 % smaller than the one from in-service data. This result demonstrates that the use of open hole S-N data for fatigue crack initiation is rationally conservative, and for the case of the lap joint from Figure 6.5.1 can be applied. The crack initiation distributions from Figure 6.5.7 are presented

in Figure 7.10.1, and it can be seen that, for example, from the early 20 % DSG (12,000 flight cycles) the cumulative probability for MSD initiation is higher than 1 % from both the simulations and in-service data. For 50 % DSG (30,000 flight cycles) the simulations indicate that there is 100 % cumulative probability for MSD initiation while the in-service data presents a probability of 95 %.

From Figure 6.5.8, it can be seen that the differences between the cumulative distributions for detectable cracks are enlarged when compared to the results from Figure 6.5.7. Considering the mean time for detectable cracks (50 % probability), the Monte Carlo simulation result is 23.1 % smaller than the in-service ones. It has to be highlighted that the Monte Carlo simulation results from Figure 6.5.8 were obtained from the results presented in Figure 6.5.7 (initiation of fatigue cracks) but adding the number of cycles to grow the corresponding lead cracks probabilistically from 1.27 mm to 5.1 mm (detectable crack length considered by Steadman [15]). This procedure needs some extra refinement, since the scatter for the detectable crack distribution was simply attributed to the scatter inherent to the crack growth process but the crack detection itself presents a scatter inherent to the inspection process; and if this scatter is added to the one from the simulations the inclination of the present cumulative distribution is expected to increase. If only the crack propagation process is considered, then the enlargement of distance between both distributions from Figure 6.5.8, when compared to Figure 6.5.7, can be attributed to conservatism in the whole crack propagation calculations performed with the model from Figure 6.5.2.

The results from Figure 6.5.8 are presented in Figure 7.10.2, and it can be seen from the simulations that at 40 % DSG (24,000 flight cycles) there is a cumulative probability of MSD detection bigger than 1 %; while for the same probability from in-service data MSD cracks would be detected from the 48 % DSG (28,800 flight cycles). Steadman [15] recommends that an inspection program for MSD detection would be required as early as the 50 % DSG (30,000 cycles) from the in-service data (around 1 % cumulative probability of MSD detection); while it can be seen from the simulations that the same number would be around 40 % DSG (24,000 cycles). At this point it is interesting to compare what the AAWG recommendations [3] indicate for the point of ISP. The ISP

was calculated in section 6.5 for the in-service data and for the simulations. These points are, respectively, equal to 18,300 (30.5 % DSG) and 14,180 flight cycles (23.6 % DSG). As it can be seen from Figure 7.10.2, from both the in-service data and the simulations, the cumulative probabilities for MSD crack detection are below 0.01 % indicating that the point of ISP is conservatively established and it is clearly concerned with very small probabilities for MSD detection when compared to what has been recommended by Steadman [15].

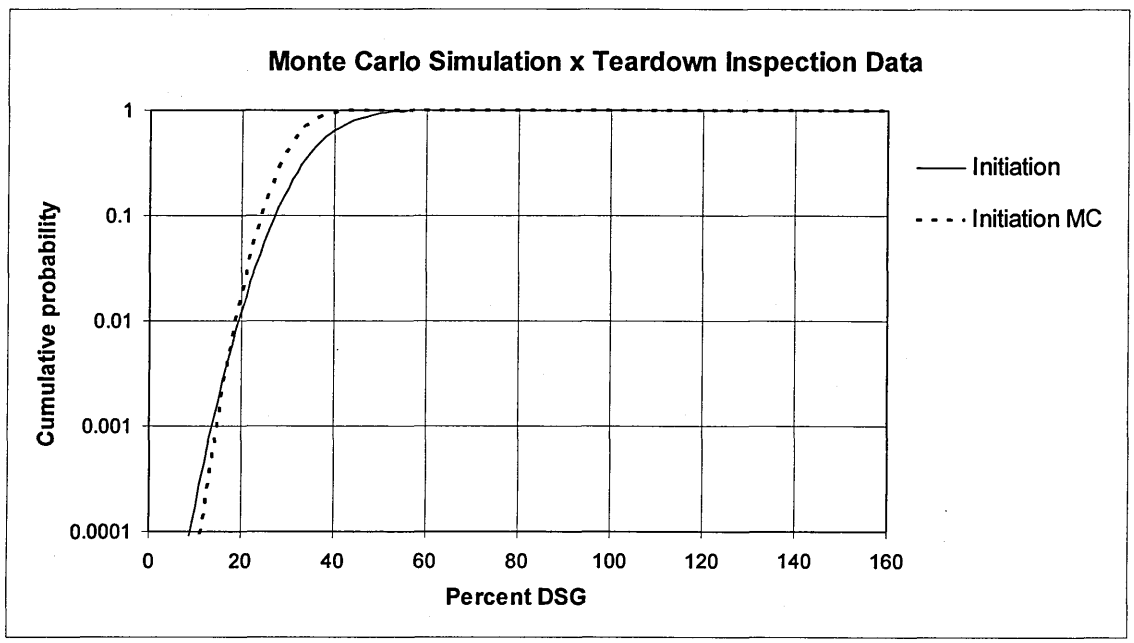

Figure 7.10.1: Cumulative probability distribution for crack initiation from Figure 6.5.7.

From Figure 6.5.9 it can be seen that the cumulative probabilities of failure from the simulations and in-service data are enlarged when compared to Figure 6.5.7. The mean time for failure from the simulations is 22.5 % smaller than the in-service one. As for the case of Figure 6.5.8, this difference can also be attributed to conservatism in the whole crack propagation calculations performed with the model from Figure 6.5.2, but other reasons apply as well. From Figure 6.5.5, it can be seen that, although the crack propagation analysis from the simulations are comparable to in-service data [111], crack propagation times ranged from approximately 16,000 to 45,000 flight cycles for Boeing 727 and 737 aircraft; while the same value given by the model from Figure 6.5.2 was 26,000 cycles. These differences seem not to be connected, so lonely, to the scatter

inherent to the crack growth process. It is possible that 'flight cycles' from Figure 6.5.5 do not necessarily mean full pressurization cycles, and this issue depends on the service history of each aircraft.

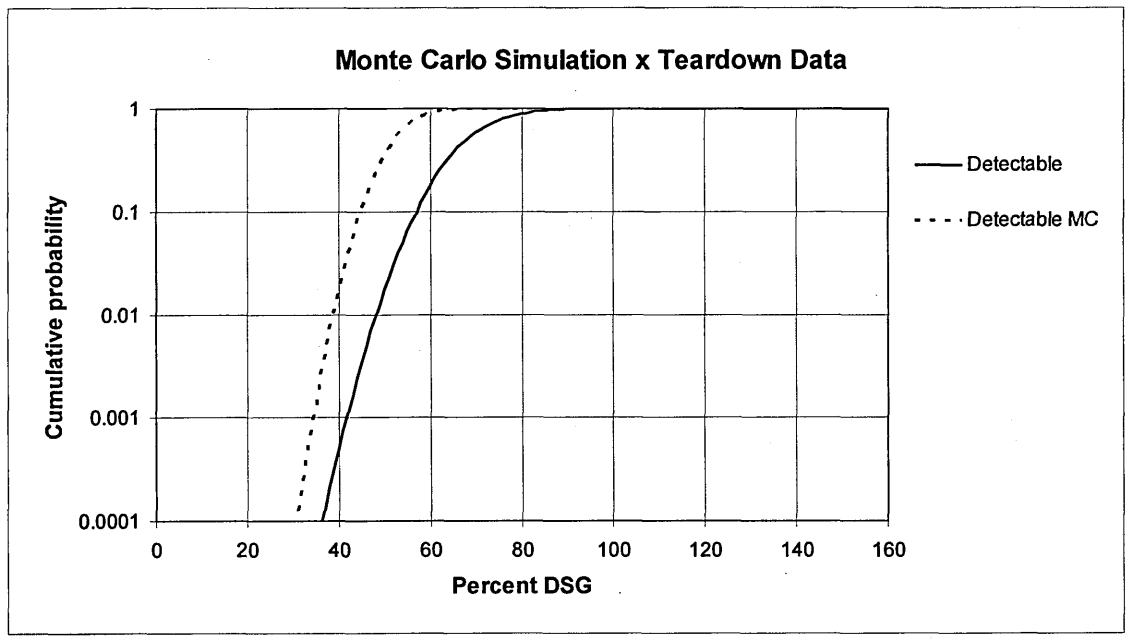

Figure 7.10.2: Cumulative probability distribution for crack detection from Figure 6.5.8.

From the point of view of the AAWG recommendations [3], the basic purpose of MSD models is to establish both the ISP and SMP points, from the 50 % cumulative probabilities of failure, to define a monitoring period in order to prevent MSD threat. If the ISP and SMP points are considered, the calculated values from the analysis are, respectively, 14,180 cycles (23.6 % DSG) and 23,270 cycles (35.5 % DSG); while the same values calculated from the in-service data are, respectively, 18,300 cycles (33.3 % DSG) and 27,480 cycles (45.8 % DSG). These results indicate that the ISP and the SMP points established from the simulations are 22.5 % smaller than the ones from in-service data. From an engineering point of view, this difference is not small; but it is far from being unacceptably conservative considering that real MSD occurrence from aging aircraft pressurized fuselage panels is being assessed. Unfortunately, the differences obtained from the current MSD assessment analysis to in-service data, as well as the hypothesis assumed for its assessment, cannot be compared to other models output;

since no similar work was found by the author from the literature review presented in chapter 2.

Returning to the points of ISP and SMP, established from both the in-service data and the simulations (section 6.5), these points define the monitoring period which is 'the period of time when special inspections of the fleet are initiated due to an increased risk of MSD' [3]; and the monitoring period ends when the SMP is reached. The SMP point, also called the 'point of WFD' (widespread fatigue damage) [3], is the point where 'no airplane may be operated without modification or part replacement' [3] or 'the point beyond which the airplane may not be operated without further evaluation' [3]; and at the SMP point, failure due to MSD should not represent a threat to structural safety due to high probabilities of occurrence. The reason for reminding the monitoring period and the SMP concepts is to verify whether these parameters (established by the simulations) are well suited to its definitions or not when compared to the in-service data; and to perform this verification the results from Figure 6.5.9 are presented in Figure 7.10.3.

From Figure 7.10.3, it can be seen that the SMP from the simulations (35.5 % DSG) is conservatively established compared to the in-service data (45.8 % DSG) demonstrating a cumulative probability of failure smaller than 1E-4, which means that MSD threat is remote to structural safety and the SMP point from the simulations is well established. This conservatism can also be observed when the SMP is established with the in-service data itself (45.8 % DSG) because the cumulative probabilities of failure are also smaller than 1E-4. If the SMP point established from the simulations (35.5 % DSG) is checked for MSD initiation behaviour using the in-service distribution presented in Figure 7.10.1, it can be seen that approximately 45 % of the fleet would have initiated MSD cracks! Although this probability is high, the cumulative probability of MSD detection from Figure 7.10.2 is still small (approximately 1E-4 using the in-service distribution) which means that cracks would not have grown far enough to represent a real threat to the residual strength of the structure. It has to be noted that in case of no detectable MSD cracks at the point of SMP; airworthiness regulators would possibly not recommend repair or structural modifications, but the extension of the point of SMP (and, consequently, the monitoring period) as a result of further evaluation of the

structure. As the SMP given from the simulations fulfils its purpose, the same conclusion applies to the monitoring period since very low cumulative probabilities of MSD failure are involved from the point of ISP to the point of SMP.

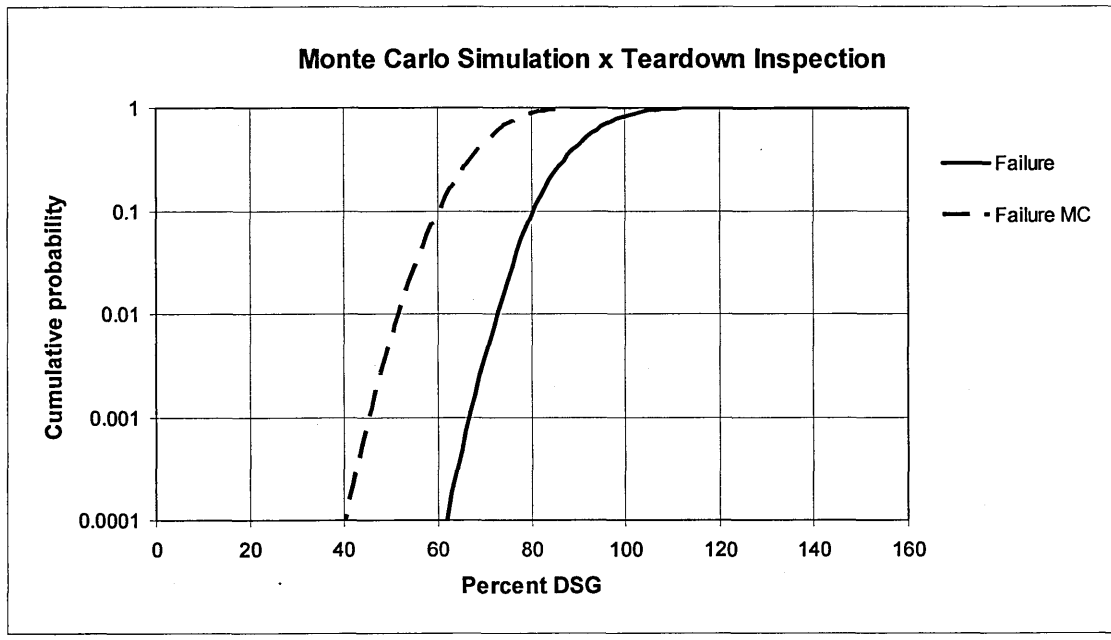

Figure 7.10.3: Cumulative probability distribution of failure from Figure 6.5.9.

In fact, what can be definitely stated from the ISP and SMP points established by the simulations is that when these values are compared to the same ones from in-service data, it can be concluded that the MSD assessment analysis discussed in this section was able to fulfil its purpose with rational conservatism. To finalize the discussion on establishment of structural safety parameters, it is worthwhile to examine the USAF criterion [75] from Figure 7.10.3. From the cumulative probability of failure corresponding to 1E-3, it can be seen that the limit to proper structural functioning (LPSF) from the simulations is approximately 46 % DSG (27,600 cycles). If the cumulative distributions from in-service data from Figures 7.10.1 and 7.10.2 are employed, it can be seen that, at 46 % DSG, the cumulative probabilities for initiation of MSD cracks and detectable MSD would be, 87 % and 0.5 %, respectively. Considering the proposed structural safety criterion from this work (section 7.5) then the SMP point would be the preferred choice for further structural evaluation and/or structural modification.

From the results presented in section 6.5, Figure 6.5.10 shows the percentage of scenarios as a function of nucleated cracks. As it can be seen, no mono-crack scenarios are present and the minimum number of cracks a damage scenario developed was 8. For the case of 21 nucleated cracks, it can be realized that 10 out of 11 holes were cracked simultaneously at the 3 and 9 o'clock positions before the lead crack could link-up. This situation resembles the worst possible MSD scenario where cracks are allowed to nucleate simultaneously from each hole both at the 3 and 9 o'clock positions.

Figure 7.10.4 presents the same results as in Figure 6.5.10 but for the percentage of scenarios as a function of cracked holes. It is interesting to note that the majority of the damage scenarios generated (40.3 %) had all holes cracked.

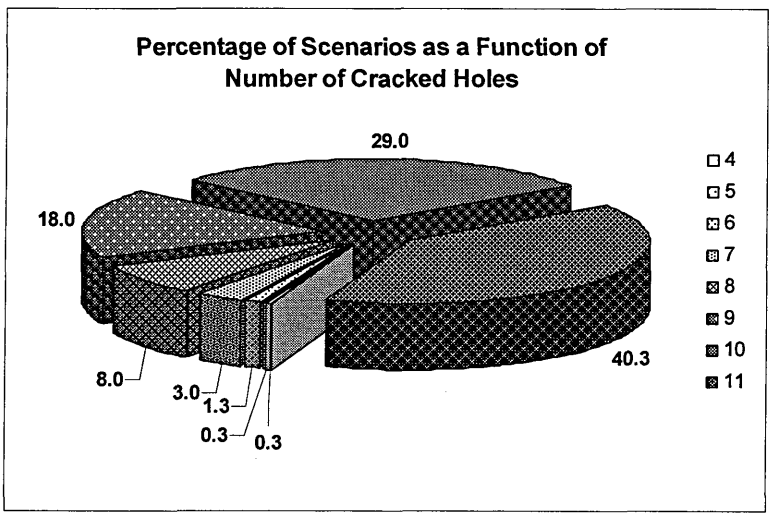

Figure 7.10.4: Percentage of scenarios as a function of number of cracked holes for the Monte Carlo simulations from Figure 6.5.6.

Figure 7.10.5 presents in-service MSD findings, reported by Schijve [128] from the work of Mayville [129], from an aging Boeing 727 aircraft with 43,400 flights and with multiple cracks in three pressurized fuselage bays. As it can be seen from Figure 7.10.5, the crack sizes are as big as 6 mm and, in the case of the bay in the centre of the figure, the only holes that are not cracked are the ones close to the frame locations. 9 out of 10 holes in the centre of the bay developed simultaneous cracks at the 3 and 9 o'clock

positions. This type of in-service cracking pattern, in the centre of a pressurized lap joint frame bay, was reproduced by the simulations performed (Figures 6.5.10 and 7.10.4).

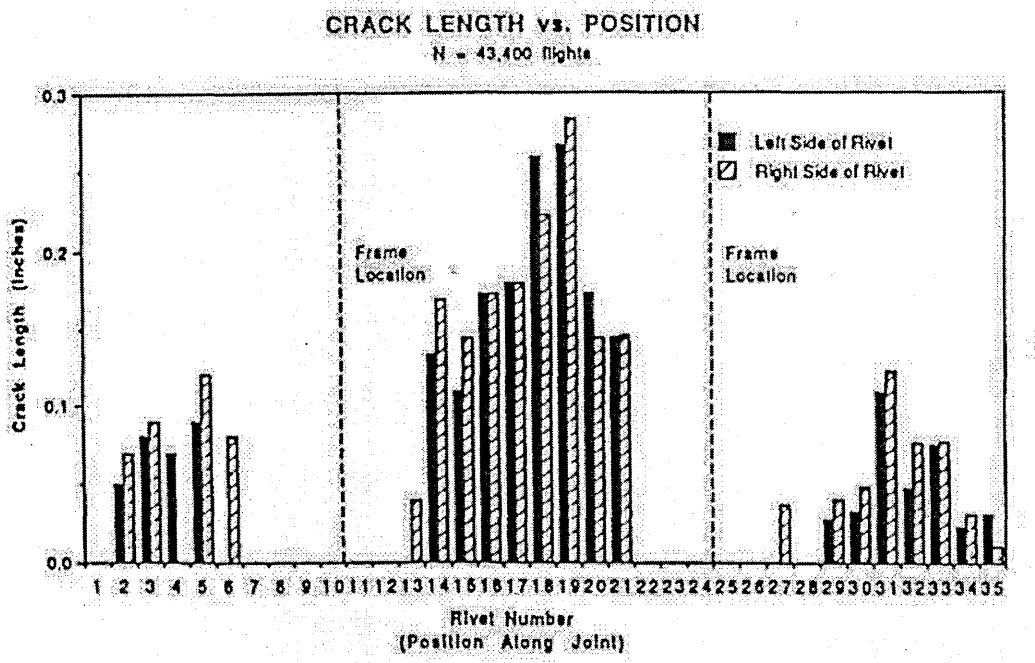

Figure 7.10.5: Fatigue cracks in riveted lap joint of an aging aircraft 727 fuselage [129].

In order to finalize the discussions of this section, there is a fundamental issue that is in need of further comments. For the specific in-service data discussed in this section, the open hole S-N fatigue data used for the Monte Carlo simulation analysis demonstrated to be reasonably suitable for MSD assessment of aging aircraft pressurized fuselage panels. The main question that has to be answered from future workers is whether open hole S-N data is always suitable or not for different geometrical configurations than the one that has been analysed (Figure 6.5.1). With this question, the author intends to let it clear that coincidences are feasible to happen; although from the arguments presented in the beginning of this section the use of open hole quality S-N data was rationally justified. It may be that for other fuselage panel configurations, open hole quality S-N data demonstrates inadequacy and, possibly, good quality riveted lap joint S-N data should be more appropriate. For this reason, it is suggested that, for example, the in-service data from Wanhill [124], where MSD cracking lives are reported for five different types of fuselage lap splices, be compared to MSD analysis performed from corresponding open hole and good quality riveted lap splice S-N data. When these

comparisons are completed, then a final conclusion can be reached about the general use of open hole quality S-N fatigue data for MSD assessment of in-service aircraft fuselage pressurized panels.

Chapter 8

8. CONCLUSIONS

The conclusions presented in this chapter follow the same order as from the discussions (chapter 7); and the main conclusions are presented as follows:

8.1. Experimental Work

1. The mean time to initiation (cycles) of fatigue cracks in riveted lap joints increases when the rivet squeeze force varies from a low to a high value, despite the stress level employed;

2. Beyond improving the mean time for initiation of fatigue cracks, the high squeeze force test specimens provided the highest standard deviation (scatter) values in cycles to failure, despite the stress level employed, and with the smallest stress range producing the biggest scatters;

3. Considering the standard deviation (scatter) value for initiation of fatigue cracks in log (cycles), the scatter increases for both high and low lives in log (cycles) and there is a region of minimum scatter which can be found between these lives, with the smallest stress range producing the biggest scatter values;

4. Considering the coefficient of variation (COV) value for initiation of fatigue cracks in log (cycles), the COV increases for both high and low lives in log (cycles) and there is a region of minimum COV which can be found between these lives, with the smallest stress range producing the biggest COV values; and the same trend is observed from a plot of COV versus squeeze force values in KN;

5. For low squeeze force value, the crack nucleation sites are close to the 3 and 9 o'clock positions of the hole and mainly take place at its border. For increasing

values of squeeze force, the boundary of the hole is not critical anymore and crack nucleation takes place away from the 3 and 9 o'clock positions and from the hole border;

8.2. MSD Assessment Model Comparison to Experimental Work and to Other Models from the Literature

1. The MSD model provided good agreement with published experimental work on fatigue of lap splice joints where both crack initiation and propagation stages from the simulations were able to incorporate the experimental data scatter and the mean lives.

2. The spread of the experimental data at both initiation and propagation lives was as large as that of the entire simulations; and this behaviour is also verified from other published work.

3. When comparing the MSD simulations from the proposed model to other published work, for different riveted joint geometrical configurations and loading conditions, it could be seen that different MSD models compared very similarly to their corresponding experimental work as for the model from this work; i.e., most of the models were able to incorporate the scatter of lives for initiation and propagation of the test points and the scatter of the test data was also comparable to the corresponding simulations.

4. By comparing the MSD model from this work to other published work, for the same lap joint geometrical configuration and loading conditions, it could be verified that continuing damage assumption and probabilistic crack growth (proposed in this work) can be used as a valid and simplifying option to a damage accumulation technique and deterministic crack growth as an engineering approach for MSD modelling. On the other hand, continuing damage assumption when employed with deterministic crack growth can not.

5. As a general trend, deterministic crack propagation performed with continuing damage assumption gives conservative crack propagation lives compared to the ones from deterministic crack propagation performed with a damage accumulation technique.

8.3. MSD Assessment Model Limitations

1. For MSD assessment models that perform a few hundreds of Monte Carlo simulations, a minimum number of simulations are needed until convergence is reached in order to use statistical tools (such as cumulative distribution functions or confidence regions) for overcoming the limited number of simulations.

2. The establishment of inspection intervals from only a few hundreds of Monte Carlo simulations can lead to non-conservatism; and the use of confidence regions demonstrated to be a valid option to overcome this difficulty.

8.4. Effect of Change in Standard Deviation on MSD Assessment

1. From the experimental data presented in this work and from published work, different standard deviation (scatter) values for the same mean time to fatigue crack initiation is far from being a pure theoretical situation; and these differences lead to significant variations while establishing the ISP and the SMP points for MSD prevention.

2. An MSD analysis of a riveted lap joint configuration, considering the same mean time to fatigue crack initiation and two possible values for the corresponding standard deviation value, has showed that the AAWG recommendations and the USAF criterion for structural safety were in conflict. When the large standard deviation value was considered the AAWG recommended criterion was non-conservative compared to the USAF one; while for the small standard deviation value the situation was the opposite.

3. The establishment of the ISP and the SMP, based solely on the mean MSD failure behaviour, was very sensitive to changes in scatter values. This situation was even worse for the establishment of the LPSF where low cumulative probabilities of failure were involved.

4. To overcome the conflict between the AAWG recommendations and the USAF safety criteria, a new criterion was proposed in this work by considering the limit for safe operation of the structure up to a lower boundary determined by either the AAWG recommendations or the USAF criterion; whichever the smallest.

5. For the same mean time to fatigue crack initiation, a decrease in the corresponding standard deviation value increases the mean time to the lead crack initiation, decreases the mean time for the lead crack propagation, and increases the mean time to failure as well as the ISP, the SMP and the percentage of MSD-like scenarios. If the standard deviation is increased the trends are reversed.

6. For the same mean time to fatigue crack initiation, and considering non-uniform pin-loading, the lead crack tended to nucleate in the highest stressed fatigue critical locations. As the corresponding standard deviation value decreased, the lead crack nucleation was exacerbated at those locations.

8.5. Effect of Change in Pin-loading on MSD Assessment

1. For the same mean time to fatigue crack initiation, and considering the uniform pin-loading, a decrease in the corresponding standard deviation value increases the mean time to the lead crack initiation, decreases the mean time for the lead crack propagation, and increases the mean time to failure as well as the ISP, the SMP and the percentage of MSD-like scenarios. If the standard deviation is increased the trends are reversed.

2. When the uniform pin-loading was established with a mean value from the non-uniform pin-loading distribution, and compared to the corresponding non-uniform pin-loading results at different scatter values for fatigue crack initiation, the general trends were that the mean time to the lead crack initiation was bigger, the mean time for the lead crack propagation were similar, the mean time to failure was bigger as well as the ISP, the SMP and the percentage of MSD-like scenarios.

3. Opposed to the non-uniform pin-loading case, the uniform pin-loading showed no tendencies regarding the lead crack nucleation sites.

4. The uniform pin-loading distribution, when implemented with mean pin-loading values from the non-uniform pin-loading distribution, resulted to non-conservatism for establishment of the SMP and, more noticeably, the LPSF which is based on low cumulative probabilities of failure. Therefore, it was recommended that if uniform pin-loading is to be used for MSD assessment, then the biggest pin-load value from non-uniform distributions should be used instead of the mean one.

8.6. Effect of Change in Stress Level on MSD Assessment

1. For the same standard deviation value for fatigue crack initiation, and considering the uniform pin-loading case, an increase in the nominal stress level (decrease in the mean time to crack initiation) decreased the mean time to the lead crack initiation, the mean time for the lead crack propagation, the mean time to failure as well as the ISP and the SMP but increased the percentage of MSD-like scenarios up to 100 %.

2. MSD-like behaviour was, more noticeably, aggravated by an increase in the nominal stress level (decrease in mean time to fatigue crack initiation) than to a decrease in standard deviation value for fatigue crack initiation.

3. For the higher stress level, it could be seen that the failure behaviour from the deterministic MSD (simultaneous fatigue crack initiation and propagation from all fatigue critical locations) was close to the simulations result and that it could be safely prevented.

4. Comparing the percentage of MSD-like scenarios obtained with two different nominal stress levels, and as in other MSD simulations from the literature, it was observed that a great number of the scenarios generated by Monte Carlo simulations contained only one crack (lower stress level), and therefore they could not represent MSD-like situations.

5. A decrease in the percentage of mono-crack scenarios (increase in the percentage of MSD-like scenarios) was observed by increasing the nominal stress level, decreasing the standard deviation for fatigue crack initiation, and by using the uniform pin-loading distribution instead of the non-uniform pin-loading one.

6. Despite of the presence of mono-crack scenarios or not, all simulations were able to establish both the ISP and the SMP before that any threat could be caused by the corresponding deterministic MSD failure situation (simultaneous fatigue crack initiation and propagation from all fatigue critical locations).

8.7. The Role of Number of Cracks and Crack Nucleation Positioning on MSD Assessment Modelling

1. A clear tendency of decreasing the mean time for the lead crack propagation with increasing number of MSD-like scenarios could be verified. But not always a bigger number of nucleated cracks per damage scenario gave the smallest time for crack propagation.

2. The crack nucleation sequence has been demonstrated to play the most important role in decreasing the mean time for crack propagation of the lead crack compared to the number of nucleated cracks per damage scenario.

3. When cracks nucleated at the same hole or at adjacent holes, before the lead crack linked-up for the first time, the mean time for crack propagation was smaller compared to damage scenarios where cracks nucleated more than one pitch distance from each other, regardless of the number of nucleated cracks.

8.8. Effect of Rivet Squeeze Force on MSD Assessment

1. When MSD assessment was performed using the input parameters from the high rivet squeeze force S-N data, compared to the same assessment but using the S-N data input from a mean squeeze force value, the results indicated that the whole MSD failure process was retarded and the number of MSD-like scenarios considerably reduced, demonstrating that high squeeze force is extremely beneficial for MSD prevention.

8.9. MSD Assessment Comparison to Teardown Inspections from In-Service Data

1. Evidences from in-service MSD detection strongly indicated that S-N input data obtained from good quality riveted flat lap joint test specimens would not be appropriate for MSD assessment of real aircraft pressurized fuselage panels. Those evidences were also supported by published MSD assessment of a full-scale fatigue test and by a probabilistic fatigue crack initiation analysis using S-N data from good quality riveted lap joints corresponding to the in-service geometrical configuration analysed.

2. The MSD assessment presented was performed with an open hole quality S-N data, and the cumulative probabilities for fatigue crack initiation, crack detection and failure were rationally conservative compared to in-service findings for the corresponding distributions. The differences were in the order of 20%, with the

smallest differences belonging to the fatigue crack initiation part of the simulations.

3. In-service data indicated that both the ISP and the SMP were well established from the simulations, and failure due to MSD occurrence was not a threat for structural safety during the monitoring period.

4. Severe in-service fatigue cracking pattern from 3 fuselage panels compared very well to the same results from the simulations. The cracking pattern obtained from analysis presented no mono-crack scenarios, 40% of the scenarios contained all holes cracked (with at least one crack per hole) and 1.3% of the scenarios developed 21 cracks out of 22 possible fatigue critical locations before the lead crack linked-up.

Chapter 9

9. FUTURE WORK

From the MSD assessment model presented in this work, some limitations of the model were discussed in chapter 7. As the great majority of published MSD assessment models, only a few hundreds of Monte Carlo simulations were performed in each simulation from this work. The direct consequence of the small number of simulations is that low probabilities of occurrence could only be assessed via the extrapolation of the simulations by means of fitted statistical distributions. Although this procedure is acceptable from the engineering point of view, the best solution would be performing as much simulations as necessary, for example 100,000 simulations, to achieve the desired results; and the main problem that has to be overcome belongs to the crack propagation stage of MSD modelling. With existing technology it is possible to perform crack propagation on a few hundreds of damage scenarios by using FE or BE based computer codes in a reasonable period of time (from two to four weeks); but thousands of simulations is completely out of purpose. As a future work, and in order to provide a solution to overcome this problem, it is recommended the development of an in-house computer code by using the compounding method for stress intensity factors calculation [49] to perform crack growth analysis. This type of approach has been reported in the literature [32] an it seems highly recommended since, instead of taking a few weeks, thousands of crack growth simulations can be performed in a few minutes. After the implementation of the suggested code, it would be quite interesting to compare the values obtained from the cumulative probabilities of failure from this work, especially for the tail of the distributions (low probability region), for establishing whether the differences are significant or not.

Considering the crack growth analysis performed with the present computer code, it is recommended that in future a damage accumulation technique routine could be implemented in order to quantify more precisely the differences between the continuing damage assumption and damage accumulation technique on MSD assessment. This comparison has been presented in the discussions chapter in general terms by

comparing the Monte Carlo simulation points as a whole. Although general good agreement was observed, the differences were established in a broad way but they were not quantified scenario by scenario. It has also to be highlighted that the use of a damage accumulation technique coupled with probabilistic crack growth, and not only with deterministic crack growth, is still in need for investigation and comparison to other models.

Regarding the MSD model presented in this work it is clear that environmental effects, such as corrosion, were not addressed. The way corrosion might be modelled in a probabilistic way for MSD assessment and what effects it demonstrates on MSD behaviour is an open field for future researchers.

Regarding the parametric studies presented, it is certain that some other variables could be studied in the future as this field has been poorly investigated from the literature. The effect of number of holes on MSD assessment is a clear example, and many others could be imagined by future workers. What differences an increase (or decrease) in the number of holes would make for establishment of MSD parameters such as the ISP and the SMP is an interesting issue only addressed by Horst [35] via theoretical examples. Another interesting example would be modelling a lap joint taking into account a real fuselage stress profile (where frames were present) and perform MSD assessment on a basis of different pin-loadings. In this case, crack propagation could even be arrested with the proximity of crack tips to frames and big differences in the whole crack propagation process could possibly happen.

Regarding the experimental work performed, the benefits that high squeeze force brings to MSD prevention by means of probabilistic analysis performed by Monte Carlo simulations was clearly established; but only a unique geometrical configuration was analysed. It may be that other geometrical configurations (or material) could provide even better improvement for MSD prevention than the one analysed. In such a sense, more fatigue test data using riveted joints with high squeeze force values are needed to generate appropriate S-N input data for MSD probabilistic assessment models. Another interesting point is to determine how much rivet squeeze force could be increased so

that benefits to MSD prevention are still valid. It can be realized that high squeeze force cannot be increased indefinitely, and the point of maximum squeeze force for different geometrical configurations may even present any relationship that has not been established yet.

For the in-service data comparison discussed in chapter 7, strong evidences were presented indicating that good quality riveted lap joint test specimens were not able to provide S-N input data for MSD assessment of real aircraft fuselage panels. The lack of approach from the literature on such an important issue is surprising. It seems that many authors do believe that, as far as the lap joints are manufactured with the same material and construction techniques employed in the production line, good quality riveted joints can provide S-N data to predict in-service behaviour. What this work showed was that open hole S-N fatigue data demonstrated to be reasonably suitable for MSD analysis of in-service structures. The main question that has to be answered from future workers is whether open hole S-N data is always suitable or not for different geometrical configurations than the one that has been analysed. It may be that for other fuselage panel configurations, open hole quality S-N data demonstrates inadequacy and, possibly, good quality riveted lap joint S-N data should be more appropriate. This issue has only been started with this work, and further MSD assessments for different in-service aircraft types are needed.

Finally, the MSD methodology from this work demonstrated to be a valid engineering tool for MSD assessment of riveted joints. Considering new design configuration for riveted joints, the current MSD model can be used to analyse such joints and then to select the configuration which would best prevent from MSD occurrence for demonstrating the highest mean MSD failure behaviour (which leads to the highest ISP and SMP points). To accomplish this task, MSD can be analysed during its different stages (initiation, propagation and failure) for each damage scenario as described in chapter 4 and, as different joint geometrical configurations can lead to different pin-loading distributions, the necessary S-N input data for MSD modelling can be obtained experimentally as in chapter 5.

10. REFERENCES

1. Aircraft Accident Report: Aloha Airlines, Flight 243, Boeing 737-200, N73711, near Maui, Hawaii, April 28, 1988. U.S. National Transportation Safety Board, Washington, 1989.
2. Tong, P., Arin, K., Jeong, D. Y., Greif, R., Brewer, J. C., Bobo, S. N., Sampath, S. G., Current DOT research on the effect of multiple site damage on structural integrity, International Conference on Aging Aircraft and Structural Airworthiness, Washington DC, Nov. 1991.
3. AAWG, Recommendations for regulatory action to prevent widespread fatigue damage in the commercial airplane fleet, a Report of the Airworthiness Assurance Working Group (AAWG) for the Aviation Rulemaking Advisory Committee Transport Aircraft and Engine Issues, March 11, 1999.
4. Jones, R., Molent, L., Pitt, S., Study of multi-site damage of fuselage lap joints, Theoretical and Applied Fracture Mechanics, no. 32, pp. 81-100, 1999.
5. Schmidt, H.-J., Schimidt-Brandecker, B., Trey, H., AIRBUS A300 fuselage program for life extension and widespread fatigue damage evaluation, The 3rd Joint FAA/DoD/NASA Conference on Aging Aircraft, Albuquerque, New Mexico, USA, September 1999.
6. Zhang X., "Fatigue and fracture mechanics", Lecture Notes, College of Aeronautics, Cranfield University, 2003.
7. Lukas, P., Kunz, L., Small cracks – nucleation, growth and implication to fatigue life, International Journal of Fatigue, no. 25, pp. 855-862, 2003.
8. Suresh, S., Fatigue of materials, 2nd ed., ISBN 0-521-57046-8, Cambridge University Press, 1998.
9. Niu, M. C. Y., Airframe structural design: practical design information and data on aircraft structures, Hong Kong: Conmilit Press, 1999.
10. Broek, D., The practical use of fracture mechanics, Kluwer Academic Publishers, The Netherlands, 1988.
11. Aliabadi, M. H., Rooke, D. P., Numerical Fracture Mechanics, Computational Mechanics Publications, Southampton and Kluwer Academic Publishers, Dordrecht, The Netherlands, 1991.
12. Irving, P. E., Damage tolerance in aircrafts, lecture notes, School of Industrial and Manufacturing Science, Cranfield University, 2003.
13. Eastaugh, G., Simpson, D., Straznicky, P., Wakeman, R., A special uniaxial coupon test specimen for the simulation of multiple site fatigue crack growth and link-up in fuselage skin splices, NASA N96-24261, 1995.
14. Vlieger, H., Ottens, H. H., Uniaxial and biaxial tests on riveted fuselage lap joint specimens, report no. DOT/FAA/AR-98/33, 1998.
15. Steadman, D., Carter, A., Ramakrishnan, R., Characterization of MSD in an in-service fuselage lap joint, 3rd Joint FAA/DoD/NASA Conference on Aging Aircraft, Albuquerque, New Mexico, September 1999.
16. Balzano, M., Beaufils, J.-Y., Santgerma, A., An engineering approach to the assessment of widespread fatigue damage in aircraft structures, The Second Joint NAS/FAA/DoD Conference on Aging Aircraft, 1998.

17. Cavallini, G., Galatolo, R., Cattaneo, G., An experimental and numerical analysis of multi-site damaged butt-joints, Proceedings of the 20th ICAF Symposium, Vol. 1, Bellevue, Washington, U.S.A., July 1999.
18. Horst, P., Lessons learned from recent European research projects on aging aircraft, Proceedings of the CEAS Forum - Life Extension – Aerospace Technology Opportunities, Cambridge, UK, 1999.
19. Schijve, J., Statistical distribution functions and fatigue of structures, International Journal of Fatigue, no. 27, pp. 1031-1039, 2005.
20. Stagg, A. M., An investigation of the scatter in constant amplitude fatigue test results of aluminium alloys 2024 and 7075, Structures Dept., R.A.E., C.P. No. 1093, 1969.
21. Press, W. H., Teukolsky, S. A., Vetterling, W. T., Numerical recipes in FORTRAN: the art of scientific computing, Cambridge University Press, 2nd Ed., 1992.
22. Griffith, A. A., The phenomena of rupture and flow in solids, Phil. Trans. Roy. Soc., Series A, Vol. 221, pp. 163-198, 1921.
23. Irwin, G. R., Fracturing of metals, Proc. ASM Symposium, ASM, pp. 147-166, Cleveland, 1948.
24. Orowan, E., Fundamental of brittle behaviour in metals, Fatigue and Fracture of Metals, edited by W. M. Murray, pp. 139-167, 1952.
25. Irwin, G. R., Analysis of stresses and strains near the end of a crack traversing plate, Trans. ASME, J. Appl. Mech., Vol. 24, pp. 361-364, 1957.
26. Paris, P. C., The fracture mechanics approach to fatigue, Fatigue – an interdisciplinary approach, edited by J. J. Burke, N. L. Reed and V. Weiss, pp. 107-132, Syracuse University Press, 1964.
27. ESDU 80036, Introduction to the use of linear elastic fracture mechanics in estimating fatigue crack growth rates and residual strength of components, ISBN 0-85679-319-1, issued November 1980, amendment A and B, July 1996.
28. Elber, W., Fatigue crack propagation: some effects of crack closure on the mechanisms of fatigue crack propagation and cyclic tensile load, Ph.D. Theses, University of New South Wales, Australia, 1968.
29. Piascik, R., Willard, S., Characterization of multi-site damage in fuselage structure, The 1st Joint DoD/FAA/NASA Conference on Aging Aircraft, Ogden, Utah, July 1997.
30. Horst, P., Schmidt, H., A concept for evaluation of MSD based on probabilistic assumptions, AGARD Conference Proceedings 568, Neuilly-Sur-Seine, France, 1995.
31. Santgerma, A., Developpement d'une methodologie de prevision du comportement des strutures d'avions civils en presence de dommages multiples de fatigue, Doctorate Thesis, Department of Mechanical Engineering, Toulouse, 1997.
32. Lazzeri, R., The PISA code, Aerotecnica Missili e Spazio, Vol. 81 – 1, Italy, 2002.
33. Horst, P., Schmidt, H.-J., On the significance of probabilistic parameters for the assessment of MSD in the case of aging aircraft, Proceedings of the 19th ICAS Congress, Anaheim, USA, Sept. 1994.

34. Horst, P., On the assessment of the criticality of crack scenarios with respect to widespread fatigue damage, 2nd Joint NASA/FAA/DoD Conference on Aging Aircraft, USA, 1999.
35. Horst, P., The influence of difference assumptions on statistical distributions on possible scatter factors in the case of widespread fatigue damage, 5th Joint NASA/FAA/DoD Conference on Aging Aircraft, Orlando, Florida, September, 2001.
36. Xiong, Y., Eastaugh, G., Shi, G., Probabilistic failure analysis of fuselage splice joints with multiple site damage and corrosion, Proceedings of the 29th Symposium of the International Committee on Aeronautical Fatigue, Seattle, USA, 1999.
37. Santgerma, A., Beaufils, J.-Y., Rosemberg, B., An example of widespread fatigue damage assessment in A300 susceptible structure, The 4th Joint DoD/FAA/NASA Conference on Aging Aircraft, St. Louis, USA, May 2000.
38. Cavallini, G., Lazzeri, R., Simulazione numerica e prove sperimentali di fenomeni di fatica in giunti metallici chiodati in presenza di widespread fatigue damage, Parte I – Attivita Teorica, DDIA 98-6, Giugno, 1998.
39. Kebir, H., Roelandt, J. M., Gaudin, J., Monte Carlo simulations of life expectancy using the dual boundary element method, Engineering Fracture Mechanics 68, 1371-1384, 2001.
40. Proppe, C., Probabilistic analysis of multi-site damage in aircraft fuselages, Computational Mechanics 30, 323-329, 2003.
41. Shkarayev, S., Krashanitsa, R., Probabilistic method for the analysis of widespread fatigue damage in structures, International Journal of Fatigue 27, 223-234, 2005.
42. Shinozuka, M., Deodatis, G., Sampath, S. G., Asada, H., Statistical Property of Widespread Fatigue Damage, AGARD SMP Specialists' Meeting on Widespread Fatigue Damage of Military Aircraft, published in CP-568, Rotterdam, The Netherlands, May 1995.
43. Shoji, H., Shinozuka, M., Sampath, S., A Bayesian evolution of simulation models of multiple-site fatigue cracks, Probabilistic Engineering Mechanics 16, 355-361, 2001.
44. Buhler, K., Grandt Jr., A. F., Moukawsher, E. J., Fatigue analysis of multiple site damage at a row of holes in a wide panel, Proc. of FAA/NASA International Symposium on Advanced Structural Integrity Methods for Airframe Durability and Damage Tolerance, Hampton, VA, NASA-CP-3274, 4-6 May 1994.
45. Moukawsher, E. J., Grandt Jr., A. F., Neussl, M. A., Fatigue life of panels with multiple site damage, Journal of Aircraft, Vol. 33, No. 5, September-October 1996.
46. Pidaparti, R. M. V., Palakal, M. J., Rahman, Z. A., Simulation of structural integrity predictions for panels with multiple site damage, Advances in Engineering Software 31, 127-135, 2000.
47. Liao, M., Shi, G., Xiong, Y., Analytical methodology for predicting fatigue life distribution of fuselage splices, International Journal of Fatigue 23, S177-S185, 2001.

48. Tong, Y. C., Literature review on aircraft structural risk and reliability analysis, DSTO Aeronautical and Maritime Research Laboratory, DSTO-TR-1110, Melbourne, Australia, February 2001.
49. ESDU 78036, The compounding method of estimating stress intensity factors for cracks in complex configurations using solutions from simple configurations, ISBN 0-85679-240-3, issued November 1978, amendment A, December 1980.
50. Silva, L. F. M., Goncalves, J. P. M., Oliveira, F. M. F., de Castro, P. M. S. T., Multiple-site damage in riveted lap-joints: experimental simulation and finite element prediction, International Journal of Fatigue 22, 319-338, 2000.
51. Virkler, D. A., Hillberry, B. M., Goal, P. K., Journal of Engineering Materials and Technology, Vol. 101, pp. 148-153, 1979.
52. Ghonem, H., Dore, S., Experimental study of the constant-probability crack growth curves under constant amplitude loading, Eng. Fract. Mech. 27(1): 1-25, 1987.
53. Chiarelli, M., Lanciotti, A., Lazzeri, L., Fatigue behaviour of metallic lap joints: a study on the effect of riveting and of specimen geometry, 20th Symposium of the International Committee on Aeronautical Fatigue - ICAF 99, Bellevue, Washington, USA, July 1999.
54. Yang, J. N., Manning, S. D., Rudd, J. L., His, W. H., Stochastic crack propagation in fastener holes, Proceedings of the 26th AIAA/ASME/ASCE/AHS Structures, Structural Dynamics and Materials Conference, Orlando, April 1985.
55. Wang, G. S., Intrinsic Statistical Characteristic of Fatigue Crack Growth Rate, Engineering Fracture Mechanics, Vol. 51, No. 5, pp. 787-803, 1995.
56. Wang, G. S., A Probabilistic Damage Accumulation Solution Based on Crack Closure Model, International Journal of Fatigue 21, 531-547, 1999.
57. Xiong, Y. and Shi, G., Stochastic Damage Growth Model for Fuselage Splices with Multisite Damage, AIAA Journal, Vol. 39, No. 3, March 2001.
58. Cavallini, G., Lanciotti, A., Lazzeri, L., A probabilistic approach to aircraft structures risk assessment, Proceedings of the 19th Symposium of the International Committee on Aeronautical Fatigue – ICAF 97, Edinburgh, Scotland, June 1997.
59. Wang, G. S., Analysing the onset of multiple site damage at mechanical joints, International Journal of Fracture 105: 209-241, 2000.
60. Ostergaard, D. F., Hillberry, B. M., Characterization of the variability in fatigue crack propagation data, Probabilistic Fracture Mechanics and Fatigue Methods: Application for Structural Design and Maintenance, STM STP 798, 1983.
61. Newman, J. C., Harris, C. E., Piascik, R. S., Dawicke, D. S., Methodology for predicting the onset of widespread fatigue damage in lap-splice joints, Langley Research Center, NAS/TM-1998-208975.
62. Tan, P. W., Bigelow, C. A., Bakuckas Jr., J. G., Widespread fatigue damage assessment approach, Applied Vehicle Technology Panel, Life Management Techniques for Aging Air Vehicles, Manchester, U.K., October 2001.
63. Lincoln, J. W., Melliere, R. A., Economic life determination for a military aircraft, Journal of Aircraft, Vol. 36, No. 5, September-October 1999.

64. Yang, J. N., Manning, S. D., Demonstration of probabilistic-based durability analysis method for metallic airframes, Journal of Aircraft, Vol. 27, No. 2, February 1990.
65. Rohrbaugh, S. M., Ruff, D., Hillberry, B. M., McCabe, G., Grandt Jr., A. F., A probabilistic fatigue analysis of multiple site damage, FAA/NASA International Symposium on Advanced Structural Integrity Methods for Airframe Durability and Damage Tolerance, Hampton, Virginia, May 1994.
66. Shah, S., Bell, R. P., Lemmers, P. L., Alford, R. E., A probabilistic approach to predict the onset of wide spread fatigue cracking in C-141 fuselage structure, ICAF 99 International Committee on Aeronautical Fatigue, Bellevue, Washington, July 12-16, 1999.
67. Kurth, R. E., Bigelow, C. A., Transport risk assessment containing widespread fatigue damage: TRACWFD analyses of longitudinal and circumferential splice joints to determine the onset of widespread fatigue damage and its probability of occurrence, The Second Joint NAS/FAA/DoD Conference on Aging Aircraft, 1998.
68. Rudd, J. L., Gray, T. D., Quantification of fastener-hole quality, Journal of Aircraft, Vol. 15, No. 3, pp. 143-147, 1978.
69. Manning, S. D., et al., Durability methods development, Vol. 1, Air Force Flight Dynamic Laboratory, TR-79-3118, September 1979.
70. Yang, J. N., Manning, S. D., Distribution of equivalent initial flaw size, Proceedings of Annual Reliability and Maintenance Symposium, pp. 112-120, January 1980.
71. Manning, S. D., Yang, J. N., USAF durability design handbook: guidelines for the analysis and design of durable aircraft structures, AFWAL-TR-83-3027, Air Force Flight Dynamics Laboratory, WPAFB, OH, January 1984.
72. Manning, S. D., Yang, J. N., Advanced durability analysis, Vol. I – analytical methods, AFWAL-TR-86-3017, Air Force Wright Aeronautical Laboratories, WPAFB, OH, July 1987.
73. Manning, S. D., Yang, J. N., Advanced durability analysis, Vol. II – analytical predictions, test results and analytical correlations, AFWAL-TR-86-3017, Air Force Wright Aeronautical Laboratories, WPAFB, OH, February 1989.
74. Harris, C. H., Piascik, R. S., Newman Jr., J. C., A practical engineering approach to predicting fatigue crack growth in riveted lap joints, NASA/TM-2000-210106, May 2000.
75. Gallagher, J. P., Babish, C. A., Malas, J. C., Damage tolerant risk analysis for evaluating the structural integrity of aircraft structures, 11th International Conference on Fracture (ICF 11), Turin, Italy, March 20-25, 2005.
76. Gallagher, J. P., Giessier, F. J., Berens, A. P., USAF damage tolerant design handbook: guidelines for the analysis and design of damage tolerant aircraft structures, Flight Dynamics Laboratory, Wright-Patterson Air Force Base, Ohio, May 1984.
77. Zhang, J., Park, J. H., Atluri, S. N., Analytical fatigue life estimation of full-scale fuselage panel, Proceedings of the FAA-NASA Symposium on the Continued Airworthiness of Aircraft Structures, DOT/FAA/AR-97/2, Atlanta, Georgia, August 28-30, 1997.
78. Slagter, W. J., Static strength of riveted joints in fibre metal laminates, ISBN 90 9007089 3, Delft University of Technology, Delft, The Netherlands, 1994.

79. Muller, R. P. G., An experimental and analytical investigation on the fatigue behaviour of fuselage riveted lap joints – the significance of the rivet squeeze force, and a comparison of 2024-T3 and Glare 3, Doctorate Thesis, Delft University of Technology, The Netherlands, 1995.
80. Muller, R. P. G., Hart-Smith, L. J., Making fuselage riveted lap splices with 200-year crack-free fatigue lives, Proceedings of the 19th Symposium of the International Committee on Aeronautical Fatigue (ICAF), Edinburgh, 18-20 June, 1997.
81. Fawaz, S. A., Fatigue crack growth in riveted joints, Doctorate Thesis, Delft University of Technology, Delft, The Netherlands, 1997.
82. Wang, H.-L., Grandt Jr., A. F., Fatigue analysis of multiple site damage in lap joint specimens, 30th Symposium of Fatigue and Fracture Mechanics, Kenneth L. Jerina and Paul C. Paris editors, ASTM STP 1360.
83. Harish, G., Farris, T. N., An integrated approach for prediction of fretting crack nucleation in riveted lap joints, AIAA/ASME/AHS/ASC Structures, Structural Dynamics, and Materials Conference, St. Louis, MO, Apr, 1999.
84. Terada, H., Structural fatigue and joint degradation, International Journal of Fatigue 23, S21-S30, 2001.
85. Harish, G., Farris, T. N., Shell modelling of fretting in riveted lap joints, AIAA Journal, Vol. 36, No. 6, June 1998.
86. Ofsthun, M., When fatigue quality enhancers do not enhance fatigue quality, International Journal of Fatigue 25, 1223-1228, 2003.
87. Salgado, N. K., Damage Tolerance Design System – DTD Computer Code (Version 5.0), Empresa Brasileira de Aeronautica (EMBRAER), Sao Jose dos Campos – SP, Brazil, 1999.
88. Portela, A., Aliabadi, H. M., Rooke, D. P., The dual boundary element method: effective implementation for crack problems, Int. J. Num. Methods Engng., Vol. 33, pp. 1269-1287, 1992.
89. Brebbia, C. A., Telles J. C. F. and Wrobel L. C., Boundary Elements Techniques: Theory and Applications in Engineering, Springer-Verlag, 1984.
90. Salgado, N. K., Aliabadi, M. H., The application of the dual boundary element method to the analysis of cracked stiffened panels, Engineering Fracture Mechanics Vol. 54, No. 1, pp. 91-105, 1996.
91. Bezerra, L. M., de Medeiros, J. M. S., Using boundary elements and J-integral for the determination of K_I in Fracture Mechanics, International Association for Boundary Element Methods, IABEM 2002, TX, USA, May, 2002.
92. Cartwright, D. J., Rooke, D. P., An efficient boundary element model for calculating Green's function in fracture mechanics, Int. J. Fracture, 27, R43-R50, 1985.
93. Portela, A., Aliabadi, M. H., Rooke, D. P., The Dual Boundary Element Incremental Analysis of Crack Propagation, Computers and Structures, Vol. 46, No. 2, pp. 237-247, 1993.
94. Salgado, N. K., Aliabadi, M. H., The analysis of mechanically fastened repairs and lap joints, Fatigue Fract. Engng. Mater. Struct. Vol. 20, No. 4, pp. 583-593, 1997.
95. Salgado, N. K., Aliabadi, M. H., Boundary element analysis of fatigue crack propagation in stiffened panels, Journal of Aircraft Vol. 35, No. 1, January-February, 1998.

96. Erdogan, F., Sih, G. C., On crack extension in plates under plane loading and transverse shear, Journal of Basic Engineering, Vol. 85, pp. 519-527, 1963.
97. Tanaka, K., Fatigue crack propagation from a crack inclined to the cyclic tensile axis, Engineering Fracture Mechanics, Vol. 6, pp. 493-507, 1974.
98. Swift, T., Fracture analysis of stiffened structure, damage tolerance of metallic structures: analysis methods and applications, ASTM STP 842, JB Cang and JL Rudd Eds., American Society for Testing and Materials, pp. 69-107, 1984.
99. Cope, D. A, Lacy, T. E., Stress intensity determination in lap joints with mechanical fasteners, 41st AIAA/ASME/ASCE/AHS/ASC Structures, Structural Dynamics and Materials Conference and Exhibit, Atlanta, GA, pp. 274-283, 2000.
100. Swift, T., Repairs to damage tolerant aircraft, Atluri, S. N., Sampath, S. G., Tong, P., eds., Structural Integrity of Aging Airplanes, Spring-Verlag Berlin, Heidelberg, 1991.
101. Hudson, R. A., Gaussian random number generator computer code - gauss3.exe, School of Industrial and Manufacturing Science, Cranfield University, 2003.
102. Harris, C. H., Newman Jr., J. C., Piascik, R. S., Starnes Jr., J. H., Analytical methodology for predicting the onset of widespread fatigue damage in fuselage structure, Proceedings of the FAA-NASA Symposium on the Continued Airworthiness of Aircraft Structures, DOT/FAA/AR-97/2, Atlanta, Georgia, August 28-30, 1997.
103. Swift, T., Widespread fatigue damage monitoring issues and concerns, Proceeding of the 5th International Conference on Structural Airworthiness of New and Aging Aircraft, Hamburg, Germany, June 1993.
104. Cherry, M. C., Mall, S., Heinimann, B., Grandt Jr., A. F., Residual strength of unstiffened aluminium panels with multiple site damage, Engineering Fracture Mechanics, Vol. 57, No. 6, pp. 701-713, 1997.
105. Smith, B. L., Hijazi, A. L., Haque, A. K. M., Myose, R. Y., Modified linkup models for determining the strength of stiffened panels with multiple site damage, The 3rd Joint FAA/DoD/NASA Conference on Aging Aircraft, Albuquerque, New Mexico, September 1999.
106. Moukawsher, E. J., Heinimann, M. B., Grandt Jr., A. F., Residual strength of panels with multiple site damage, Journal of Aircraft, Vol. 33, No. 5, September-October, 1996.
107. Miner, M. A., Cumulative damage in fatigue, Trans. ASME J. Appl. Mech. No. 12, A159-A164, 1945.
108. Xing, J., Hong, Y. J., A maximum likelihood method for estimates of the statistics of the crack growth behaviour, International Journal of Pressure Vessels and Piping, Vol. 76, pp. 641-646, 1999.
109. Chatfield, C., Statistics for technology: a course in applied statistics, 3rd ed., Chapman and Hall, New York, 1983.
110. Meyer, E. S., Fields, S. S., Reid, P. A., Projecting aircraft fleet reliability, 5th Joint NASA/FAA/DoD Conference on Aging Aircraft, Florida, USA, September 10-13, 2001.
111. Jones, R., Peng, D., A simple method for computing the stress intensity factors for cracks at notches, Engineering Failure Analysis, no. 9, pp. 683-702, 2002.

112. Orringer, O., How likely is multiple site damage, International Symposium on Structural Integrity of Aging Airplanes, Atlanta, 1990.
113. Raikher, V. L., Fatigue and damage tolerance scatter models, FAA/NASA International Symposium on Advanced Structural Integrity Methods for Airframe Durability and Damage Tolerance, NASA Conference Publication 3274 Part 2, Washington, May 1994.
114. Raikher, V. L., Effective method of working out an optimum inspection schedule, The Second Joint NASA/FAA/DoD Conference on Aging Aircraft, 1998.
115. Ahmed, A. A., Bakuckas, J., Smith, C., Bigelow, C., Awerbuch, J., Lau, A., Tan, T.-M, Evolution of multiple-site damage in the riveted lap joint of a fuselage panel, 8th FAA/NASA/DoD Conference on Aging Aircraft, Palm Springs, CA, Jan. 31-Feb. 3, 2005.
116. Schijve, J., Fatigue of structures and materials in the 20th century and the state of the art, International Journal of Fatigue, No. 25, pp. 679-702, 2003.
117. Garcia, A. N., Irving, P. E., MSD simulation in lap joints using a DBEM model, 24th International Congress of the Aeronautical Sciences (ICAS 2004) Yokohama, Japan, 29 August – 3 September, 2004.
118. Garcia, A. N., Irving, P. E., Lap joint MSD assessment using a probabilistic model, 11th International Conference on Fracture (ICF 11), Turin, Italy, March 20-25, 2005.
119. Arnold, B. C., Shavelle, R. M., Joint confidence sets for the mean and variance of a normal distribution, The American Statistician, Vol. 52, no. 2, May 1998.
120. Hoggard, A. W., Fuselage longitudinal splice design, International Symposium on Structural Integrity of Aging Airplanes, Atlanta, GA, 1990.
121. Nesterenko, G. I., Basov, V. N., Fatigue strengh of al-alloys in case of random spectra loading, 24th International Congress of the Aeronautical Sciences (ICAS 2004) Yokohama, Japan, 29 August – 3 September, 2004.
122. Garcia, A. N., Irving, P. E., A study of geometrical correction factors in a MSD scenario, Presented at the Civil Aviation Authority – U.K., Report no. CAA/W30637E/57, Cranfield University, Damage Tolerance Group, U.K., 2003.
123. Okada T., Terada H., Dybskiy P., Fatigue behaviour of lap joint of fuselage model structure. Fifth Joint NASA/FAA/DoD Conference on Aging Aircraft, Orlando, Florida, 2001.
124. Wanhill, R. J. H., Koolloos, M. F. J., Fatigue and corrosion in aircraft pressure lap splices, International Journal of Fatigue, No. 23, pp. S337-S347, 2001.
125. Bakuckas, J. G., Carter, A., Destructive evaluation and extended fatigue testing of retired aircraft fuselage structure, 11th International Conference on Fracture (ICF 11), Turin, Italy, March 20-25, 2005.
126. Bellinger, N. C., Forsyth, D. S., Komorowski, J. P., Damage characterization or corroded 2024-T3 fuselage lap joints, 5th Joint NASA/FAA/DoD Conference on Aging Aircraft, Orlando, Florida, September, 2001.
127. Liao, M., Bellinger, N., Komorowski, J. P., Analytical methodologies for fatigue life prediction of corroded fuselage splices, 5th Joint NASA/FAA/DoD Conference on Aging Aircraft, Orlando, Florida, September, 2001.
128. Schijve, J., Fatigue life until small cracks in aircraft structures. Durability and damage tolerance, FAA/NASA International Symposium on Advanced

Structural Integrity Methods for Airframe Durability and Damage Tolerance, Charles E. Harris Ed., NASA Conference Publication 3274, Part 2, September, 1994.

129. Mayville, R. A., Warren, T. J., A laboratory study of fracture in the presence of lap splice multiple site damage, Structural Integrity of Aging Airplanes, Spring Verlag, pp. 263-273, Berlin, 1990.

APPENDIX A - Fatigue Test Results for a Riveted Unstiffened Lap Joint.

The current appendix presents the rough cracking chronology for 6 unstiffened riveted lap joints from Figure 6.2.1.1 (chapter 6) obtained from the literature [31].

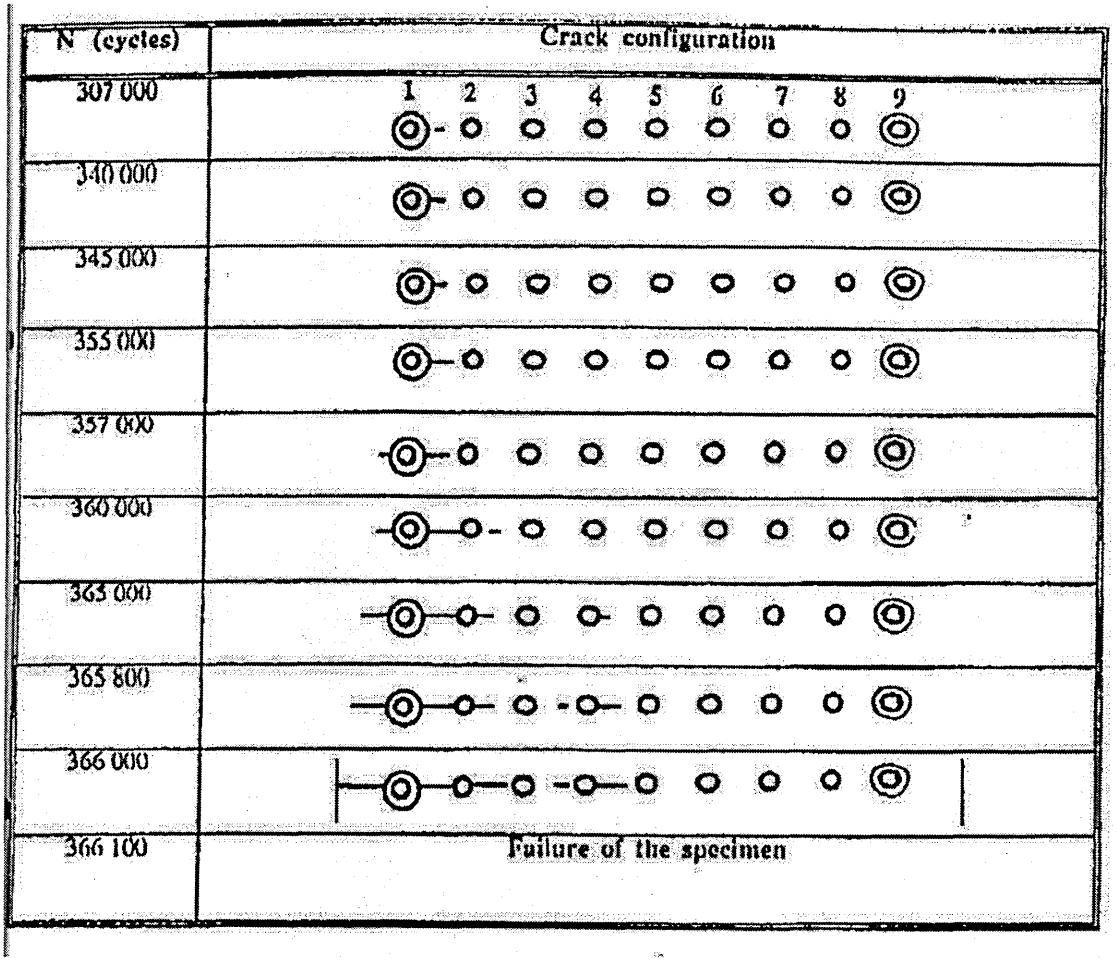

Figure A.1: Test specimen no. 1.

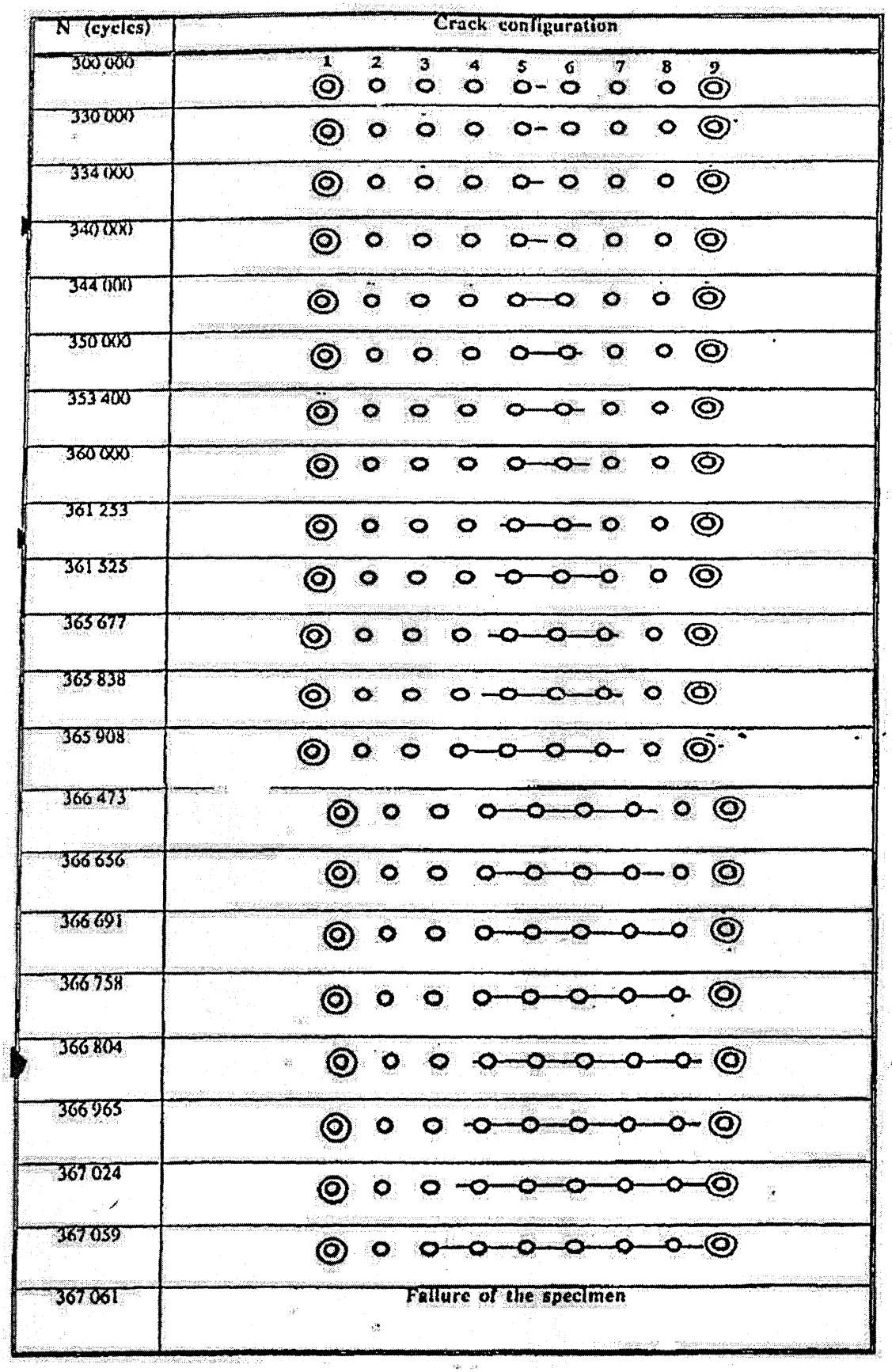

Figure A.2: Test specimen no. 2.

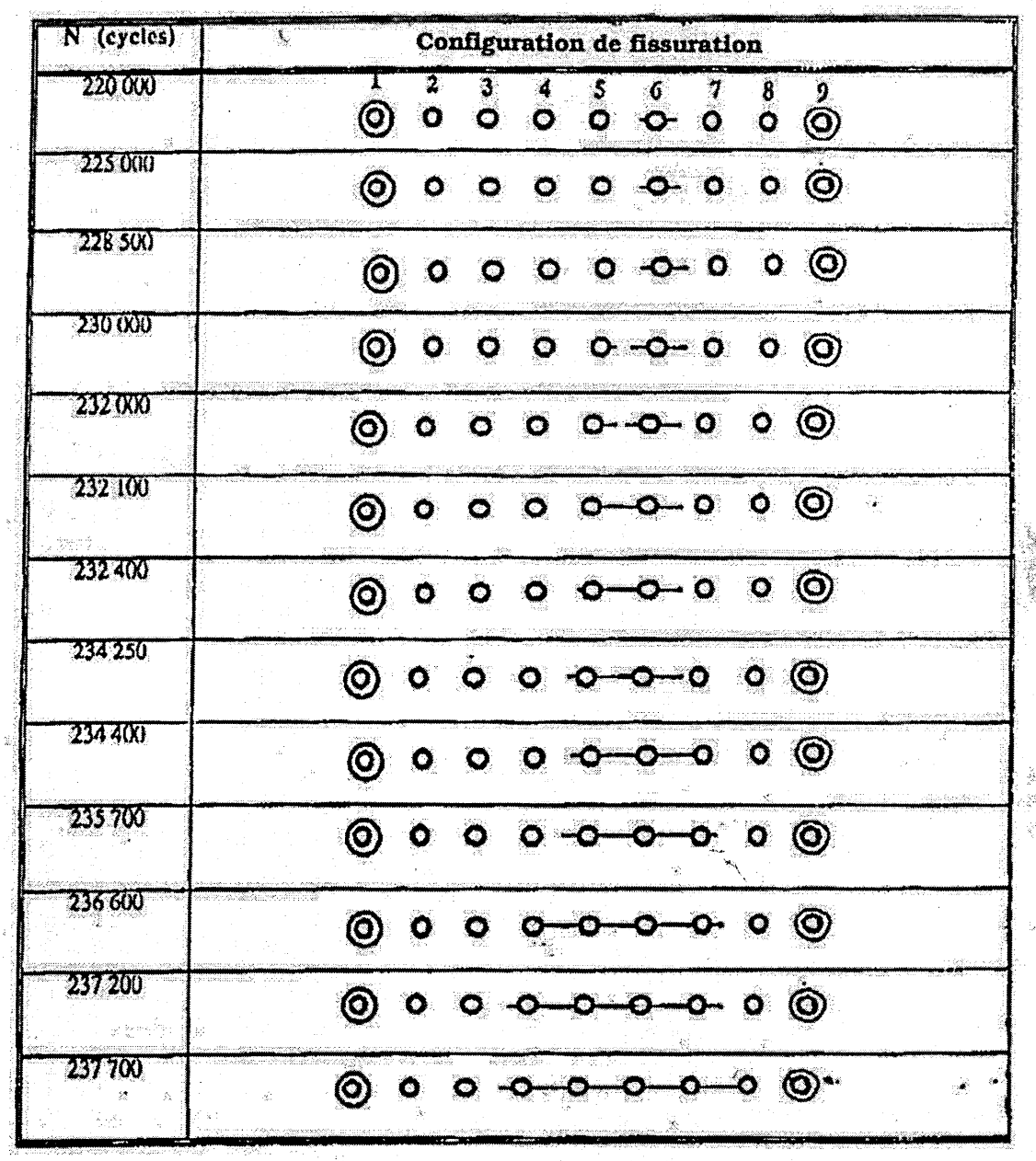

Figure A.3: Test specimen no. 3.

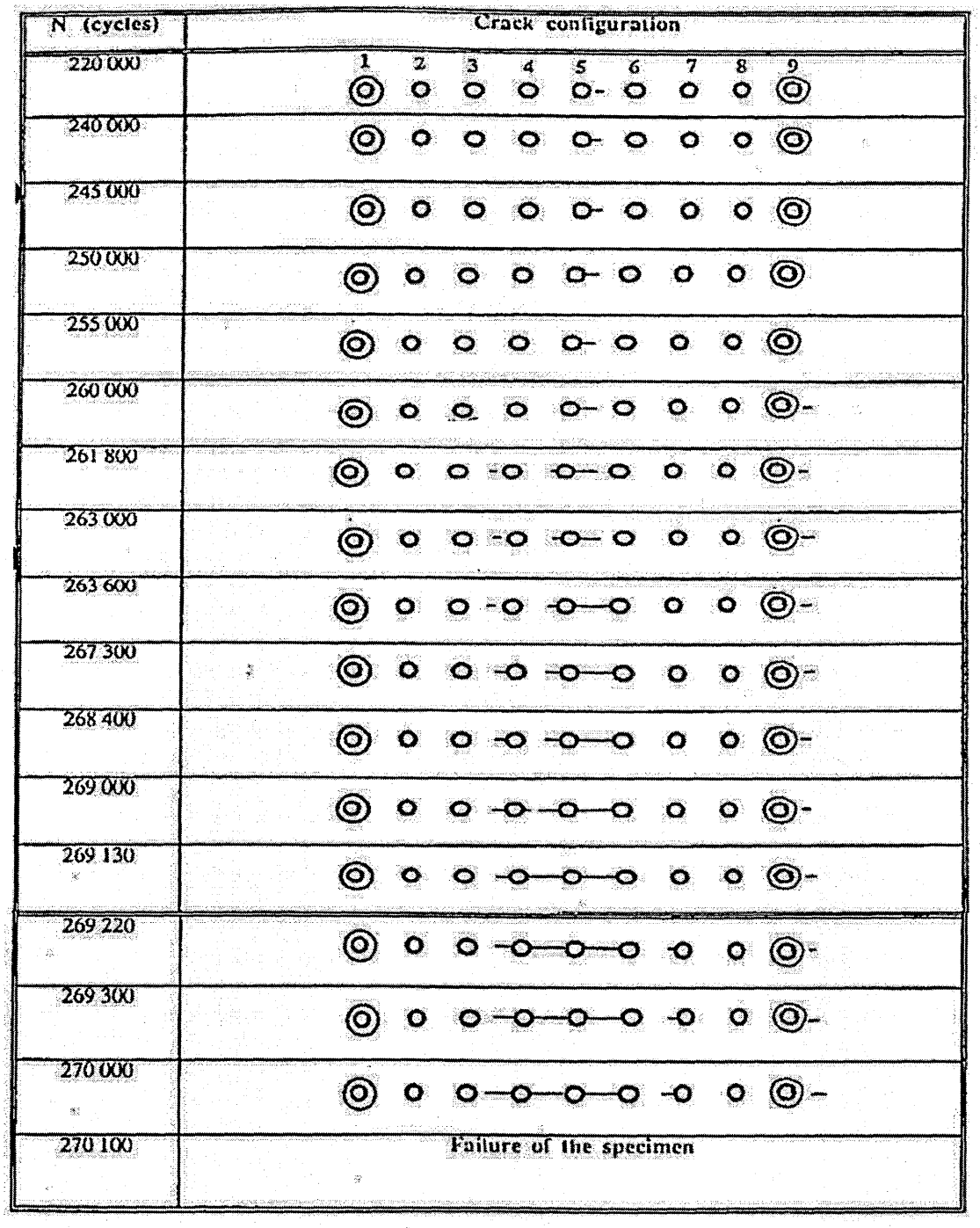

Figure A.4: Test specimen no. 4.

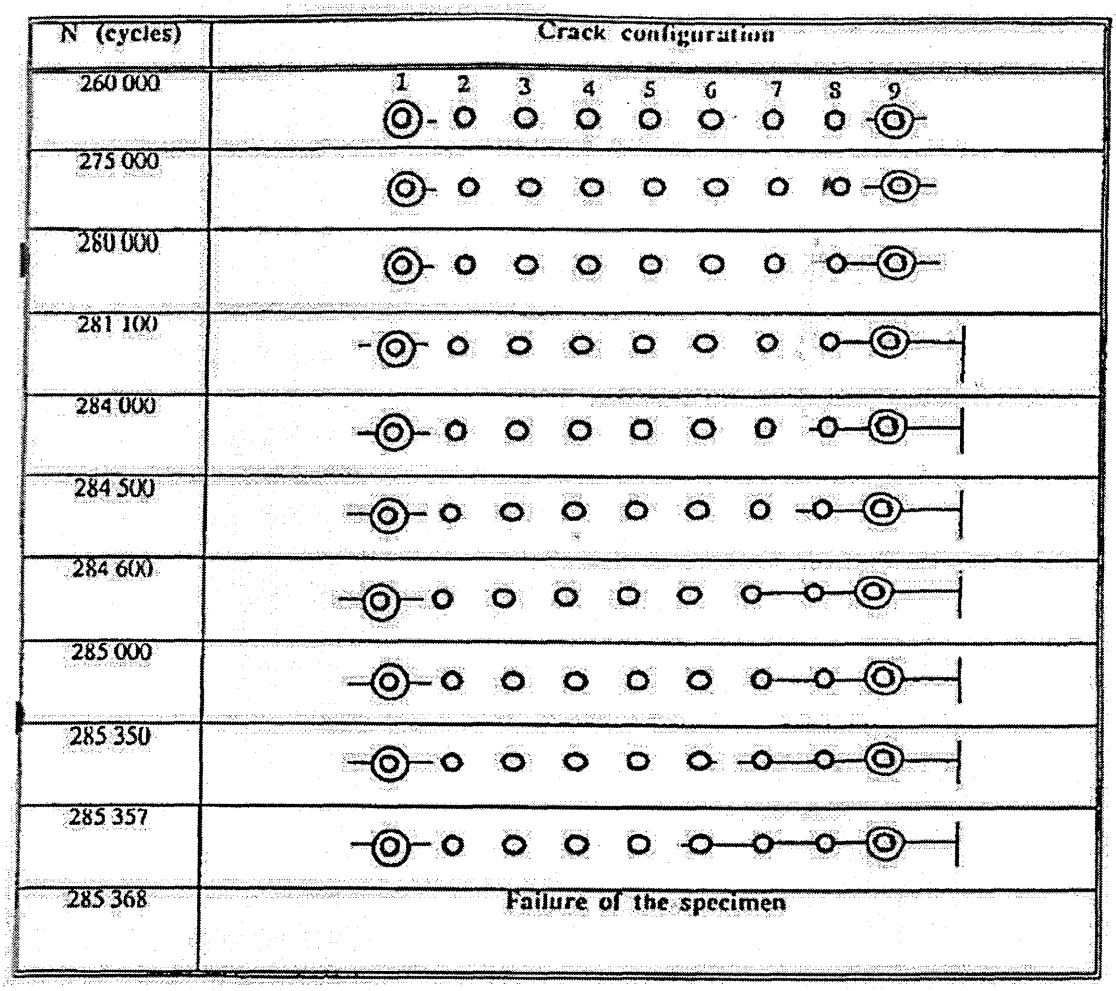

Figure A.5: Test specimen no. 5.

N (cycles)	Crack configuration
120 000	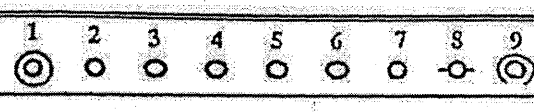
130 000	
135 000	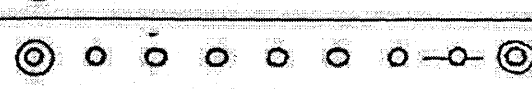
135 900	
136 500	
139 750	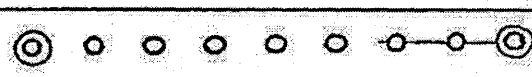
140 500	
142 270	
142 585	
142 646	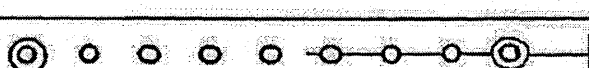
142 681	
142 790	
142 827	Failure of the specimen

Figure A.6: Test specimen no. 6.

APPENDIX B - The Dual Boundary Element Model for the Lap Joint Configuration from Figure 6.2.1.1.

B.1. Lap Joint Dual Boundary Element Model

In order to calculate the rivet reaction loads and the stress intensity factors necessary for performing the crack propagation stage of the MSD model; the DTD code [87] is employed to model the lap joint from Figure 6.2.1.1 using the same DBE lap joint model idealization as presented in chapter 3, i.e., only the upper row of pin-loaded holes (Figure 6.2.1.1) is modelled when cracks are present, the concept of load transfer applies for the middle and lower rows of pin-loaded holes and fastener flexibility is taken into account.

To determine the load transferred by the rivets, a tensile stress level of 100 MPa was applied to the lap joint illustrated in Figure 6.2.1.1. To obtain the rivet reaction loads, the model idealized with the DTD Code consists of two rectangular sheets discretized by 48 boundary elements and 96 nodes each. The sheets are connected by 27 fasteners simulated by spring elements. To take fastener flexibility into account, the fastener shear deformation coefficient was calculated with the following empirical equation from Swift [98]:

$$\Phi=\left[A_1+A_2\left(\frac{\phi}{h_1}+\frac{\phi}{h_2}\right)\frac{1}{E\phi}\right] \qquad \text{B.1.1}$$

Where A_1 and A_2 are empirical constants which, for aluminium fasteners, are $A_1=5.0$ and $A_2=0.8$ according to experimental work from Swift [98]. ϕ is the fastener diameter ($\phi=4.0\,mm$), h_1 and h_2 are the sheet thicknesses ($h_1=h_2=1.6\,mm$) and E is the modulus of elasticity for the aluminium ($E=73{,}000\,MPa$).

The DBE model from Figure B.1.1, which is used for the crack propagation stage of the MSD model, consists of one rectangular sheet, 464 mm long and 200 mm wide,

discretized by 142 boundary elements and 284 nodes, with a central row of nine pin-loaded holes (representing the upper row of holes of the lap joint illustrated in Figure 6.2.1.1). The constraints D_x and D_y are placed half-way at, respectively, the upper and lower borders and at the left and right borders of the model where no displacements are expected due to symmetry. The upper traction vector (T_y) placed in the upper border of the model represents the gross stress; while the lower traction vector (T_y) placed in the lower border of the model represents the bypass stress. All the nine holes are loaded using the same principle of load transfer as described in chapter 3. The hole diameter, pitch distance, sheet thickness and material properties are the same as for the lap joint illustrated in Figure 6.2.1.1.

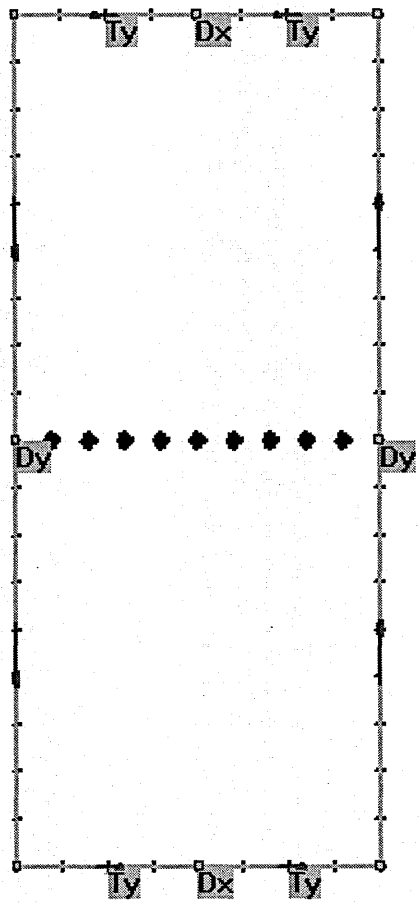

Figure B.1.1: DBE model for the upper row of holes from Figure 6.2.1.1.